The development of calibration and adaptive filtering procedures for neuromagnetic studies of human visual function.

Gareth Robert Barnes

Doctor of Philosophy

The University of Aston in Birmingham

March 1995

The University of Aston in Birmingham

The development of calibration and adaptive filtering procedures for neuromagnetic studies of human visual function.

Gareth Robert Barnes

Doctor of Philosophy

1995

This thesis first considers the calibration and signal processing requirements of a neuromagnetometer for the measurement of human visual function. Gradiometer calibration using straight wire grids is examined and optimal grid configurations determined, given realistic constructional tolerances. Simulations show that for gradiometer balance of $1:10^4$ and wire spacing error of 0.25mm the achievable calibration accuracy of gain is 0.3%, of position is 0.3mm and of orientation is 0.6°. Practical results with a 19-channel 2nd-order gradiometer based system exceed this performance. The real-time application of adaptive reference noise cancellation filtering to running-average evoked response data is examined. In the steady state, the filter can be assumed to be driven by a non-stationary step input arising at epoch boundaries. Based on empirical measures of this driving step an optimal progression for the filter time constant is proposed which improves upon fixed time constant filter performance. The incorporation of the time-derivatives of the reference channels was found to improve the performance of the adaptive filtering algorithm by 15-20% for unaveraged data, falling to 5% with averaging. The thesis concludes with a neuromagnetic investigation of evoked cortical responses to chromatic and luminance grating stimuli. The global magnetic field power of evoked responses to the onset of sinusoidal gratings was shown to have distinct chromatic and luminance sensitive components. Analysis of the results, using a single equivalent current dipole model, shows that these components arise from activity within two distinct cortical locations. Co-registration of the resulting current source localisations with MRI shows a chromatically responsive area lying along the midline within the calcarine fissure, possibly extending onto the lingual and cuneal gyri. It is postulated that this area is the human homologue of the primate cortical area V4.

Keywords : *MEG; gradiometer; evoked response; V4.*

Acknowledgements

I am lucky to have made a number of inspirational friendships during my time spent in Birmingham and Moscow.

At Aston, Paul Furlong, Vivica Tipper, Judith Dunne and Andrea Edson have provided consistent and enthusiastic technical and moral support. Likewise, the guidance provided by Ian Holliday and Steve Anderson has been invaluable especially whenever I have attempted to present or write anything. In particular, many thanks to Krish Singh whose ever evolving S-MEG package I used to analyse the results of the evoked potential studies.

Amongst others, Andrey Matlashov, Valodya Slobodchikov and Serge Nikulin from the Radioengineering Institute in Moscow made my time spent in Russia hugely enjoyable and productive.

Of course, the postgraduates helped too. I am especially grateful to Ola Willis, Fiona Fylan, Lu Wei, Catherine Suttle and James Bedford for their help, advice and friendship.

Finally, many thanks to my supervisor Prof. Graham Harding, without whose enthusiasm neither the MEG team, nor our Russian collaboration would have been possible.

Index

List of figures

Chapter 1.

Introduction

The human visual system performs specific data-processing operations on the neural image formed by photo-transduction of the optical image at the retina. Evidence suggests that this system is composed of neurons organised into functionally distinct areas or elements. The system output is in the form of a subjective percept or an objectively measurable response (Figure 1.1).

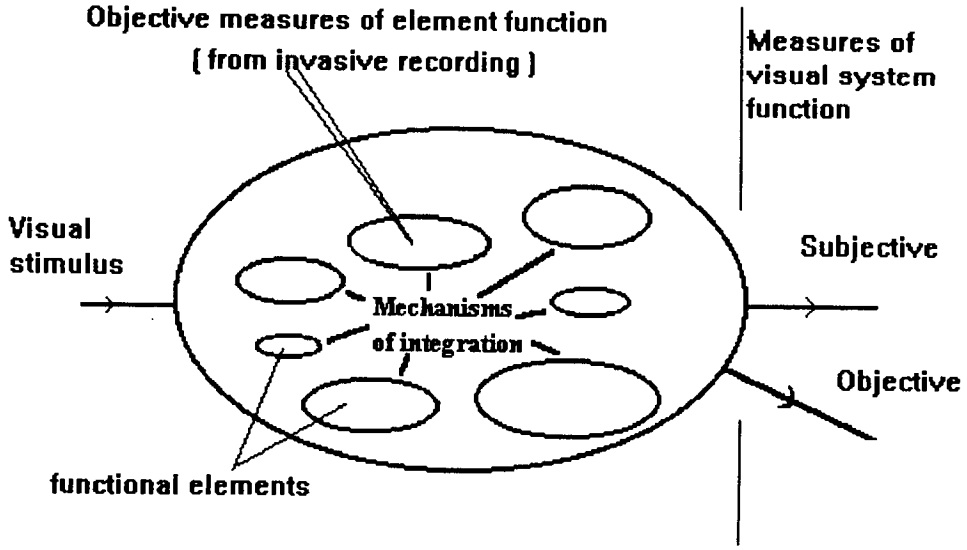

Figure 1.1. Schematic representation of the human visual system in terms of functionally distinct elements.

Our understanding of element function is largely dependent upon the results of studies using invasive micro-electrode recording techniques in primates, but these results cannot provide a reliable description of human visual function. In the human, behavioural studies can indirectly investigate the function and interdependence of these elements, and a schematic description of visual processing developed (figure 1.1). However such descriptions do not relate to the physical composition of the brain. That there is a link between function and anatomy is apparent in brain damaged patients where lesions in specific sites have been shown to cause selective functional deficits (Verrey 1888, Hendricks et al. 1981).

If the physical location of these functional elements can be established in the human, then the neural structures which underlie them can be examined. On the basis of the anatomical information, more concrete cross-species comparisons may be drawn. Magnetic Resonance Imaging (MRI) provides accurate anatomical images of living tissue (figure 1.2) and has revolutionised the study of brain structure. Techniques are required which can show the correlation of function and structure in humans, this is known as functional imaging.

This chapter consists of three main sections. Firstly, the functional imaging tools which dominate present day research are introduced. Secondly (section 1.2) the functional imaging technique of neuromagnetometry is focused upon. Finally (section 1.3) the aims of this thesis, namely the use neuromagnetometry in the examination of the human visual system, are outlined.

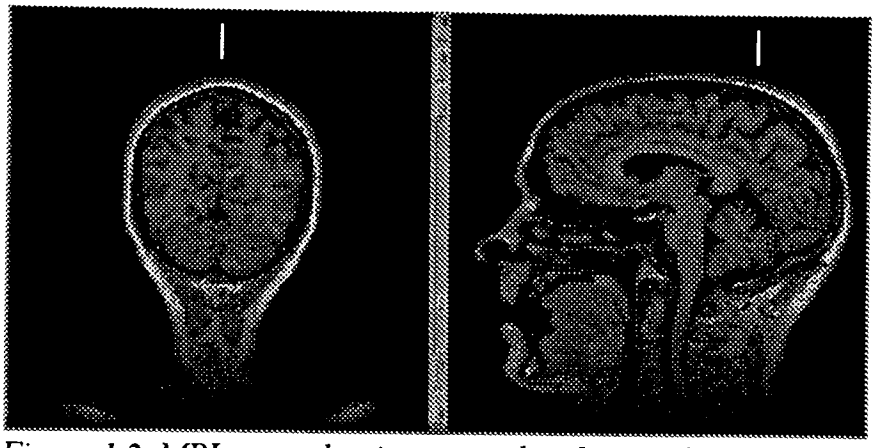

Figure 1.2. MRI scans showing coronal and sagittal sections through a living brain. In each diagram, the position of the partner slice is indicated by a solid line.

1.1. Functional Imaging

There are two basic approaches to functional imaging which rely on two properties of active neurons : firstly, like all cells, neurons absorb more nutrients when active; secondly, neurons transmit signals along their cell bodies by electrical impulse. In this chapter, these neuronal properties are referred to as *metabolic* and *electromagnetic* respectively.

1.1.1. Metabolic Imaging techniques

Positron Emission Tomography (PET) and functional Magnetic Resonance Imaging (fMRI) are functional imaging techniques aimed at highlighting local increases in neural metabolism.

PET

PET involves the introduction of a radioactive tracer (normally radioactive water) into the subject's blood stream. By monitoring the emission of high energy positrons as the tracer decays, it is possible to build up a picture of the density of the tracer element within the brain. Since heightened neural activity results in local increases in blood flow, by subtracting pre- and post-stimulus PET images, it is possible to establish which area of the brain became more active in response to the stimulus. Although the half life of the tracer is relatively short (~2 minutes), the process is potentially harmful and exposure of the subject to the radioactivity must be carefully controlled. Typically PET has a spatial resolution of around 1cm, and temporal resolution of the order of minutes (figure 1.5).

fMRI

Imaging using fMRI is based on the observation that, although during increased activity a neuron's glucose consumption increases (and hence the demand for increased local blood flow), the cell's oxygen consumption remains constant. That is, around regions of active neurons, there is excess oxygen in the blood which is not metabolised. fMRI uses the high spatial selectivity of the standard MRI scanner to highlight such local variations in oxygen concentration. As in the case of PET, the activity before and after presentation of a specific stimulus is measured, and the difference between the two states is taken to correspond to the area of the brain activated.

Unlike PET, fMRI does not involve the introduction of any foreign substance into the blood stream, and also provides superior spatial resolution (~2mm). However, metabolic processes are relatively slow (of the order of seconds) and thus both PET and fMRI fail to resolve neural events which are separated by less than a few seconds.

1.1.2. Electromagnetic Imaging techniques

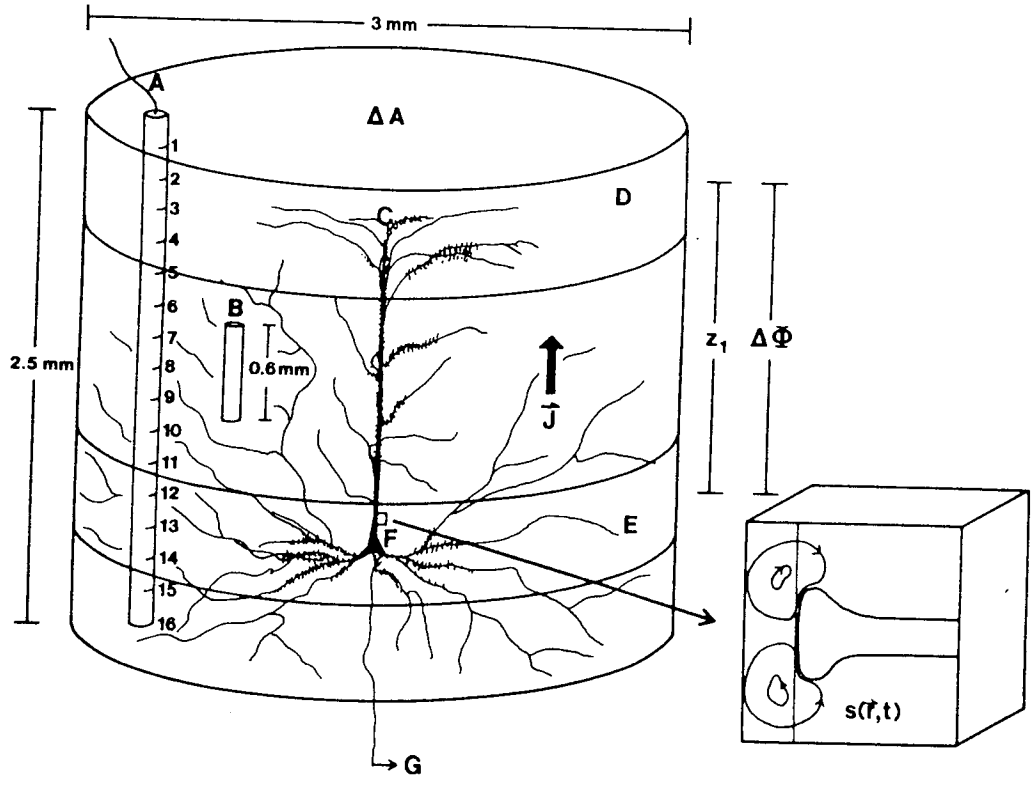

Figure 1.3. A macrocolumn of neocortex for a single large pyramidal cell. A macrocolumn is defined by the spatial extent of the axonal branches which remain within the cortex. The cell shown is one of approximately 10^5 to 10^6 neurons in the macrocolumn. Approximately 70% of all cortical cells are pyramidal cells. Each pyramidal cell has 10^4 to 10^5 synaptic inputs which cause microscopic current sources and sinks (s(r,t)) along the membrane surface. It is through instantaneous imbalance of these sources and sinks that a net macroscopic current density **J** *and potential difference* $\Delta\Phi$ *can be measured across the cortex. This current distribution is often conveniently modelled as a current dipole oriented perpendicular to the cortical surface. (from Nunez 1990).*

Since neurons have a high degree of alignment and interconnectivity (figure 1.3), the activity of a small area of neural tissue can result in a net local current flow. This primary current flow, often modelled as a current dipole, results in electric and magnetic fields which can be measured outside the head (figure 1.4). The aim of electromagnetic-based imaging techniques is to infer the neural activity by measurement of its external electromagnetic effects. Since the electromagnetic phenomena are effectively instantaneous current based imaging techniques have very high temporal resolution, of the order of milli-seconds. Their spatial resolution, on the other hand, is limited by the accuracy of the mathematical models used to describe the head and the underlying current generators.

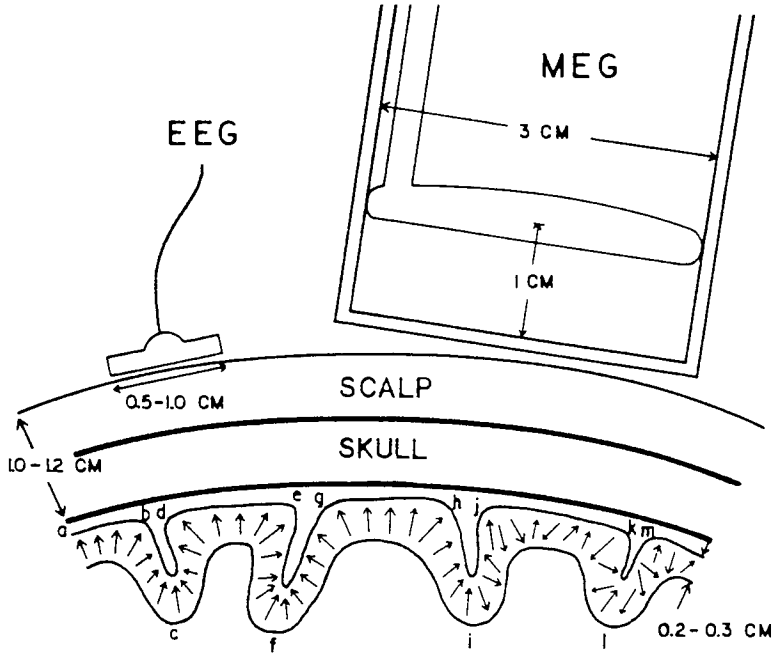

Figure 1.4. Extra-cranial recording of EEG and MEG data. EEG is most sensitive to the correlated dipole layer in cortical ridges or gyri (ab,de,jk), whereas to MEG such radially oriented dipoles are invisible. (The external magnetic field due to a radial dipole in a medium of spherically symmetric conductive layers is zero). MEG is most sensitive to correlated uncancelling dipole layers in the cortical folds or sulci (hi). The electrical potential measured by EEG is highly dependent on the skull and scalp conductivities, the external magnetic field however is independent of such factors (providing the boundaries are spherically symmetric). from Nunez 1989.

Electroencephalography (EEG) is the measurement of the volume currents which flow across the scalp due to the underlying primary current. However, EEG has relatively poor spatial resolution (figure 1.5) since the path of the volume currents is highly dependent on the cranial conductivity profile, which is complex and highly variable between individuals (Ducla-Soares 1989).

Magnetoencephalography (MEG or neuromagnetometry) is the measurement of the magnetic fields due to the primary current. Around the occiput the skull-brain conductivity boundaries are well approximated as spherical and concentric. Given this, the external magnetic field due to the primary current source depends solely on the sphere centre coordinates. Because few modelling assumptions are required to define

the simple head model, neuromagnetometry has potentially high spatial as well as temporal resolution (figure 1.5). However, in order to realise this potential, it is necessary to overcome a number of instrumentational and signal processing obstacles, which manifest themselves as noise. A focus of this thesis will be to develop methods by which the effects of this noise can be minimised.

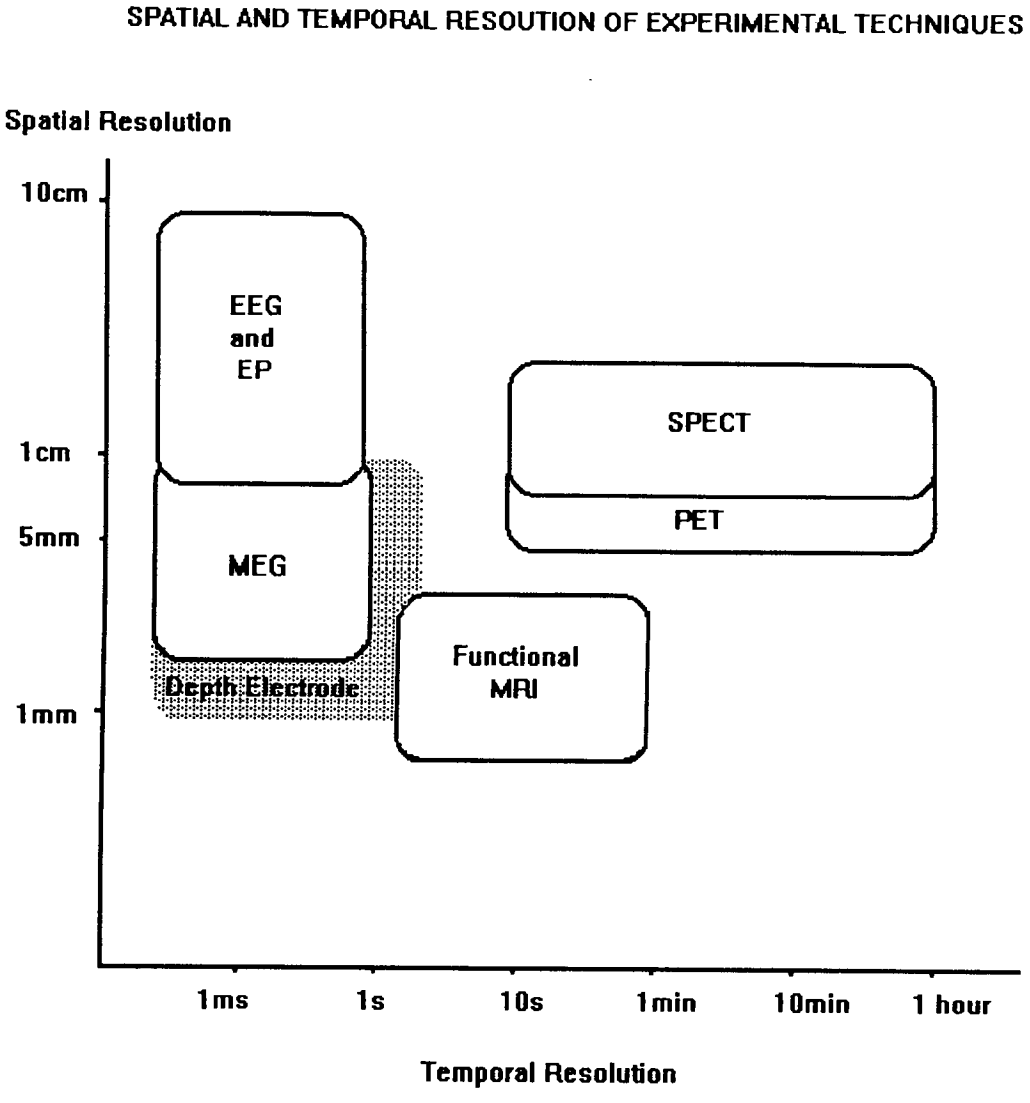

Figure 1.5. Relative spatial and temporal resolution of available functional imaging techniques. adapted from Harding (1993).

1.2. Neuromagnetometry

The magnetic fields due to neuronal activity have magnitudes outside the head of the order of femto Tesla (1fT = $1x10^{-15}$ T) (figure 1.6). In this section the instrumentation required to measure such fields is introduced.

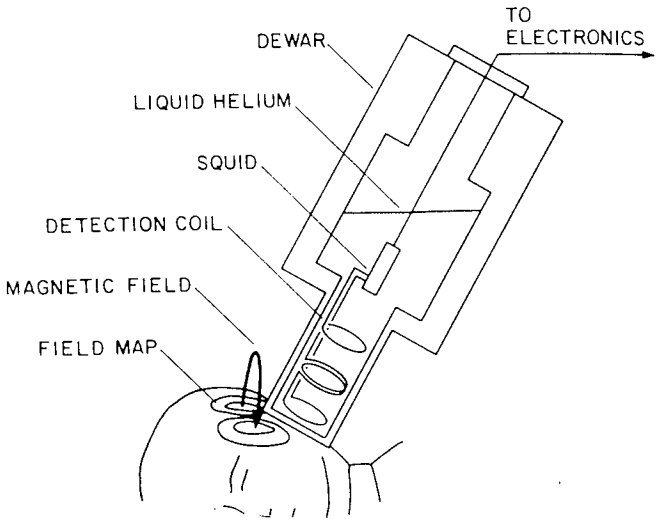

Figure 1.6. Schematic of a single channel neuromagnetometer from Williamson and Kaufman (1986). The SQUID and detection coils are maintained in a liquid helium environment within a non-magnetic cryogenic vessel known as a dewar.

1.2.1. The Superconducting QUantum Interference Device (SQUID)

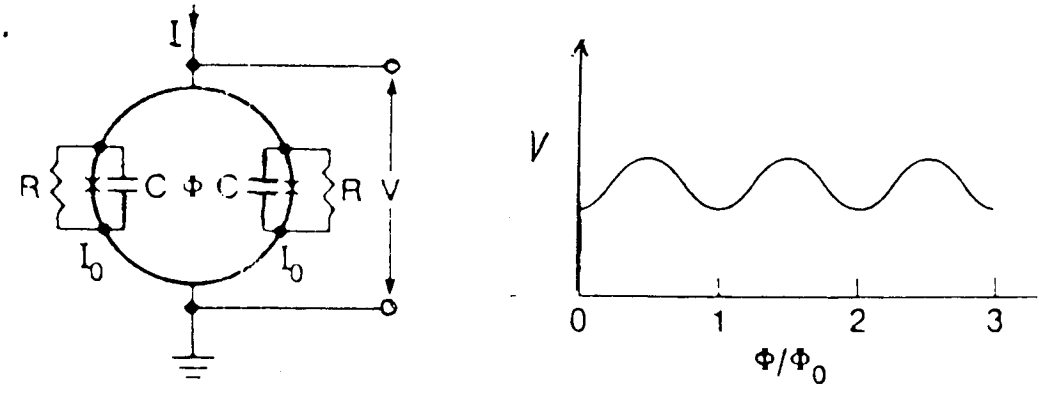

Figure 1.7. The DC SQUID gives voltage output periodic in applied flux, of period the flux quanta Φ_0.

SQUID devices are the essential components of high sensitivity magnetometers. The SQUID has a normal current-voltage characteristic which is dependent on the flux within its area. At a fixed current bias the voltage across the SQUID is a periodic function of the applied flux (figure 1.7). In a neuromagnetometric system a linear flux-voltage characteristic is required and feedback circuitry is used to maintain the SQUID at a fixed operating point in its characteristic. The integral of the feedback applied to the SQUID over time gives a linear measure of the *relative* change in magnetic flux within the SQUID. At frequencies above a few Hertz, SQUID-based detector systems have a

sensitivity limited by intrinsic white noise of around $10^{-6}\Phi_0/\sqrt{Hz}$. At low frequencies (<5Hz for niobium SQUIDs) SQUID noise increases monotonically with decreasing frequency ('1/f noise',see Clarke 1989).

1.2.2. Detection coils

The small area of the SQUID device makes it a relatively insensitive transducer for the measurement of magnetic fields. For neuromagnetic measurements the SQUID is generally inductively coupled to an input coil which forms part of a network of larger coils forming a 'flux transformer'. The simplest form of flux transformer is the magnetometer, consisting of an input coil coupled to a single pick-up coil (figure 1.8a). The magnetometer effectively couples flux within the relatively large area of the pick-up coil through the area of the SQUID loop. Due to the change in device sensitivity brought about by the flux transformer, the intrinsic device noise is expressed in terms of its equivalent flux density at the gradiometer pick-up coil (fT/√Hz).

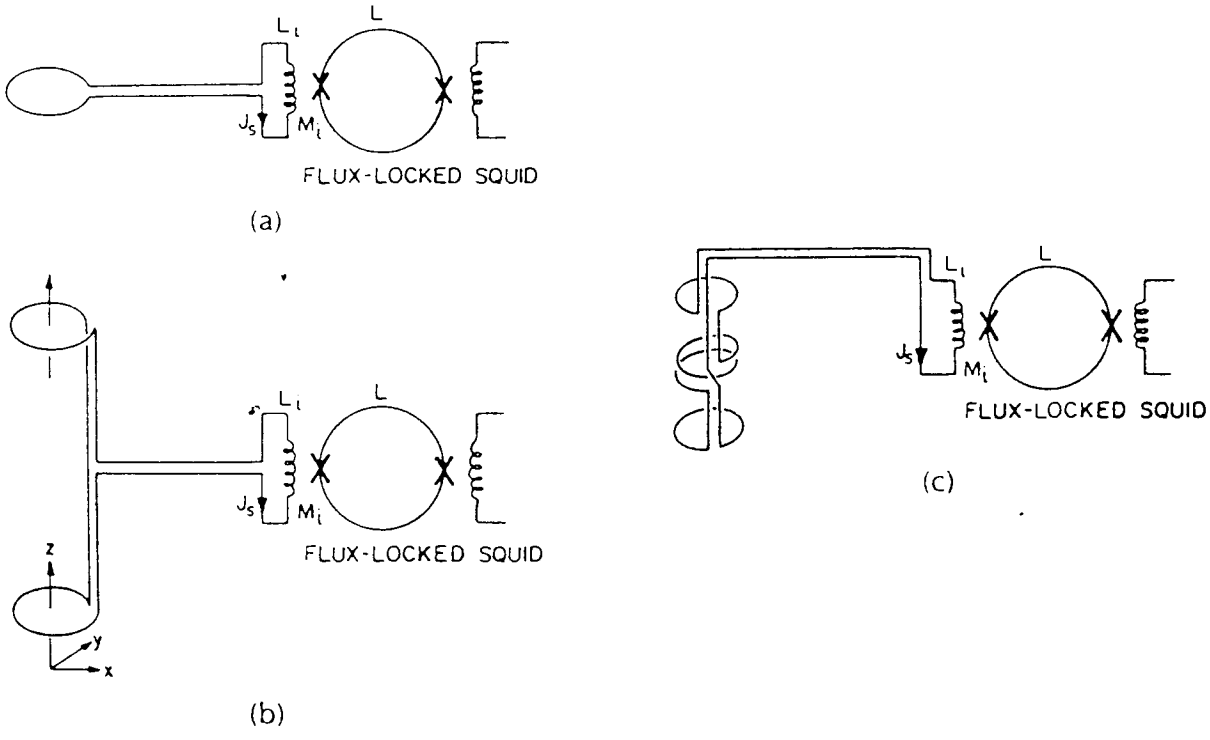

Figure 1.8. a) Magnetometer (b) first order and c) second order axial gradiometer configurations (redrawn from Clarke 1989).

It is possible to attenuate environmental noise without strongly affecting signal sensitivity by using a coil structure known as a gradiometer (figure 1.8b). A first-order gradiometer consists of a pick-up and a compensation coil of identical dimensions wound in opposite directions and separated by a distance known as the baseline. Fields due to remote noise sources are relatively uniform over the distance of the baseline and therefore cause comparable and opposing currents to flow in the pick-up and compensation coils. However, fields due to nearby sources give rise to differential

Miscalibration

Errors can arise in a neuromagnetic data set because detector positions and orientations and their relative sensitivities are imprecisely specified. As an example, figure 1.9 shows estimates of the positional error of a single current dipole model fit to ideal responses contaminated only by measurement and detector noise. As the effect of measurement noise is reduced by increasing the SNR, it becomes clear that the limit to system performance is set by the accuracy with which the detectors are modelled. A high degree of accuracy is necessary to adequately describe even the simplest model. The problem of the accurate determination of all parameters describing the detectors is addressed in **Chapter 2**.

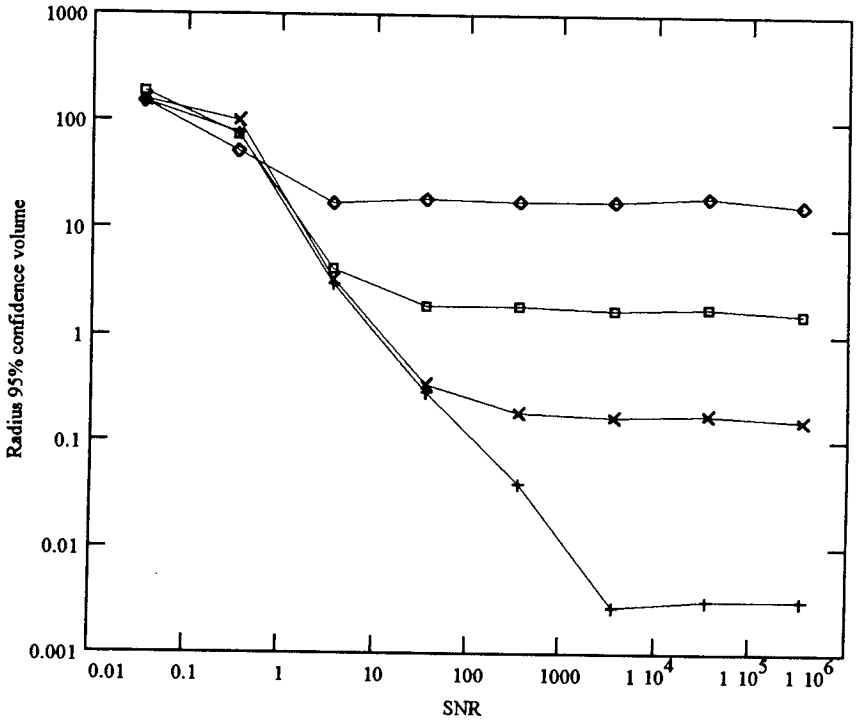

Figure 1.9. Radius of 95% confidence volume (mm) for dipole location as a function of SNR for fits to data from an ideal dipole displaced 4cm off centre and 2.5cm below an array of identical specification to that at Aston, with its detector parameters perturbed by different levels of Gaussian white noise. A confidence volume for dipole position based on 32 successive fits was calculated at various SNRs. Standard deviation of the noise added : 3mm, 6^c (diamonds); 0.3mm, 0.6^c (boxes); 0.03mm, 0.06^c(crosses); plus signs show the no added noise case. Note that all the curves saturate showing that beyond a certain point improvements in fit are constrained by poor knowledge of the detector array. The saturation in the 'no noise' case is due to the finite tolerance limits set in the fit algorithm.

Measurement noise

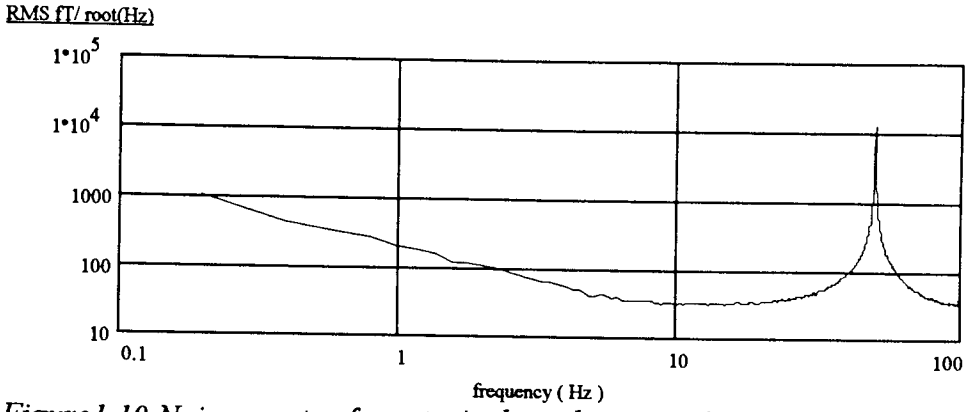

Figure1.10 Noise spectra for a typical gradiometer channel. The system white noise plateau is 30-40fT / √Hz and the low frequency noise corner at around 6 Hz. Environmental noise is dominated by the 50Hz power line interference.

For visual evoked magnetic fields, environmental and system noise (figure 1.10) limit the SNR on any single measurement trial to around 0.1 (figure 1.11). For the limited number of detector channels available at Aston, such a low SNR cannot give stable trial-to-trial inversions (figure 1.9). In order to increase the SNR of the data, some filtering operation is required. Frequency discrimination filtering relies on prior knowledge of signal bandwidth, which is not available; furthermore, system noise is distributed across the frequency spectrum (figure 1.10). It is necessary to make the assumption that neural activity is deterministic; that is, any stimulus will evoke an identical temporal sequence of activity regardless of when it is presented. For the early (pre-cognitive) stages of visual cortical processing this assumption seems reasonable.

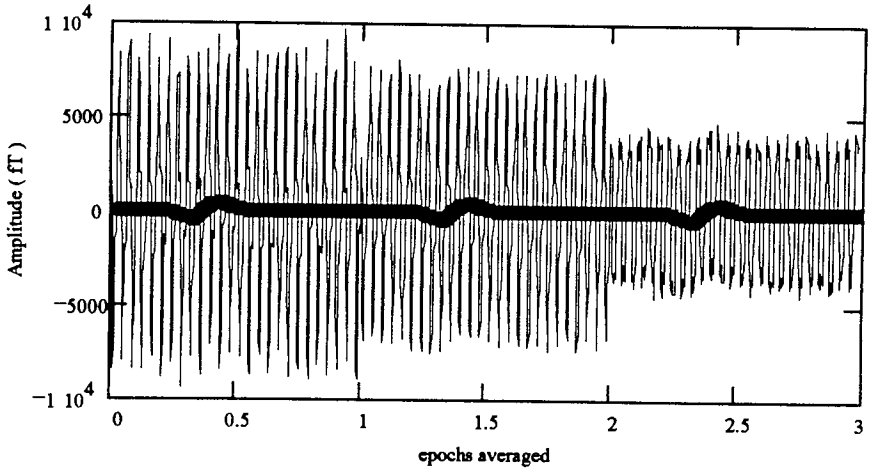

Figure 1.11. Typical noise (thin trace) compared with simulated signal (thick trace) during a recording of an averaged evoked response.

After each stimulus presentation, the magnetic field distribution outside the head is recorded for a length of time known as an epoch. Given that the stimulus-related activity is deterministic, averaging a number of epochs will attenuate all noise and neural activity which is non-coherent with the stimulus. Importantly, the noise on the data can be

quantified by calculating an average of alternately phase reversed epochs, the anti-average.

In practice, averaging is often not sufficient to give SNRs which result in stable dipole fit parameters. For example, environmental noise due to the stimulus is unattenuated by averaging. Some further signal processing is required to extract the underlying neural signal from the noise background. The removal of this noise should not be at the expense of the signal information. **Chapter 3** highlights an adaptive technique for real-time removal of environmental noise specific to evoked response applications. This technique requires no a-priori assumptions about the bandwidth of the environmental noise.

1.3.2. Application

The final three chapters of this thesis describe the application of neuromagnetometry to the identification of distinct functional elements involved in the cortical processing of colour and luminance modulated patterns in humans.

The known physiology and interconnectivy of the functional elements (figure 1.1) involved in primate vision are discussed in **Chapter 4**. The following observations are made. Neurons specific to colour visual processing have been identified in primate cortical areas V1 (the striate cortex), V2 and V4. In particular, the activity of neurons in primate V4 has been shown to correlate with human colour perception, yet the activity of cells in primate V1 has been shown to correlate with human behavioural sensitivity to simple chromatic patterns.

Chapter 5 then describes what is known about human colour vision from behavioural measures, behavioural deficits in brain damaged patients, EEG and PET. It is noted that lesions in extra-striate cortex have been shown to cause exclusive loss of colour vision. Furthermore, PET scans reveal activity in the extra-striate cortex when a subject views a coloured stimulus. However, EEG responses to simple chromatically modulated stimuli are thought to arise in the striate cortex. If there is a human cortical area which is specialised for colour, then why is it not observed in the EEG experiments?

In **Chapter 6,** using the neuromagnetic instrumentation and signal processing developed in chapters 2 and 3, an analysis of the evoked magnetic responses to chromatic and luminance patterns reveals the activity of two temporally and anatomically distinct cortical areas.

Chapter 2.

Calibration of a gradiometer array

2.1. Introduction

All biomagnetic measurements aim to discover the characteristics of underlying electric current in some source space. Magnetic field measurements from physical sensors are compared to the modelled sensor output due to some proposed current distribution (Supek and Aine 1993). A reasonable current distribution is that which gives minimum deviation between the theoretical and measured field. Biomagnetic sensors are located in a bath of liquid helium; thermal contraction effects may cause unpredictable shifts in sensor positions. Likewise, precise sensor output per unit flux depends on a number of inaccurately predictable factors, such as the coupling coefficient between SQUID and input coil. Due to such factors, constructional parameters are generally relaxed, and precise knowledge of the sensor array is achieved by some *a posteriori* calibration technique.

Imprecise knowledge of sensor position or sensitivity will set a systematic noise threshold and limit system performance (Cuffin 1986; Ribiero et al. 1988; Buchanan 1989). This performance limit will result in consistent modelling errors and source estimates which may be highly repeatable yet highly dependent on dewar position. The literature is in disagreement as to how much such modelling errors affect a particular source estimate, since, the stability of the dipolar sources fit depends on the number of measurement channels available (Buchanan 1989), or more precisely, the number of degrees of model freedom. What is clear however is that as models become more complex, that is the number of degrees of freedom decreases, calibration errors will become more significant (see figure 1.9).

Many calibration techniques have been proposed and are in current use, rarely however have the validity of such techniques been assessed. For example, calibration relies on making model assumptions concerning gradiometer coil area, balance etc.; how sensitive are the estimated gradiometer parameters to deviations from model assumptions ? This chapter outlines the optimisation and implementation of a straightforward calibration technique using a grid of long straight wires. This technique has been mentioned by Guy et al. (1989) although to my knowledge, no detailed analysis exists in the literature. Extensive simulation studies are presented in order to show the physical constraints which define the envelope of operation of this technique.

2.2. Recent work

Ribiero et al. (1988) outline a technique for calibration of an array of second order gradiometers using a large square coil. The technique relies on producing a known, homogeneous, 2nd-order gradient field and complete *a priori* knowledge of detector

geometry. Buchanan and Paulson (1989) use a small single turn coil placed at discrete points on an accurately machined grid. By the use of minimisation techniques, they are able to reproduce all parameters [2] describing each gradiometer.

Large coils create low spatial frequency fields, that is, fields whose magnitude and direction change slowly relative to the gradiometer baseline. Such fields create comparable currents in the gradiometer pick-up and compensation coils (Figure 2.1). Comparison of ideal gradiometer output with actual gradiometer output can therefore be largely influenced by gradiometer imbalance (Ribeiro et al. 1988 estimated 5%). Alternatively, small coils create high gradient fields which cause the current in the compensation coil to be insignificant compared to that in the pick up coil. Imbalance effects do not therefore greatly influence the predicted gradiometer output (Figure 2.1). Bruno et al. (1989) show, by the use of Fourier methods, that calibration using low spatial frequency fields is degraded primarily by gradiometer imbalance, whereas calibration using high spatial frequency fields is sensitive to errors in the construction of the calibration rig.

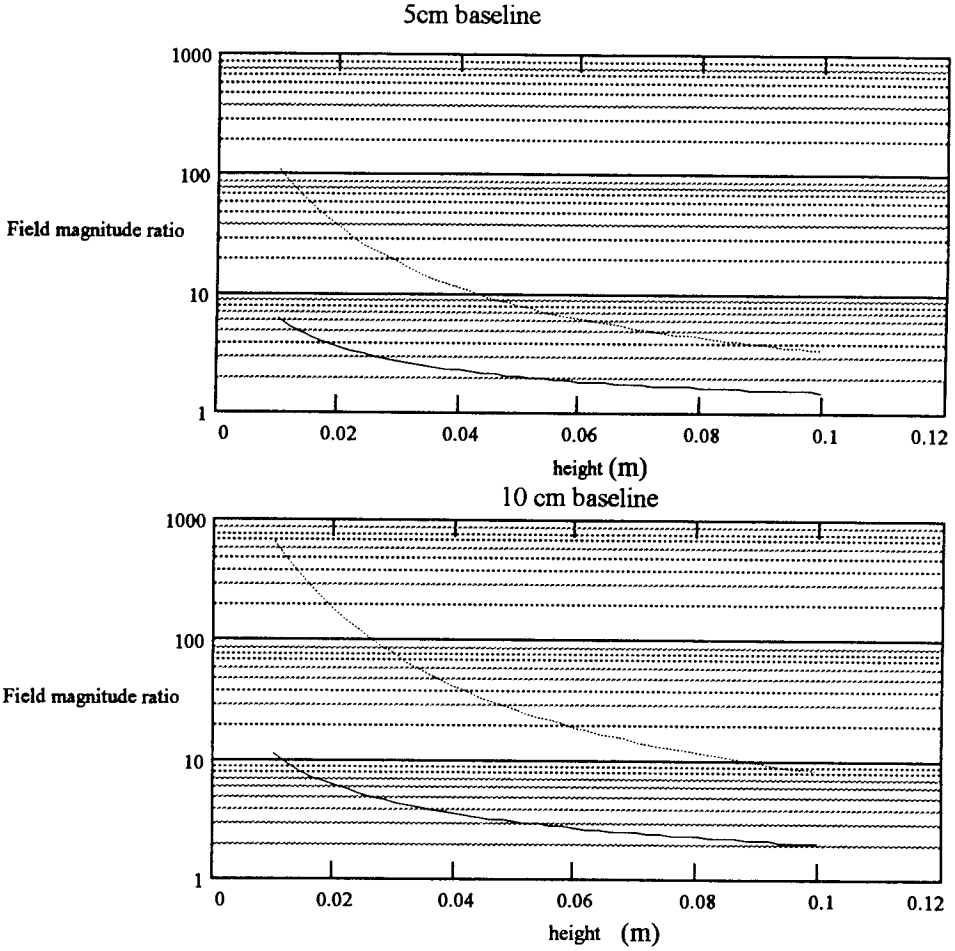

Figure 2.1. Ratio of field through pick up and compensation coils for a first order gradiometer of 5cm baseline and 10cm baseline for long straight wire (solid) and for small coil (dotted). For a small (2cm diameter) coil, the field through the pick up coil is typically an order of magnitude greater than that through the compensation coil at moderate distances (2-4cm) whereas, the long straight wire produces comparable fields in both coils.

[2] Relative gain coefficient to within 1.5%, position 0.5mm, orientation 1 degree.

This study will discuss the calibration of the gradiometer array at Aston using a set of long straight wires. A straight wire produces a field which falls off as 1/r, where r is distance from the wire. A technique based on such an approach should be broadly tolerant of small errors in r, whilst still being relatively unaffected by gradiometer imbalance. Section 2.3 deals with the basic apparatus and signal processing stages necessary to obtain as high as possible SNR (Signal to Noise Ratio) from the data. As groundwork for future simulations, an equivalent level of Gaussian white noise is defined which describes typical noise conditions. The modelling task and the chi-square measure is outlined (section 2.4) and through analytical and simulation modelling techniques it is examined how the variance of calibrated gradiometer parameters can be minimised by appropriate choice of grid dimensions (section 2.5). The analysis in this section assumes that all noise is Gaussian white, and arises from measurements alone. Section 2.6 moves away from the ideal case and examines the effects of modelling errors due to non-ideal grid construction and non-ideal gradiometers.

The equipment and considerations necessary to relate the measured gradiometer parameters to some physical coordinate system are outlined in section 2.7. Given the information available from the modelling simulations, the performance of the physically realised calibration grid is assessed (section 2.8). Section 2.9 outlines compensation for analogue filter inhomogeneities such that the calibration remains valid across the signal pass-band.

2.3. Instrumentation

A square grid of evenly spaced wires is placed approximately symmetrically at a given depth below the dewar containing the gradiometer array (Figure 2.2). Each wire is driven in turn at a given frequency and current (typically 33.2 Hz, 0.3mA), a copy of this signal or reference is passed directly to a 16 bit ADC (sampling at 1kHz). The outputs of the individual detectors are pre-amplified, filtered (typically 0-100Hz), and sampled by the same ADC. The data is collected in epochs, time locked to the reference signal, and averaged. The averaged data is Welch windowed and the Fast Fourier Transform (FFT) gives a spectral estimate of signal amplitude and phase. Theoretically, for an ideal sinusoid in white noise, such an estimate should improve on a peak-peak measure of amplitude by $\sqrt{(N/2)}$. However, in coloured noise, effects such as leakage introduced by the finite length data sequence will degrade this estimate (Press et al. 1989).

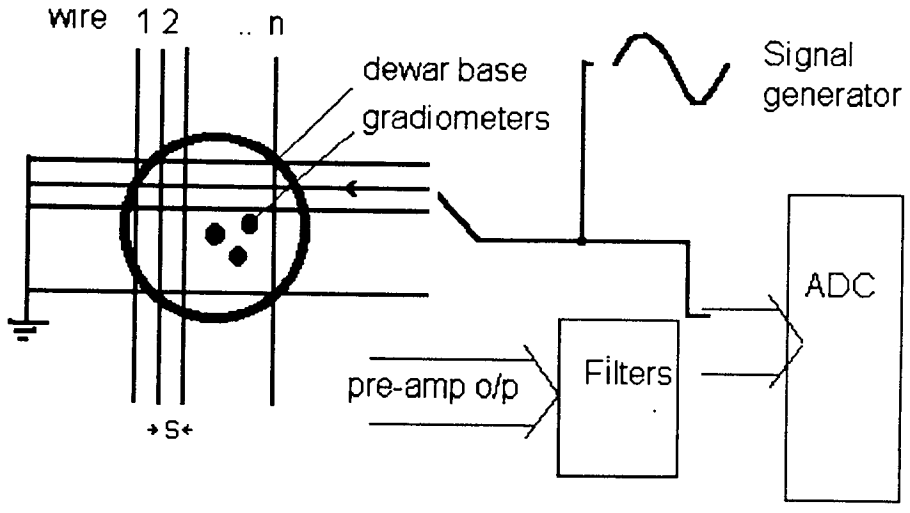

*Figure 2.2. Schematic of calibration grid and system layout. A grid of n*n wires, spacing s cm is positioned below the dewar. A sinusoidally modulated current is passed along each wire in turn.*

Having completed the measurements, a 3D digitiser pen (Polhemus 3Space Isotrak system^{TM}) [3] is passed along wire zero of both axes. The digitiser pen provides a real-time readout of pen tip position (resolution 2.25mm RMS) and attitude (resolution 0.35 ° RMS). The resulting set of points is used to construct a reference plane from which all subsequent measures of gradiometer positions and orientations are offset (see section 2.7).

[3] the same instrument is used for measurement of subject head position during recording.

2.3.1. Real noise performance

The next sections detail simulations and analytical performance estimates where fields sensed at the gradiometer are ideal sinusoids in Gaussian white noise. It will be necessary to compare the simulated results with those achieved in practice. System noise is non white and consists of a large low frequency, and 50Hz components (figure 2.3). It is necessary to establish the performance of the signal estimation technique in coloured noise. In order to do this, the algorithm was fed with epochs of data recorded from a gradiometer channel in ambient noise with an ideal signal sinusoid superimposed.

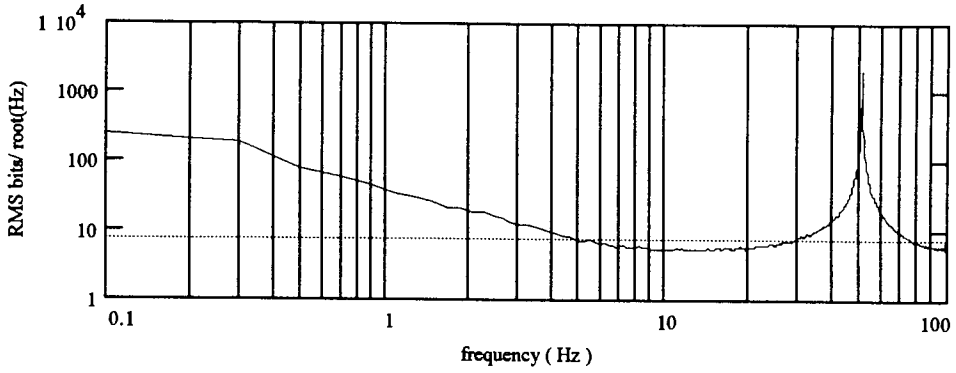

Figure 2.3. Spectra of typical noise epoch (solid curve). Superimposing a 32.2Hz sinusoid on the data, and then applying the spectral estimate algorithm gives equivalent performance to that as if the data had been originally white noise, of amplitude shown by the dotted curve. (epoch 128 samples).

The true sinusoidal amplitude is known, and therefore the performance of the algorithm can be quantified. Multiplying this empirically achieved RMS error by the improvement factor calculated for Gaussian white data (in this case $\sqrt{(128/2)}$) gives an equivalent initial pure white noise level (figure 2.3). This extrapolated noise level is slightly higher than the intrinsic white noise level of the system, and possibly reflects spectral leakage effects. Throughout this chapter the assumption is made that this white noise is Gaussian in its distribution.

2.4. Fitting a gradiometer

Each gradiometer is now characterised by a set of n*n amplitude readings, where n is the number of wires. There are six gradiometer parameters to be estimated : three position (x,y,z) two orientation (a,b) (components of a unit vector) and a calibration coefficient (γ). Figure 2.4 shows a schematic of the experimental set up alongside a typical gradiometer response profile. Given that n>3, it is possible to calculate the absolute gradiometer calibration coefficient γ and all geometrical parameters relative to the position of the wire set[4].

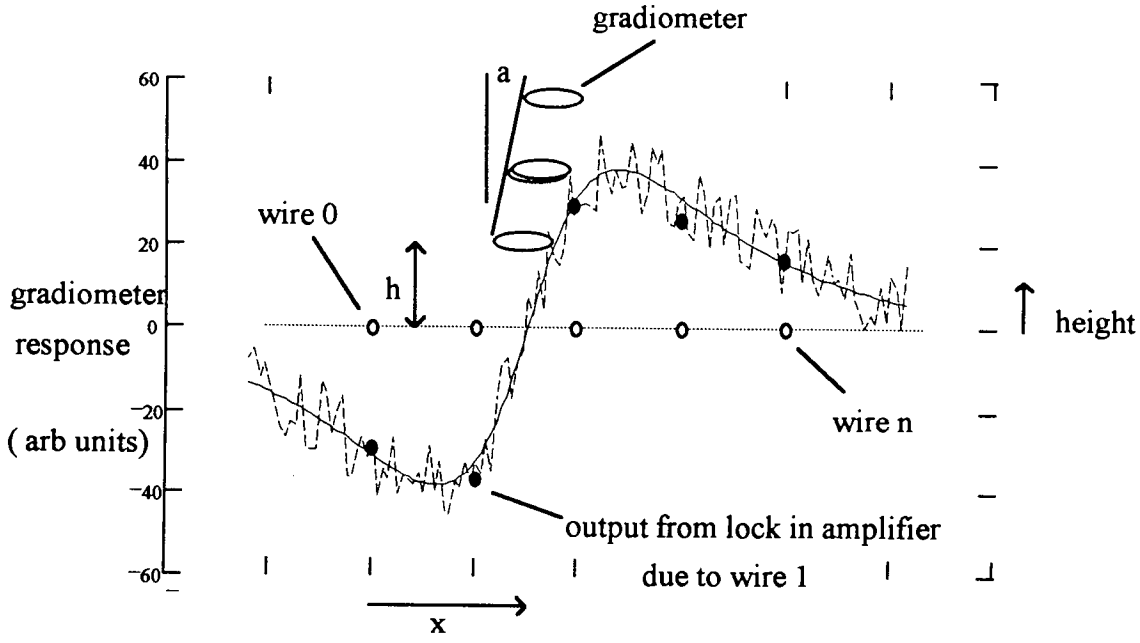

Figure 2.4. An ideal (solid) and noisy (dashed) gradiometer response to a wire at any position x (solid curve). Since there are finite number of wires, only n points of the characteristic are sampled (dark blobs). Alongside in the diagram are schematics of the gradiometer and wire set. Note the main characteristics of the curve : zero crossing approximately below the gradiometer and response extrema whose separation is proportional to gradiometer height.

[4] Although there are six parameters in total, the pairs {x,y} and {a,b} are independent giving the requirement of at least four wires in each orthogonal direction.

Given that the measurement errors are normally distributed and independent, the χ-square statistic is useful as a measure of the goodness of fit :

$$\chi^2 := \sum_{i=1}^{nwires} \frac{\left[\psi_i - (\Psi(h,\gamma,x,y,a,b))_i\right]^2}{(\sigma_i)^2}$$

Where
i : is the wire number
ψ : the measured response
σ : the measurement noise
Ψ : the model response
and the model parameters are :
h : height of pick up coil centre
γ: calibration coefficient
(a,b) : orientation vector
(x, y) : displacment of centre of pick up coil from axis.

Given that the model $\Psi(...)$ is appropriate, the parameter set (h,γ,a,b,x,y) which minimises the value of the above function should be good estimates of the parameters of the physical device. The validity of the model can subsequently be determined from the minimum χ^2 value and the number of degrees of freedom (v) of the fit.(*Press et al. 1989*):

P(χ-square value did not occur by chance)= $Q(v/2, \chi^2/2)$

where Q is the incomplete gamma function, from now on referred to as the Gamma Q probability..

$$Q(a,x) := \frac{1}{\int_0^{\infty} t^{a-1}\cdot e^{-t}\,dt} \cdot \int_x^{\infty} t^{a-1}\cdot e^{-t}\,dt$$

and v is the number degrees of freedom..

v = number of measurement points - number of parameters

in this case, for an n*n wire grid and 6 parameter model,

$$v = 2.n - 6$$

In this chapter, the relative chi-square values are quoted, that is, χ^2/v. Relative chi-square values should be comparable across model fits based on any wire grid.

2.5. To design the optimal calibration grid.

Given an imperfect measurement process, there will be a wire configuration which minimises errors in gradiometer parameter estimates. This optimal configuration will be a function of gradiometer height and angle. For the sake of simplicity, let the gradiometer be nominally vertical. There exist two methods for estimating the variance of each parameter for a given amount of measurement noise : analytical and empirical (in the form of simulation). The first method relies on complete knowledge of the mathematical form of the model, the second is based on an iterative fitting procedure. The analytical estimates are used in this first section to give credence to the simulation data, which in turn we must rely on exclusively when it becomes necessary to examine the effects of modelling errors (section 2.6).

2.5.1. Analytical determination of parameter variance

The solution of any χ^2 minimisation is the point at which the gradient of the χ^2 function with respect to all model parameters is zero. By examining the function gradient with respect to a particular parameter around this minimum point, the variance of the parameter due to Gaussian white measurement noise can be estimated (Press et al. 1988). In order to simplify this calculation, the gradiometer response to wires running perpendicular to the plane of gradiometer tilt (Figure 2.5) is used as the model function. Having calculated the expected parameter variance for the two dimensional case, the results are extrapolated to three dimensions.

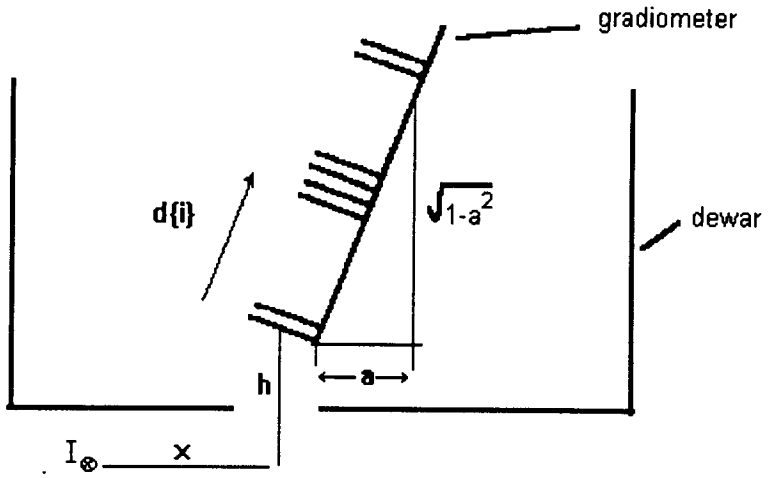

Figure 2.5 Schematic of an Aston type gradiometer. position (x, h) , orientation (a, $\sqrt{(1-a^2)}$), wire current I ; gradiometer coil i displaced from the pick up coil by distance d{i} (see below).

The response of a gradiometer, displacement (x, h) from the wire, orientation $(a, \sqrt{1-a^2})$ and gain γ, to a wire carrying current I is given by.

$$\psi(\gamma, x, h, a, I) = \sum_{j=0}^{7} sgn_j . \gamma . I . \frac{\mu}{4.\pi} \left[\frac{x.\sqrt{1-a^2} - a.h}{(x + d_j . a)^2 + (d_j . \sqrt{1-a^2} + h)^2} \right]$$

where j indexes gradiometer coils,

axial distances from each coil to pick up are given by d_j ,

direction of winding of each coil is given by sgn_j where sgn_j=+1 or -1.

Using the above model, the expected parameter variance due to measurement noise is now calculated. Let **p**(i) be the vector of effective function parameters for each wire position i. Let the gradiometer be displaced from the first wire by distance x, and let the length of the perpendicular from gradiometer to the line of parallel wires be height h. For wire spacing s:

$$\mathbf{p}(i) = (x - s.i \quad h \quad a \quad \gamma)^T$$

(where ^{T} is the matrix transpose)

The effect of measurement noise on each of the parameters is given by inverting the Hessian matrix α. (Press et al. 1988).

where

$$\alpha_{k,l} = \sum_{i=1}^{n\_wires} \frac{1}{\sigma_i^2} \left[\frac{d}{d\mathbf{p}_k(i)} \psi(\mathbf{p}(i)) \right] . \left[\frac{d}{d\mathbf{p}_l(i)} \psi(\mathbf{p}(i)) \right]$$

and k and l go from 0 to 3.

The covariance matrix **C** is given by inverting the Hessian :

$$\mathbf{C} = \alpha^{-1}$$

The diagonal elements of the covariance matrix C contain the expected variance of individual parameters. For convenience, the covariance matrix is evaluated numerically for the two dimensional case, and the results then extrapolated into three dimensions. For example, the errors in y and b are taken to be identical to the errors in x and a respectively.

2.5.2. Determination of parameter variance by simulation

The gradiometer response to a long straight wire is modelled in a software algorithm. This gradiometer is given a random parameter set **p**. The response of this ideal gradiometer to a particular wire configuration is then calculated and noise added to the output (see Figure 2.6). An independent algorithm then fits a gradiometer with estimate parameter set p' to the noisy data so that the error in fit is given by **e=p-p'**.

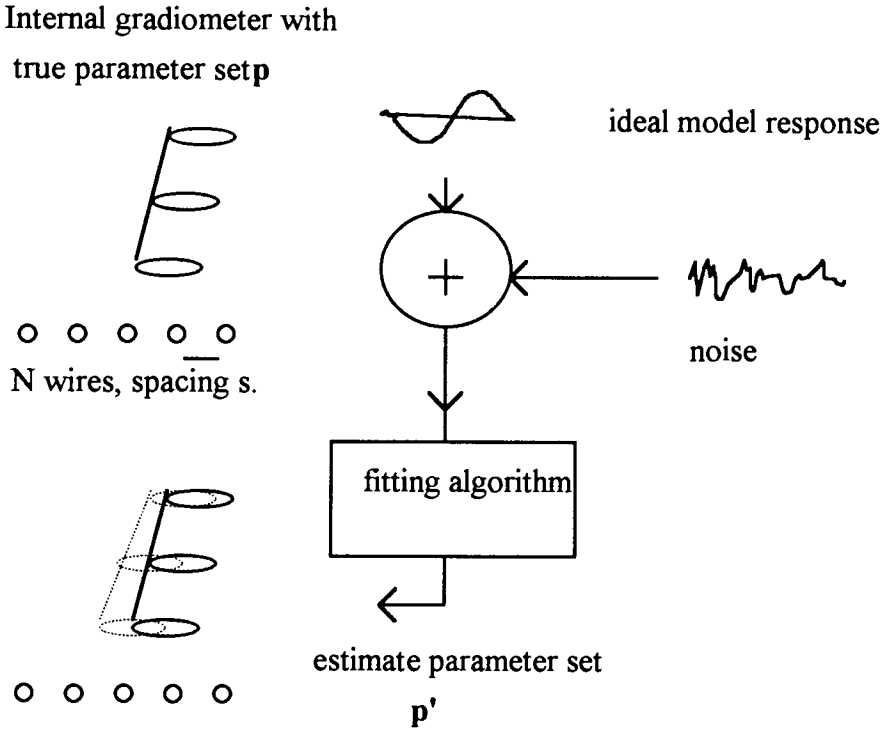

Figure 2.6. The simulation procedure consists of adding experimental noise to the model and then assessing the performance of the fit algorithm.

By repeated simulation, it is possible to build up statistics of the error in each parameter for a particular experimental configuration. The method will be of use later when we wish to examine the effect of system imperfections which do not result in a tractable analytical form.

The data which follows is based on a grid of n*n wires placed symmetrically below a single gradiometer. The true gradiometer parameter set **p** is chosen by a random shift in horizontal position (σ =0.5cm) and orientation (σ =2°) away from the symmetrical midpoint of the grid, for a fixed height and calibration coefficient. Where possible, simulated and analytically derived results are compared.

2.5.3. Optimal wire spacing

It is evident that the ideal wire spacing is determined by the total number of wires available. Outside a certain region, only very poor signal to noise ratios are achievable (Figure 2.4). It is intuitive that the more wires congregated towards the wire positions which give large gradiometer output, the better. Figure 2.7 shows the RMS error in position, orientation and percent calibration coefficient for gradiometers at 2,4 and 8cm height. The results show that the optimal spacing is approximately equal to half the gradiometer height, the minimum becoming broader as the gradiometer moves higher. The sharp increase in error at small spacings is the result of carrying out an extrapolation from a small range of values to a model which has much larger spatial extent. The optimal spacing of 5 wires at h/2 cm is reasonable since the samples of the gradiometer response function just overlap the function peaks, situated approximately a distance 2h apart (Figure 2.4). At larger spacings the increase in RMS error would seem to be mainly due to poor signal to noise ratio. For smaller spacing values, the analytical curves fit the simulated data well in an absolute sense. Glitches in the empirical data towards the larger spacing values are due to the fit algorithm being destabilized by the very low SNR of the data. The achieved errors increase with increasing height simply due to the fall off in field strength. Note interestingly that minimum expected error for all three parameters occur at slightly different wire spacings. Note also the relatively broad minima in the estimate of calibration coefficient error.

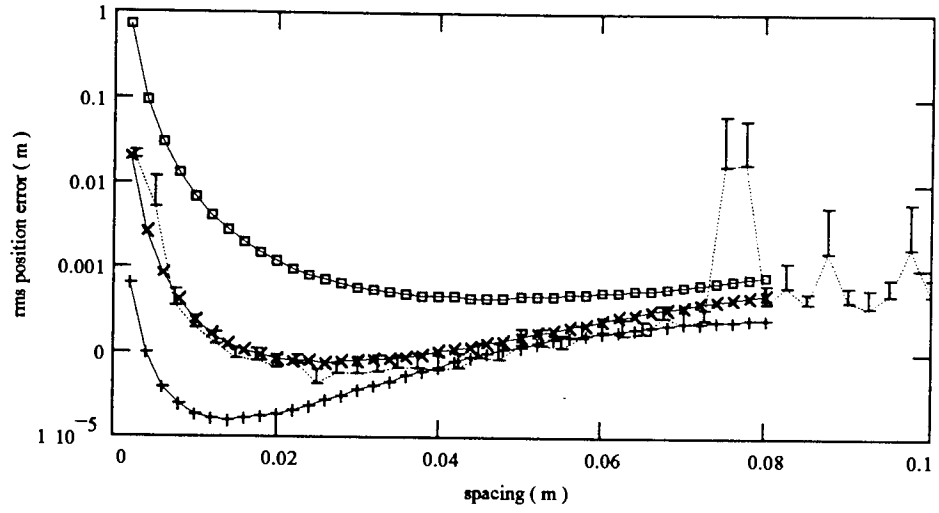

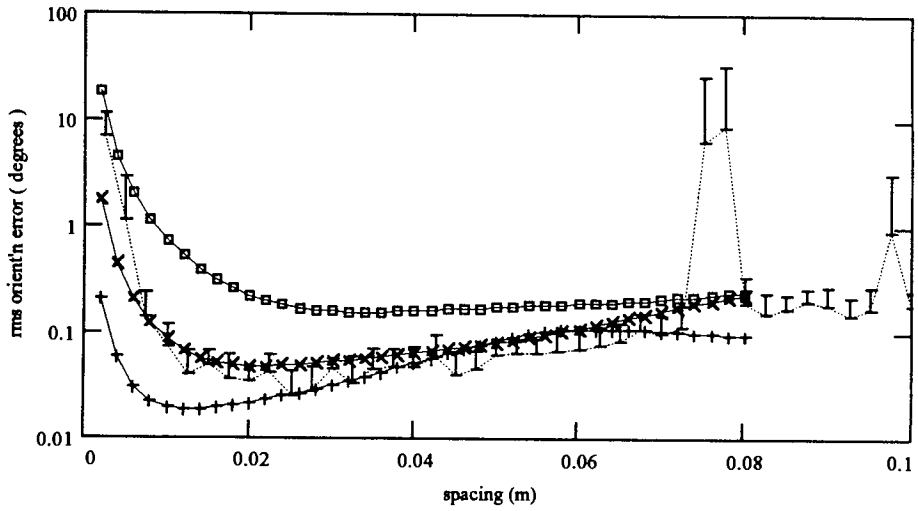

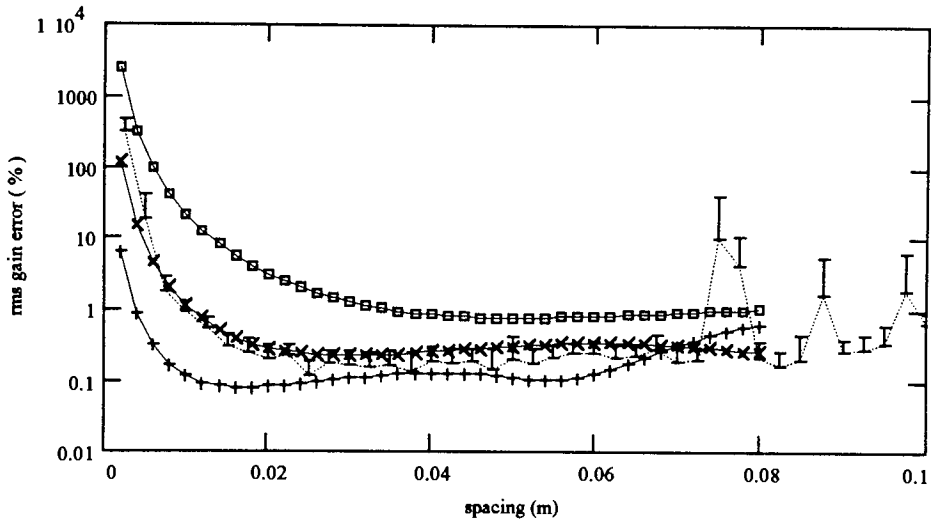

Figure 2.7. RMS parameter errors for 4 cm height simulated (dotted curve with error bars) and predicted (crosses); alongside predicted errors for gradiometer of 2cm height (pluses),and 8cm height (boxes) as wire spacing is varied. (5 wire grid, 10bits white noise). Note that error bars extend from the mean to the mean plus one standard deviation, they no not extend below the mean due to problems of scaling.

2.5.4. Effect of wire number

Given that wire spacing is chosen so as to be smaller than optimal for a given gradiometer height, the total number of wires will affect the stability of the solution. In order to investigate this effect, it is helpful to define

coverage_length = number of wires* spacing

That is, coverage length is simply the length of a grid side. Figure 2.9 shows the effect of increasing coverage length for various wire spacings. Simply, more wires give more measurement points within the same length and improve the fit. For Gaussian white measurement noise, the improvement in RMS parameter error is proportional to √ (number of wires). For example, referring to figure 2.9, when the RMS errors for 1cm spacing are scaled up by √2 they overlay those for 2cm spacing. Since the fit continues to improve exponentially as coverage length is increased, as a working measure, optimal coverage length is defined as the minimum distance over which the RMS error is within 71% of its minimum value (figure 2.8).

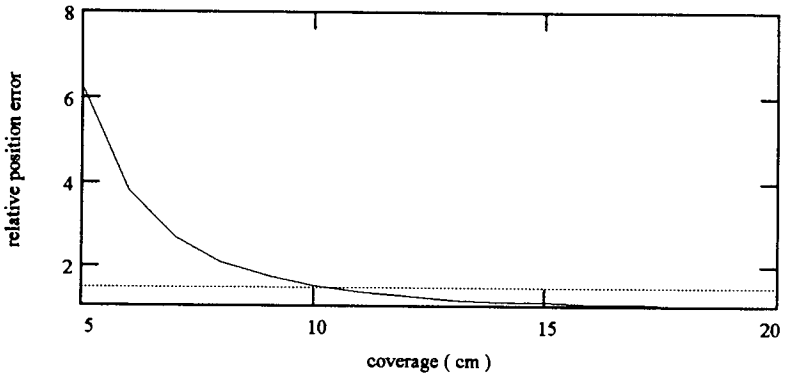

Figure 2.8. The position error for 1cm spacing data of figure 2.9 plotted relative to position error achieved at 20cm coverage. The baseline is 1.0, the dotted line shows relative RMS error of 1.714. In this case, optimal coverage length is around 10.5 cm.

4.1.3. Wire current

Increasing the current in the wires will increase the SNR of the data, and should result in lower variance of fitted parameters. Figure 2.10 shows how RMS parameter error decreases with increasing SNR. The early portion of the graph is flat because the ideal gradiometer is never perturbed far from the grid centre where the initial fitting guess is made. In the central portions of the graphs, the analytical and simulated results show good agreement. At higher SNRs, the simulated ADC is saturated by the large magnitude signal, hence the deviation from ideal. Figures 2.10 a) and d) show the chi-square remainder and gamma Q probability respectively. Note that at ADC saturation, chi square increases and gamma Q decreases rapidly. This indicates that measurement noise no longer accounts for deviations from the model.

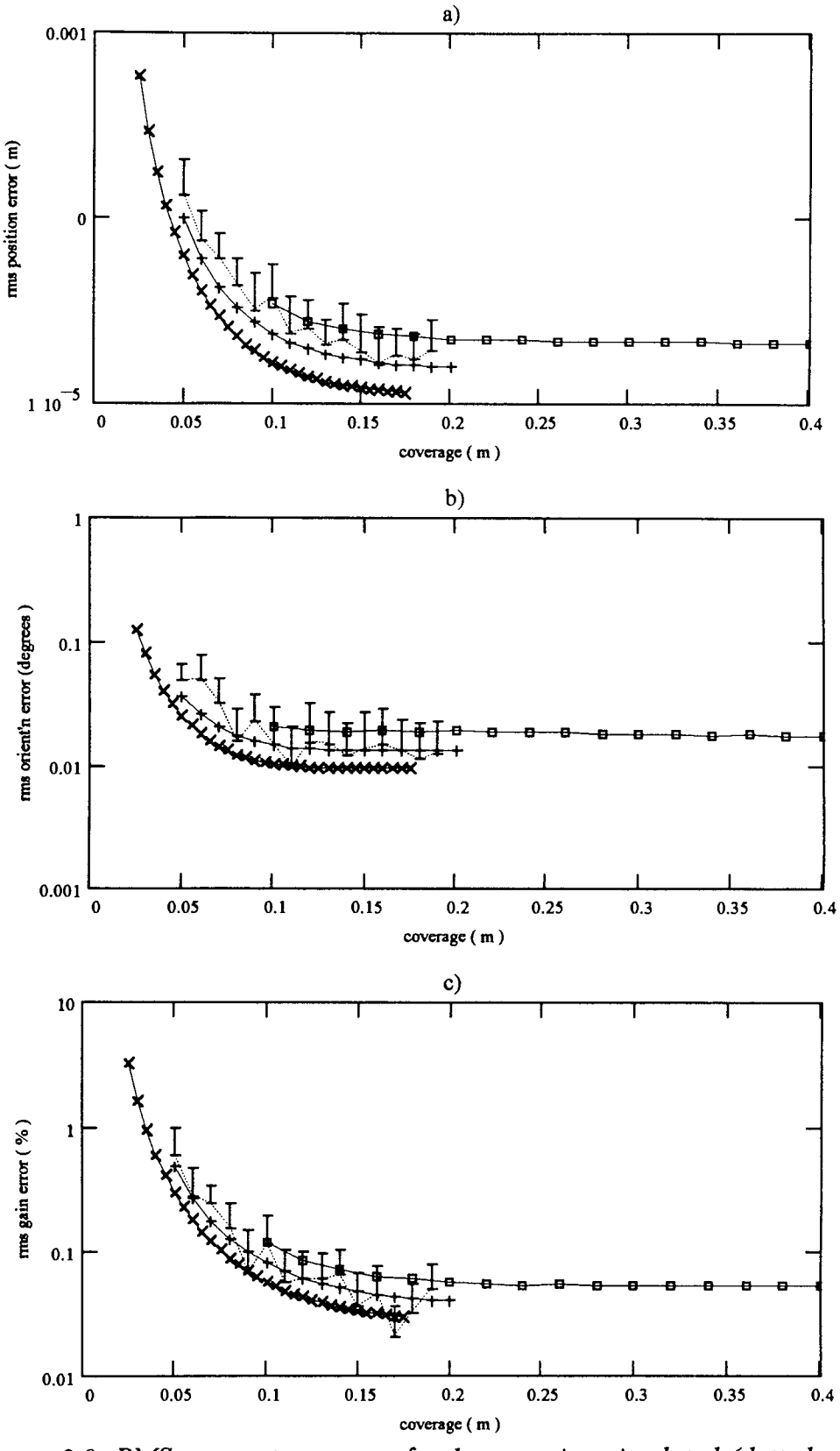

Figure 2.9. RMS parameter errors for 1cm spacing simulated (dotted with error bars) and predicted (pluses), alongside predicted for.5cm (crosses) and 2cm spacing (boxed) curves as number of wires is varied. The abcissae show coverage defined as : number of wires wire spacing. (4cm height, 10bits white noise)*

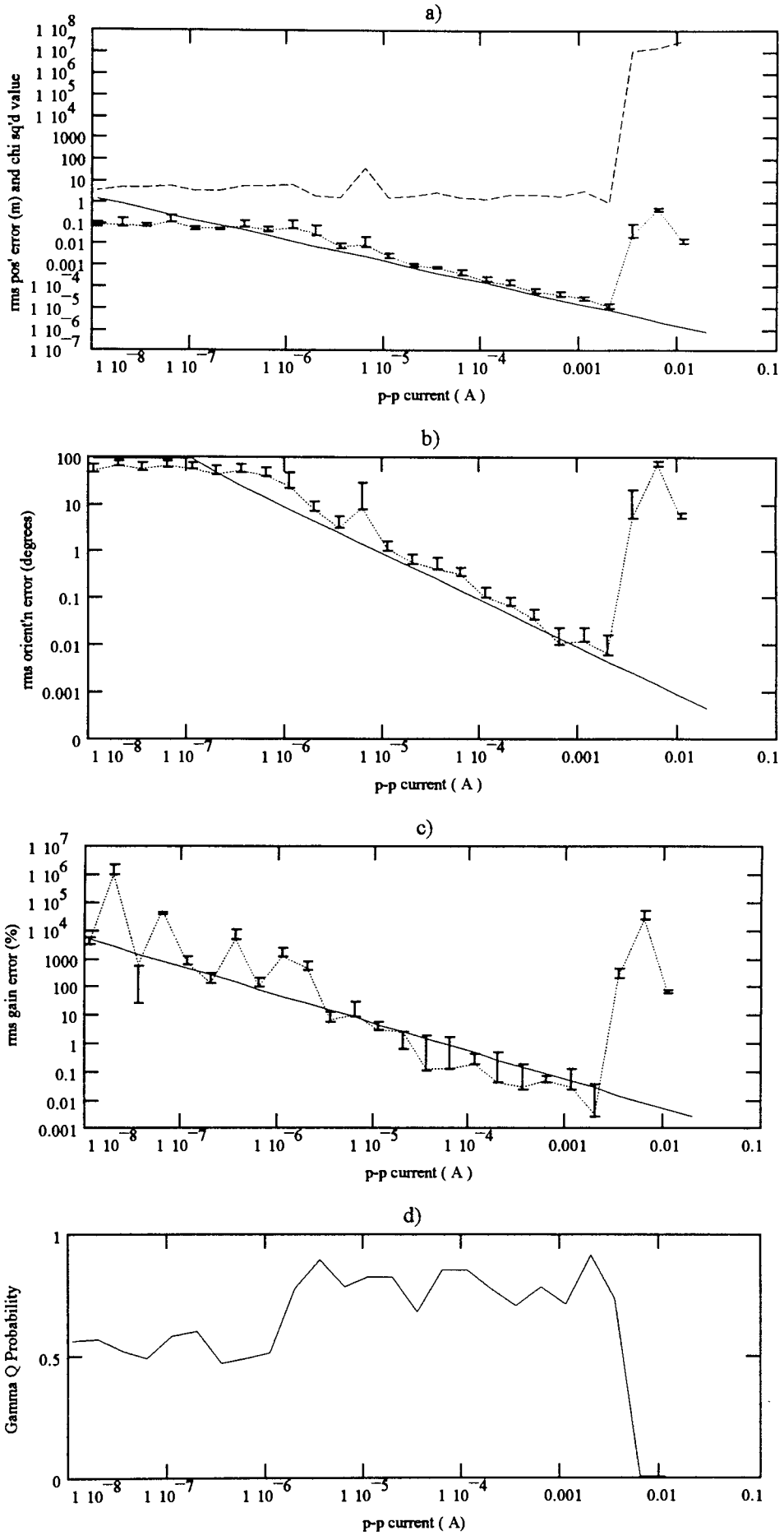

Figure 2.10. RMS parameter errors as current is increased. a) shows RMS position error alongside chi-squared remainder for the fit; d) shows the corresponding gamma Q probability. At larger currents, the dynamic range of the ADC (simulated) is

exceeded hence the sudden decrease in performance. (5 wires ; 2cm spacing ;4 cm height; 10 bits white noise)

2.6. Effect of physical constraints

The simulations and analytical estimates of the previous section were based on the ideal gradiometer response to wires in an ideal calibration grid in the presence of some Gaussian white measurement noise. In practice however, no computer model precisely characterises a physical situation, there is always some modelling error. Modelling errors are only a problem when they introduce parameter error comparable to that caused by measurement noise. For example, this modelling error may be small, and only become apparent as measurement noise tends to zero. The chi-squared measure is a measure of deviation of the model from the measured values, normalised to account for measurement noise. When the difference between the model and measured values ceases to be accounted for by measurement noise the chi-squared measure increases rapidly, indicating that the model is inappropriate.

Let all modelling errors be represented by the quantity Δ, if Δ is small compared to the RMS errors on the data σ, then a reasonable chi-square value will result.

$$\chi_r^2(..) = \left[\frac{\left(\sigma_{true} + \Delta\right)}{\sigma_{est}}\right]^2 \qquad (1)$$

Assume that the true standard deviation of some empirical data corresponds to that estimated ($\sigma_{true}=\sigma_{est,}$), once the standard deviation of the data becomes comparable to Δ, the chi-square value begins to increase quadratically (or, on the log-log plots, linearly at 40dB/ decade). It is required to see what effect finite model imprecisions will have on gradiometer parameter estimates. By allowing measurement noise to tend to zero, the point at which modelling noise becomes the major source of fit error should be clear. The goal of this section is to show the tolerance of the fitting algorithm to modelling errors. The modelling errors considered are those due to an imperfect wire grid, and those due to gradiometer imbalance. If σ_{true} and σ_{est} are known and chi-square is large, Δ can be calculated. Once Δ is known, the point where the parameter variance plots diverge from the ideal can be calculated.

2.6.1. Wire noise

The accuracy to which the calibration board needs to be constructed will be an important factor for cost and realisation. There will always be some 'noise' in the construction process, and this modelled as a small Gaussian white deviation in position at each end of each wire.

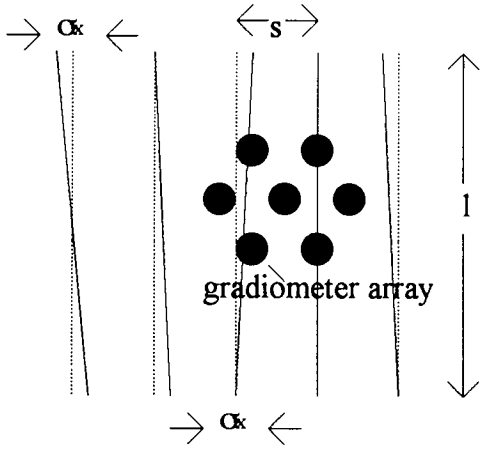

Figure 2.11. Wire set length l, spacing s, perturbed at either end by Gaussian white noise σ_x.

The model gradiometer function takes no account of wire noise, that is, the model is imprecise. From figure 2.13 it is clear that beyond a certain point, there is no improvement in fitted parameters. The point of saturation indicates where noise due to the imperfect model becomes comparable to the measurement noise. Note that the point of parameter variance saturation corresponds to the knee of the chi-square curve (figure 2.13a). The effect of wire noise can be compensated for to an extent by increasing the number of wires within the optimal coverage length. As has been shown (Figure 2.9), fitted parameter variance decreases proportionate to the number of wires within the optimal coverage length. In the case where wire position noise is introduced, increasing the number of wires at known spacing also improves the estimate of the mean position of the wire set. Figure 2.12 shows the improvement in gradiometer position estimation when using a larger number of wires. A twenty wire and five wire set up are compared. The implicit SNR improvements of the twenty wire set up are removed by halving the wire current as is clear at low wire noise where the two curves correspond. As the wire noise is increased the improvement due to number of wires becomes evident.

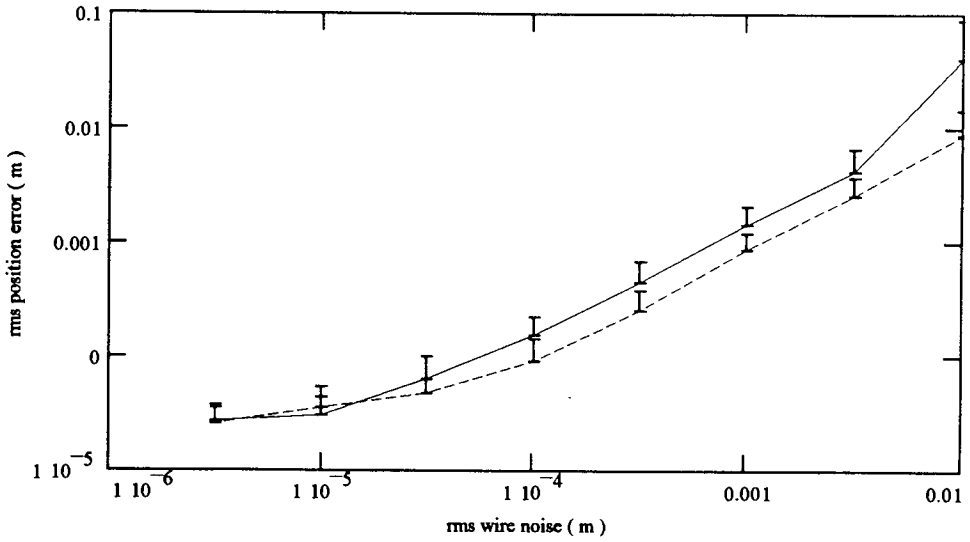

Figure 2.12. The effect of wire noise on position error for 5 (solid) and 20 (dashed) wire grids within the same coverage area (10cm^2). The increased SNR implicit with the 20 wire grid is factored out by using half the current. Remaining improvements in position error are due to more wires decreasing the uncertainty in overall grid position. (4cm height, 10bits white noise, current for 5 wire case = 0.3mA)

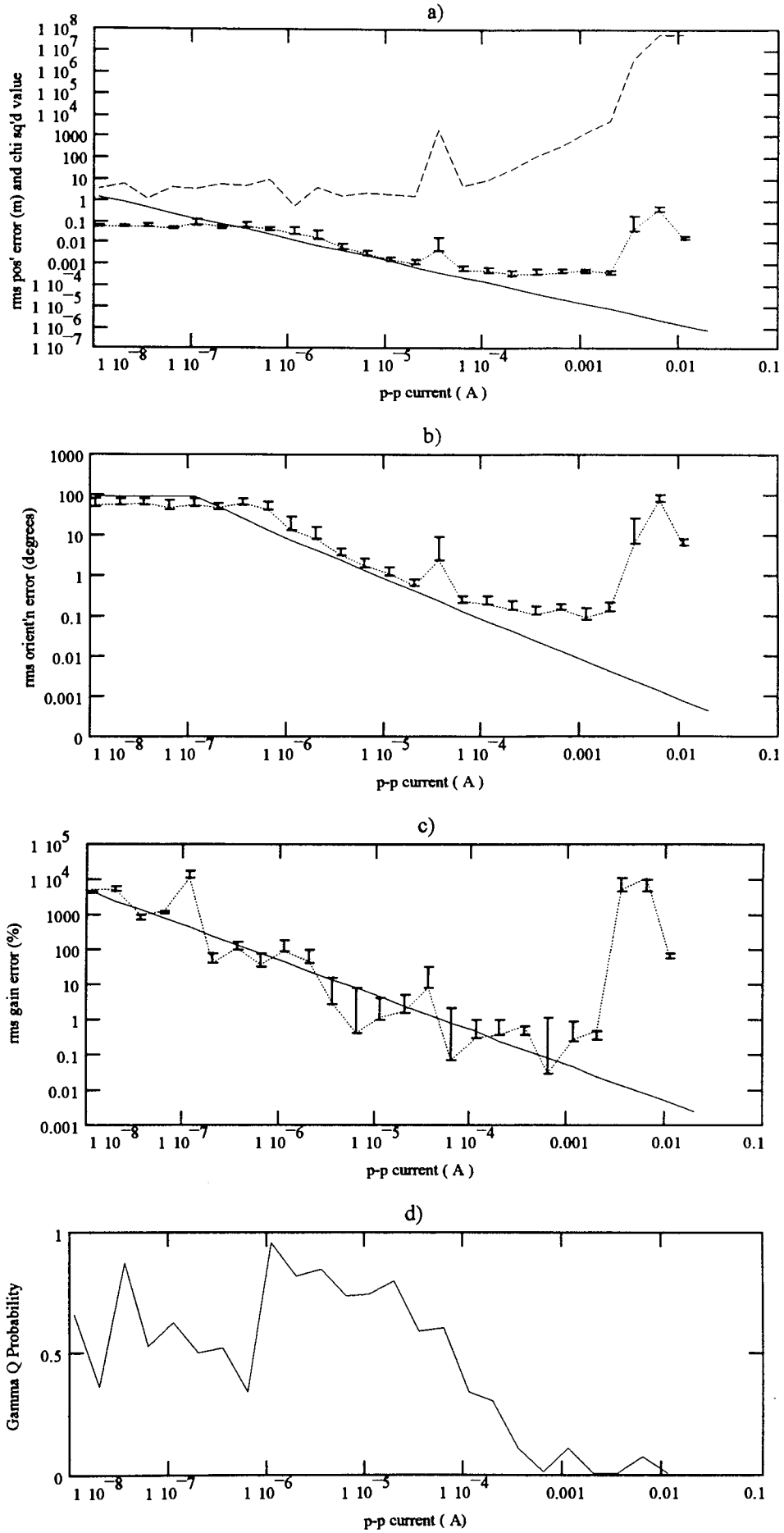

Figure 2.13. SNR vs. parameter variance, theoretical (no wire noise) and simulated. Note at around 10^{-4} A, the curve flattens giving no possible improvement in accuracy. At this point, the noise on the data ceases to account for the deviation from the model,

and hence the chi squared value begins to increase rapidly. (5 wires, 10bits white noise, 4cm height)

2.6.2. Gradiometer balance.

The gradiometer balance is set at the construction of a commercial magnetometer, it is a factor beyond the control of most end-users and therefore an important consideration in any calibration technique. Neuronal activity results in fields which fall off as at least an inverse square with distance (see section 1.1). Both well and poorly balanced gradiometers will respond similarly to nearby neuronal sources since the majority of flux passes through the pick up-coil. A calibration technique has to somehow avoid 'calibrating the imbalance', and return parameters which best describe the pick up coil. The gradiometers at Aston consist of eight coils, spaced as in figure 2.5, of which the two base coils constitute the pick up coil. In order to simulate an imbalance, the remaining 6 coils were shifted in orientation by Gaussian white random noise, so as to change each of their effective areas by σ_{imb} imbalance (Figure 2.14).

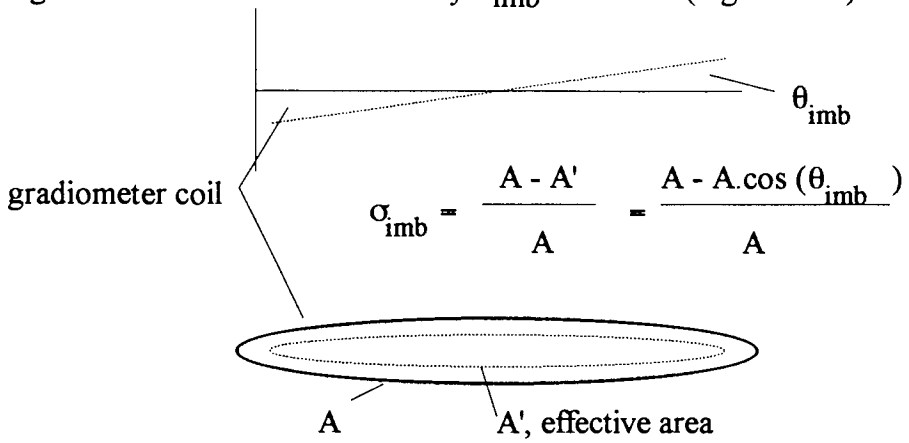

Figure 2.14. Each of the gradiometer coils are displaced by a Gaussian white random angle 6 so as to change the effective coil area by a proportion σ imbalance.

As in the case for wire noise, the signal to noise ratio of the data is increased until the errors introduced by the modelling assumptions show up. Figure 2.15 shows that as SNR is increased, a plateau is reached beyond which, no improvement in parameter error is possible. This plateau, for the five by five wire grid of figure 2.15, and imbalance 10^{-2} indicates the minimum achievable parameter errors are (3mm, 4° and 3%). For an imbalance of 10^{-4} the corresponding errors are (0.2 mm, 0.4°, and 0.1%). Setting a moderate wire current, and increasing the imbalance gives an idea of the fit sensitivity to the modelling errors introduced (figure 2.16). It is interesting to note that the gain parameter seems to be relatively unaffected by moderate imbalance. This is desirable, indicating that the calibration gain reflects that of the pick-up coil and is not unduly sensitive to homogeneity of the compensation coils. Conversely, it seems that good balance, or rather precise knowledge of gradiometer structure, is necessary to recover accurate positional and orientational information.

Figure 2.15 Initial balance of 10^{-4} (boxed) and 10^{-2} (dotted) , also ideal analytical curves (solid) as current is increased. (4 cm height, 5 wires, 2cm spacing, 5 bits white noise). see overleaf.

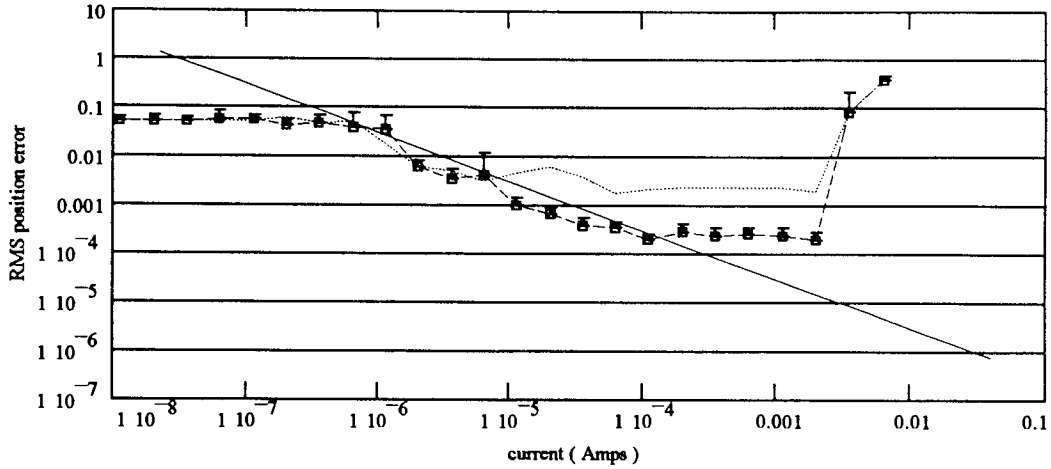
RMS position error
10
1
0.1
0.01
0.001
1 10^-4
1 10^-5
1 10^-6
1 10^-7
1 10^-8
1 10^-7
1 10^-6
1 10^-5
1 10^-4
0.001
0.01
0.1
current (Amps)

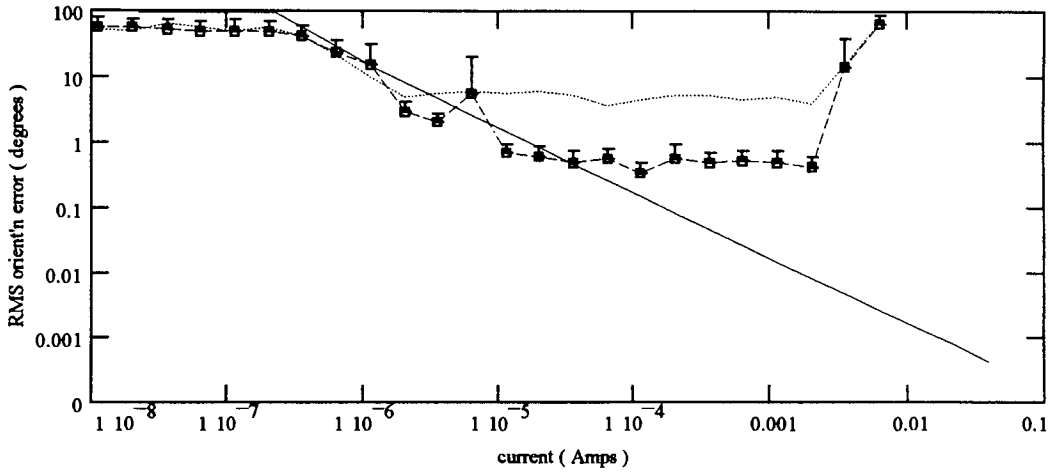
RMS orient'n error (degrees)
100
10
1
0.1
0.01
0.001
0
1 10^-8
1 10^-7
1 10^-6
1 10^-5
1 10^-4
0.001
0.01
0.1
current (Amps)

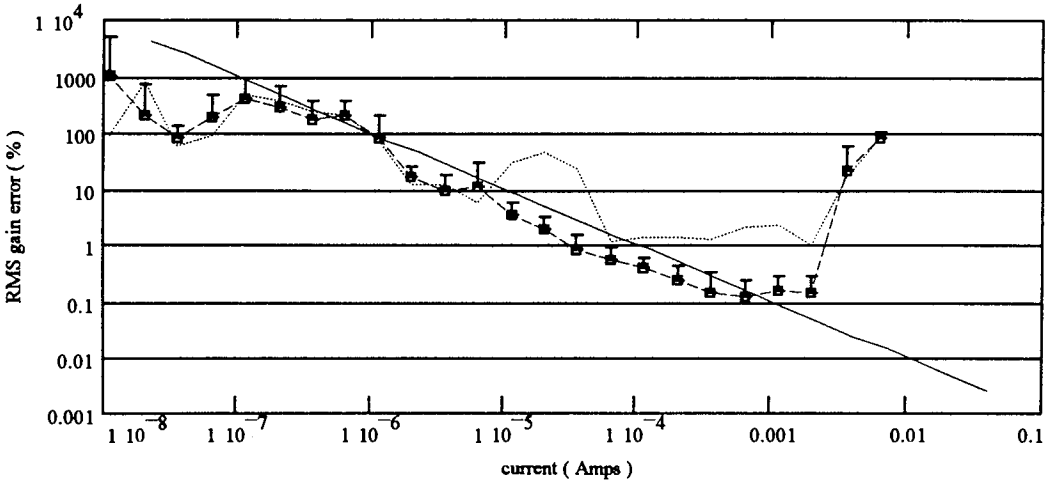
RMS gain error (%)
1 10^4
1000
100
10
1
0.1
0.01
0.001
1 10^-8
1 10^-7
1 10^-6
1 10^-5
1 10^-4
0.001
0.01
0.1
current (Amps)

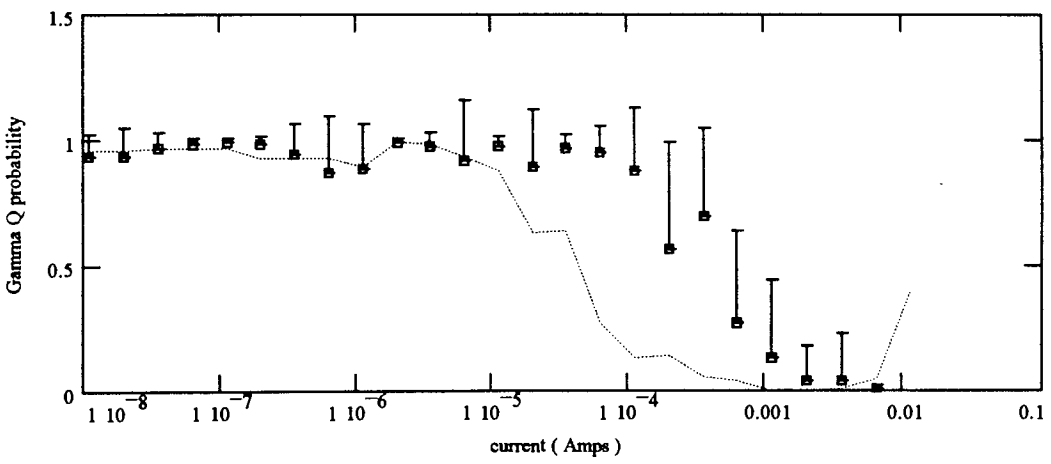
Gamma Q probability
1.5
1
0.5
0
1 10^-8
1 10^-7
1 10^-6
1 10^-5
1 10^-4
0.001
0.01
0.1
current (Amps)

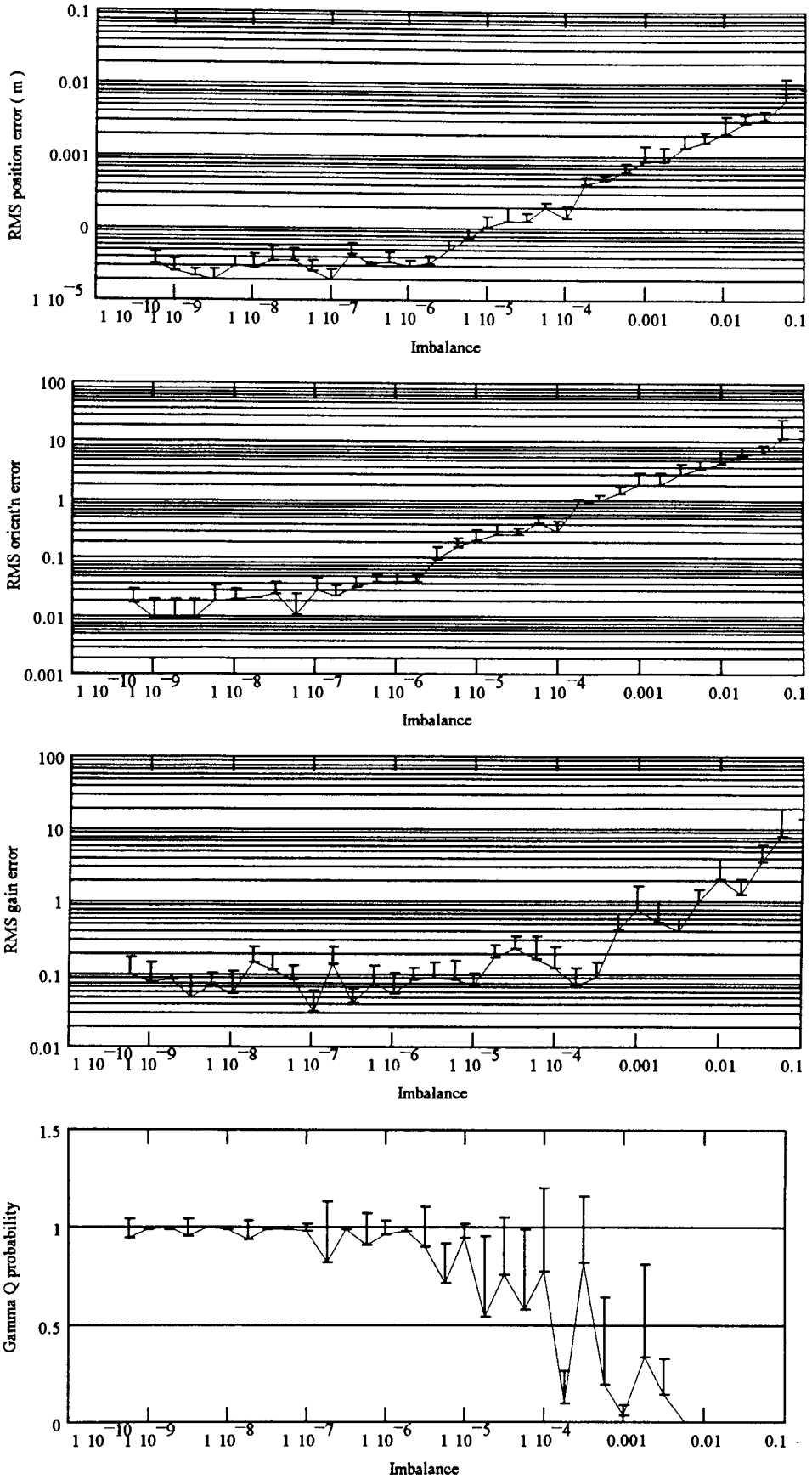

Figure 2.16. Relative error in parameter fits as gradiometer balance is varied. Note the gain error is considerably less sensitive to imbalance than the position and orientation. (4cm height, 5 wires, 2cm spacing, 10 bits white noise, wire current 0.3 mA)

2.6.3. The final model

The limiting criterion on the feasibility of calibration by this method is imbalance. Imperfect wire positioning can be countered by increasing the number of wires (figure 2.12) or simply rebuilding the calibration rig. Parameters for a physical calibration rig are now selected and simulations studied which attempt to predict the performance of the real system.

Physical constraints, such as the thickness of the dewar base and positioning of the Polhemus pen, set 4cm as a reasonable gradiometer height above the grid. For a single gradiometer, this results in an optimal wire spacing of 2cm for 5 wires (see figure 2.7) or an optimal coverage length of 10.5cm (see figure 2.9). The gradiometer array at Aston has maximal dimension of 11.7cm. For each gradiometer to have acceptable coverage area, the wire grid must therefore span approximately 23cm. The more wires within this length, the lower the resulting parameter variance (see figure 2.12) yet the more complex the grid construction.

A twenty by twenty grid of 1cm spacing was chosen. This gives each gradiometer approximately 10cm of coverage, and increases immunity to wire noise. The increase in immunity to wire noise means that the 20 wire grid can be constructed with wires $\sqrt{5}$ times less accurately placed than a 4 wire grid. Figure 2.17 predicts performance of a single gradiometer within the array, as wire current is increased. Coverage length for the gradiometer is taken to be 10cm, realistic values for wire noise and imbalance are used. The predicted accuracy of the results *(0.3mm, 0.6^c, 0.3%)* is acceptable; in section 2.8 this is compared to that physically achieved.

*Figure 2.17. Increasing the SNR for constructed calibration set up with the effects of gradiometer imbalance and wire noise. Estimated achievable parameter accuracy : (0.3mm, 0.6^c, 0.3%). (10*10 wires, 4cm height, 1cm spacing, 5 bits white noise, 0.25mm wire noise, 10^{-4} imbalance). see overleaf.*

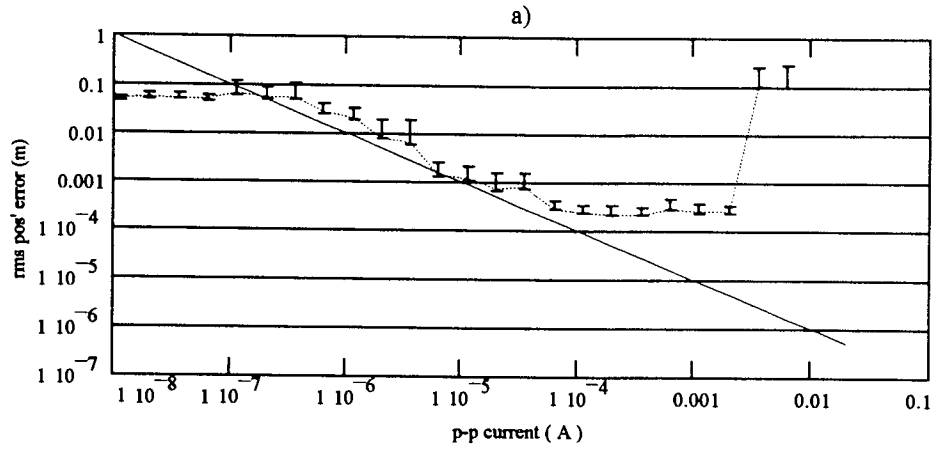
a)
rms pos' error (m)
1
0.1
0.01
0.001
1 10^-4
1 10^-5
1 10^-6
1 10^-7
1 10^-8
1 10^-7
1 10^-6
1 10^-5
1 10^-4
0.001
0.01
0.1
p-p current (A)

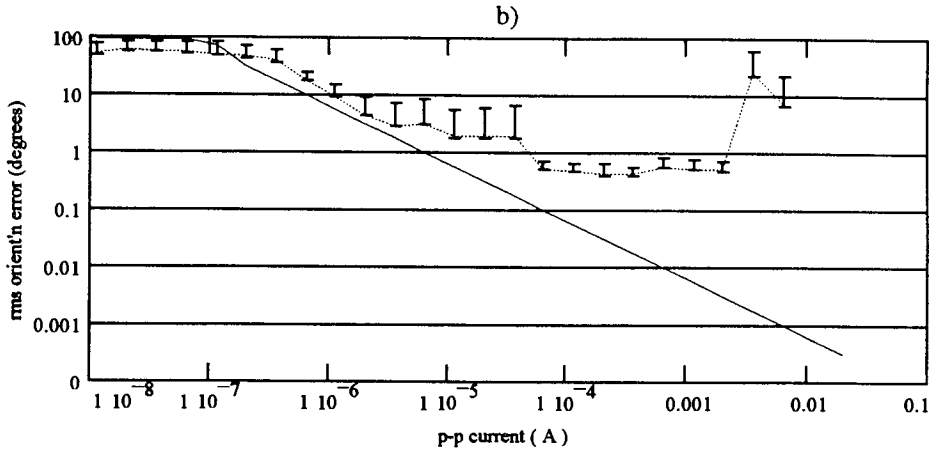
b)
rms orient'n error (degrees)
100
10
1
0.1
0.01
0.001
0
1 10^-8
1 10^-7
1 10^-6
1 10^-5
1 10^-4
0.001
0.01
0.1
p-p current (A)

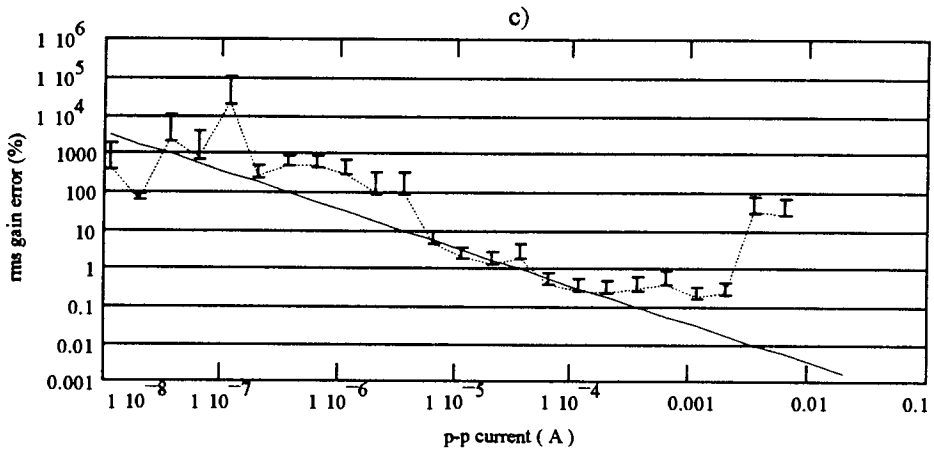
c)
rms gain error (%)
1 10^6
1 10^5
1 10^4
1000
100
10
1
0.1
0.01
0.001
1 10^-8
1 10^-7
1 10^-6
1 10^-5
1 10^-4
0.001
0.01
0.1
p-p current (A)

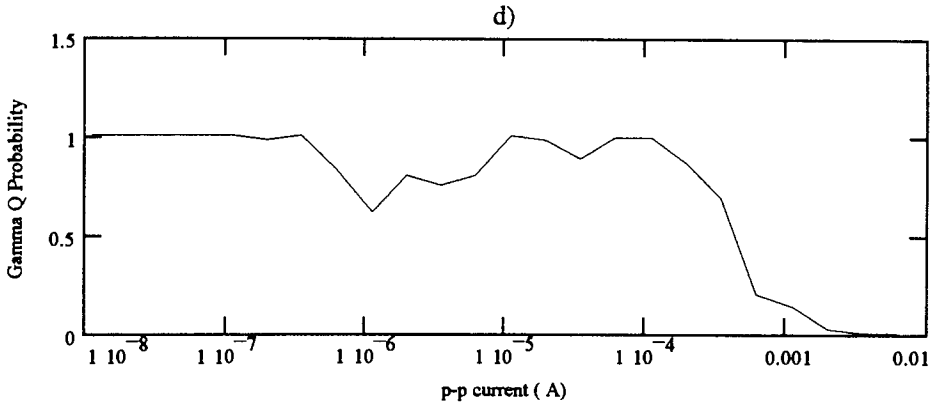
d)
Gamma Q Probability
1.5
1
0.5
0
1 10^-8
1 10^-7
1 10^-6
1 10^-5
1 10^-4
0.001
0.01
p-p current (A)

2.7. Location of Calibration grid

The gradiometer gain has been calculated in an absolute sense. However, the channel positions and orientation are defined only with respect to the wire grid. A commercially available 3D pen position sensor (Polhemus 3Space Isotrak system^{TM}) is used for all position measurements. The device consists of a sensor which is fixed to the dewar base[5], and a remote pen probe. The output of the device is the position and attitude of the pen tip. The device has an accuracy of 2mm and resolution of 1mm. That is, the readout at a particular position is repeatable to within 1mm, but the values represent the centre of a sphere of radius 2mm uncertainty.

There are five parameters which determine the position of the calibration board relative to the Polhemus sensor: 3 translational and 2 rotational. A minimum of 3 independent points are required to completely describe this plane. Using the minimal number of points to describe the grid and hence channel positions would result in an error of 2mm. It is undesirable to lose the high channel position accuracy gained by the calibration procedure simply by not knowing the position of the calibration grid. In practice, the calibration grid is localised by drawing the Polhemus pen along the two axes of the grid and recording a large number of points along these axes. Typically, 100 points are measured along each axis which spans 30cm. Each of the measured points has some measurement noise and some systematic inaccuracy. A straight line is fit to each axis or set of measured points. The grid is defined from the position of intersection of the two axes, and the normal vector to these axes. Empirically, the achieved standard deviation in the position and orientation of this normal vector is 0.63 mm and 0.44 degrees. Were the resolution limited by random rather than systematic noise, one would expect 200 data points to give a resolution of approximately $\frac{2mm}{\sqrt{200-3}} = 0.142mm$.

The angular error is potentially more serious since its effect increases with distance, however even at 20cm the resulting position error is less than 2mm. Although such errors are of comparable magnitude if not greater than achievable calibration channel positional and orientation errors (figure 2.17), their effect is considerably less destructive. Firstly, modelling assumptions depend on relative, not absolute channel positions and orientations. Secondly , absolute positional errors, although systematic, are small compared to the cortical volumes that it is possible to image using magnetometry (~100-1000mm^3, Hamalainen et al. 1991).

2.8. Performance of physical set up.

Typically, in order to estimate the efficacy of any calibration, the achieved results are compared to some known values. Unfortunately, we have only an approximate idea of

---

[5]The sensor contains ferro-magnetic components and is therefore only attached to the dewar before of after neuro-magnetic measurements are made.

where the gradiometer array should be and even X-rays of the dewar are unlikely to confirm the accuracy of calibration claimed in this chapter. There are two sources of calibration error to consider: measurement noise and modelling noise. Firstly, the repeatability of individual gradiometer parameter sets between calibrations will tell us the effect of measurement noise. If the dewar is displaced and rotated between each calibration, then some of the effects of modelling error should also be apparent.

Four calibration runs were carried out. Between each calibration, the dewar was removed, tilted slightly and approximately repositioned above the grid. The channel position and orientation deviations from mean position were assessed for each channel in a working array of 18 (figure 2.18). The average standard deviation per channel in absolute position was found to be 1.1 mm, in orientation 1.03°, in percentage gain 0.049. In order to factor out the systematic positional errors due to locating the calibration board (see section 2.7), the average channel position and orientation of each array was calculated and subtracted from the measured data. Relative standard deviation of channel position was found to be 0.27mm, and channel orientation 0.055°. The data show that the calibration is highly repeatable in an absolute coordinate frame; furthermore, relative channel position and orientation error improve upon simulated estimates of performance (refer to figure 2.17).

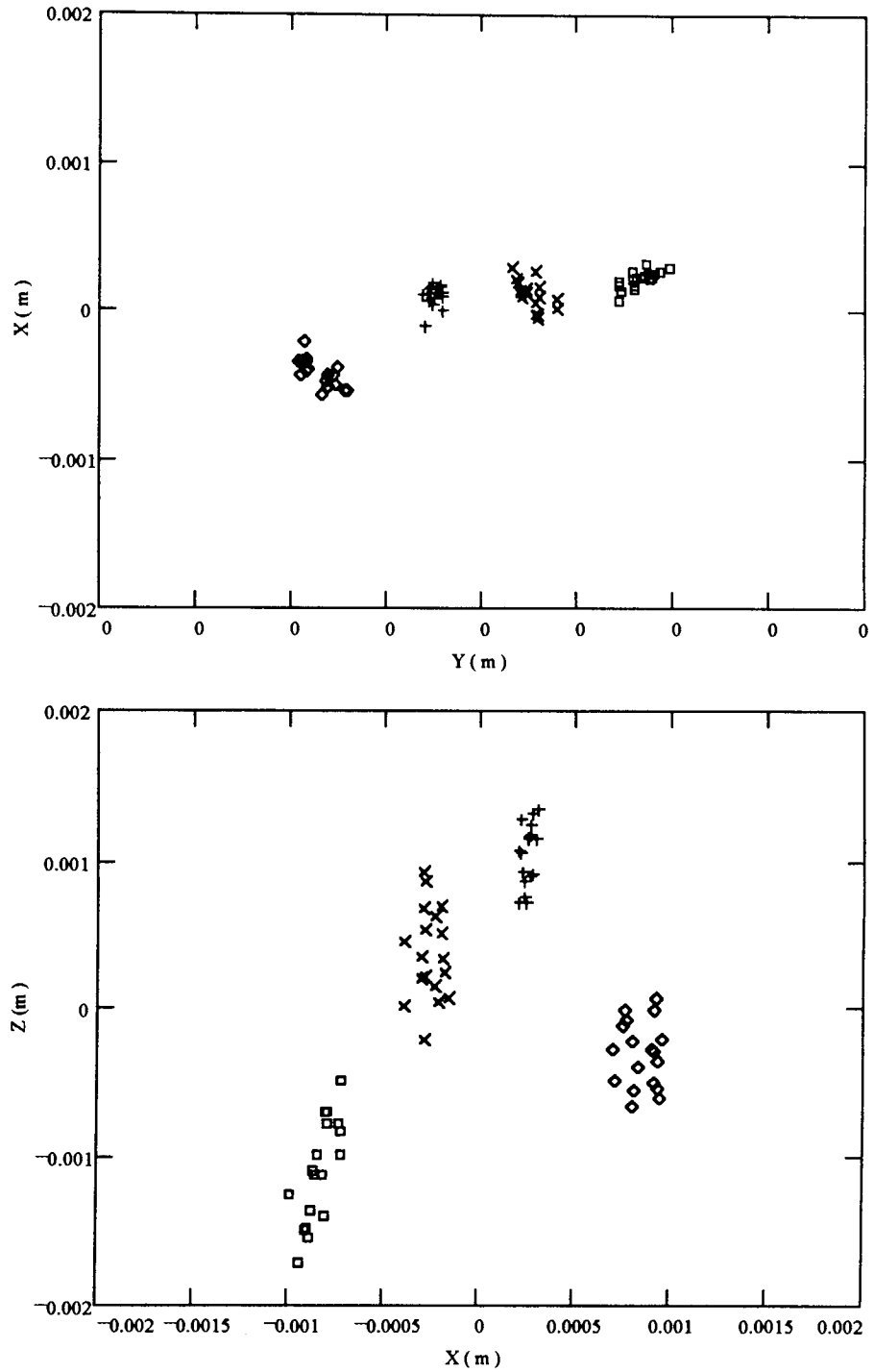

Figure 2.18. 2D Scatter plots (z is up) for the deviation of each channel from its absolute mean position over four calibration runs (each shown as a cluster of different symbols). There is a systematic deviation between clusters which reflects imperfect positional knowledge of the calibration board. The sizes of the individual clusters reflect relative positional error. Note that the largest positional error is in the z direction.

The repeatability of absolute positional and orientation parameters with different dewar positions encourages the proposition that the results are not due to modelling error. However, especially in the case of the gain parameter, it is still necessary to discount the possibility that this repeatability is not due to mis-modelling. Given that the estimation of measurement noise is correct, performing a model fit to empirical data should give a comparable chi-square measure to that obtained from the mismodelled simulation study (section 2.6). If the empirical chi-square value exceeds the simulated chi, then the simulations have underestimated or failed to model errors in the system. Alternatively, if the empirically achieved chi-square value is less than or equal to that achieved by simulation, then the simulation study must be valid. If the simulation studies relate to the physical situation, then we can directly read off limits for physically achievable parameter variances from a wealth of computer generated results. The simulation data of figure 2.17 is replotted in figure 2.19 along with the chi-square measure, the usual 40dB/ decade increase past saturation point (at around 10^{-4} amperes) is clear. Figure 2.20 shows the empirically achieved chi-square values alongside the simulated chi-squared due to the modelling errors. On average, the modelling errors measured are less than those simulated. Individual channel chi-square values (figure 2.21) , show that the simulation under models two or three channels in each calibration run; these channels are identical across runs. Since the modelling error is channel specific, it is probably due to higher than anticipated gradiometer imbalance or some other geometric factor. For the large proportion of channels however, the achieved chi-square values indicate that the non-idealities of the physical set up have been accounted for in the simulation studies.

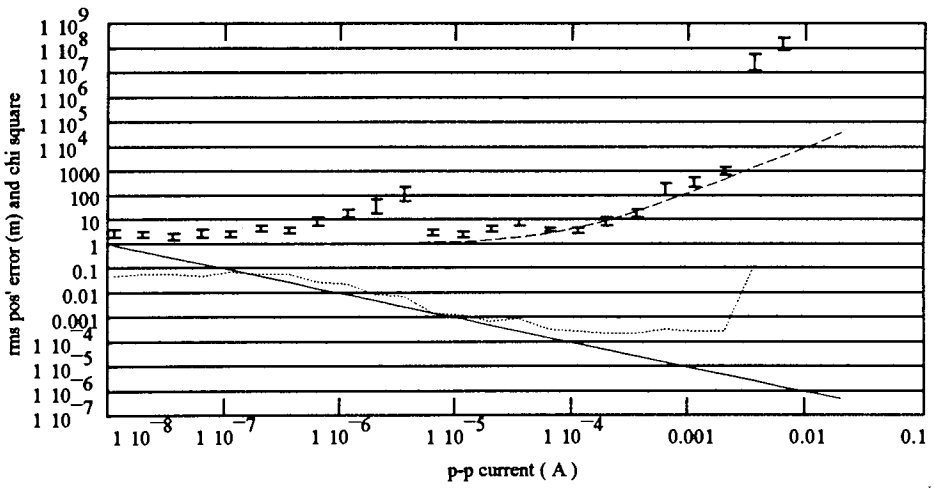

Figure 2.19. Data of figure 2.17, position error vs. current in wire. The dotted line shows the quadratic curve of (1) fit to the data. Where $\sigma^2_{est}=\sigma^2_{true}=1/$ current, and $\Delta=10^4$. Note that it is the relative, not actual values of these parameters which are important.

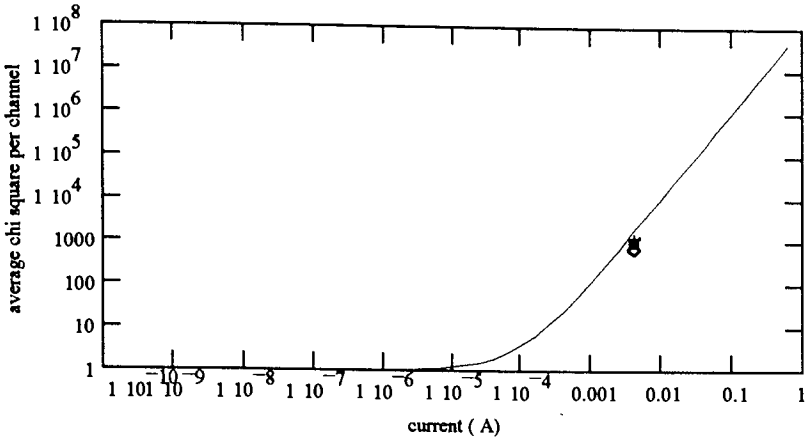

Figure 2.20. Average chi-square value per channel for the four calibration runs (symbols), as compared to the chi-square value obtained with simulated modelling errors of figure 2.17 (solid curve).On average, the physical situation is better described by the model than anticipated.

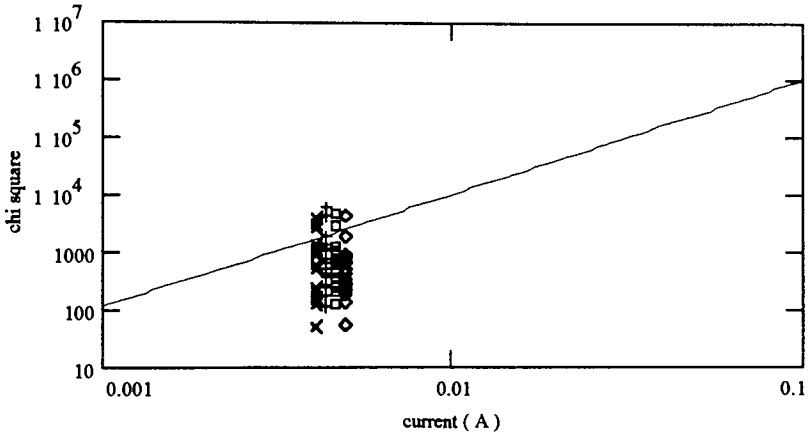

Figure 2.21. Chi square value obtained from the 18 individual channels for four calibration runs (symbols). For clarity the data are displayed over an expanded section of the current axis and have been displaced ,the abcissae of all data points actually correspond to that of the crosses. It is clear that the majority of the channels are more precisely modelled than anticipated from simulations. Actually, the relative distribution of chi-square across channels is consistent between runs, that is, the data reflects variation in physical characteristics of individual channels.

2.9. Analogue Filter Calibration

All pre-amplified neuromagnetic signal data must pass through some bank of anti-aliasing analogue filters (figure 2.22) before it can be adequately digitally sampled. The advantages gained by careful calibration at a certain frequency can easily be lost if these filters have poor homogeneity. Let each analogue filter i have amplitude characteristic H_i (f) and phase characteristic ϕ_i (f). Figure 2.23 shows a sample of amplitude and phase characteristics of the Aston filter bank. It is clear that any calibration estimate of relative channel gain carried out at 33.2Hz will be inappropriate at 80Hz due to the inter-filter variability of phase and amplitude characteristics.

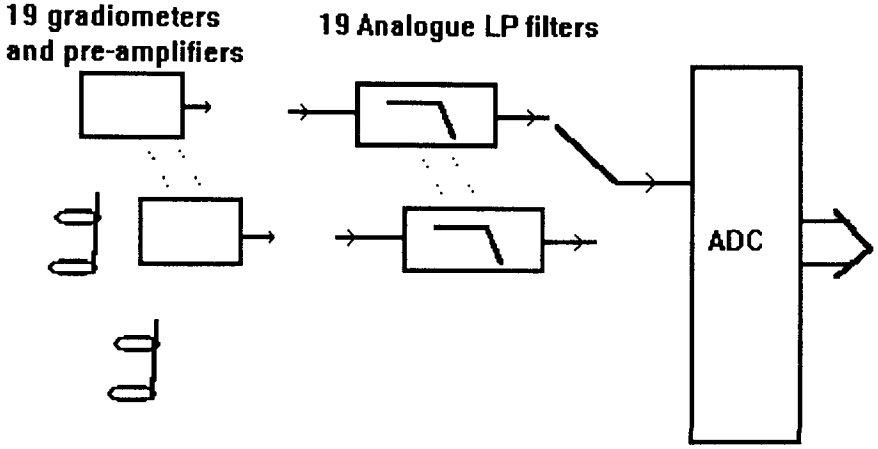

Figure 2.22. The output of each gradiometer passes through a separate analogue anti-aliasing filter, before being sequentially sampled by a 16 bit ADC.

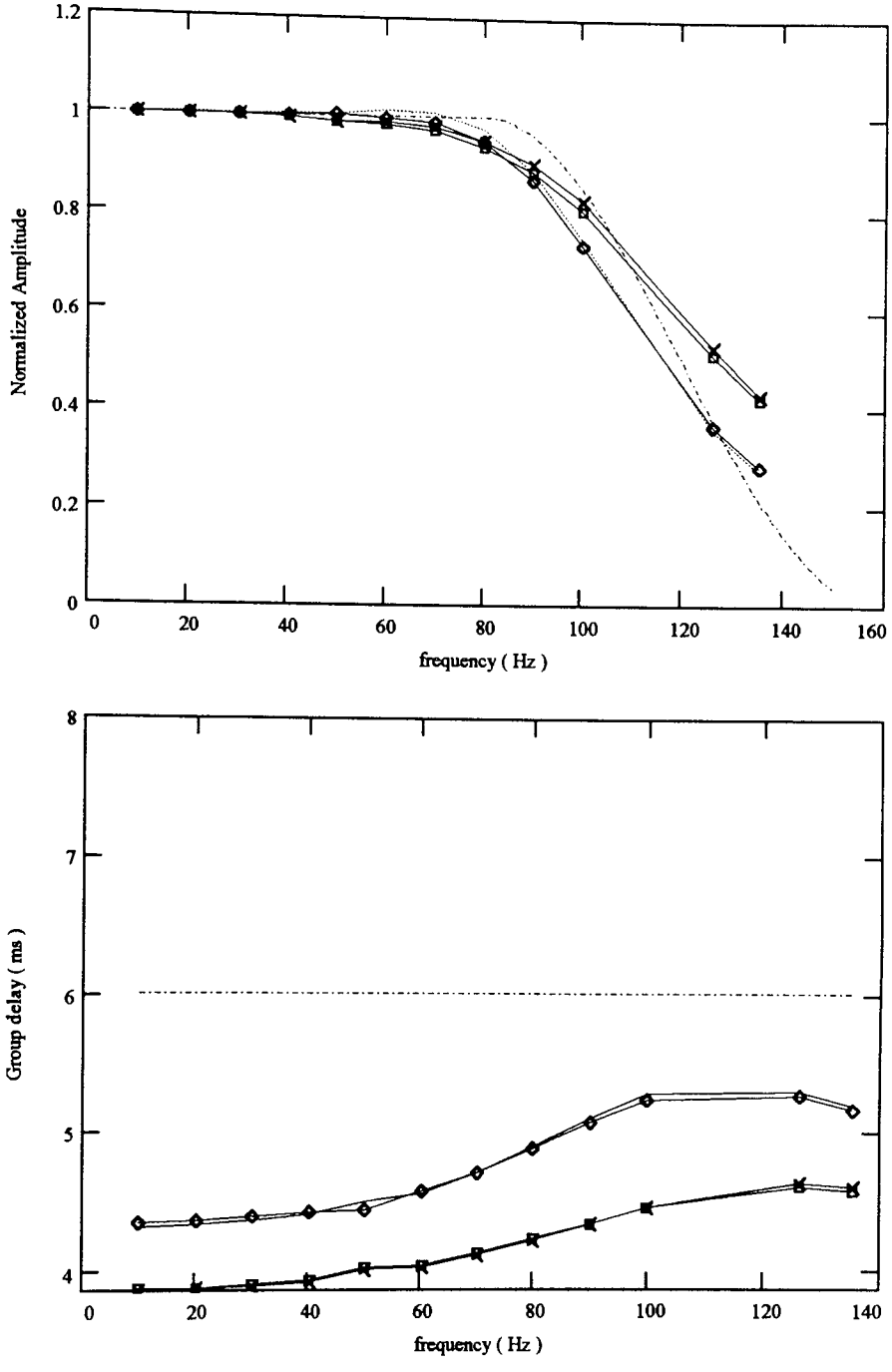

Figure 2.23. Relative amplitude and group delay for first four of the nineteen 100Hz fourth order Butterworth filters at Aston. Dashed traces show ideal filter pass-band - completely flat up until 80Hz where it cuts off smoothly in a $\cos^2$ window.

Analogue filter inhomogeneities can be suppressed by passing the recorded data through a set of digital correcting filters. By defining some ideal filter impulse response, and having measured individual filter impulse responses, it is possible to specify the amplitude and phase characteristics of a set of correcting filters :

Digital filter i has amplitude response

$$H(f)_i := \frac{response\_ideal(f)}{response\_filter\_i(f)}$$

and group delay characteristic given by

$$d(f)_i := delay\_ideal(f) - delay\_filter\_i(f)$$

or alternatively, phase characteristic

$$\phi(f)_i := d(f)_i \cdot 2 \cdot \pi \cdot f$$

In order to quantify errors due to filter inhomgeneity, the term 'coherence noise' is defined as the RMS deviation from mean of N filter outputs when driven with common input sinusoid at any time instant. In fact, the system at Aston does not accommodate a single input sinusoid to all individual filter, the input must first pass through a set of 19 pre-amplifiers which have some intrinsic disparity of gain. This disparity of gain is small compared to the disparity between filters and can be ignored in the first stage analysis:

Define Coherence noise for an input sinusoid freq f at sample s:

$$Nc(f)_s := \sum_{i=1}^{19} \frac{\left(c(f)_{i,s} - m(f)_s\right)^2}{19}$$

where channel mean ..

$$m(f)_s := \sum_{i=1}^{19} \frac{c(f)_{i,s}}{19}$$

and

$$c(f)_{i,s} := \left(A(f) + \sigma_a\right) \cdot \sin\left[2 \cdot \pi \cdot \frac{f}{F} \cdot s + \left(\sigma_d \cdot f + \phi(f)\right)\right]$$

Where f is the frequency of the input sinusoid, F the sample rate, A(f) and $\phi(f)$ are ideal amplitude and phase response, and

σ_d and σ_a represent rms deviations of particular filter channel in group delay and amplitude from ideal output.

Total coherence noise for *nsmp* samples of a sinusoid :

$$NC := \sum_{s=1}^{nsmp} Nc_s$$

Now consider the coherence noise to signal ratio

$$percent\_coherence\_noise := \sqrt{\frac{NC(f)}{\sum_{s=1}^{nsmp} \left(m(f)_s\right)^2}} \cdot 100$$

For an ideal system, each filter would be identical giving NC(f)=0

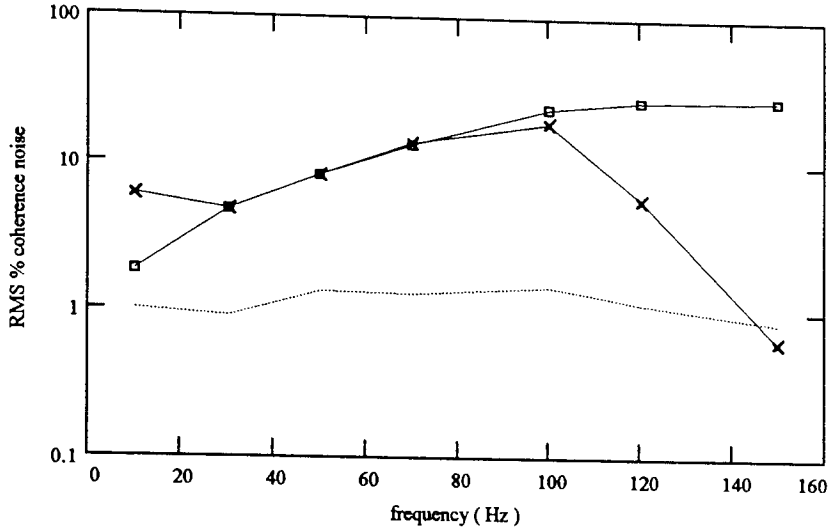

Figure 2.24. RMS % coherence noise on input sinusoid to 19 channel 100Hz filter bank at Aston. Before compensation (boxes) , after amplitude compensation only (crosses) and after both amplitude and phase compensation (dotted trace).

Figure 2.24 shows that coherence noise increases monotonically with frequency in the uncompensated filter bank. Correcting for the amplitude differences in response across channels has relatively little effect at lower frequencies, but is more noticeable at higher frequencies where filter amplitude characteristics are more disparate. Within the pass-band, filter phase deviations are the dominant source of coherence noise. Correction for both filter phase and amplitude reduces coherence noise to 1% of RMS amplitude.

It is possible that this 1% error level does not reflect the filter stage, but is due partly to the individual pre-amplifier stage. This gain error is accounted for in the overall calibration, yet needs to be factored out in order to assess actual coherence noise. Consider the pass-band data only: error in the pass-band is accounted for primarily by phase noise (figure 2.24).

Assuming phase errors only, the relative difference between ideal and phase shifted sinsuoid is given by

$$\text{phase\_err}(f,s) := A\cdot\sin\left(2\cdot\pi\cdot f\cdot\frac{s}{F}\right) - A\cdot\sin\left(2\cdot\pi\cdot f\cdot\frac{s}{F} + \sigma_d\cdot f\right)$$

equivalent to

$$\text{phase\_err}(f,s) := 2\cdot A\cdot\cos\left(2\cdot\pi\cdot f\cdot\frac{s}{F}\right)\cdot\sin\left(\frac{\sigma_d\cdot f}{2}\right)$$

So for a given frequency, we can predict coherence noise due to phase as

$$NC(f) := \sum_{s=1}^{nsmp} \text{phase\_err}(f,s)^2$$

Taking account of relative pre-amplifier gain error σ_{pre_amp} gives expected coherence noise

$$NC(f) := \sum_{s=1}^{nsmp} \left(\text{phase\_err}(f,s) + \sigma_{pre\_amp}\cdot A\right)^2$$

Empirical data has the form of the above function (figure 2.25) and fitting the function to the data gives an approximate estimate of the achieved phase noise. The correction of filter phase and amplitude has reduced effective phase noise in the system to around 0.04ms.

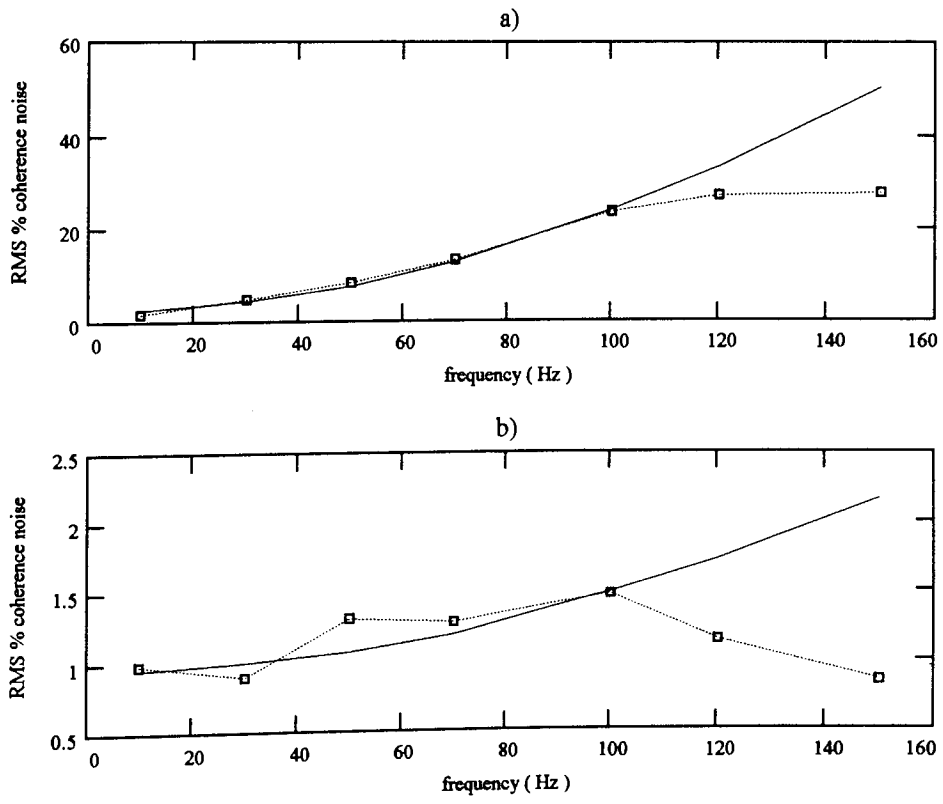

Figure 2.25. RMS % coherence noise, boxes show empirical data, smooth curves are fit to the data over the range 0-100Hz. a) Uncompensated system, b) compensated : the deviation above 100Hz is accounted for by the increase in importance of amplitude compensation. Fitted curves have the following parameters :

Uncompensated : $\sigma_d = 0.14$ *ms*, $\sigma_{preamp} = 1.9\%$;
Compensated : $\sigma_d = 0.040$ *ms*, $\sigma_{preamp} = 1.2\%$.

2.10. Concluding remarks

A grid of long wires has been shown to be a practical technique for calibration of a second order gradiometer array providing the gradiometers are well balanced ($\approx 10^{-4}$). The results improve upon the repeatability measures reported by Buchanan and Paulson (1989) who used a small coil to calibrate their array. Furthermore, simulation studies show that the repeatability of these results is not due to some mismodelling of the physical situation. In this study, all significant errors arise not in the calibration itself but at some peripheral stage. For example, relative channel positional errors have been shown to be small compared to those systematic errors introduced by the Polhemus digitisation system. Likewise, the largest stage of channel gain error has been found to be due to the analogue anti-aliasing filters.

The study adds to the body of existing work in a number of ways:

i) It is the first detailed study of the utility of a long straight wire calibration technique.

ii) Analytical fomuli have been derived which predict the achievable accuracy of calibration given any ideal wire grid. These formuli provide a fast and convenient platform to begin any design stage. The approach in previous work has been to construct a calibration rig and then subsequently assess its performance based on repeatability measures.

iii) The sensitivity of the technique to imprecise modelling of the physical situation has been assessed. By simulation, acceptable bounds to the measure (chi-squared) of this modelling error have been shown. The chi-square provides an extra parameter with which to assess the validity of any physical calibration. For example, the results in this study improve on all previously reported; this is likely to reflect the fact that previous studies were limited my modelling rather than measurement noise, yet since no expected chi-squared bounds for such models had been examined, the unsuitability of such models was not discovered.

Chapter 3.

Adaptive Filtering of Neuromagnetic Data

3.1. Introduction

Commonly, extraction of useful signal from noise is achieved by attenuation of some part of the frequency spectrum (figure 1a). In the case where noise and signal spectra overlap (figure 1b), or indeed if either the noise or signal spectral density is unknown a-priori, other filtering techniques must be employed.

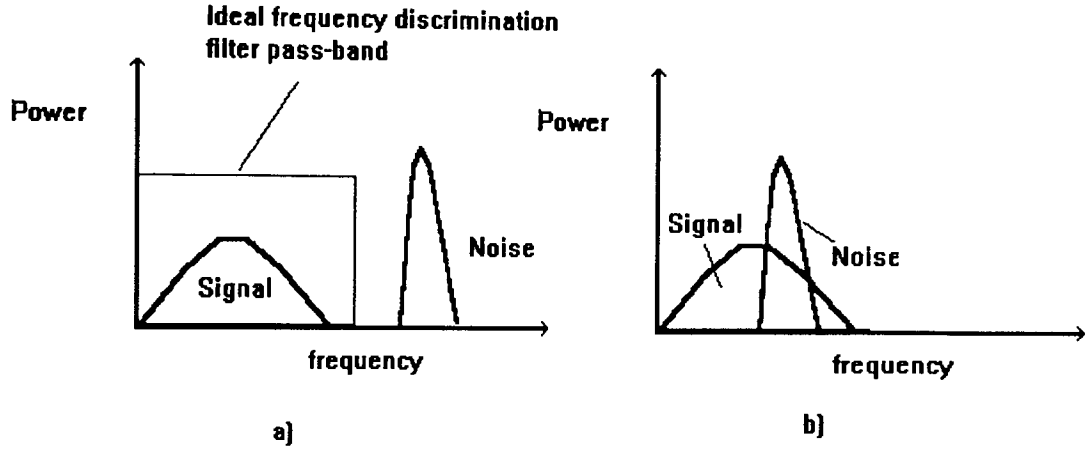

Figure 3.1 a) Frequency discrimination is appropriate when the signal and noise are known to occupy non-overlapping frequency bands. b) Where signal and noise share the same frequency bands, or the signal and noise spectra are unknown a-priori, frequency discrimination filtering may result in loss of signal information.

The noise cancellation techniques addressed in this chapter rely on the discrimination of signal and noise on the basis their spatial, rather than frequency distribution. The form of spatial filtering applied has led to analogies with the gradiometer structure and the technique is sometimes referred to as 'electronic balancing'. Essentially, an independent measure of environmental noise from a set of reference channels is made use of (figure 3.2); this measurement will be highly correlated with any environmental noise on the signal channel. By subtraction of a weighted proportion of this measure from the signal channel, the environmental noise component can be removed. The technique is appealing since it requires no a-priori assumptions concerning the spectra of either the signal or noise source.

Reference noise cancellation has been widely applied in the field of biomagnetism. Hansen and Bowser (1983) used an orthogonal accelerometer array and flux- gate magnetometer as reference channels; their primary aim was to cancel environmental noise due to vibrations of the gradiometer sensors in the earth's field. Williamson et al. (1984) and Robinson (1989) used magnetometer and gradiometer combinations as reference channels to improve rejection of generalised far-field noise sources.

Shimogawara and Kado (1993) apply the techniques to rejection of signals due to small magnets, such as those present in hearing aids, attached to the subject. Both Robinson (1989) and Hansen et al. (1983) found better results could be obtained by pre-filtering the reference channels.

In the literature, algorithm performance is frequently judged, in noise only conditions, by total filter output power. Furthermore the time evolving or non-stationary nature of any reference noise cancellation solution is rarely mentioned.

In this chapter, section 3.2 introduces the mathematical formalism of the adaptive filtering problem (Widrow and Stearns 1985; Alexander 1986; Proakis and Manolakis 1988). The concept of stationarity is introduced. The calculation of the Wiener solution is shown to be the identification of a simple parabolic error surface minimum. Ideal gradient descent to the base of this surface is discussed, and then the operation of the more practical LMS algorithm is derived. Measure of the LMS filter performance in terms of its misadjustment is introduced and misadjustment errors due to filter lag and steady state filter performance are quantified. Finally, the Recursive Least Squares (RLS) and other forms of fast Kalman filters are mentioned. Importantly, the conclusion of Widrow (1977) is reiterated, that misadjustment due to steady state error is present in all adaptive algorithms, including that based on the Wiener solution.

Section 3.3 deals with the implementation of the LMS algorithm as a real-time filter of running average evoked response data. The importance of DC level removal, and the order of averaging and filtering are discussed.

In section 3.4, an experimental trial using a known signal is used to create a filter performance measure which reflects signal integrity. This performance is compared to that predicted from LMS filter theory (section 3.5) and the algorithm performance shown to be deterministic over 0.5 second epochs of data.

In section 3.6, excess noise arising due to changes in the optimal solution is modelled a driving non-stationary step at the beginning of each epoch. Given such stationarity measures, optimal time constant progression for any adaptive algorithm is proposed. Finally, the advantages and disadvantages of using additional time derivative reference channels are discussed.

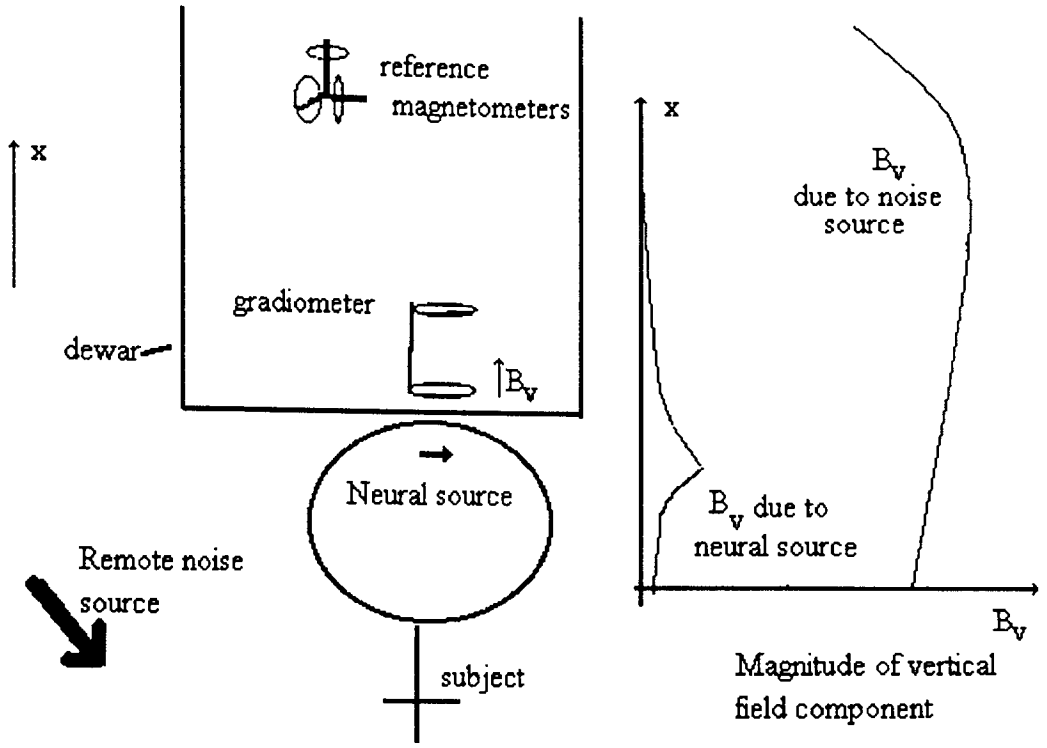

Figure 3.2. Magnetometer reference sensors, placed remote from the main gradiometer array, contain a measure of environmental noise. The gradiometer output consists of the neural signal plus some component of this environmental noise.

3.2. Reference noise cancellation

Consider sample *n* of a measured signal *d*, *d(n)*,which is comprised of a neural signal *s(n)* along with some environmental noise *c(n)*.

$$d(n) = s(n) + c(n)$$

Let *y(n)* be the output of some filter structure operating on *d(n)*. The goal of any filter is to give an output *y(n)* which is closest to *s(n)*. This chapter is concerned with a particular class of filter known as the multiple reference noise canceller, the simplest form of which (the single reference noise canceller) is illustrated in figure 3.3. Consider a reference signal *x(n)* (figure 3.4), which provides a measure of environmental noise highly correlated with *c(n)*. The influence of *c(n)* can be attenuated by the subtraction of a proportion *w* of the noise reference *x(n)*.

$$y(n) = d(n) - w^*.x(n)$$

Note that no a-priori information regarding *c(n)* is required, the problem is calculation of the ideal proportion or weight *w**. Generally, the optimal solution *w** will be time variant, that is, an adaptive algorithm which tracks the time variant optimal solution *w*(n)* is required.

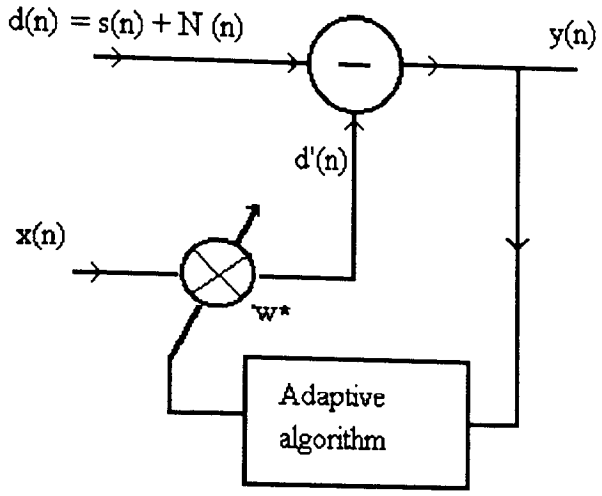

Figure 3.3. Single weight noise canceller. d(n) is the signal corrupted by some noise source. x(n) contains a measure of this noise. The algorithm selects a value of w such that d'(n) is closest to d(n) by some measure. The result is the removal of correlations between the filters output y(n), and the noise reference x(n).

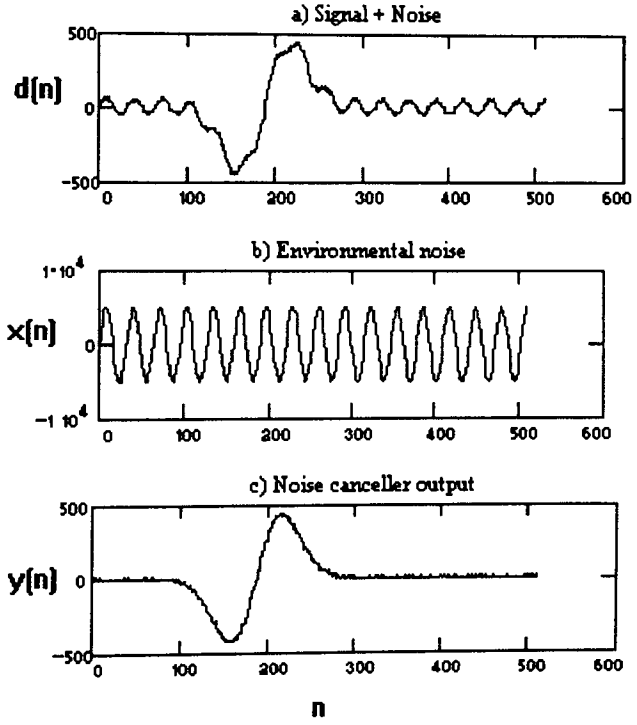

Figure 3.4. Demonstration of operation of basic noise canceller; the correlations between the noisy signal in a) and the reference in b) are removed by appropriate choice of weight w in c).

3.2.1. Stationarity

The term stationarity is used to describe the stability of a random temporal sequence. A signal is said to be stationary in the mean, if the "expectation", E, of all samples in an infinite sequence is constant

$$E(x(n)) = \mu_x \qquad \text{for all n.}$$

A signal is said to be stationary in the auto correlation if the auto correlation function is identical regardless of the time at which it is evaluated

$$r_{xx}(n) = E\{x(k)x(k-n)\} \qquad \text{for all n and k.}$$

A signal which is stationary in both the mean and auto-correlation, and has finite variance, is said to be *wide-sense stationary*.

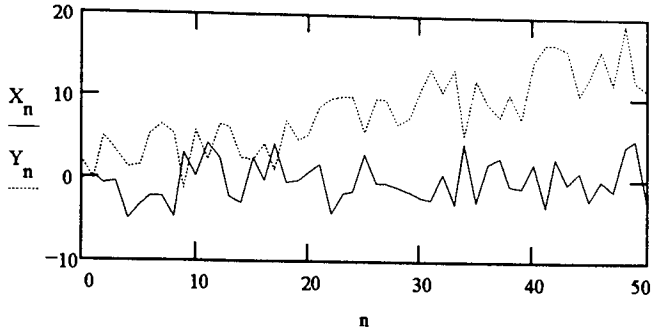

Figure 3.5. It is clear that Y(n) is non-stationary both in the mean, and auto-correlation since the data trend makes data statistics dependent on n. Whereas from initial examination X(n) appears stationary, at least in the mean.

Most signals can be classed as approximately wide sense stationary when considered over a small enough time interval (Cadzow 1987). The implications of non-stationarities in neuromagnetic data are considered in section (3.3).

3.2.2. Mean Square Error criterion

For the multiple reference canceller, let N reference channels at sample n be represented by a vector **x**(n), the corresponding weights **w**(n). The adaptive filtering problem is the location and tracking of the optimal solution vector **w***(n). It is required to use the reference noise channels to create a best estimate of the signal d'(n) which is closest to d(n) by some criterion (see figure 3.1). A typical criterion is the expected filter output power, often referred to as the Mean Square Error (MSE).

$$\text{MSE}(n) = E(y(n)^2) \qquad (1)$$

The filter output is referred to as error since it is the difference between the actual signal and that predicted by the filter.

$$y^2(n) = (d'(n) - d(n))^2 \qquad (2)$$

and d'(n) is

$$d'(n) = \mathbf{w}^T(n).\mathbf{x}(n) \qquad (3)$$

Combining (1), (2) and (3) gives

$$\text{MSE}(n) = E[y(n)^2] = E[\ (d(n) - \mathbf{w}(n)^T.\mathbf{x}(n))^2\ ] \qquad (4)$$

$$\text{MSE}(n) = E[\ d^2(n)\ ] - 2\,E[\ \mathbf{w}^T(n).\mathbf{d}(n).\mathbf{x}(n)\ ] + E[\mathbf{w}^T(n).\mathbf{x}(n).\mathbf{x}^T(n).\mathbf{w}(n)] \qquad (5)$$

Equation (5) gives the expected MSE ,or filter output power, at sample n for any time variant weight vector **w**(n). Note that the equation is quadratic in **w**(n). In the next section, the time variant behaviour of the weights is removed and the optimal solution for a fixed length stationary data sequence is assessed.

3.2.3. The Wiener solution

It is required to find the time invariant solution vector **w*** that will minimise the MSE criterion for a block of K data samples.

$$MSE = \sigma^2_d - 2.\mathbf{w}^T.E[\,\mathbf{d}(n).\mathbf{x}(n)\,] + \mathbf{w}^T.E\,[\,\mathbf{x}(n).\mathbf{x}^T(n)].\mathbf{w}$$

where $E[\,d^2(n)\,]$ is replaced with average signal power σ^2_d.

Let $\mathbf{P} = E[\,\mathbf{d}(n).\mathbf{x}(n)\,]$, the N component cross-correlation vector between signal and reference channels.

Let $\mathbf{R} = E\,[\,\mathbf{x}(n).\mathbf{x}^T(n)\,]$, the N*N cross-correlation matrix of reference channels. For example, the two dimensional case, for a block of n samples gives:

$$\text{For } \mathbf{x}(n) = \begin{pmatrix} x_0(n) \\ x_1(n) \end{pmatrix} \text{ and } \mathbf{w} = \begin{pmatrix} w_0 \\ w_1 \end{pmatrix}$$

$$\mathbf{P} = \frac{1}{K}\begin{bmatrix} \sum_{n=0}^{n=K-1} x_0(n).d(n) \\ \sum_{n=0}^{n=K-1} x_1(n).d(n) \end{bmatrix} \text{ and } \mathbf{R} = \frac{1}{K}\begin{bmatrix} \sum_{n=0}^{n=K-1} x_0(n).x_0(n) & \sum_{n=0}^{n=K-1} x_0(n).x_1(n) \\ \sum_{n=0}^{n=K-1} x_1(n).x_0(n) & \sum_{n=0}^{n=K-1} x_1(n).x_1(n) \end{bmatrix}$$

For stationary data, the quantities **R**, **P** and **w** are independent of n, the expected error for a given weight vector **w**, is therefore given by

$$MSE(\mathbf{w}) = \sigma^2_d - 2.\mathbf{w}^T.\mathbf{P} + \mathbf{w}^T.\mathbf{R}.\mathbf{w} \qquad (6)$$

In order to calculate the optimum weight vector for a given data set **w** that sets the derivative of (6) to zero is calculated

$$\frac{d(MSE(\mathbf{w}))}{d\mathbf{w}} = -2.\mathbf{P} + 2.\mathbf{w}^T.\mathbf{R} \qquad (7)$$

At the minimum $\mathbf{w} = \mathbf{w}^*$.

$$0 = -2.\mathbf{P} + 2.\mathbf{w}^T*.\mathbf{R}$$

$$\mathbf{w}^* = \mathbf{R}^{-1}.\mathbf{P} \qquad (8)$$

This result (8) is commonly referred to as the Wiener solution. For real, non zero data, **R** is real and symmetric and therefore invertible. The Wiener solution returns a fixed weight solution vector by estimation of data statistics over finite length data block. If the data is stationary, the Wiener solution will provide optimal weights for that data block. Non-stationarities in the data imply that a temporally evolving solution is required.

Define the minimum MSE as E_{min}

$$E_{min} = \text{MSE}(\mathbf{w}^*) = \sigma^2_d + 2.\mathbf{w}^{*T}.\mathbf{P} + \mathbf{w}^{*T}.\mathbf{R}.\mathbf{w}^* \qquad (9)$$

which combining with (8) gives

$$E_{min} = \sigma^2_d - \mathbf{P}^T.\mathbf{w}^* \qquad (10)$$

In the case where all noise is reference correlated, the filter output contains only the underlying useful signal.

$$E_{min} = \sigma^2_s$$

Two commonly used measures of filter performance are excess MSE and misadjustment (Widrow 1976) due to non-optimal weights.

where

$$\text{Excess\_MSE} = \text{MSE} - E_{min}$$

and misadjustment (M) expresses excess MSE as a fraction of E_{min}.

$$M = \frac{Excess\_MSE}{E_{min}}$$

3.2.4. The MSE surface

Equation 6 is quadratic in the weight vector **w**. By changing the weight vector, the different MSE values obtained map out a surface. The surface is a parabolic bowl of dimension N, its minimum lying at the optimum weight vector **w***. The two reference case (figure 3.6) is straightforward to conceptualise. Any adaptive algorithm will begin at arbitrary initial weight values which give some excess error. The task of the algorithm is to adjust **w** so as to move down the MSE surface and track the minimum point.

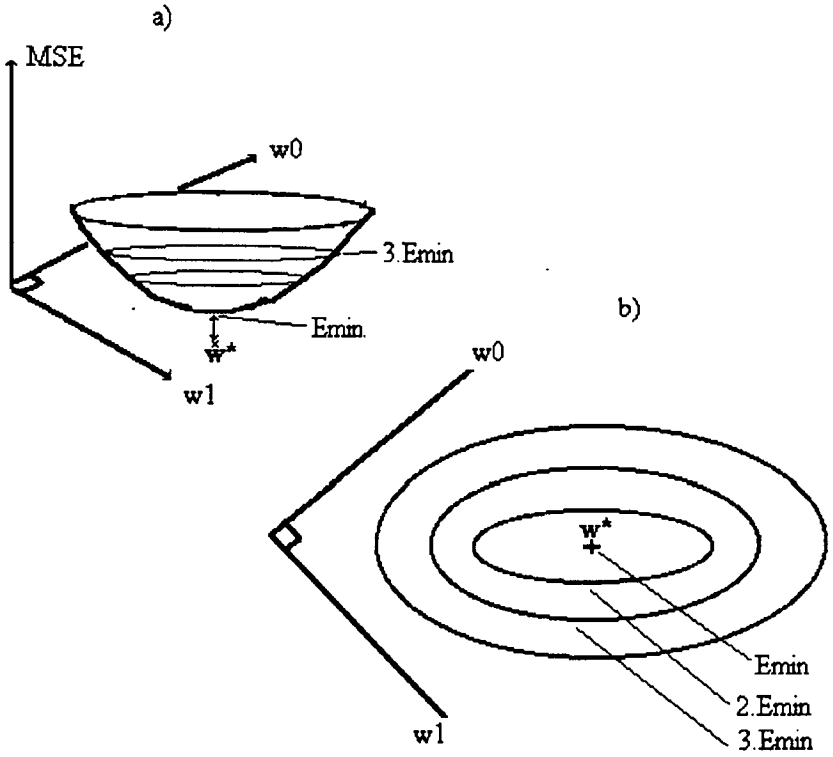

Figure 3.6. An example of the two reference error surface. a) The MSE surface is parabolic in shape and has a minimum corresponding to minimum error power Emin at $\mathbf{w}^*$*, Any deviation from this solution vector leads to increase in error power. b) The contour plot shows the same information in terms of contour lines at integer multiples of Emin.*

3.2.5. Orthogonal filter modes

If the N reference channels contained mutually orthogonal noise measures, the main axes of the MSE surface would run parallel to the N weight axes. That is, increasing any weight w_i would result in a maximal increase in the MSE value along this axis. In practice this is not the case (figure 3.6), generally all environmental noise sources are picked up to some extent by all reference channels. That is, there is cross-coupling of information between reference channels which results in cross-coupling between weights. This cross-coupling considerably complicates analysis, and it is desirable to

break down the information into N orthogonal components or system modes. The orthogonalization is achieved by a translation and rotation of the main weight axes so that they sit centred on the optimal solution, and aligned with the main elliptical axes..

The translation

Using the parameter **v** which is deviation from optimal solution.

$$\mathbf{v} = \mathbf{w} - \mathbf{w}^*,$$

combining with (6) and (10) gives

$$\mathrm{MSE}(\mathbf{v}) = \mathrm{Emin} + \mathbf{v}^T.\mathbf{R}.\mathbf{v} \qquad (11)$$

The error surface now lies centred above the origin in **v** coordinate space. That is, the minimum MSE is obtained for **v** the null vector.

The rotation

The correlation matrix **R** is real and symmetric, it can therefore be expressed as its similarity transform

$$\mathbf{R} = \mathbf{M}.\Lambda.\mathbf{M}^{-1} \qquad (12)$$

Where the columns of **M** consists of the eigenvectors of **R**, and Λ is the diagonal matrix of eigenvalues.

Combining (11) and (12) gives

$$MSE(\mathbf{v}) = E\min + \mathbf{v}^T.\mathbf{M}.\Lambda.\mathbf{M}^{-1}.\mathbf{v}$$

now letting

$$\mathbf{v}' = \mathbf{M}^{-1}.\mathbf{v} \qquad (13)$$

gives

$$MSE(\mathbf{v}') = E\min + \mathbf{v}'^T.\Lambda.\mathbf{v}' \qquad (14)$$

or

$$Excess\_MSE(\mathbf{v}') = \mathbf{v}'^T.\Lambda.\mathbf{v}' \qquad (15)$$

The error surface plotted in **v'** space remains centred on the origin. In (14), the diagonal matrix of eigenvalues Λ means that any changes in an individual weight results in an increase in MSE independent of other weights. That is, the **v'** axes are aligned with the axes of the MSE ellipse (figure 3.7). The total excess MSE can now be described as a linear summation of the MSE due to each independent mode.

Expanding (15)..

$$\mathrm{Excess}\_MSE(\mathbf{v}') = \mathbf{v}'^T.\Lambda.\mathbf{v}' = \sum_{i=0}^{i=N-1} \lambda_i.(v_i')^2 \qquad (16)$$

Example

Consider the two reference case

$$\mathbf{v}' = \begin{pmatrix} v_0' \\ v_1' \end{pmatrix} \text{ and } \Lambda = \begin{pmatrix} \lambda_0 & 0 \\ 0 & \lambda_1 \end{pmatrix}$$

$$Excess\_MSE(\mathbf{v}') = (v_0')^2.\lambda_0 + (v_1')^2.\lambda_1 \qquad (17)$$

Looking at the intersection of the plane of constant excess MSE, E_{plane}, with the error surface

$$E_{plane} = \begin{pmatrix} v_0' & v_1' \end{pmatrix} \begin{pmatrix} \lambda_0 & 0 \\ 0 & \lambda_1 \end{pmatrix} \begin{pmatrix} v_0' \\ v_1' \end{pmatrix}$$

or

$$\frac{(v_0')^2}{a^2} + \frac{(v_1')^2}{b^2} = 1$$

that is, the intersection of the plane and the error surface form an ellipse with principle axes along the **v'** axes (figure 3.7). Note that at any excess error value, the shape of the ellipse (18) is governed exclusively by the system eigenvalues.

$$a^2 = \left(\frac{E_{plane}}{\lambda_0} \right) \text{ and } b^2 = \left(\frac{E_{plane}}{\lambda_1} \right) \qquad (18)$$

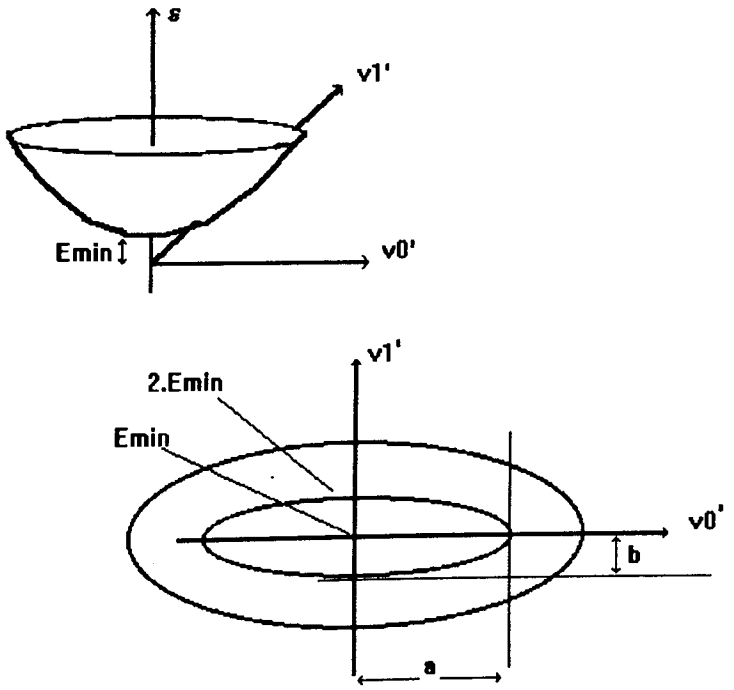

Figure 3.7. Error surface plotted on decoupled weight axes v'. Note the principal axes of the error contours are now aligned with the weight axes, the form of the ellipse (i.e. the values of a and b) is governed purely by the system eigenvalues Λ.

3.2.6. Adaptive algorithms

The MSE surface comprehensively defines the adaptive filtering problem: For stationary data, the algorithm must locate the optimal solution vector at the base of the MSE bowl. For non-stationary data, the algorithm must locate and actively track the time variant solution. Performance of the algorithm will be judged by its speed of adaptation, the average excess error introduced, and the computational cost of its implementation. Two basic algorithms are examined in this chapter, the Wiener and the Least Mean Squares filter or LMS. The Wiener solution is highly computationally intensive yet, for stationary data, its performance is largely data independent. Conversely, the LMS requires minimal computational resources, yet has convergence properties which are highly data dependent.

Firstly, the Wiener solution as a block processing algorithm is introduced. Based on the MSE surface, the ideal gradient descent Minimum Mean Square Error (MMSE) filter is outlined, and the stochastic approximation which gives rise to the LMS algorithm shown. At the end of this section the class of Root Least Square (RLS) or fast Kalman algorithms, which bridge the gap between data dependency and computational efficiency, are discussed.

Wiener solution

The Wiener solution, discussed in section 3.2.3, can be implemented as a block processing algorithm. The cross-correlation statistics **R** and **P** (6) of a block of K data samples assumed to be statistically stationary are evaluated. The optimal solution vector is calculated by a matrix inversion (8). The result is an algorithm which makes a single step to the optimal solution vector after a delay of K data samples (figure 3.8). The algorithm has an effective time constant of K samples. The block must be long enough to provide a good estimate of data statistics, yet short enough to ensure stationarity of data within the block. The delay in filter output (K samples) and high computational cost make the Wiener solution unattractive for practical real-time applications.

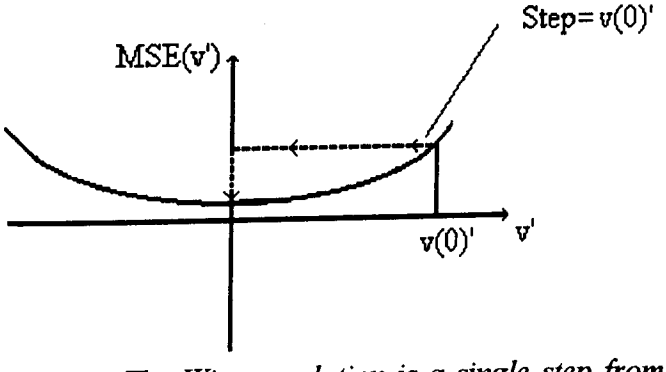

Figure 3.8.The Wiener solution is a single step from initial conditions to the MSE surface minimum.

Ideal Gradient descent

The goal of any adaptive algorithm is to reach the bottom of some error surface. In the case of the LMS and Wiener algorithms, this error surface is defined by the statistical MSE surface outlined in section 3.2. Gradient descent algorithms operate by stepping down this error surface in the direction of the steepest slope. That is, at some starting point on the surface the gradient vector is evaluated, a step is then made in the opposite direction and proportional to this gradient vector. For a small constants of proportionality, the step will result in a point on the error surface which is closer to the minimum than the previous point. The procedure is repeated until the minimum point or optimum weight vector is reached, at this point, the function gradient evaluates to zero, hence the no further steps are taken.

From (7), define

$$\nabla(n) = \frac{d[MSE(\mathbf{w}(n))]}{d\mathbf{w}(n)} = -2.\mathbf{P} + 2.\mathbf{w}(n)^T.\mathbf{R} \qquad (19)$$

alternatively, differentiating (11) gives

$$\nabla(n) = 2.\mathbf{R}.\mathbf{v}(n) \qquad (20)$$

Moving along the negative gradient by constant of proportionality or step size μ gives a time update equation at sample n.

$$\mathbf{w}(n+1) = \mathbf{w}(n) + \mu(-\nabla(n)) \qquad (21)$$

Combining (21), (20) and (13) gives the decoupled weight time update equation

$$\mathbf{v}'(n+1) = (\mathbf{I} - 2.\mu.\Lambda).\mathbf{v}'(n)$$

In the case of stationary data, algorithm convergence can be predicted from the initial conditions. At sample n, the decoupled weight vector is given by

$$\mathbf{v}(n)' = (\mathbf{I} - 2.\mu.\Lambda)^n.\mathbf{v}(0)' \qquad (22)$$

Consider a single weight v_i, and corresponding eigenvalue λ_i.

$$v_i(n)' = (1 - 2.\mu.\lambda_i)^n v_i(0)' \qquad (23)$$

For convergence

$$-1 < (1 - 2.\mu.\lambda_i) < 1$$

Since the value of μ is identical for all modes, its limiting value is set by the maximum eigenvalue :

$$\frac{1}{\lambda_{max}} > \mu > 0 \qquad (24)$$

Graphically, the condition for convergence can be visualised as in (figure 3.9). The speed of convergence of any particular mode of the algorithm is governed by the geometric progression outlined in (22). For small μ, the progression towards $\mathbf{v}'=(\mathbf{0})$ can be approximated as an exponential decay (Widrow 1976).

$$v(n)_i' = e^{-\frac{n}{\tau_i}} v(0)_i' \qquad (25)$$

where the τ_i the time constant of the i th mode given by

$$\tau_i = \frac{1}{2.\mu.\lambda_i} \qquad (26)$$

That is, larger μ (within the bounds of stability) gives a smaller time constant and hence faster convergence. It is clear that the larger eigenvalues, or the steeper sides of the MSE surface, govern the maximum value of μ. Since there is a single value of μ for all modes of convergence, any error power distributed in the shallower sides of the bowl will take longer to cancel due to this fact. The speed of convergence of the algorithm can therefore be compromised by large eigenvalue spreads.

Since the MSE is proportional to the square of the decoupled weights (16), MSE due to mode i decreases twice as quickly as the weight v_i.

$$\tau_{i,mse} = \frac{1}{4.\mu.\lambda_i} \qquad (27)$$

The time constant of the fastest mode is therefore

$$\tau_{\min,mse} = \frac{1}{4.\mu.\lambda_{\max}} \qquad (28)$$

The output of the adaptive algorithm as it converges is therefore a combination of the decaying exponentials which govern each system mode. This summated independent activity can be approximated by taking the average system eigenvalue (Widrow et al. 1975).

$$\lambda_{av} = \frac{\lambda_0 + \lambda_1 + \lambda_2 + .. + \lambda_{n-1}}{n} \quad \text{for n reference inputs} \qquad (29)$$

which, for nominally orthogonal reference inputs (**R** has dominant diagonal components), gives an approximate filter time constant of

$$\tau_{av,mse} \cong \frac{n}{4.\mu.tr(\mathbf{R})} \qquad (30)$$

Where system eigenvalues are not of comparable magnitude,

$eigenvalue\_spread = \frac{\lambda_{\max}}{\lambda_{\min}}$ is often quoted.

The MMSE algorithm is rarely used in practice since its weight update requires calculation of the exact function gradient. Such information, involving calculation of both **R** an **P** matrices, effectively provides the Wiener solution and hence the process of descent becomes redundant. The algorithm however provides the underlying concepts of more efficient gradient descent processes, such as the stochastic gradient or LMS algorithm.

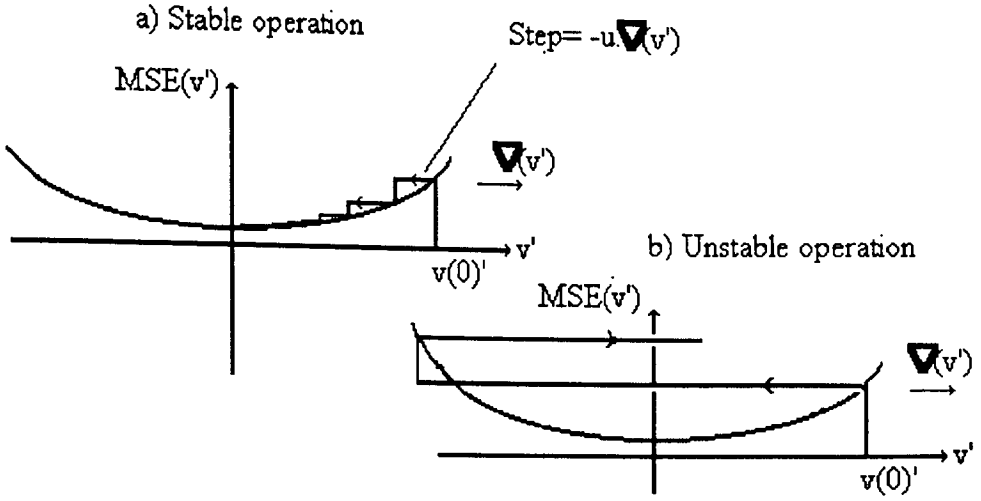

Figure 3.9. a) Adaptation of a single decoupled weight to the solution by gradient descent. The step size is set by multiplying the negative of the function gradient ∇by constant μ. As the surface minimum is approached, the function gradient , and hence also the algorithm step, tends to zero. b) If μ is too large however, the algorithm over-steps and becomes unstable.

LMS (Least Mean Square) Algorithm

The LMS is a direct extension of the MMSE algorithm. The MMSE algorithm relies upon a-priori knowledge of the data statistics, its behaviour is deterministic. The LMS algorithm relies on individual signal samples to provide approximations of the MSE surface gradient. The performance of the LMS algorithm is therefore stochastic yet surprisingly close to the MMSE algorithm.

The MSE gradient, from (4), is given by

$$\nabla(n) = \frac{d[MSE(\mathbf{w}(n))]}{d\mathbf{w}(n)} = \begin{pmatrix} dE[y^2(n)]/dw_0 \\ dE[y^2(n)]/dw_1 \\ \\ dE[y^2(n)]/dw_{N-1} \end{pmatrix}$$

The true function gradient can be approximated by removing the expectation operator to give an instantaneous of 'noisy' gradient estimate

$$\tilde{\nabla}(n) = \begin{pmatrix} 2.y(n).x_0(n) \\ 2.y(n).x_1(n) \\ \\ 2.y(n).x_{N-1}(n) \end{pmatrix}$$

Using this gradient estimate in (21), the complete gradient descent algorithm reduces to

$$\mathbf{w}(n+1) = \mathbf{w}(n) + 2.\mu.y(n).\mathbf{x}(n)$$

Note that a step along a multidimensional function derivative is being made yet the algorithm makes no use of squaring, averaging or differentiaton. The 'noisy' gradient

estimate has been shown to be unbiased (Widrow et al. 1967), and figure 3.10 shows how the LMS weights track MMSE weights for moderate time constants. In the steady state, however, the algorithm performances differ. In the MMSE algorithm, convergence to the optimal solution is obtained when the function gradient evaluates to zero and hence the step size becomes zero. The stochastic descent algorithm however relies on the instantaneous product of the error and reference signals, which although statistically may be orthogonal, instantaneously, will have a finite product. At, and around the optimal solution, there is therefore some *jitter* noise introduced by the algorithm (figure 3.11). This jitter or steady-state noise is further discussed in section 3.2.8.

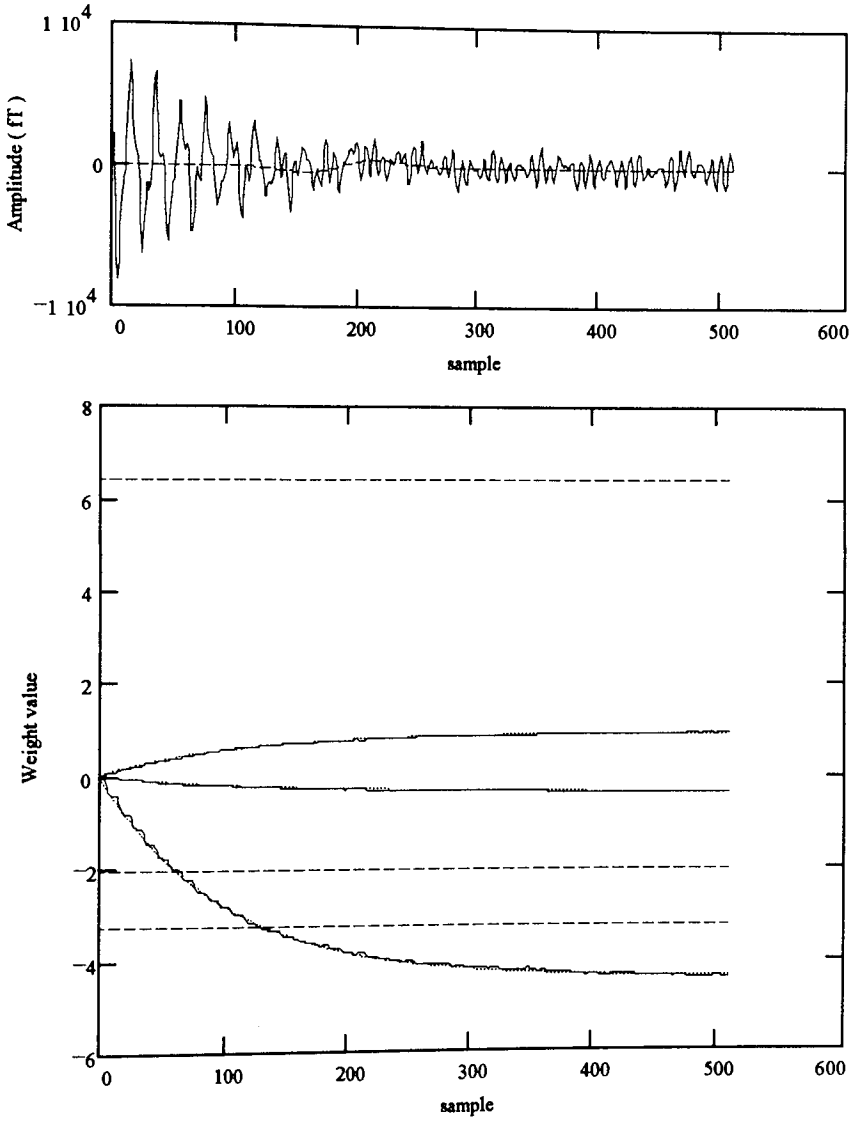

Figure 3.10. First epoch of simulated evoked response $T_{mse,min}$= 50 samples. Above, LMS filter output (solid) is overlaid by MMSE filter output (dotted). The underlying signal is shown by the dashed curve. The decrease in output power is clear as the algorithm weights (lower plot, LMS solid, MMSE dotted) adjust, albeit slowly, towards the Wiener weights (dashed).

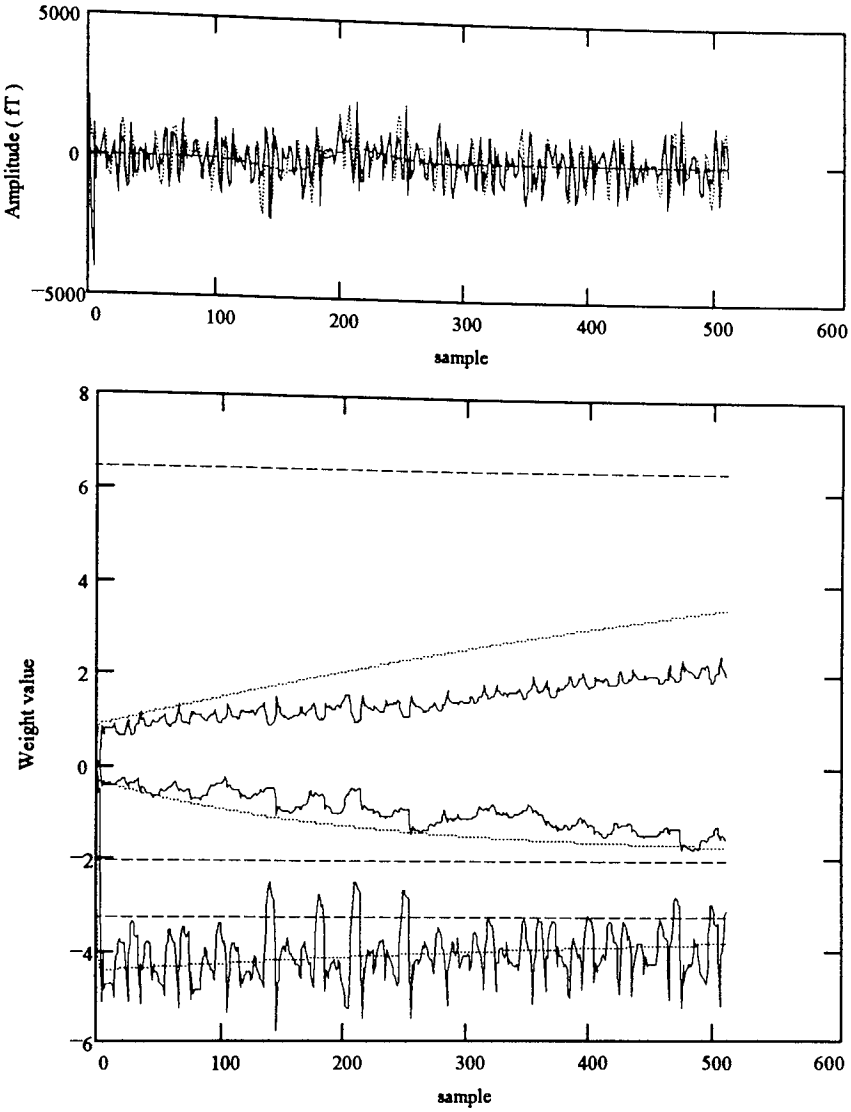

Figure 3.11. First epoch of simulated evoked response $T_{mse,min}$= 0.75 samples. Above, LMS filter output (solid) and MMSE filter output (dotted). The underlying signal is shown by the dashed curve. The stochastic progression of the LMS weights (solid) is now clear, there is some 'jitter' or steady state noise about the ideal MMSE curves (dotted).

RLS (Recursive Least Squares)

The RLS is introduced since the family of algorithms it represents have computational and convergence properties which fall between the extremes represented by Wiener and LMS filters. Whereas the LMS and MMSE algorithms minimise the statistical expectation value of square error, the RLS algorithm is designed to minimise the square error in an absolute sense. That is, data values rather than data statistics govern the algorithm progress. In the case of RLS, the error of the current sample, added to the weighted sum of L previous samples, is minimised:

$$\varepsilon(n) = \sum_{i=0}^{L-1} \lambda^i . y^2(n-i)$$

The quantity λ is termed the 'forgetting factor', a value of unity makes past and present samples equally valid; minimisation of ε will result in the Wiener solution for that block of data. Lower values of λ (<1.0) give past samples less importance in the calculation of filter weights, that is, the filter 'forgets' , such behaviour is useful when the underlying data is non-stationary. The RLS algorithm uses a vector, sometimes referred to as the Kalman gain vector, rather than scalar (μ for the LMS) weight update step. The gain vector is recomputed after each iteration and allows a separate convergence step for each filter mode.

The effective time constant of the RLS algorithm is given by

$$T_{eff} = \frac{2}{1-\lambda}$$

The many RLS algorithms (see Alexander 1986) vary mainly in computational efficiency (7N to $7N^2$ operations per iteration) and susceptibility to round-off error (Ling and Proakis 1984). However the use of real data rather than statistical estimates, and the optimised vector step, mean RLS algorithms consistently improve upon the convergence properties of the LMS algorithms (See figure 3.12).

3.2.7. Descent properties of adaptive algorithms

All adaptive algorithms have a certain rate of convergence, expressed in algorithm iterations, to solution (figure 3.13). This convergence is obtained at the expense of some computation per iteration. Generally, the faster the convergence the more computation per iteration is required. For example, the convergence performance of the RLS algorithm is consistently better than that of the LMS, at the expense of at best four times the arithmetic operations. Likewise, the Wiener solution is instantly attained for a block of data, yet at a greater computational cost again than the RLS (Figure 3.12). The choice of algorithm is generally set by the hardware available and based on the trade-off between computation and algorithm convergence time.

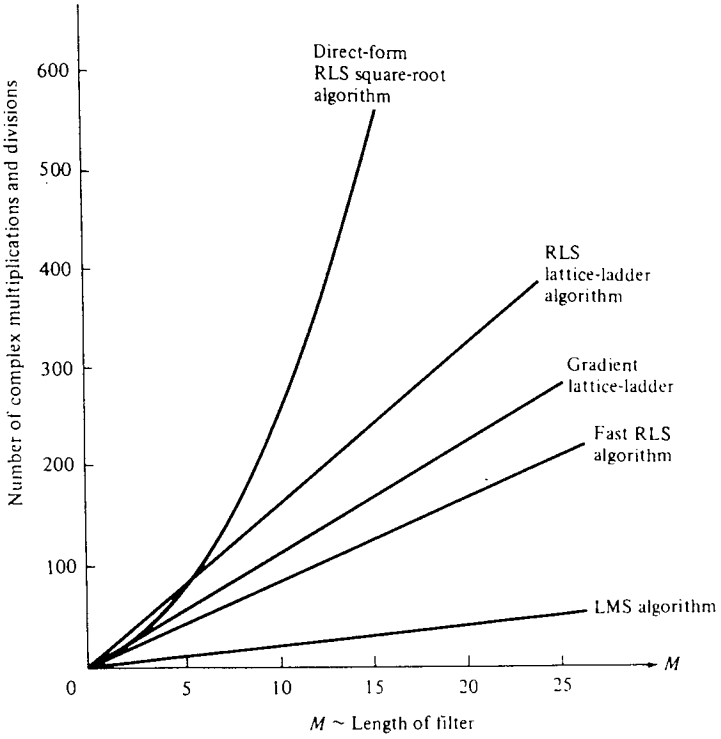

Figure 3.12. Computational complexity of various RLS implementations, as compared to the LMS. From Proakis and Manolakis (1988).

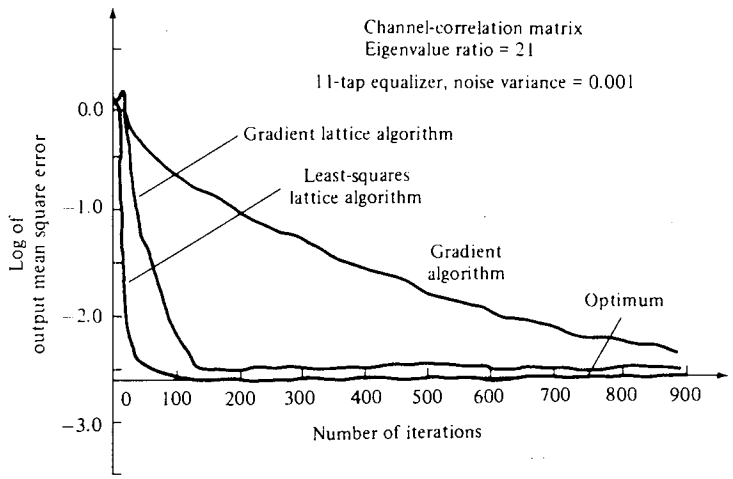

Figure 3.13. Typical convergence comparison for RLS and LMS, N=11, eigenvalue spread=11. LMS step constant=0.02. From Proakis (1983).

3.2.8. Steady state properties of adaptive algorithms

The process of determining a solution from a finite length data sample inevitably results in some noise in the steady state. Consider for example, calculating the Wiener solution for a single reference noise canceller using K data samples. Let the signal d(n) and reference channel x(n) be uncorrelated. From (8), for K=1, it is clear that the Wiener estimate

$$w^*(n) = \frac{\sum_{i=n}^{i=n+K-1} x(i).d(i)}{\sum_{i=n}^{i=n+K-1} x(i).x(i)} = \frac{d(n)}{x(n)}$$

will lead to a complete annihilation of d(n) in the filter output y(n) regardless of its true correlation properties with x(n).

$$y(n) = d(n) - w^*(n).x(n) = 0$$

That is, for d(n) and x(n) uncorrelated, the signal output power will be in error or misadjusted by 100%. As better estimates of the underlying data statistics are made, that is, as more samples are included within the estimate, the misadjustment will steadily decrease. Such noise is present in all adaptive algorithms and was shown by Widrow et al. (1976) to be given by

$$M = \frac{\text{Number of weights}}{\text{Number of training samples}} \qquad (31).$$

where M is the "Misadjustment" or proportion of excess power to minimum signal power.

As an example, both Wiener and LMS algorithms are applied to the reference noise canceller problem for a Gaussian-white signal and two reference channels (figure 3.14). The LMS weights are initialised at the Wiener solution. The time constant of the LMS filter and the block size of the Wiener filter are varied, the predicted misadjustment vs. the actual misadjustment is shown in figure 3.14. It is clear that both the Wiener and LMS algorithm suffer the same effects of steady state noise.

In the case of the LMS filter, steady state misadjustment noise is clear, and manifests as 'jitter' caused by the finite solution step (see figure 3.11). The appendix details the estimation of jitter noise for the LMS algorithm, which is approximated by (32).

$$\text{Jitter noise} = \mu.E_{min}.\text{tr}(\mathbf{R}) \qquad (32)$$

and when expressed as misadjustment gives

$$M_{jitter} = \frac{\text{Jitter\_noise}}{E_{min}} = \mu.tr(\mathbf{R})$$

when the eigenvalues of **R** are of similar magnitude, then from (27)

$$M_{jitter} = \frac{N}{4.\tau_{av,mse}} \qquad (33)$$

That is, if convergence time of LMS filter is taken to be four filter time constants, the results in (31) and (33) accord.

The emphasis of this section has been that small algorithm time constants give faster convergence rates to solution and better tracking of non-stationary data yet ,as a trade off, increase steady state misadjustment error. Concisely, for any filter :

$$M_{total} = M_{lag} + M_{jitter} \qquad (34)$$

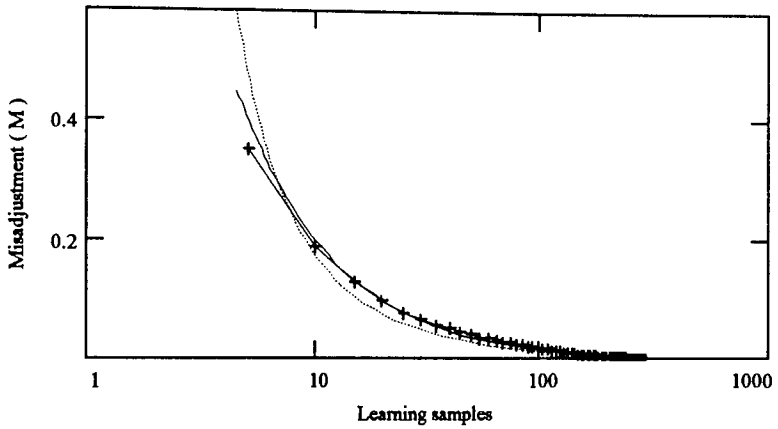

Figure 3.14. Curve showing predicted misadjustment (solid curve) alongside achieved steady state misadjustment for Wiener (crossed) and LMS (dotted) algorithms. Data is for a two reference noise canceller with white signal and references. For the prediction of M, the LMS algorithm was taken to have a learning period of four time constants, and initial weights set to the Wiener solution.

3.3. Proposed Algorithm

It is required to provide a real-time running average or epoch by epoch display of visual evoked responses. Real-time display is preferable since it gives the user a clear idea of the quality of data collected, and enables the monitoring of spontaneous neuronal activity. In certain clinical cases, for example, large bursts of abnormal spontaneous activity can precurse epileptic attacks. At Aston, evoked responses of peak amplitude 100-1000fT are recorded against a background of 20pT mains interference and system white noise of 300-400 fT RMS (see chapter 1). Typically data is recorded over a period of 500ms at a sample rate of 1kHz, with a one second inter-stimulus interval.

The neuromagnetometer at Aston contains a vector magnetometer probe situated approximately 15cm from the dewar base. The vector magnetometer consists of a 1cm cube on which three SQUIDs (X,Y,Z) are mounted orthogonally. These SQUIDs are not coupled to pick up coils, and each has an effective intrinsic white noise level of around 880 fT /√ Hz. The low sensitivity and remote location of these sensors means

that they provide no measure of neuromagnetic field and are good candidates for noise cancellation reference channels (figure 3.2). The signal processing is based around a 486 IBM PC with 16bit ADC interface to the neuromagnetic system output.

The LMS or stochastic descent algorithm requires 2N arithmetic operations per iteration. For a PC based realisation, the algorithm is attractive because of its minimal computational requirements. Figure 3.15 shows the basic computational steps in the acquisition procedure. The order and utility of these steps are discussed in the following sections:

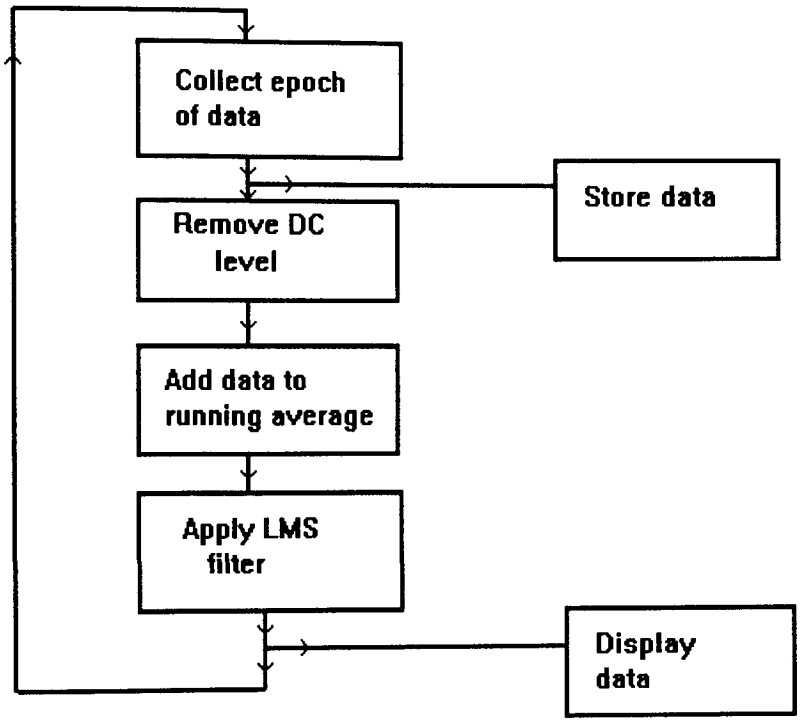

Figure 3.15. The neuromagnetic data acquisition algorithm used at Aston. Note that all raw data is stored, and that the LMS filter is applied after averaging. In practice, the display routine runs parallel and secondary to the main acquisition loop.

3.3.1. DC level removal

The DC level on neuromagnetic data contributes no useful information (chapter 1) it also impairs the performance of any reference noise canceller. Consider a signal channel d(n) consisting of neural signal s(n) some proportion h of cancellable environmental noise c(n) and DC offset D_1.

$$d(n) = s(n) + h.c(n) + D_1$$

Likewise, a reference channel with some intrinsic noise u(n), a measure of environmental noise c(n) and DC bias D_2.

$$x(n) = u(n) + c(n) + D_2$$

For stationary data, all adaptive algorithms will converge to the Wiener solution. For the single reference canceller and a block of K samples, this is given from (8)

$$w^* = \frac{\sum_{n=0}^{n=K-1} x(n).d(n)}{\sum_{n=0}^{n=K-1} x(n).x(n)}$$

It is clear that the Wiener solution will be dominated by those terms in x(n) and d(n) which result in the largest cross-correlation measure. Unfortunately, the DC bias on neuromagnetic data is often of the order of, if not greater than, the maximum noise components recorded. That is, the calculation of the adaptive weights will be dominated by the DC signal components.

$$D_1 >> s(n) + h.c(n)$$

$$D_2 >> c(n) + u(n)$$

$$w^* = \frac{D_1}{D_2}$$

In effect, the algorithm acts as a straightforward DC level remover.

A solution is the introduction of a bias reference (Widrow 1975). That is, a "dummy" reference channel is used which contains a fixed amplitude value. The filter will tend to use this dummy mode for removal of the DC components. The trade-off in the case of the Wiener solution is excess misadjustment due to the increased filter order (31). In the case of the LMS solution however, the DC bias leads to high correlations between reference channels, giving large eigenvalue spread hence slow convergence. If the bias channel is chosen to be too small, it will have no effect; too large, and it will form the largest system eigenvalue and hence impose an artificial limit on the maximum value for μ. Since the DC bias level on each reference and signal channel is largely arbitrary, there is no amplitude of the bias reference which precludes either of the latter. In practice, therefore, the DC level is removed from all channels prior to filtering.

3.3.2. Filter then average or Average then filter

The next question of implementation is at which stage of the averaging process to apply the LMS filter. Each DC corrected epoch of data can be filtered then added to the running average, or, the DC corrected running average can be calculated and the filter applied to this data.

Filter then average

Besides the neural signal, the raw epoch of data contains a full complement of system white noise, plus raw environmental noise. The LMS step-size must be large in order to adapt to sudden non-stationarities, a large step size implies large jitter or steady state noise. However, any steady state noise is uncorrelated with the stimulus onset and is therefore attenuated by averaging.

Average then Filter.

During averaging, all activity uncorrelated with stimulus onset is attenuated (figure 3.16). The statistics of the running average change more slowly and smoothly than those of individual epochs (see figure 3.35). For this reason, the step size can be chosen to be relatively small, giving less jitter noise than in the above case. Jitter noise on the running average is, however, the absolute jitter noise and is not removed by further averaging. The method has complexity in that as the averaging progresses, the reference channels are attenuated causing an increase in the effective filter time constant (27). Also, the averaging process itself changes the data statistics, if these statistics change differentially between signal and reference channels, some non-stationarity in solution will be introduced.

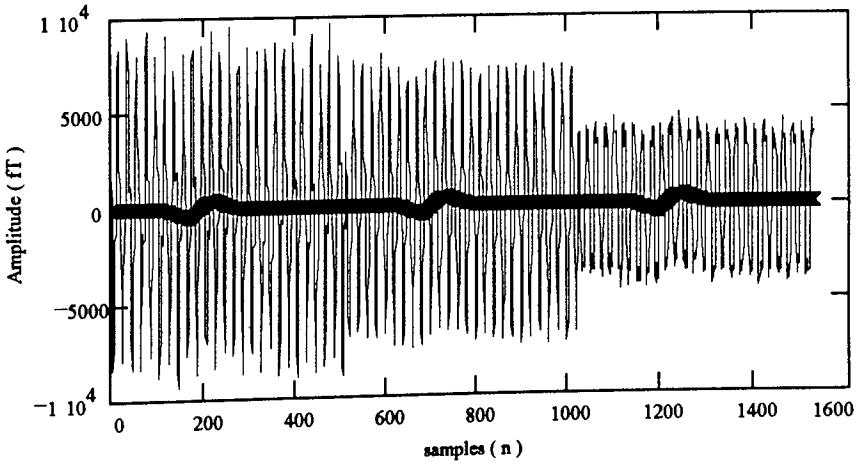

Figure 3.16. The running average as a continuous time sequence. The first three epochs are shown above, the underlying signal is shown by the thick trace.

Given more than a single cancellable noise source, any adaptive algorithm leads to a compromise solution where maximal noise is attenuated. This was the justification for DC level removal prior to filtering. Therefore if any noise source is attenuable by averaging, it makes sense to average and then apply the filter. In practice the improvement in performance is most marked when observing the low frequency noise

effects caused by the interference of the 110Hz visual stimulus CRT and 100Hz mains harmonic. The superposition of the two noise sinusoids leads to 'beating' pattern in the data with an envelope of the frequency difference. The phase of this pattern is highly dependent on the phase of the component sinusoids and is observed in slightly different phase across all signal channels, and in phase quadrature with this in the reference channels (Figure 3.17). These phase differences across channels perhaps reflect poor homogeneity of the 100Hz filters (see chapter 2). The phase shift between the signal and reference channels perhaps reflects activity of both ambient and gradient noise sources within the CRT. As a result, in each epoch, the higher frequency signal and reference channel components are poorly correlated and reference noise cancellation has little effect. However, in the average, the mains harmonic is attenuated, removing the beating effect, and exposing the signal-reference CRT noise correlations (Figure 3.18).

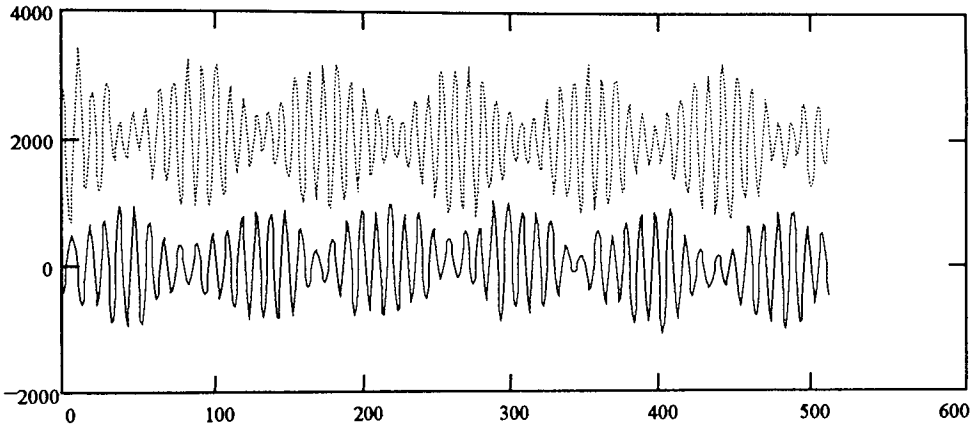

Figure 3.17. Epoch 1, band-pass filtered 60-120Hz, X reference (solid) and signal (dotted trace). Monitor interference (here at 110Hz) and mains harmonic of 100Hz result in a low frequency noise source in the form of a periodic 'beating' pattern, the phase of this envelope is highly dependent on the phases of the two component sinusoids. Slight differences in the phases of reference and signal channels result in envelopes which are uncorrelated.

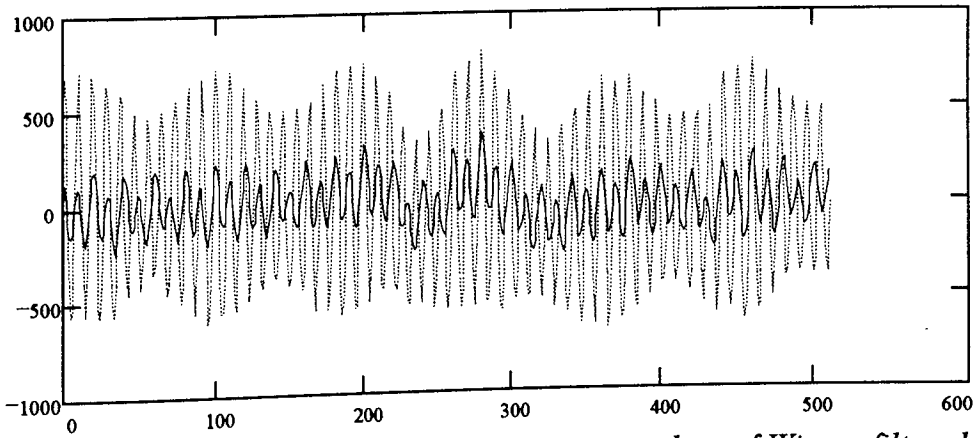

Figure 3.18. Visual evoked response data for averaged set of Wiener filtered epochs (dotted) as compared to the Wiener filtered average (solid).

3.4. Algorithm performance

Section 3.2 mathematically characterised the operation of the LMS filter algorithm. The derivations of filter performance were made using the assumption that signal and reference channels contained stationary random data sequences. In practice, neuromagnetic data is highly self correlated and not necessarily statistically stationary. It is necessary to verify that the performance predicted analytically describes the true algorithm performance.

In this section, epoch-length stationarity of data is assumed. A known signal is input to the system in typical recording conditions and 'noise' is defined as the difference between filter output, and this known signal. Since the statistics of the running average change with each epoch introduced; an LMS filter is defined where effective time constant is maintained despite such changes.

3.4.1. The benchmark signal

It is necessary to remove environmental and system noise from gradiometer output whilst not distorting the underlying neural signal. The problem is that the neural signal that one wishes to measure is, of course, unknown. In order to assess the quality of algorithm performance however, signal and noise must be clearly defined. A known pseudo-neural signal is therefore manufactured, and the performance of the algorithm gauged by comparing this known signal and the filter output. In order to simulate evoked response measures, a small magnetic dipole was placed beneath the gradiometer array (Figure 3.19) in typical recording conditions. The dipole current was modulated so as to generate a difference of Gaussian function of similar amplitude and temporal characteristics to a typical evoked response (Figure 3.20). One hundred epochs of data, time locked to the dipole current modulation, were collected. The running average signal has three major components (Figure 3.21) :

i) The signal. This is known.

ii) Uncancellable noise. For the purposes of this discussion, all uncancellable noise sources, including environmental noise not measurable by the reference channels, will be classed as white noise.

iii) Cancellable environmental noise. That is, noise which is correlated between signal and reference channels. It is clear from figures (4.20) and (4.21) that the removal of such noise from the running average will considerably enhance the SNR ratio, especially during early epochs.

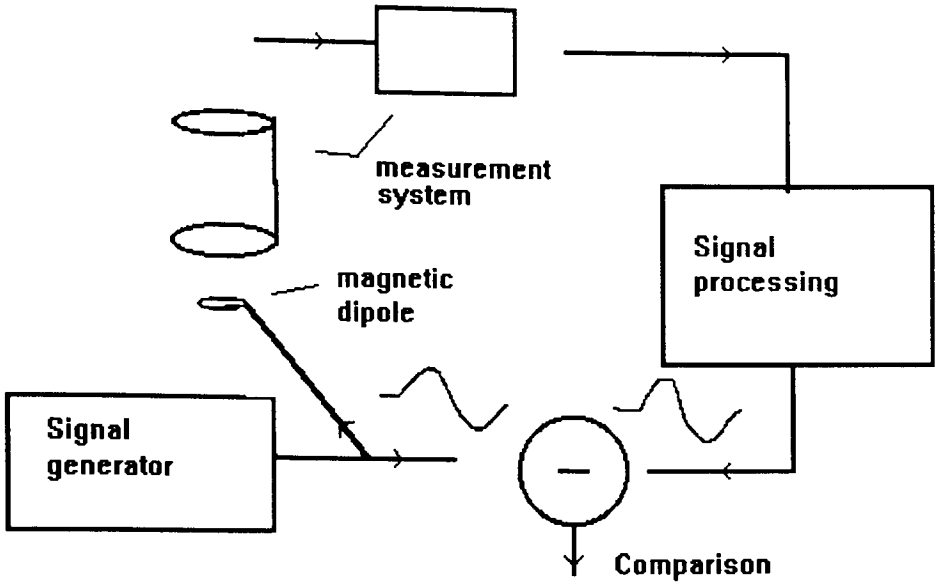

Figure 3.19. A magnetic dipole is driven with a known current close to the gradiometer array in typical noise conditions. The field modulation sensed by the gradiometer is recorded, processed and compared to the ideal. In practice, the precise amplitude scaling factors are estimated by least squares fitting of an averaged set.

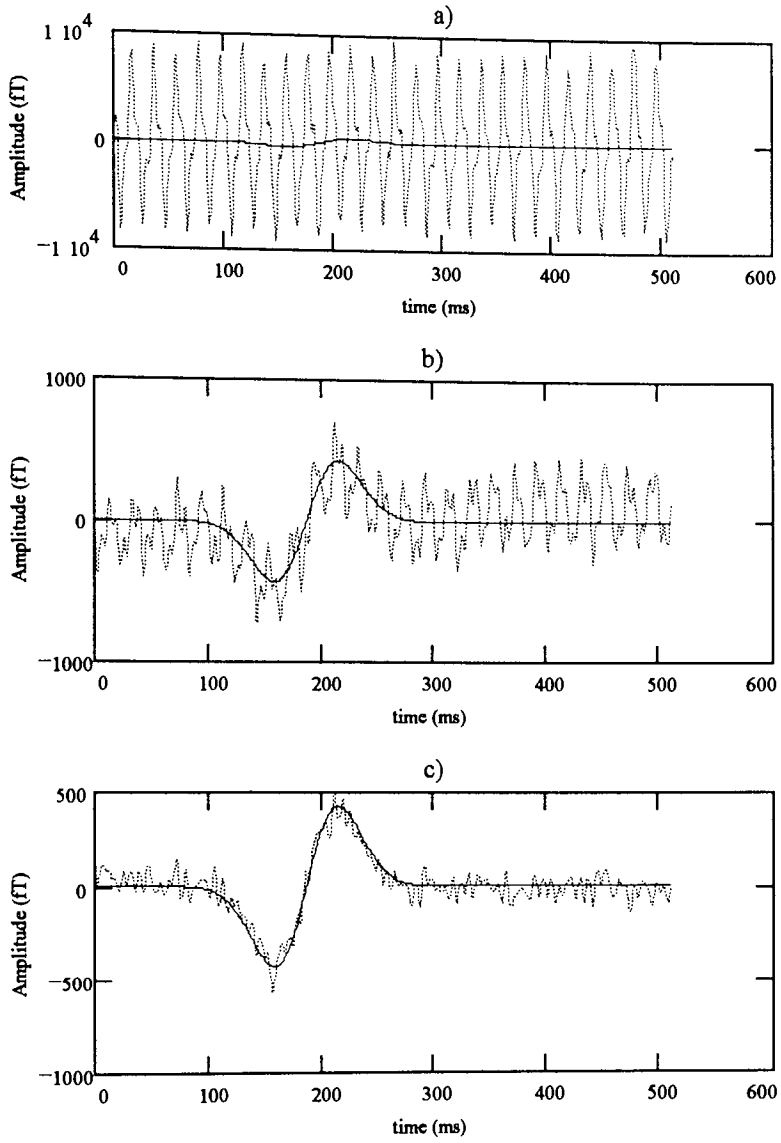

Figure 3.20. The benchmark signal (solid) trace underlies a) a raw epoch ;b) the average of 100 epochs; c) the Wiener filtered average of 100 epochs

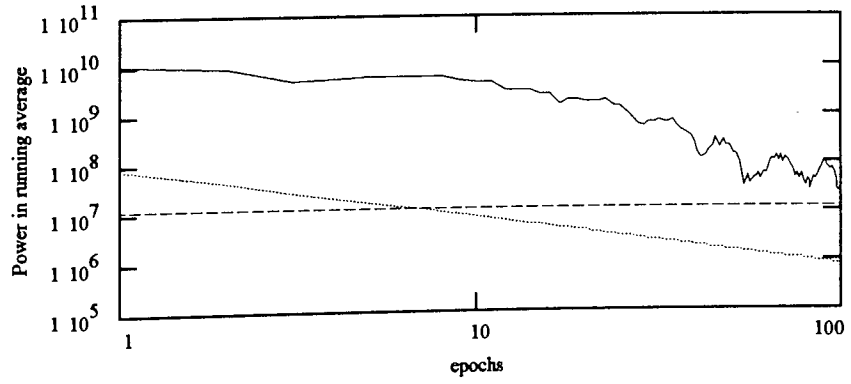

Figure 3.21. Total power in running average epoch (512 samples) (solid) trace. The dotted trace shows estimated white noise power (taking 40ft/√Hz over 100Hz bandwidth). The dashed trace indicates power in benchmark. The difference between total power and white-plus-signal power is due largely to power-line interference (figure 3.20a). This interference is well represented on the reference channel inputs and can be almost completely nulled by reference noise cancellation.

3.4.2. Normalised LMS time constant

In section 3.2, the eigenvalues of the reference inputs were shown to completely define the of the shape of the MSE surface (figure 3.7). Each eigenvalue defines the steepness of a side of the N dimensional MSE bowl (see equation 16). If the noise in the reference channels is predominantly uncorrelated with the epoch start, the process of averaging will cause an effective shallowing of the MSE surface (figure 3. 22). From (27), this change of shape of the error surface will mean that for a fixed μ the filter time constant will change. That is, the value of λ_{max} decreases, giving a larger upper bound for μ (figure 3.23) and requiring a larger value of μ to maintain the same convergence rate. For the purposes of this analysis, it is convenient to deal with a filter structure with known time constant irrespective of the point in the running average. Therefore, from (28), the values of μ used for the stochastic descent algorithm are pre-calculated to maintain a constant relationship to the progression of system maximum eigenvalue. That is, the value of μ at epoch a is adjusted so as to give the filter the required fastest time constant $T_{mse,min}$.

$$\mu_a = \frac{1}{\lambda_{max}(a).4.\tau_{mse,min}}$$

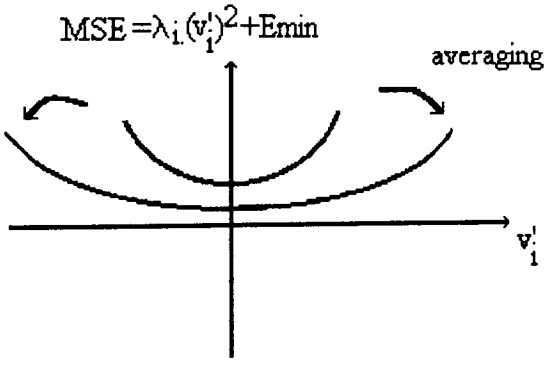

Figure 3.22. As the reference inputs and hence system eigenvalues λ_i are attenuated by averaging, the sides of the MSE bowl become shallower. The averaging process also causes an attenuation of reference uncancellable noise sources in the signal channel (such as white noise) leading to a decrease in Emin.

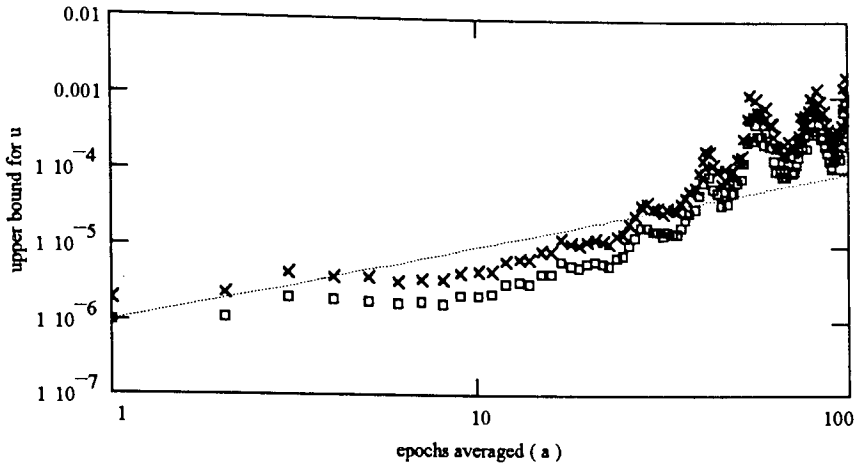

*Figure 3.23. Max value of μ (or $1/\lambda_{max}$) (crosses) as a function of epochs averaged for benchmark signal. Also shown is [trace(**R**(a))]$^{-1}$ (boxes) and dotted line of gradient a. The more epochs within the running average, the larger the upper bound for μ. The periodic performance in later epochs is due to the non-random inter-stimulus interval resulting in the sequential averaging in and out of 50Hz interference.*

3.4.3. Empirical Performance measures

The signal underlying the noise is known, therefore filter performance can be precisely assessed. The power of the deviation between the signal and filter output at running average epoch *a* is defined as

$$Error_{emp}(a) = \sum_{n=0}^{n=s-1} (F\_lms(a,n) - B(n))^2 \qquad (35)$$

where B(n) is the benchmark, F_lms(a,n) the output of the LMS filter. The removal of useful signal data by the algorithm will be reflected in this measure (Figure 3.24b).

Note that (35) does not correspond to the power in the filter output (36), traditionally the performance criterion when the underlying signal is unknown.

$$Error_{tot\_power}(a) = \sum_{n=0}^{n=s-1} (F\_lms(a,n))^2, \qquad (36)$$

This measure is independent of the underlying signal and continues to improve as the underlying signal is decimated (Figure 3.24a). It will be shown that this signal decimation is well described by the steady state error due to short filter time constant. The algorithm essentially views the signal as slowly varying data trend and attempts to remove it. Such behaviour is apparent when filter weights become highly correlated with the underlying signal (figure 3.25).

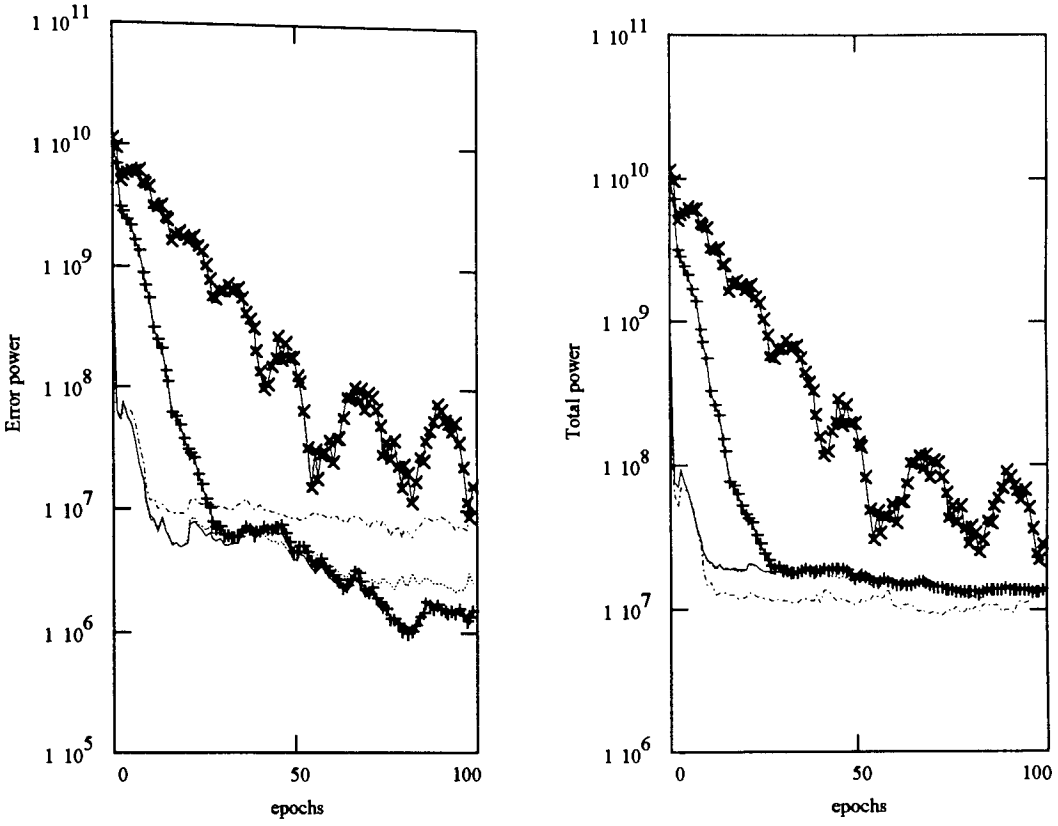

Figure 3.24. a) Total error power and b) total power in LMS filtered running average for various $T_{mse,min}$ ($T=25*10^3$ crosses, 250 pluses, 50 solid, 5 dotted, 0.83 dash-dot). For b) Notice how total power decreases with decreasing time constant, this reflects not improved filtering but increasing signal annihilation. Error to signal power is therefore a more useful measure. For a) Large time constants give slow descent, whereas small time constants give fast descent but large jitter noise in the steady state.

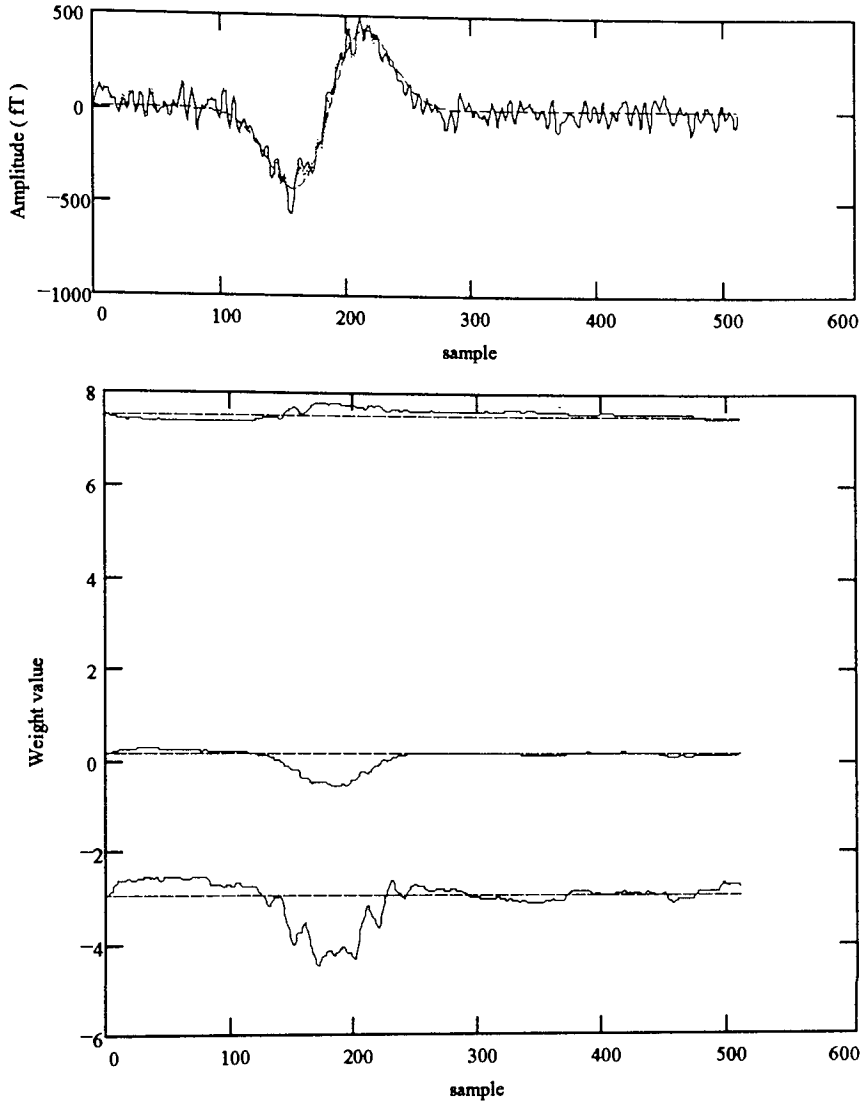

Figure 3.25. Top trace shows filter output. Ideal benchmark (dashed), LMS (solid), MMSE (dotted). The lower trace shows MMSE weights (dashed) and LMS weights (solid). The small time constant causes weight behaviour to be highly correlated with the underlying signal. This correlation introduces misadjustments which attenuate the signal, and results in a decrease in total filter output power.

3.5. LMS Filter performance

A generalised filter and a performance measure have been defined; it is now necessary to verify that LMS filter performance can be deterministically modelled. Taking the running average to be piecewise stationary between epoch boundaries, it is possible to estimate a set of statistical quantities based on each epoch. For example, for each epoch, the cross correlation matrices **R** and **P** can be evaluated and the corresponding Wiener solution calculated, the data can then be described in terms of its orthogonal modes. The effects of passing the running average through LMS filters of various time constants will be estimated and compared to the empirical performance measure derived in section 3.4. Due to the changing statistics of the running average, the characteristic eigenvalues and minimum error will be functions of the epoch number (section 3.4).

The performance of any adaptive algorithm is a trade off between its convergence rate and steady state misadjustment. From (34), the amount of excess noise due to imperfect filtering at any sample instant n, can be expressed as

$$\text{Excess\_MSE(n)} = \text{lag\_MSE(n)} + \text{Jitter\_MSE(n)}$$

from (Appendix, (48)).

$$\text{Jitter\_MSE(a)} = \mu_a . E_{min}(a) \sum_{i=0}^{n-1} \lambda(a)_i . \left(\frac{1}{1-\mu_a \lambda_i(a)}\right)$$

where the quantities λ, and E_{min} are estimates based on the statistics of the running average epoch a, and μ_a set to give the required filter time constant.

Combining (16) with (23) gives an estimate for the amount of cancellable noise at the start of each new epoch based on the eigenvalues and decoupled Wiener weights for that epoch

$$Initial\_lag\_MSE(a) = \sum_{i=0}^{i=N-1} \lambda_i(a) . v_i^2(a,0)' \qquad (37)$$

that is, if no adaptation is made throughout the epoch then this MSE will result.

Where $\mathbf{v}(a,0)'$ is the decoupled weight at the 0th sample of epoch a,

To recap (13)

$$\mathbf{v}(a,n)' = \mathbf{M}_a^T . (\mathbf{w}(n) - \mathbf{w}_a^*(n))$$

where $\mathbf{w}^*$ and $\mathbf{M}$ are calculated from epoch a.

NB. Note that the Wiener weights are based on statistical estimates from a finite data sample, the true optimal weights can only be known from perfect statistical knowledge of the data. The error introduced by making the Wiener estimate is discussed further in section 3.6.1.

Assuming stationarity within the epoch, and using the approximation of (25), an estimate of the excess error power due to lag at any instant n throughout epoch a is given by

$$Lag\_MSE(a,n) = \sum_{i=0}^{i=N-1} e^{-\frac{2.n}{\tau_i}} v_i^2(a,0)' \lambda_i \qquad (38)$$

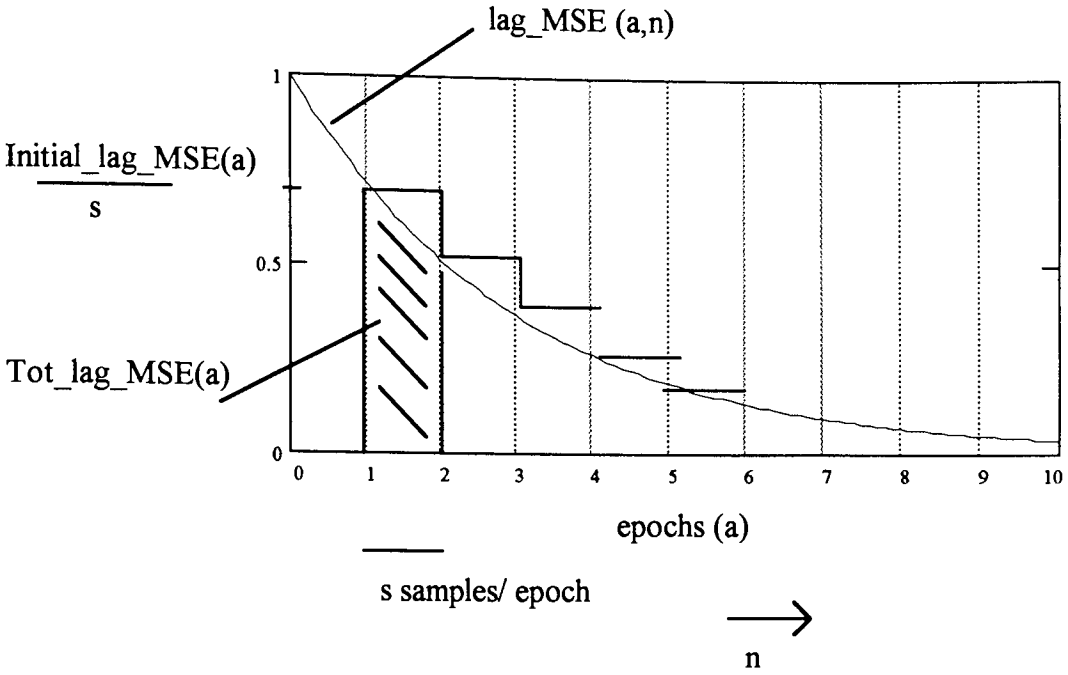

Figure 3.26. The idealised behaviour of the LMS filter for stationary data. At sample 0 ,epoch 0, there is excess power due to weight misadjustment. The filter time constant is maintained across epochs, and the excess power at the start of each epoch decreases as the filter approaches the optimal solution. The total excess power contained within an epoch is represented by the shaded area.

It is more convenient to deal with the total excess MSE per epoch represented by the shaded area in figure 3.26. Integrating (38) with respect to the sample n

$$Lag\_MSE(a) = \sum_{i=0}^{i=N-1} \int_{n=0}^{s} e^{-\frac{2.n}{\tau_i}} v_i^2(a,0)'\lambda_i \delta\ n$$

gives total MSE per epoch for specific initial conditions and filter weight time constant.

$$Tot\_lag\_MSE(a) = \sum_{i=0}^{i=N-1} \left(1 - e^{-\frac{2.n}{\tau_i}}\right) . \frac{\tau_i}{2} . v_i^2(a,0)'\lambda_i \qquad (39)$$

So, the total predicted error power due to the filter over any epoch a of the running average is given by

$$Error_{filt}(a) = Tot\_lag\_MSE(a) + MSE\_jitter(a) \quad (40)$$

Given stationarity, the best estimate of the amount of uncancellable noise in an epoch is given by the deviation of the benchmark from the Wiener solution. Since, in this application, such noise is predominantly white, define

$$White_{wnr}(a) = \sum_{n=0}^{s-1} (B(n) - F\_wnr^*(n))^2$$

Where F_wnr*(n) is the output of the ideal Wiener filter, and B(n), the benchmark.

The total deviation-from-signal power will be due to the filter error plus any uncancellable noise within the epoch.

$$Tot\_err(a) = Error_{filt}(a) + White_{wnr}(a) \qquad (41)$$

Figure 3.27 shows the estimate (41) alongside the empirical measure of (35). It is clear that the analytical estimates based on whole epoch statistics predict the behaviour of the stochastic algorithm.

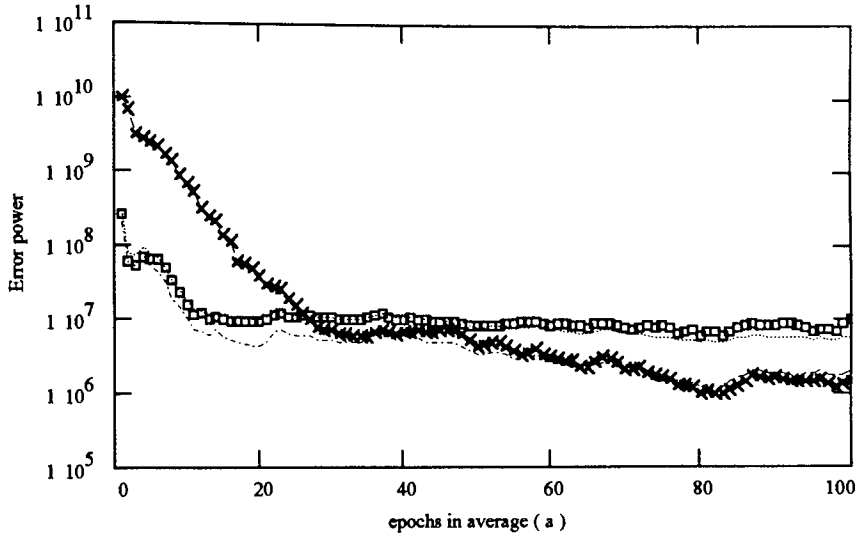

Figure 3.27. Comparison of empirically observed and predicted LMS algorithm performance. For $T_{mse,min}$= 2500 : empirical crosses , analytical plus Wiener white noise estimate dashed trace lies underneath, almost obscured. For $T_{mse,min}$= 0.83 : empirical boxes , analytical dotted. Wiener white noise estimate ($White_{wnr}(a)$) is shown as the dot-dash trace.

Alternatively, it is instructive to compare predicted filter misadjustment (Figure 3.27), where

$$M_{est}(a) = \frac{Error_{filt}(a)}{E\min(a)} \qquad (42)$$

with a measure for the empirical misadjustment

$$M_{emp}(a) = \frac{Error_{emp}(a) - White_{wnr}(a)}{E\min(a)}$$

A comparison of M_{est} and M_{emp}, as averaging progresses, is shown in Figure 3.28 for two normalised filter time constants. By considering average misadjustment per epoch, it is clear (figure 3.29) that the analytical form well describes filter performance over a wide range of filter time constants. That is, even signal decimation, which leads to lower filter output power (figure 3.24a), is correctly categorised by the analytical form as noise.

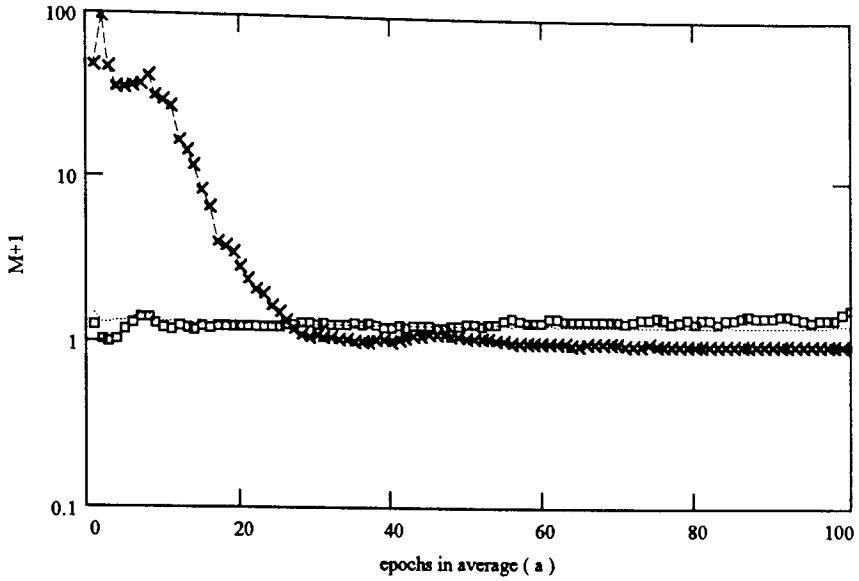

Figure 3.28. Comparison of M_{est} +1 and M_{emp}+1. For $T_{mse,min}$= 2500 : M_{emp} crosses , M_{est} dashed trace. For $T_{mse,min}$= 0.83 : M_{emp} boxes , M_{est} dotted. Unity is added to both traces since M_{est} becomes negative complicating logarithmic the plotting procedure.

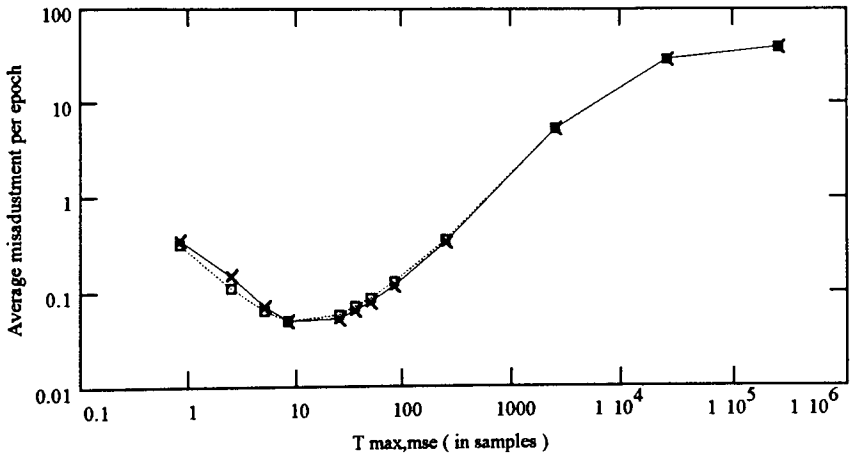

Figure 3.29. Empirically observed (crosses) and estimated (boxes) average misadjustment (M) per epoch. For large T, the filter converges too slowly to the solution, whereas for small T, jitter noise is dominant. For all time constants, the stochastic algorithm performance is well described by the deterministic equations based on whole epoch statistics.

3.6. Steady state filter performance

In the previous sections, data stationarity has been assumed. That is, all filter lag has been assumed to be due to progression from some initial conditions to an optimal solution. In practice, data sequences are non-stationary, and this optimal solution is time variant (figure 3.30). The adaptive filter is required to track this drifting solution, and failure do so results in non-stationary noise. Filter performance in non-stationary noise is important since generally, having positioned the dewar and the subject, the algorithm is allowed to converge close to the optimal solution before recording any data. During the

running average therefore, the algorithm must only track non stationary noise in the data. The goal of this section is to quantify this non-stationary noise. Firstly, it must be confirmed that the previous assumption of piecewise (in this case, epoch length) stationarity of data is valid. Non-stationary noise is then defined as a step input to the filter arising between epoch boundaries. Finally, given average measures of non-stationarity, an optimal progression for filter time constant is proposed.

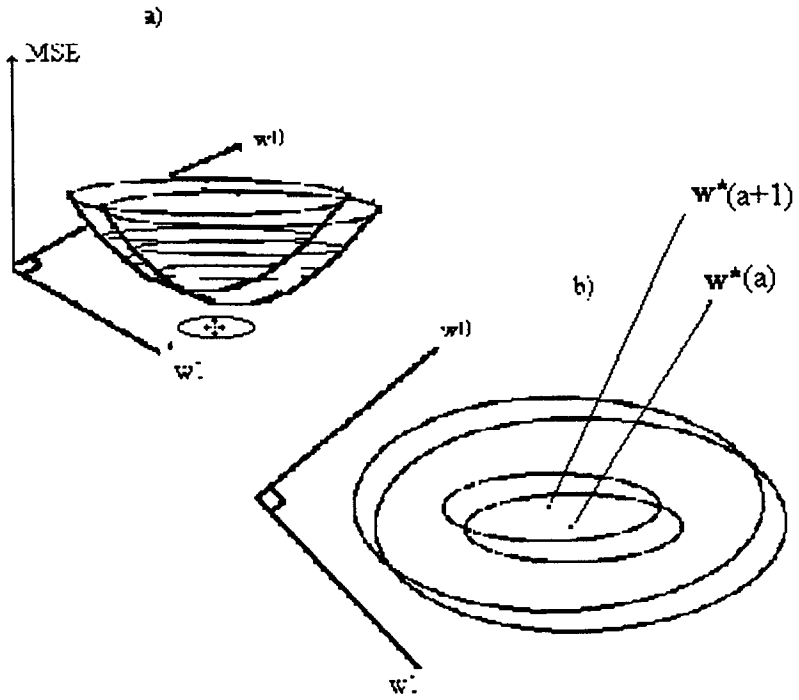

Figure 3.30. In practice, the base of the error surface moves around as the data statistics change. Any adaptive filter must not only be able to track to the bottom of the surface, but also follow the movement of the minimum point $\mathbf{w}^*$.

3.6.1. Confirmation of piecewise stationarity

Confirmation of data stationarity is complicated, since it relies on statistical estimates based on a number of finite length data segments. For stationary data, the longer these segments, the better the optimal solution will reflect the underlying data. For non-stationary data, these segments must be long enough to provide good statistical estimates, yet short enough to assure stationarity within the segment. There will be some optimal segment length where the costs of steady error balance with those of non-stationarity. In previous sections, stationarity across epoch length data segments has been assumed. The results have shown that the statistical quantities estimated from these epochs well describe filter performance. That is, epoch-length stationarity has already, indirectly, been confirmed. In this section, the costs involved in assuming epoch-length stationarity are compared to the costs of using a variety of segment lengths.

It is acknowledged that there is some steady state error in the epoch based Wiener solution. An estimate of N weights based on an epoch of s samples gives an inherent steady state misadjustment (31) of N/s. However, if the assumption of piecewise stationarity is invalid, then improvement over the Wiener solution by more than this steady state error should be achievable using filters based on shorter segment lengths (or smaller effective time constants). For longer segment lengths, it is not applicable to apply the Wiener solution to data which cross epoch boundaries of the running average, however the normalised LMS filter can be used with any time constant.

The LMS filter is initialised at the Wiener solution (for epoch 1), and filter misadjustment for various time constants plotted (figure 3.31). It is clear that the continuous algorithms do improve upon the Wiener solution (M= 0). However this improvement is bounded by the steady state error implicit in the Wiener solution itself. That is, the assumption of epoch-length stationarity is valid for this data since all misadjustment is accountable for through Wiener steady state error. Extrapolating beyond the number of epochs averaged, it is also clear that the assumption of epoch-length stationarity will break down. This is because the environmental noise on the filter input, which is periodic and stationary across the epoch length, becomes attenuated revealing the underlying and more transient benchmark signal.

The trade off between steady state error and non-stationary lag noise is clear when looking at average filter misadjustment for various time constants (Figure 3.32). For stationary data, the curve would reflect only steady state error, that is , it would be monotonic decreasing with increasing T_{mse}. In fact, the function has well defined minimum indicating that minimum excess error is achieved through balancing the effects of steady state error with those of non-stationary lag noise.

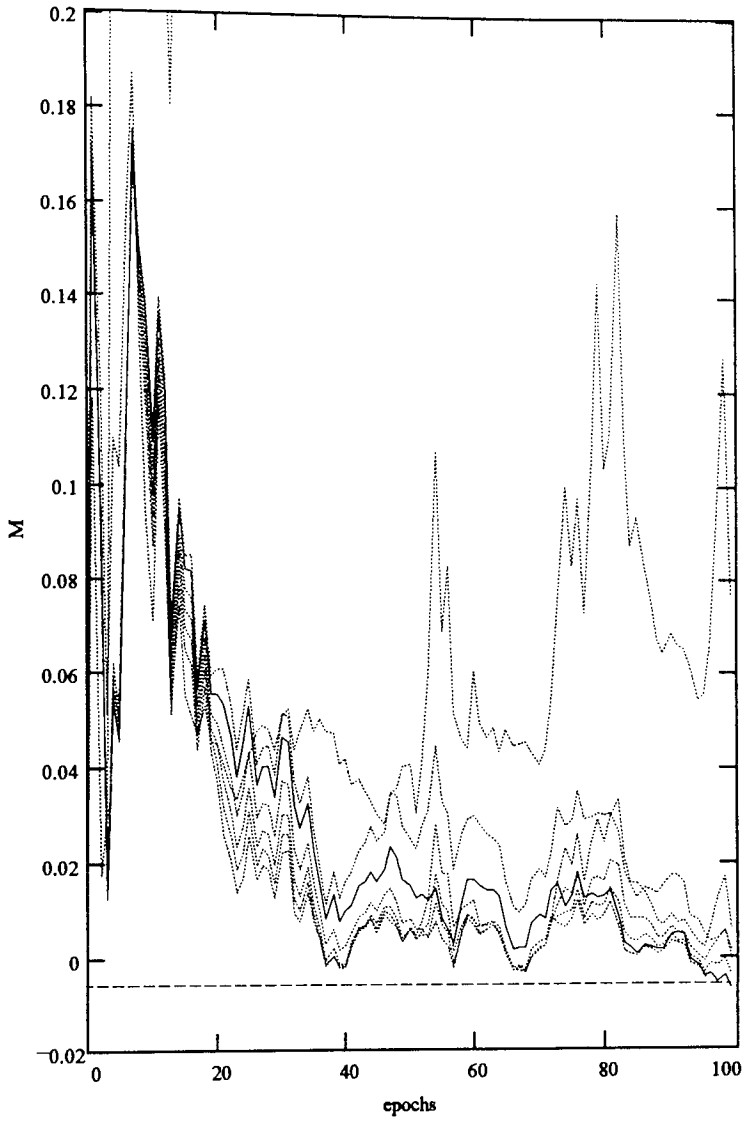

Figure 3.31. Misadjustment achieved with a variety of stochastic gradient filter time constants ($T_{mse,min}$= 2500, 250, 83 , 50 (solid curve) , 35, 25, 0.83). Negative values indicate improvement over the Wiener solution. The dashed line indicates performance deficit due to steady state error for the Wiener solution given three references and 512 samples (3/512). Note also that the curves are normalised to E_{min}, yet misadjustment error continues to decrease with epochs averaged.

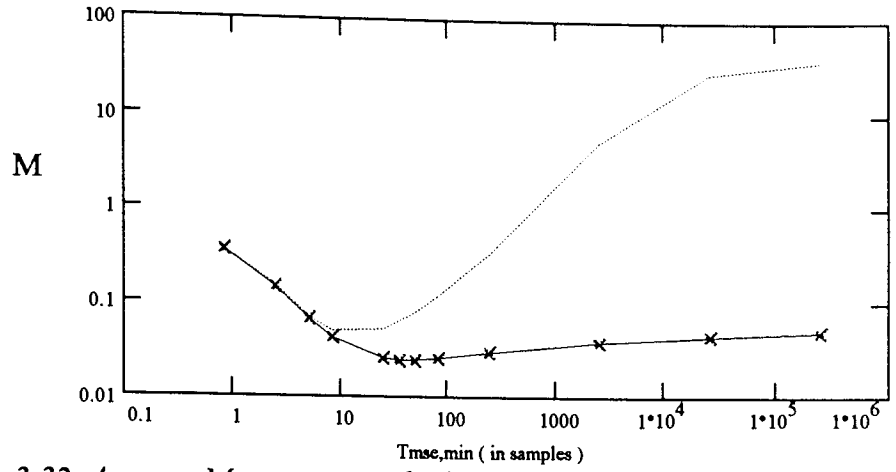

Figure 3.32. Average M_{emp} per epoch for LMS filter initialised at Wiener weights. Note that the minimum is not for large T as would be expected for statistically stationary data. The dotted trace is M_{emp} for the converging filter from figure (4.29.).

3.6.2. Quantifying non-stationarities.

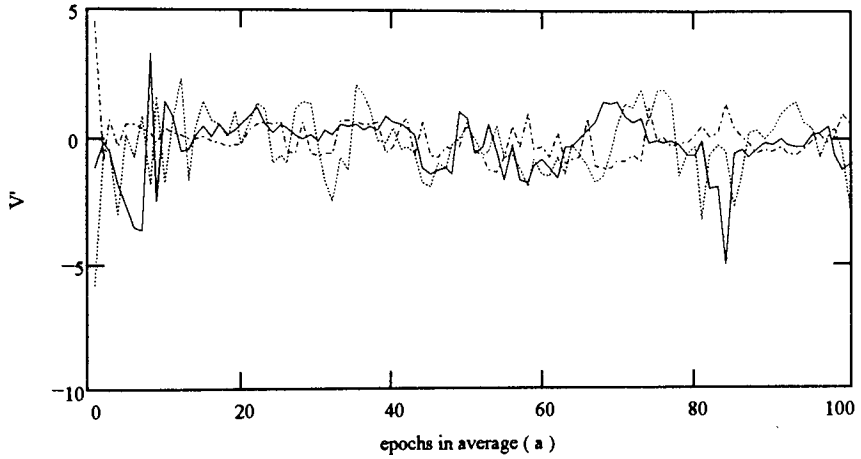

Figure 3.33. Change in decoupled weight values at the beginning of each epoch (v'_0 solid, v'_1 dotted, v'_2 dash-dot) For stationary data, the vector v' would remain null throughout.

Piecewise stationarity confirmed, it is now reasonable to assume that all non-stationary noise arises between epoch boundaries. For the benchmark data, the initial values of decoupled weights **v'** (figure 3.33) show the non-stationary nature of the solution as epoch boundaries are crossed. When system eigenvalues are of similar magnitude, decoupled weight variance provides a measure of data stationarity (Widrow et al. 1976; Gardner 1987). In practice, high correlations between reference channels lead to system eigenvalues with a large magnitude spread; for example, at Aston, all three reference magnetometers sense a strong 50Hz field component. Since the amount of excess error due to the variant decoupled weight relates to a particular system eigenvalue (16), the weight variance becomes a less useful measure of stationarity. That is, for small eigenvalues or shallow sides of the MSE surface, a large weight variance results in little excess error power. Conversely, tiny changes in any decoupled weight may introduce considerable excess error if it is associated with a large eigenvalue. It is

more practical therefore to describe a non-stationarity in terms of the amount of excess error it introduces (figure 3.34).

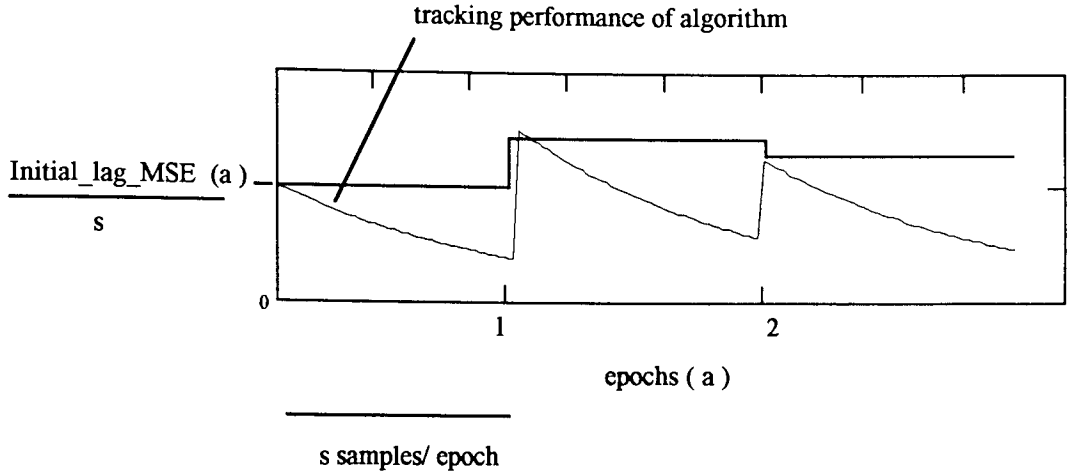

Figure 3.34. The non-stationary noise is modelled as step like at the beginning of each epoch. The task of the filter is to track the new optimal solution and attenuate this step.

The total excess error due to a non-stationarity occurring between epochs *a* and *a-1* is given from (37) by

$$Initial\_lag\_MSE_{ns}(a) = \sum_{i=0}^{i=N-1} \lambda(a)_i.(v(a,0)'_i)^2$$

Alternatively, moving back into the Wiener form, this can be expressed as the excess error introduced when the optimal weights from the previous epoch are used in place of the weights for the present :

$$Initial\_lag\_MSE_{ns}(a) = E_{\min,wnr,\mathbf{w}^*(a-1)} - E_{\min,wnr,\mathbf{w}^*(a)}$$

Expressing non-stationary noise as a fraction of E_{min} gives the misadjustment due to non-stationarities (figure 3.36).

$$M_{ns}(a) = \frac{E_{\min,wnr,\mathbf{w}^*(a-1)} - E_{\min,wnr,\mathbf{w}^*(a)}}{E_{\min,wnr,\mathbf{w}^*}} \qquad (43)$$

Note that this estimate has the inherent steady state noise of two Wiener solutions =2N/s.

Figures 3.35-36 illustrate that non-stationary misadjustment noise is most significant when the individual epochs, rather than the running averaged is filtered. The misadjustment due to non-stationarity in the running average decreases with epochs averaged.

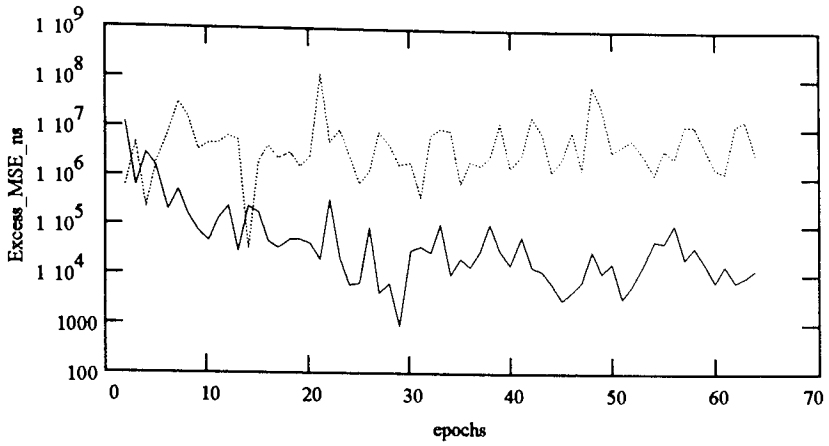

Figure 3.35. Total error due to non-stationarities (Tot_MSE_ns(a)) for running average (solid trace) and raw epochs (dotted) trace.

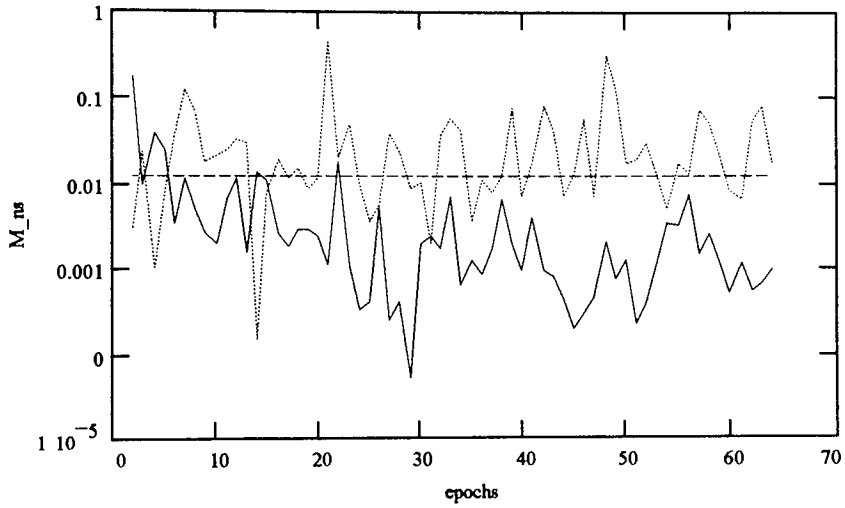

Figure 3.36. The misadjustment due to non-stationarities $M_{ns}(a)$ for running average (solid) and unaveraged epochs of benchmark. The dashed line indicates the misadjustment implicit in the Wiener estimate of stationarity (6/512). Points below this line have therefore no significance.

3.6.3. Measurement of stationarity of neuromagnetic data

The benchmark signal has been helpful in verifying the analytical form, and defining some measures of performance. However, it reflects only one signal channel and one recording instance. It is necessary to get a broader picture of the stationarity of data in more typical operating conditions. Given that the assumptions of piecewise stationarity verified for the benchmark are valid, it is possible to apply (43) ,the Wiener non-stationarity measure, to the general case. Figure 3.37 shows M_{ns} for a number of evoked response recordings over different dewar positions, subjects and days. The resulting curves have high variability yet show typical initial M_{ns} of 0.2 exhibiting monotonic decrease with averaging. This decrease is perhaps associated with the 'folding out' of the MSE surface as averaging progresses (figure 3.22) where a constant weight variance will result in consistently less misadjustment error.

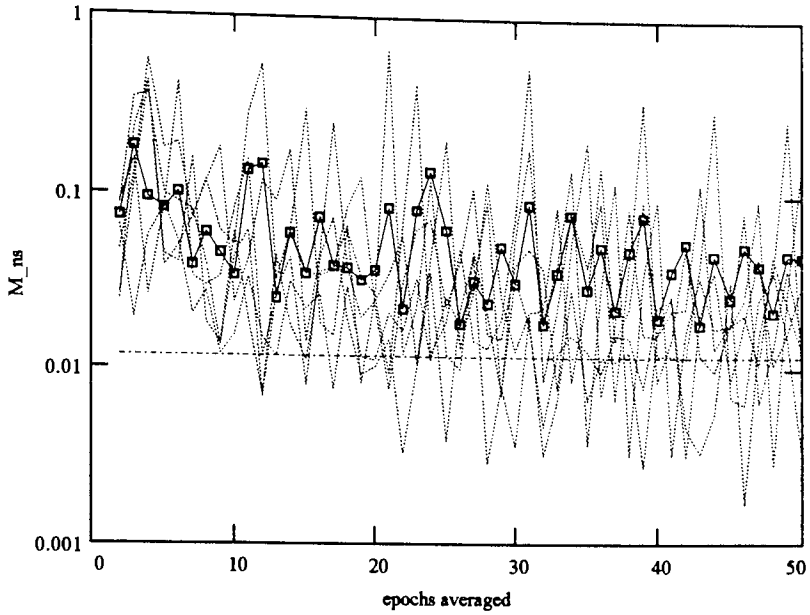

Figure 3.37. The average (boxes) of M_ns evaluated from 14 sets of evoked response data using the CRT stimulus. The dotted traces show 5 of the 14 individual estimates of M_ns, each of these estimates is constructed from average M_ns of each of the nineteen channels of the gradiometer array. The data consists of 3 separate dewar positions for three subjects recorded within a two week period. The dashed line shows Wiener steady state error (6/512) in the non-stationarity estimate. Initial M_{ns} is around 0.2 and tends to decrease with averaging.

3.6.4. Optimisation of filter time constant

Section 3.6.3 has quantified the step misadjustments due to non-stationarity which must be tracked by any adaptive algorithm. If M_{ns} were a constant, a single filter time constant would optimise the average misadjustment per epoch. However since M_{ns} decreases with epochs averaged, a monotonically increasing in filter time constant is required to provide fast tracking in early epochs giving way to slower tracking yet less steady state noise in later epochs.

From (39) , (48) and (40)

$$Error_{filt}(a) = MSE\_lag(a) + MSE\_jitter(a)$$

$$Error_{filt}(a) = \sum_{i=0}^{i=N-1}\left(1-e^{-\frac{2.n}{\tau_i}}\right).\frac{\tau_i}{2}.v_i^2(a,0)'\lambda_i \; + \mu_a.\mathrm{Emin(a)}\sum_{i=0}^{n-1}\lambda(a)_i.(\frac{1}{1-\mu_a\lambda_i(a)})$$

Consider a system with a single mode

$$Error_{filt}(a) = \left(1-e^{-\frac{2.n}{\tau}}\right).\frac{\tau}{2}.v^2(a,0)'\lambda \; + \mu.\mathrm{Emin(a)}\lambda(a)_i.(\frac{1}{1-\mu_a\lambda_i(a)})$$

assuming that all initial lag error is due to the non-stationarity, that is

$$v^2(a,0)'\lambda \; = \frac{M_{ns}.\mathrm{Emin(a)}}{s}$$

and replacing μ with weight time constant τ (27) gives

$$Error_{filt}(a) = \left(1 - e^{-\frac{2.s}{\tau}}\right).\frac{\tau}{2.s}.M_{ns}(a).\mathrm{E_{min}(a)} + \mathrm{E_{min}(a)}.\left(\frac{1}{2.\tau - 1}\right)$$

or in terms of misadjustment

$$M_{filt}(a) = \left(1 - e^{-\frac{2.s}{\tau}}\right).\frac{\tau}{2.s}.M_{ns}(a) + \left(\frac{1}{2.\tau - 1}\right) \qquad (44)$$

Widrow et al. (1976) estimated optimum μ for a continuous data sequence with *n* equal eigenvalues and constant weight variance σ^2 due to a non-stationary driving term. They derived

$$(M_{sum})_{\tau_{w^*} >> \tau_p} = \mu.tr(R) + \frac{1}{\mu}.\frac{n\sigma^2}{4.E_{\min}}$$

where τ_{W^*} and τ_p are time constants of the filter and non-stationarity respectively. Using n=1, and substituting τ for μ gives

$$(M_{sum})_{\tau_{w^*} >> \tau_p} = \frac{1}{2\tau} + \left[\frac{(\sigma^2\lambda)}{E_{\min}}\right]\frac{\tau}{2} \qquad (45)$$

The term in square brackets in (45) is the proportion of excess error due to weight variance at any sample that is, $M_{ns}(n)$. Expressing this as an average evaluated over *s* samples gives $M_{ns}(a)/s$. The form of Widrow et al. (1976) equation is equivalent to (44) when τ is of comparable magnitude to s. Graphically, the relationship between (45) and (44) is shown in (figure 3.38). The two functions diverge for large τ, but have the same minimum point. Differentiating (45) with respect to τ and equating the derivative to zero, gives

$$\tau_{opt} = \sqrt{\frac{2s}{M_{ns}}} \quad .. (46)$$

That is, for any measured step non-stationarity M_{ns} over an s sample epoch, the optimal filter time constant is given by (46).

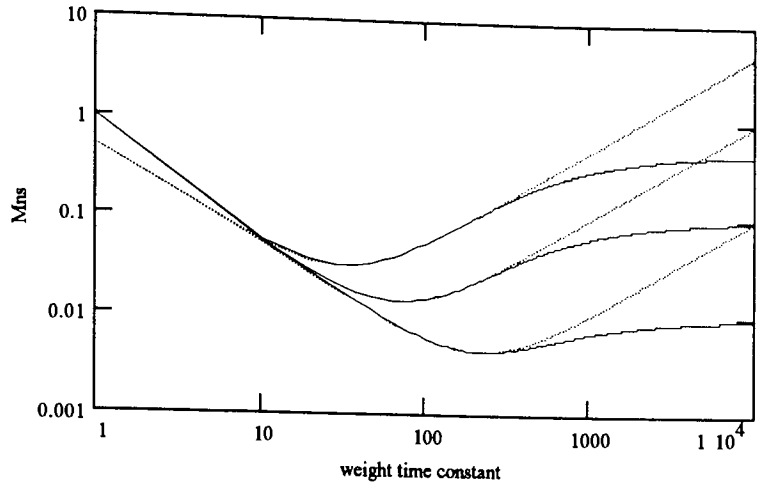

Figure 3.38. Graphical form of equation (44) (solid) and (45) (dotted).For constant misadjustment M_ns over an epoch vs. filter MSE time constant. M_ns =0.5, =0.1 , = 0.01 in order of descending minima. Both the Widrow estimate (45) (dotted) and epoch based calculations (44) (solid) have the same minima. The curves diverge for large filter time constants. In the continuous case misadjustment increases monotonically with τ,whereas in the epoch based case, this increase is bounded by the total non-stationary misadjustment present.

3.6.5. Generalised optimal RLS time constant progression

Algorithms such as the RLS have a time constant which is independent of the underlying data and it is therefore possible to estimate an optimal progression based on (46).

For τ comparable to s, the non-stationary misadjustment at the start of any epoch is likely to be large compared to any remaining uncancelled non-stationary misadjustment due to the previous epoch boundary. Filter performance is therefore assumed to be independent between epochs. Since in the running average, the non-stationarity decreases monotonically with epochs averaged (figure 3.37), the filter applied to each epoch will have a different optimal time constant.

The curves of figure 3.37 fall off at a rate of approximately $1/\sqrt{a}$. Taking some initial M_{ns} , and combining with (46) gives a τ_{opt} as a function of epoch a.

$$\tau_{opt}(a) = \sqrt{\frac{2s.\sqrt{a}}{M_{ns,init}}} \qquad (47)$$

For a single experimental trial figure 3.40 shows the average misadjustment due to an RLS filter with optimal time constant progression of (47). The RLS filter, with optimal time constant progression, improves on the normalised time constant LMS. The optimal time constant progression for the LMS filter results in poorer filter performance. Figure 3.41 shows that the reason for this is that, although its fastest mode has equivalent time constant to that of the RLS, the effective time constant of the LMS filter is much greater than that of the RLS filter.

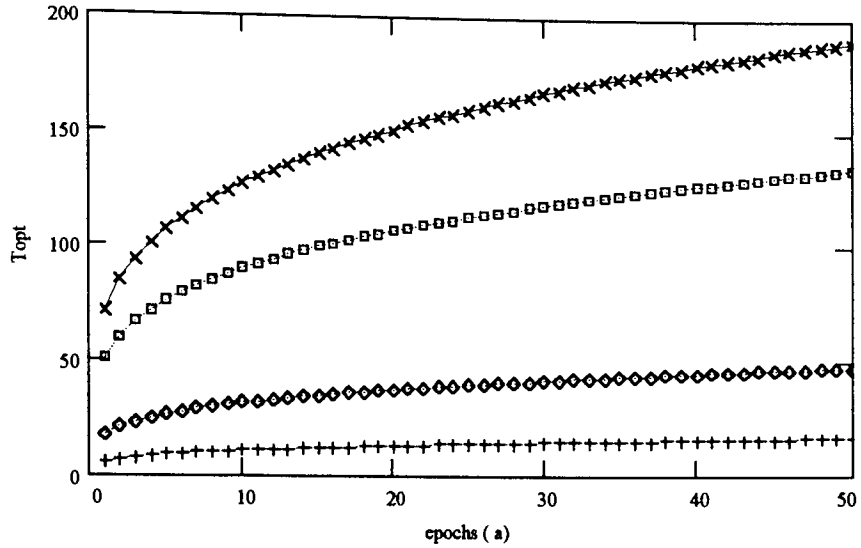

Figure 3.39. Optimal time constant progression calculated from (47) on the basis of non-stationary misadjustment decreasing as 1/√a (from best fit curve to data in figure 3.37). For initial misadjustments ($M_{ns,init}$)of 0.2 crosses; 0.4 boxes; 3.2 diamonds; 25.6 pluses.

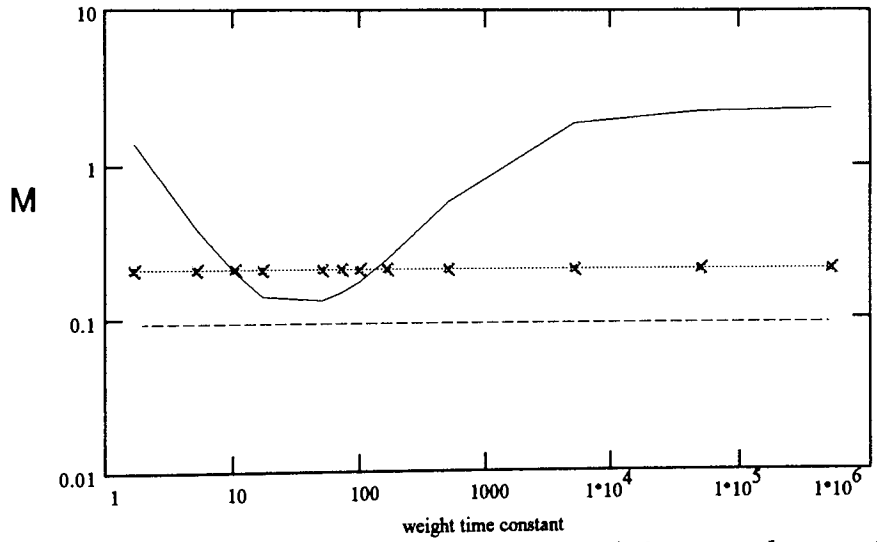

Figure 3.40. Average misadjustment per epoch for a single experimental run. Solid curve shows performance of normalised LMS filter. Using the optimal time constant progression of using (47), with $M_{ns,init}$ =0.2, performance of the RLS (dashed) and LMS (crosses).

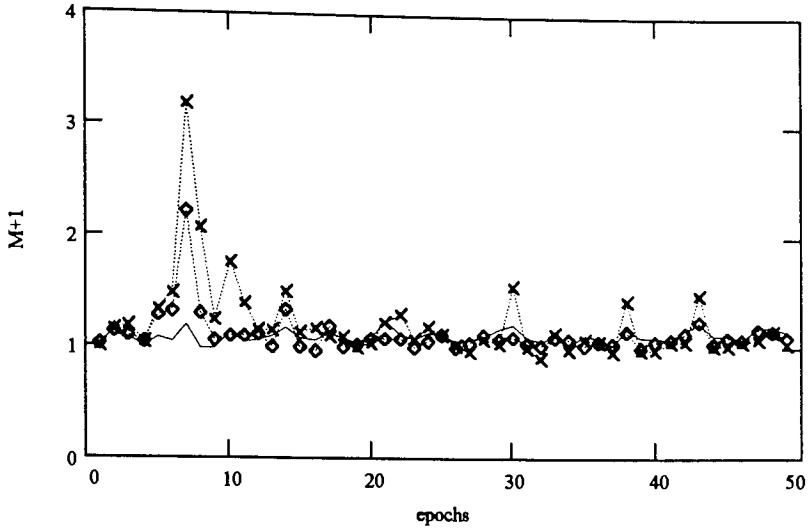

Figure 3.41. The same trial as in figure 3.40 plotted as misadjustment vs. epochs averaged for optimal time constant progressions. LMS : M_{init}=0.2 (crosses), M_{init}=3.2 (diamonds) ;and RLS M_{init}=0.2 (solid). Although the fastest mode of the LMS filter has the same time constant as the RLS, it is not this mode which dominates filter performance, and hence it fails to track the early non stationarities in the data.

3.6.6. Generalised LMS implementation

Application of the time constant optimisation of (46) to an LMS implementation is not practical due to the algorithm's inherent data dependent convergence properties. That is, steady state and lag noise do not necessarily arise from the same LMS filter mode. The average LMS time (30) constant is derived based on nominally equal eigenvalues, in practice however, there is a large eigenvalue spread (figure 3.42). In order to pre-specify the effective LMS filter time constant for a multiple reference application therefore, complete a-priori knowledge of signal and reference channel statistics is required.

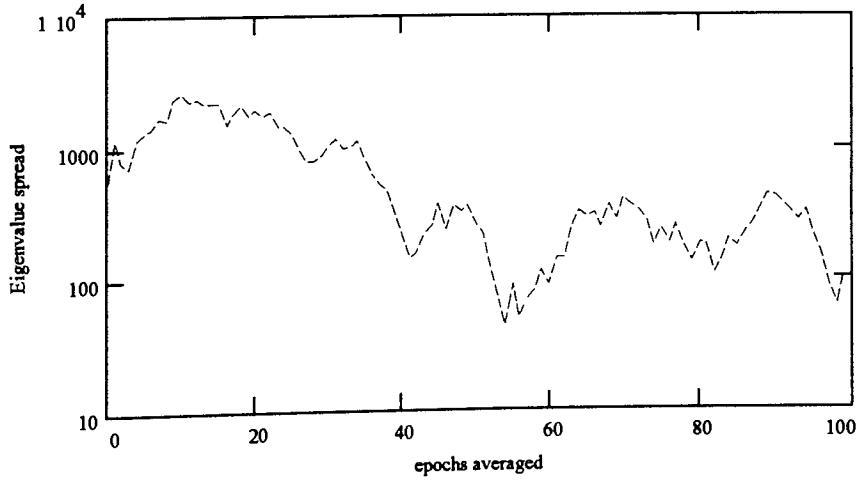

Figure 3.42. Eigenvalue spread vs. epochs averaged for the benchmark data. The large spread indicates that the three reference channels contain highly correlated information.

For a practical implementation, optimal LMS filter time constant can be estimated from an ensemble of misadjustment curves (figure 3.43). Although this time constant is for a normalised LMS filter, typical signal and noise amplitudes are known,

and the decrease in eigenvalues with averaging can be approximated as linear (figure 3.23). That is, the generalised LMS filter would have a step size (μ), calculated on the basis of typical reference noise amplitude and an 80 sample weight time constant (figure 3.43), which increased linearly with epochs averaged. Such an approach is computationally highly efficient and appropriate for a running average display. Off-line, and prior to analysis, more precise yet computationally intensive filters can be applied to the averaged data.

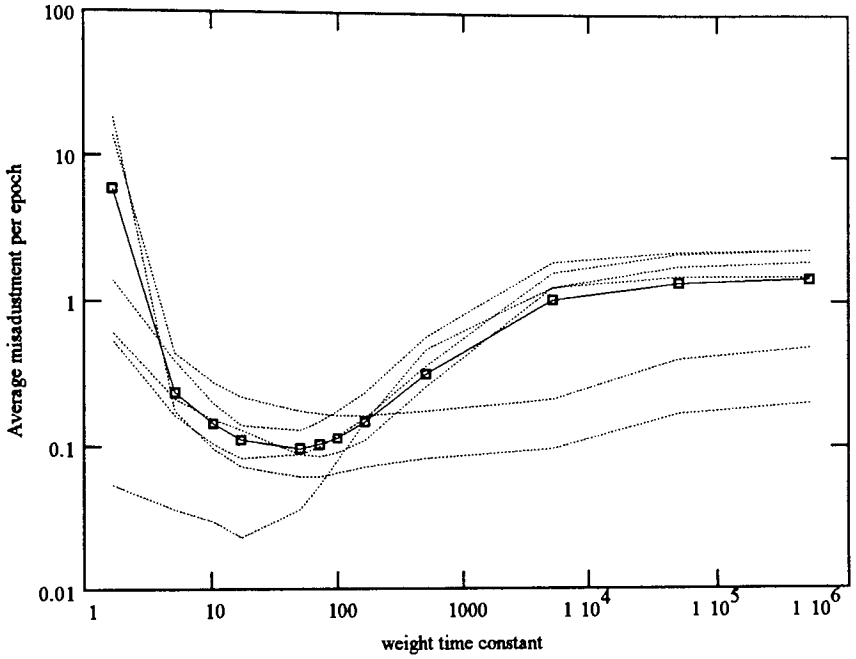

Figure 3.43. Six misadjustment curves obtained from three dewar positions from the data in figure 3.37 along with ensemble average (boxes).For the 3 reference LMS filter of normalised time constant.

3.7. Time derivative Reference inputs

Any noise source, such as the CRT, is the superposition of many generated fields of different sources and spatial gradient. Furthermore, all reference and signal channels pass through individual anti-aliasing filters. These filters introduce phase shifting effects (see chapter 2). The noise sensed in the gradiometer channels may therefore be out of phase with that sensed by the reference magnetometer channels. This phase shift gives lower correlation between signal and reference channels, and means that less of the environmental noise can be removed from the signal by reference noise cancellation. It is possible to account for these effects by introducing extra weights into the filter algorithm, which allow the phase shifting of reference channels. This is achieved by using three extra reference channels which are time derivatives of the vector magnetometer outputs, and therefore in phase quadrature (figure 3.44). The weighted sum of the cosine and sinusoidal components in the reference channel and its time derivative partner should theoretically allow a sinusoid of any phase and amplitude to be constructed by the algorithm. The use of time derivatives means that the phase shifting operation should be concentrated in the higher frequency region of the spectrum (figure 4.45) where phase distortion is most likely.

Note that by introducing freedom of phase to the algorithm, the reference noise canceller moves towards a frequency discrimination filter with notches at the dominant reference frequencies. That is, there is potential for the annihilation of useful signal data around these notches.

Defining

$$M_{gain} = \frac{E_{\min,3refs} - E_{\min,6refs}}{E_{\min,3refs}}$$

that is, M_{gain} is the extra proportion of noise power which is cancellable using the six, rather than three reference channels. Note that the implicit cost in using these extra channels is given by is an increase in steady state misadjustment (31) of 3/512. Figure (4.46) shows M_{gain} for a number of experimental trials. The curves indicate that improvement is best in the earlier epochs, levelling out to around 10% E_{min} in later epochs. The results in figure 3.46 are in contrast to those from the benchmark trial (figure 3.47), where improvement with increasing number of references is outweighed by the steady state noise introduced. The critical factor appears to be the CRT, which was not on during the recording of the benchmark signal. This is reasonable, since the CRT is run at 100-110Hz where the analogue filters used (106Hz) have poorest phase homogeneity. That is, any adaptive implementation will benefit by removing this phase shift.

From figure 3.46, in early or unaveraged epochs, the use of derivative references can result in error power improvements of 30-50% E_{min}, or a 15-20% increase in amplitude SNR. In later epochs improvements of 10% E_{min} or 5% amplitude SNR are achievable. These improvements are at the cost of potential misadjustment errors due to the cancellation of neural signal around these reference frequencies. Where viewing unaveraged data, for example spontaneous activity, the improvement gained by the use

of extra references may be worth the computational and misadjustment overheads. For averaged data however the conclusion is that the expense of extra reference channels is unjustified.

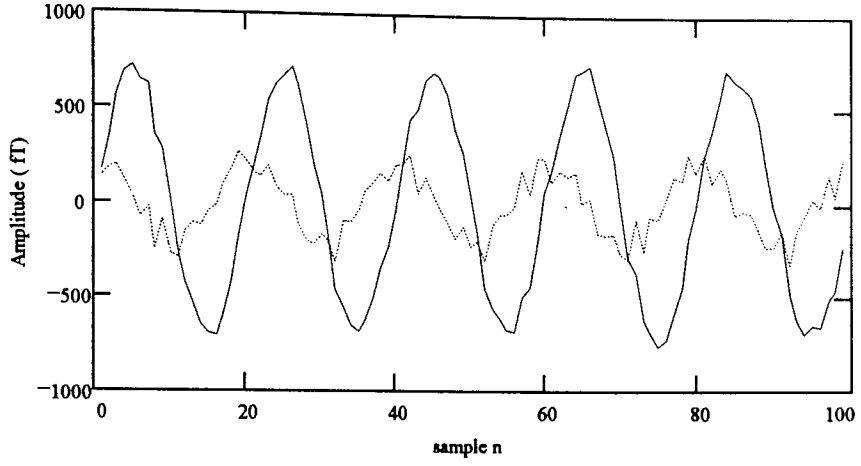

Figure 3.44. Software derivatives (dotted) of sinusoidal reference channel (solid) values are cosinusoidal. By the weighted addition of sin and cosine terms, a sinusoid of any phase or amplitude can be obtained.

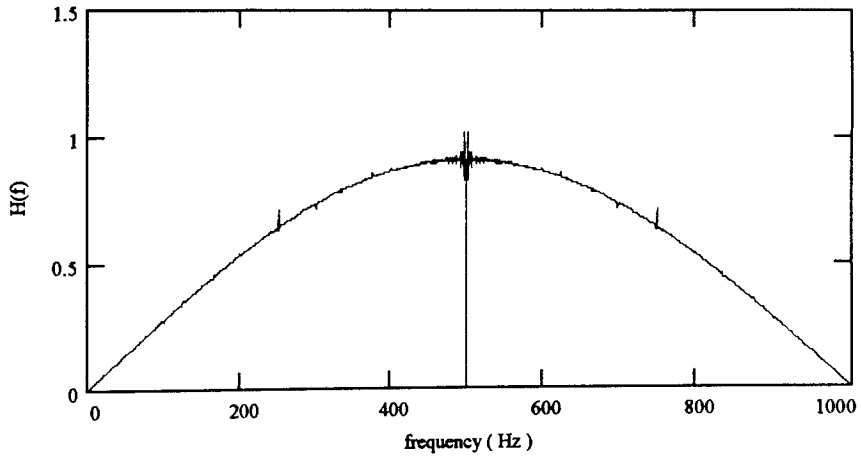

Figure 3.45. The transfer function of the finite difference software derivative function for sample rate 1kHz. Time derivative reference channels are created by subtraction of successive reference samples.

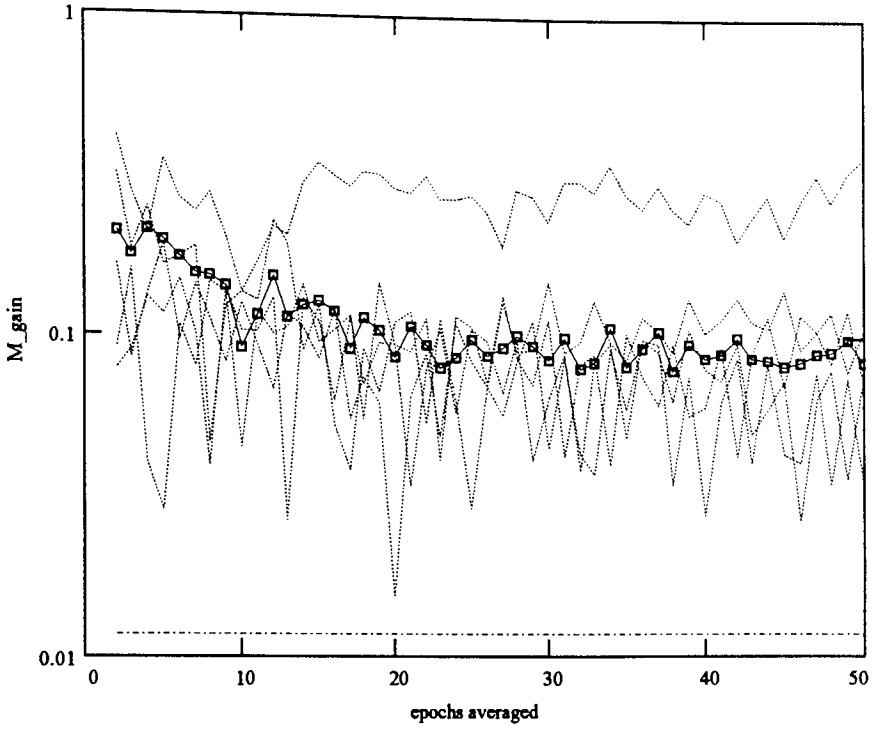

Figure 3.46. The relative excess noise M_{gain} for the data in figure 3.37 removed by including three derivative reference channels. The boxed trace is grand average of 14 evoked response data sets. The dashed line shows minimum error due to Wiener estimate, and also noise penalty for increased number of references (6/s). Derivative references provide the greatest improvement during the early epochs, this improvement levelling out at about 10% E_{min} in the later epochs.

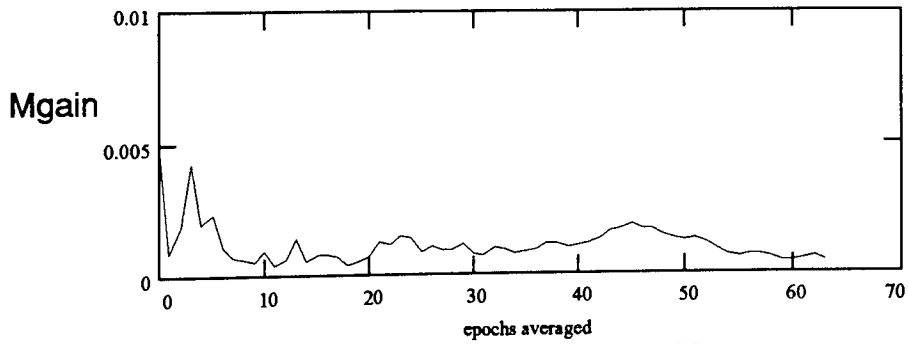

Figure 3.47. M_{gain} for the benchmark data. The improvement in algorithm performance is well below the extra steady state misadjustment introduced by the use of extra reference channels (0.012).

3.8. Concluding remarks

A basic algorithm structure has been proposed for the adaptive filtering and averaging of neuromagnetic data. Signal processing advantages gained by averaging and DC level removal prior to filtering have been outlined.

In this installation, it has been shown that the performance of the LMS filter is well modelled by taking epochs (0.5s) of the running average to be statistically stationary. All non-stationarities have been modelled as step driving terms arising between epoch boundaries. The error predicted by the analytical form has been shown to predict not

only error due to non-stationary lag, but also steady state error, even when this error results in reduced filter output power.

In the steady state, examination of an ensemble of neuromagnetic data sets shows that, initial non-stationarity misadjustment is around 20%, and decreases monotonically as the signal is averaged. Based on the decreasing non-stationary noise, an optimal progression for filter time constant has been proposed. This optimal, time constant progression has been found inappropriate for LMS filter because of the algorithm's intrinsic sensitivity to eigenvalue spread. Other adaptive implementations, such as the RLS, have been shown to benefit from such a progression.

The option of using extra references, in the form of reference software derivatives, has been discussed. The conclusion is that the intrinsic misadjustment penalty of the extra references, the extra processing time, and possible loss of signal pass-band, does not merit the improvement in noise cancellation.

This study adds to the existing body of work in a number of ways:

i) Adaptive filtering algorithms are used mainly in signal processing applications where the underlying signal is known a-priori. This study has shown that analytical prediction of filter performance can also be applied to evoked response measures. Previous work (Robinson 1989) has evaluated filter performance in noise-only conditions, where consistent reduction in total output power is desirable. This study has shown that such measures of filter performance are inappropriate when some underlying signal is present.

ii) The effects of non-stationarity of the neuromagnetic data has been addressed for the first time and a measure of this non-stationarity has been introduced.

iii) Given the measures of non-stationarity, and analytical tools describing filter performance, it has been shown possible to tailor adaptive filter design to suit the environment in which an evoked response is to be recorded.

Chapter 4.

Element function and architecture

The heading of this chapter derives from figure 1.1, the aim is to outline the neural structures of the primate visual system, their connectivity and function. Much data in this section is due to invasive micro-electrode studies in the macaque. The discussion begins with the photoreceptor array housed in the retina, follows the path of visual information via retinal ganglion cells, through the lateral geniculate nucleus (LGN) and into the visual cortex (figure 4.1). Finally the role of the less extensively studied subcortical structures (such as the superior colliculus) in primate vision is examined.

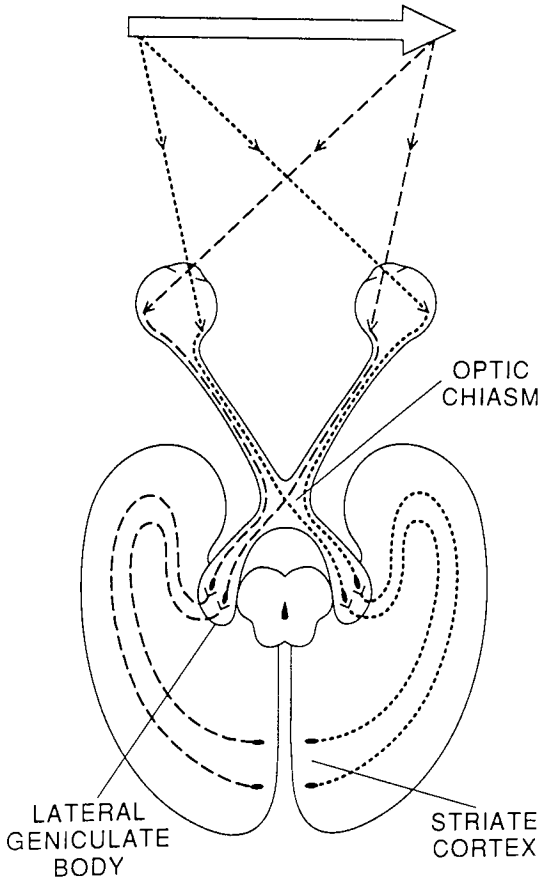

Figure 4.1. Schematic of neural connections in the geniculo-cortical pathway. from Regan (1989).

4.1. The retina

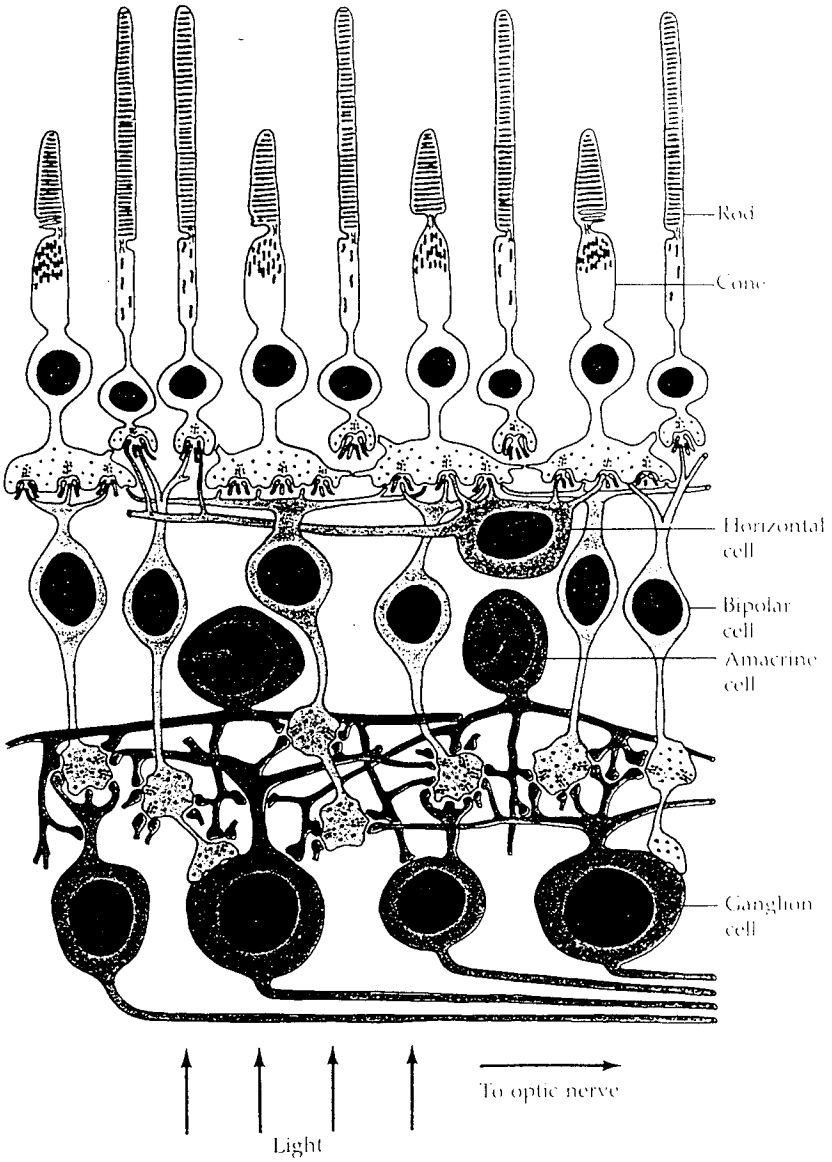

Figure 4.2. Organisation of the primate retina (from Dowling and Boycott 1966).

The retina is the multi-layered structure housing the photoreceptors and the neurons which form first stages of visual processing. Superficial examination of the retina reveals a 5mm diameter yellowish region known as the macula lutea, to which the central 5 degrees of the visual field are focused. Within the macula lies the fovea-centralis, approximately 2mm in diameter bordering a small depression housing the foveola where the receptors responsible for the very central 1-2 degrees of vision are situated.

4.1.1. The photoreceptors

Each photoreceptor contains laminae of pigmented material (Figure 4.2) and releases neurotransmitter chemicals on the absorption of light photons. The absorption spectrum of the laminar pigment determines the band of wavelengths over which the

photoreceptor is optimally sensitive. The human retina contains two basic types of photo-receptor: rods and cones.

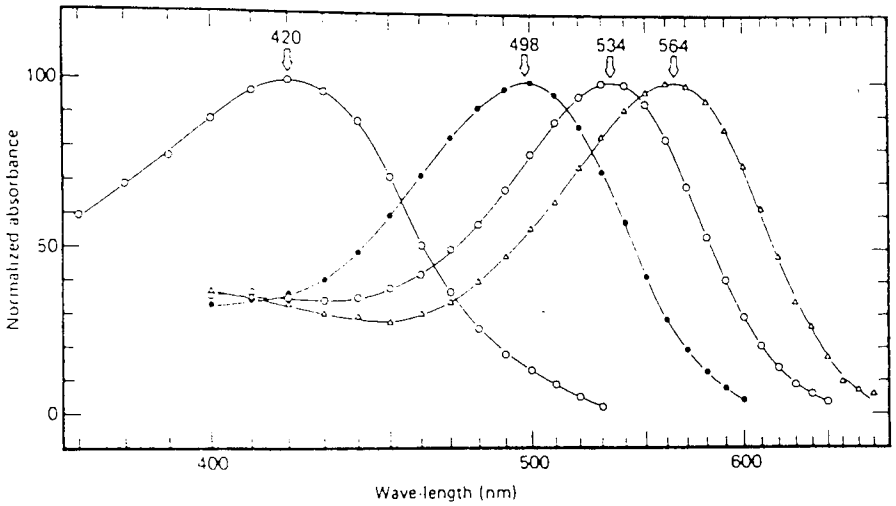

Figure 4.3. Mean absorption spectra of human rods (solid circles) and cones, obtained by micro spectrometry (from Bowmaker and Dartnell 1980).

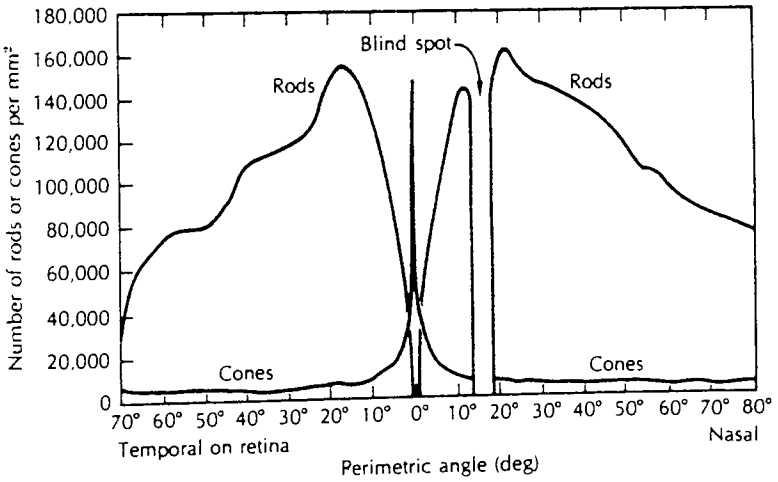

Figure 4.4. Rod and cone densities vs. retinal eccentricity (from Cornsweet 1970.)

Rods

Rods are long thin structures (2 μm diameter, 40-60μm in length) containing the purplish photo pigment rhodopsin (Figure 4.3). Rods predominate in the retinal periphery being almost absent in the foveola (Figure 4.4). Rods have more efficient quantal absorption than cones, responding to as few as one or two photons (Baylor et al. 1979), and are therefore responsible for vision at low luminance levels.

Cones

There are three cone types, classified according to the wavelength of light that gives peak absorption, namely Long, Medium, and Short wavelength sensitive (Figure 4.3).

Cones vary in size and shape across the retina and are extremely densely packed in centre (Figure 4.4). The fine retinal mosaic corresponding to the central few degrees of the visual field means that cones govern the limits of acuity and resolution of fine pattern. Colour vision stems from the wavelength discrimination provided by the range of absorption spectra found in cones.

4.1.2. Post-receptoral retinal elements

The photoreceptors connect to a complex array of retinal neurones (Figure 4.2). These cells perform the first stages of neural processing of the visual information. There are four main categories of retinal neuron : bipolar , horizontal, amacrine and ganglion. Retinal ganglion cells are discussed in the next subsection.

Bipolar cells

Bipolar cells mediate the connections between the rods and cones to the retinal output or ganglion cells. They form a variety of complex interconnections and to some extent group or weight receptor output. For example, as many as fifty rods can synapse to a single *rod bipolar* cell which in turn connects to up to four ganglion cells (Saude 1993). By pooling the output from a large number of photoreceptors, the cell has increased the sensitivity to incoming photons at the expense of losing acuity due to the large spatial extent (or receptive field) of the receptors. There are two main classes of bipolar cell: those which hyperpolarize to light (OFF bipolars) and those that depolarise (ON bipolars). That is, distinct groups of bipolar cells fire at the appearance and disappearance of any stimulus. Hubel (1988) postulates that such an ON-OFF (or push-pull) mechanism maintains equal sensitivity to light increment and decrement and is also a more stable signalling mechanism, since no constant neural firing is required to indicate the equilibrium state. This ON-OFF pathway segregation is maintained at least up to the level of the lateral geniculate nucleus (LGN) (Schiller and Colby 1984).

Horizontal cells

Horizontal cells extend laterally and connect with both bipolar and photoreceptor elements. Although little primate data is available, such cells are thought to contribute to the receptive field surrounds of retinal ganglion cells (Werblin and Dowling 1969, Mangel and Miller 1987).

Amacrine cells

Amacrine cells lie within the ON and OFF laminae of the retinal interplexiform layer, like horizontal cells their processes extend laterally. Synapsing with both bipolar and retinal ganglion cells, such cells make feedback synaptic connections which can modulate bipolar transmitter release (Werblin 1972). Amacrine cells have been identified as retinal motion detector units in a number of vertebrates (Barlow and Levick 1965; Cleland and Levick 1974). However, the function of amacrine cells in the primate is still unclear.

4.1.3. Retinal Ganglion cells

Ganglion cells are the last stage of information processing in the retina, their axons form the optic nerve leaving the eye. Retinal ganglion cells are easily classified in terms of their transient response to stimuli : tonic and phasic (Gouras 1968, Gouras and Zrenner 1981). Tonic cells give a sustained increase in firing to a sustained stimulus, whereas phasic cells only respond to stimulus change. The tonic/phasic distinction can be thought of as analogous to the dc/ac coupling of an electronic circuit.

Receptive fields of retinal ganglion cells

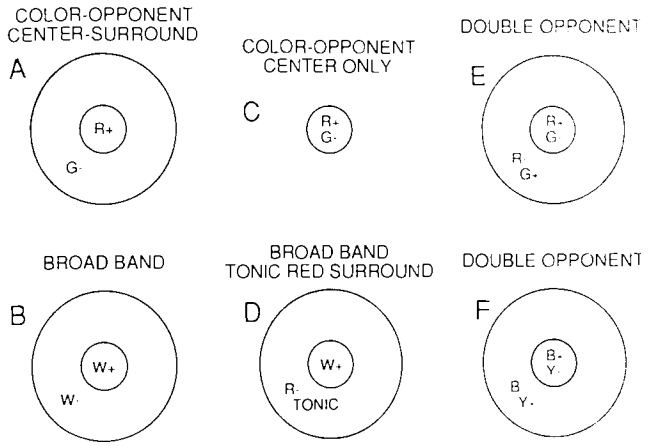

Figure 4.5. Some receptive field structures, from Regan (1989). A,C,B correspond to ganglion cell types I,II and III respectively (Wiesel and Hubel 1966). Cells with double opponent receptive fields (E,F) begin to exist at the level of the primary visual cortex.

The receptive field of a neuron is that region of the visual field in which a stimulus can modify the neuron's firing rate. Wiesel and Hubel (1966) identified three distinct ganglion cell groups : types I, II and III. Type I cells were both spatially and spectrally opponent, Type II cells were only spectrally opponent, Type III cells only spatially opponent. These correspond to the groupings adopted by De Monasterio and Gouras (1975) of 'colour opponent', 'non-concentric' and 'broad-band' respectively (see Figure 4.5: A,C,B). Retinal ganglion cell types I and III arise from a concentric groupings of receptors (Figure 4.6), the cells in the centre operating in antagonism with those in the surround (Kuffler 1953). The structure is often modelled as having a Difference of Gaussian or DOG spatial sensitivity profile (Rodieck 1965).The antagonism in the receptive field is useful since it nulls the response to uniform illumination giving high contrast sensitivity over a huge dynamic range of operation. Gouras and Zrenner (1981) found all phasic cells to be broad band, chromatic information being carried exclusively by tonic cells.

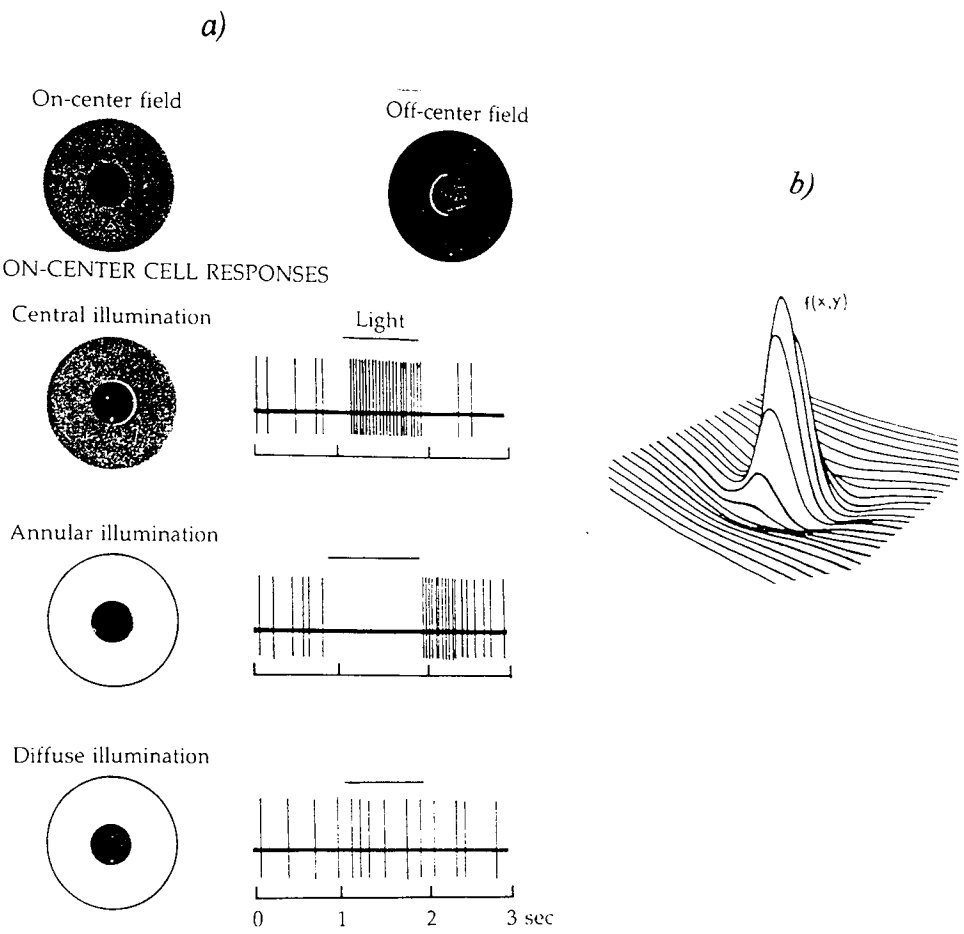

Figure 4.6. a) The figure (from Hubel and Wiesel 1966) shows retinal ganglion recordings to central, annular, and diffuse field stimulation for an ON centre type cell. b) The concentric receptive field structure has been modelled as a Difference of Gaussian sensitivity profile (redrawn from Rodieck 1965).

M and P cells

Property	P cells	M cells
Spectral selectivity	yes	no
Luminance contrast gain	lower	higher
Receptive field size	smaller	larger
LGN projection target	parvocellular	magnocellular
Conduction velocity	lower	higher
Cell size	smaller	larger
Response to light steps	tonic	phasic
Linearity of spatial summation	linear ('X')	75% 'X', 25% 'Y'
Pattern vision at scotopic levels	no	yes
Number of cells (in millions)	1.2	0.15

Figure 4.7. Summary of primate M and P cell properties (from Kaplan 1991).

M and P cells correspond to subsets of tonic and phasic cells which project from the retina to the lateral geniculate nucleus (LGN). Kaplan (1991) provides a concise summary of primate M and P cell properties (Figure 4.7). The M (magno-cellular) and P (parvo-cellular) terms refer to the relative cell size in the LGN layers to which the

ganglion cells project. M type cells tend to have thicker axons, and larger cell bodies than P-type. For recording purposes, much retinal ganglion cell recording is made at the level of the LGN where the distinction between cells is obvious. Studies of the retinal ganglion cells at the level of the primate LGN (Lee and Martin 1989, Derrington and Lennie 1984) indicate that P cells are more suited to high resolution, chromatic, stationary stimuli. Whereas M cells are predominantly colour insensitive and respond optimally to large, fast moving, stimuli of relatively low contrast. The M/ P functional distinction has been more crudely demonstrated (Merigan 1987) by treatment of the primate LGN with acrylamide and ibotenic acid, destroying the P and M cells respectively. Destruction of P cells severely degraded perception of colour and fine pattern, whereas destruction of M cells was found to compromise motion sensitivity. It should be pointed out that the two systems are not mutually exclusive, P cells respond preferentially to chromatic modulations but will also respond to achromatic stimuli (Wiesel and Hubel 1966). Likewise, Schiller and Colby (1983) were unable to null the response of M-cells to isoluminant flicker, a result they attributed this to the generally higher sensitivity of such cells. A contributing factor could be a slightly uneven weighting of cones in the cell's receptive fields.

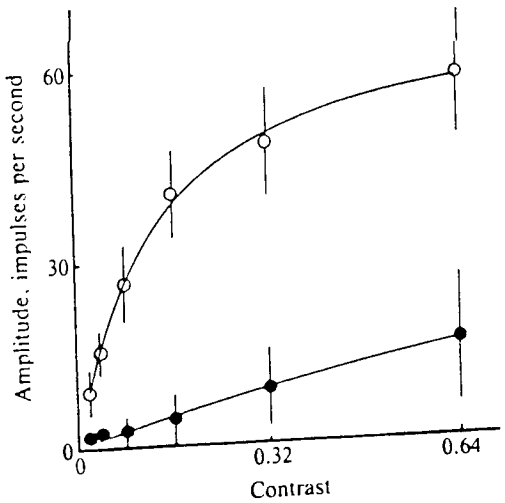

Figure 4.8. Average response vs. contrast for 28P (filled) cells and 8M cells (empty circles) to grating stimuli drifting at 4Hz. (from Kaplan and Shapley 1986). The P cell response is linear with increased contrast. The M cell response curve begins to flatten off at around 15% contrast, having a similar slope to that of the P cell at higher contrast.

Kaplan and Shapely (1986), showed that M cells are 8-10 times more sensitive than P cells (Figure 4.8). Specifically, at low contrast the M cells possess a much higher contrast gain, that is increase in firing rate to increase in contrast. This increased contrast gain could be directly related to the area of the receptive field centre (Shapely and Enroth Cugell 1984) since M cells are typically 4-9 times the area of P cells (De

Monasterio and Gouras 1975). Lee and Martin (1989) , show that minimisation of subjective flicker (in humans) corresponds to the minimisation of M cell response (in primates) (Figure 4. 9). They thus postulate that it is the M cell population which forms the physiological basis of the perceptual luminous efficiency or V_λ curve.

The larger receptive field sizes of M cells would imply that their spatial resolution is poor with respect to P cells. However, due to the order of magnitude difference in sensitivity, monkey M cells have shown similar spatial resolving power to P cells regardless of retinal eccentricity (Blakemore and Vital-Durand 1986). In the human retina however, histology indicates (Dacey and Petersen 1992; Dacey 1993) that the M to P cell ratio is different, and therefore acuity may by limited by different factors.

At light levels below one troland, Purpura et al. (1988) showed that P cells ceased to respond to patterned stimuli. P cells would therefore seem to have minimal rod input, leaving M cells responsible for vision at low mesiopic and scotopic lighting conditions. Figure 4.7 gives a summary of M and P cell properties.

Spatial Linearity

The DOG response profile model (Figure 4.6) of Rodieck (1965) is essentially dependent on linearity of spatial summation, such linearity is however not observed in all cell types. Enroth-Cugell and Robson (1966) examined the linearity of spatial summation of cells in the cat retina. They found two main cell groupings which they named X and Y. X type cells exhibited linear properties of spatial summation, that is, the cell's response to a sinusoidal grating could always be nulled at some spatial phase. Also, the firing of X cells was temporally modulated at the frequency of stimulation. The response of Y type cells however could not be nulled by alterations in spatial phase, that is they were spatially non-linear. Y type cell responses were found to be modulated at twice the frequency of stimulation. The X, Y type classification scheme of Enroth-Cugell and Robson (1966) has been extended to studies of the primate retina. Retinal ganglion cells projecting to the parvo-cellular (P) layers of the LGN have been found to be exclusively X like. Whereas 75% of M cells have been found to be of type X and 25% type Y (Blakemore and Vital Durand 1981; Derrington and Lennie 1984). There is danger in extending classification schema across species, as pointed out by Casagrande and Norton (1991): the cat is a nocturnal predatory carnivore, we are diurnal omnivorous primates, in other words, there are good reasons for the existence of different visual processing mechanisms in the cat and human.

Temporal properties

Tonic cells have a low pass temporal response characteristic, whereas phasic cells are more bandpass (Figure 4.9). The high frequency cut-off for both tonic and phasic cells is around 40Hz (Lee and Martin 1989). It is unclear however how much of this bandwidth is exploited by the visual system.

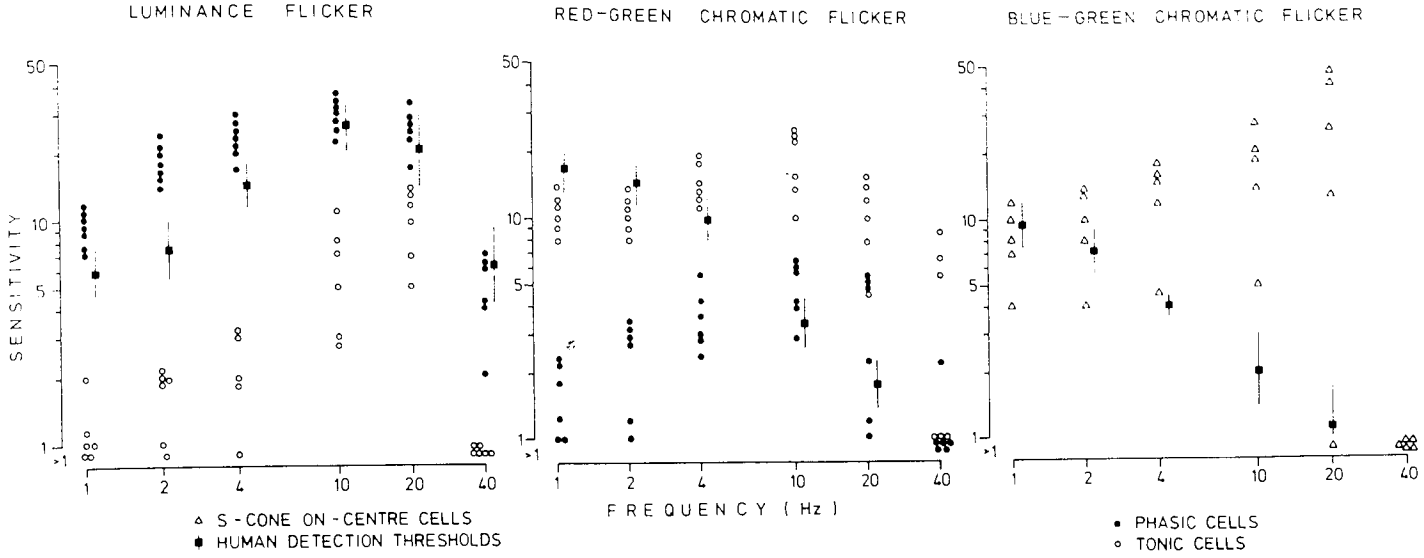

Figure 4.9. A comparison of monkey M and P cells to chromatic and achromatic flicker with human psychophysical data. Note that in the case of chromatic flicker, tonic cell sensitivity is not reflected in the psychophysical data. from Lee and Martin (1989).

Dual role hypothesis

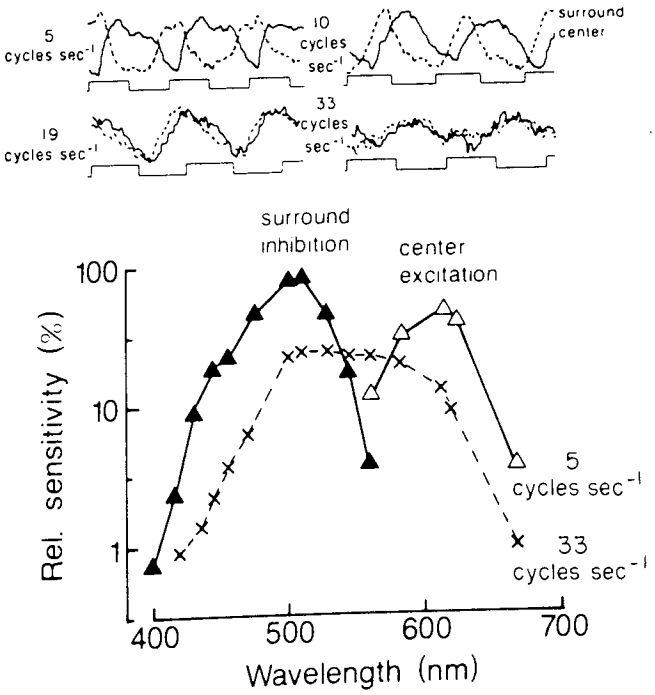

Figure 4.10. The triangles show the action spectra of an R-G opponent retinal ganglion cell in the monkey at 5Hz. At flicker rates of 33Hz, the phase shift between centre and surround results in loss of colour opponency. from Zrenner (1983).

At high temporal frequencies, phase differences between the signals from centre and surround of the receptive field of chromatically opponent (hence tonic) ganglion cells (Figure 4. 10), can cause an apparent switch from chromatic to luminance sensitivity (Gouras and Zrenner 1979). Lee and Martin (1989) reject the proposition that P cells become responsible for luminance detection at higher temporal frequencies since, although the P cell is firing, nothing is perceivable (de Lange 1958, Wisowaty 1981) or recordable with VEPs (Kulikowski et al. 1989).

Frequency doubling

Schiller and Colby (1989) reported an M cell response at twice the stimulation frequency around isoluminant flicker conditions. Similarly Lee and Martin (1989) observe this frequency doubling of M cell output to high contrast pattern stimulation, and suggest that the phenomenon is due to a non-linear summation of long and medium wave sensitive cone inputs.

Projections of retinal ganglion cells

Approximately 90% (80% P , 10% M) of retinal ganglion cells project to the lateral geniculate nucleus (Perry et al. 1984; Rodieck 1988). The superior colliculus (Leventhal et al. 1981, Stein and Meredith 1989) receives a nominal direct retinal input in the form of W (large receptive fields and slow axonal conduction) and Y type cells.

4.2. The Lateral geniculate nucleus

The lateral geniculate nucleus is the main thalamic structure conveying information from the retina to the striate cortex. The function of the LGN is still unclear. It is known however that retinal input accounts for only 20% of the geniculate synapses (Schiller 1986; Casagrande and Norton 1991). Such anatomical evidence hints that the structure is functionally more than a relay station for retinal information on its way to the visual cortex.

4.2.1. Retinal inputs to the LGN

The primate LGN consists of six distinct layers separated by inter laminar zones populated with smaller, sparser cells. The layers of the LGN are grouped according to their relative component cell size: large or magno-cellular, small or parvo-cellular. The cells in each layer of the LGN maintain distinct yet identical retinotopic maps of the contra-lateral visual hemi-field. In the macaque, the inputs from each eye remain segregated and represented on different layers (Hubel 1989).

4.2.2. Cortical Visual Input

A tightly topographic pathway projects from the striate cortex *back* to the LGN, this pathway is thought to provide more input to the LGN than the retina (Koch 1987). Likewise, in primates, connections from higher visual areas such as MT have been found to project back to the inter laminar zones (Lin and Kaas 1977).

4.2.3. Non-cortical input

A number of deeper structures are likely to feed into the LGN. To date, projections have been identified from the superior colliculus (Fitzpatrick et al. 1980) and brainstem (Pasik et al. 1988). It is also reasonable to assume that other thalamic structures (such as the Accessory Optic System (Casagrande and Norton 1991) play a large part in LGN operation.

4.2.4. LGN Output

LGN output in primates is almost exclusively to layer 4 of the striate cortex. Parvo-cellular axons project to layer 4Ca, magno-cellular to layer 4Cb (Hubel and Wiesel 1977). There is also evidence that the smaller cells have projections to layers 1 and 3 of V1 (Casagrande and DeBruyn 1982). In the cat, although as yet not in the primate, projections have been found from the LGN to higher cortical areas (Sherman 1985). Rodman et al. (1989) show that the freezing of monkey V1 has little effect on the function of higher cortical visual area MT, indicating that the primate physiology may not be so different.

4.2.5. LGN Function

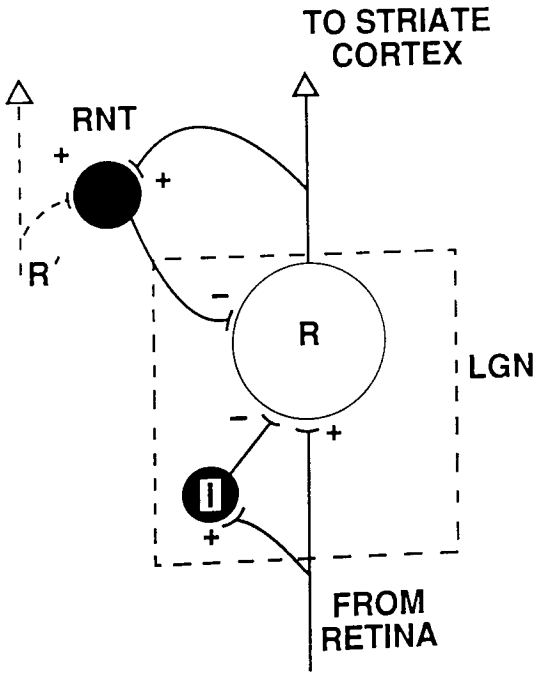

Figure 4.11. A proposed LGN circuit (from Casagrande and Norton 1991), highlighting the connections between LGN relay cells (R) , feedforward interneurones (I), and feedback cells in the reticular nucleus of the thalamus which in turn is influenced by the activity of other relay cells (R').

The model proposed by Koch (1985) demonstrates the neural circuitry of feedforward and feedback inhibitory structures which comprise the LGN (Figure 4.11). Such circuitry provides the basis for tuning of function as well as selective enhancement or suppression of visual information (Sherman and Koch 1986). The LGN's regulatory or gating role is possibly at reflected at both a global and local level. Globally, it is thought to be involved in regulating the input to the visual cortex dependent on the importance of visual information, and the animal's state of arousal (Francesconi et al. 1988). Locally, the strong retinotopic projection from cortex to LGN provide the basis for very precise regulation of visual information. Sherman and Koch (1986) propose a differential regulation of X and Y cells depending on the animals visual needs. Valera and Singer (1987) showed that the responsiveness of LGN cells to a drifting grating could be inhibited by the stimulation of the non dominant eye with another drifting grating. This inhibition was most severe when the two gratings differed in orientation, that is, when the images were in binocular rivalry. Removal of the visual cortex was found to abolish such effects.

Spatially

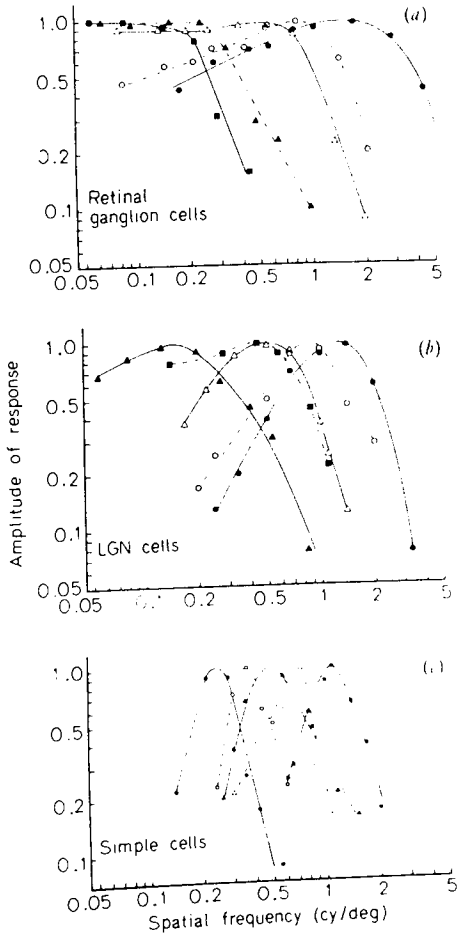

Figure 4.12. Responses of cat retinal ganglion (a), LGN (b) and simple striate cortical cells (c) to grating stimuli (20% contrast). In (a) and (b) the velocity of the grating was 4Hz, in (c) it was 2Hz. from Maffei 1978.

Kaplan et al. (1987) measured the 'transmission' of the LGN by comparing the retinal input, in the form of an extracellular postsynaptic or S-potential, with the LGN action potential output to V1. The LGN was found to exhibit a reduced contrast gain to stimuli with respect to its retinal ganglion input. This loss was especially prominent al low spatial frequencies. This observation is reflected in the work of Maffei (1978) who demonstrates increasing spatial tuning as one passes from the retina along the geniculo-striate pathway (see Figure 4.12).

Temporally

It is has been observed (Cleland et al. 1971) that LGN cells exhibit more phasic behaviour than their retinal ganglion inputs. This is consistent with the behaviour of a unit that removes low level information, responding preferentially to changes in the visual scene. Interestingly, Mastronarde (1988) demonstrated that some cat LGN cells show a temporal lag in their response. This provides the striate cortex with phase shifted visual information. The utility of such cells has yet to be demonstrated, yet they could provide the basis of 'binding' (Milner 1974; Eckhorn et al. 1988), reinforcing feedback from higher visual areas to V1.

- The LGN projects almost exclusively to the striate cortex in primates and therefore deals with visual information. The dominant LGN input is however not from the retina but from the visual cortex. Such a structure suggests that the LGN has a modulatory or control role, probably concerned with early mechanisms of visual attention and possibly underlying the management of neural image processing.

4.3. Visual Cortex

The visual cortex is that region of cortex which deals exclusively with the processing of visual information. This cortical region has been found to consist of a number of areas, each area maintaining an individual representation of the contra-lateral half visual field. The main stream of visual information arrives from the LGN at the primary visual cortex or area V1 (figure 4.13a). Area V1 is located on the occipital pole of the primate brain, in the human, it extends down the calcarine fissure (Figure 4.14). The primary visual cortex is bounded by area V2, which in turn borders on area V3 , and so on as the visual cortex extends into the parietal and temporal lobes (figure 4.13b).

A number of visual areas can be distinguished using anatomical clues from mylo-and cyto-archictectural structure of the cortex. For example, V1 has clearly layered structure (figure 4.14), whereas the motion sensitive area (MT or V5) lies in the lateral occipital gyri and can be distinguished by its heavily mylenated projections. Often callosal connections, which link hemispheric representations of the vertical meridian, are good indicators of area boundaries (Zeki 1977). Clarke and Miklossy (1990) attempt to reconcile the human cortical architecture with the visual areas identified in the macaque (Figure 4.15). Figure 4.15(a) shows how the labelling of human visual areas is largely based on callosal connectivity patterns and tentative analogies with the macaque.

The following sections outline the functional properties of the dominant visual areas in the primate cortex.

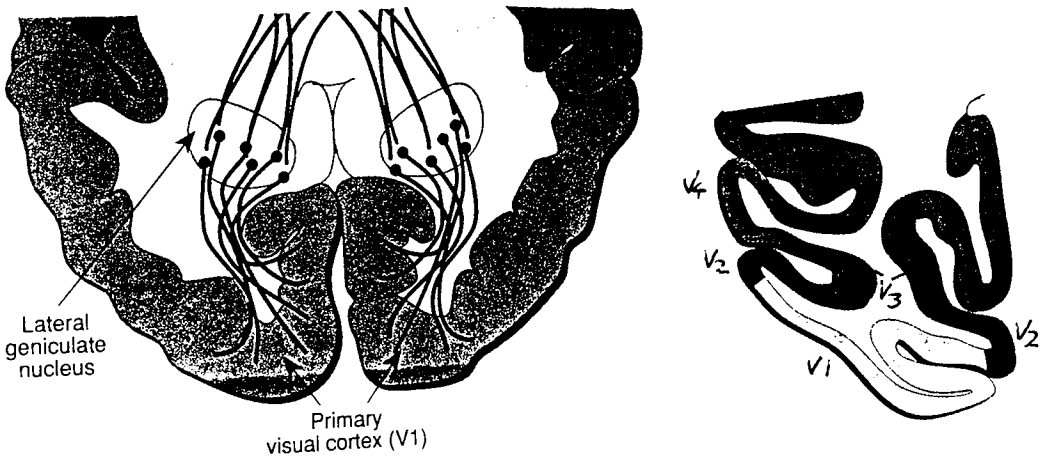

Figure 4.13. A schematic of the macaque visual cortex showing the concentric arrangement of visual areas. In the human, V1 is skewed more medially extending from the occipital poles down the calcarine fissure. redrawn from Davidoff and Concar (1993).

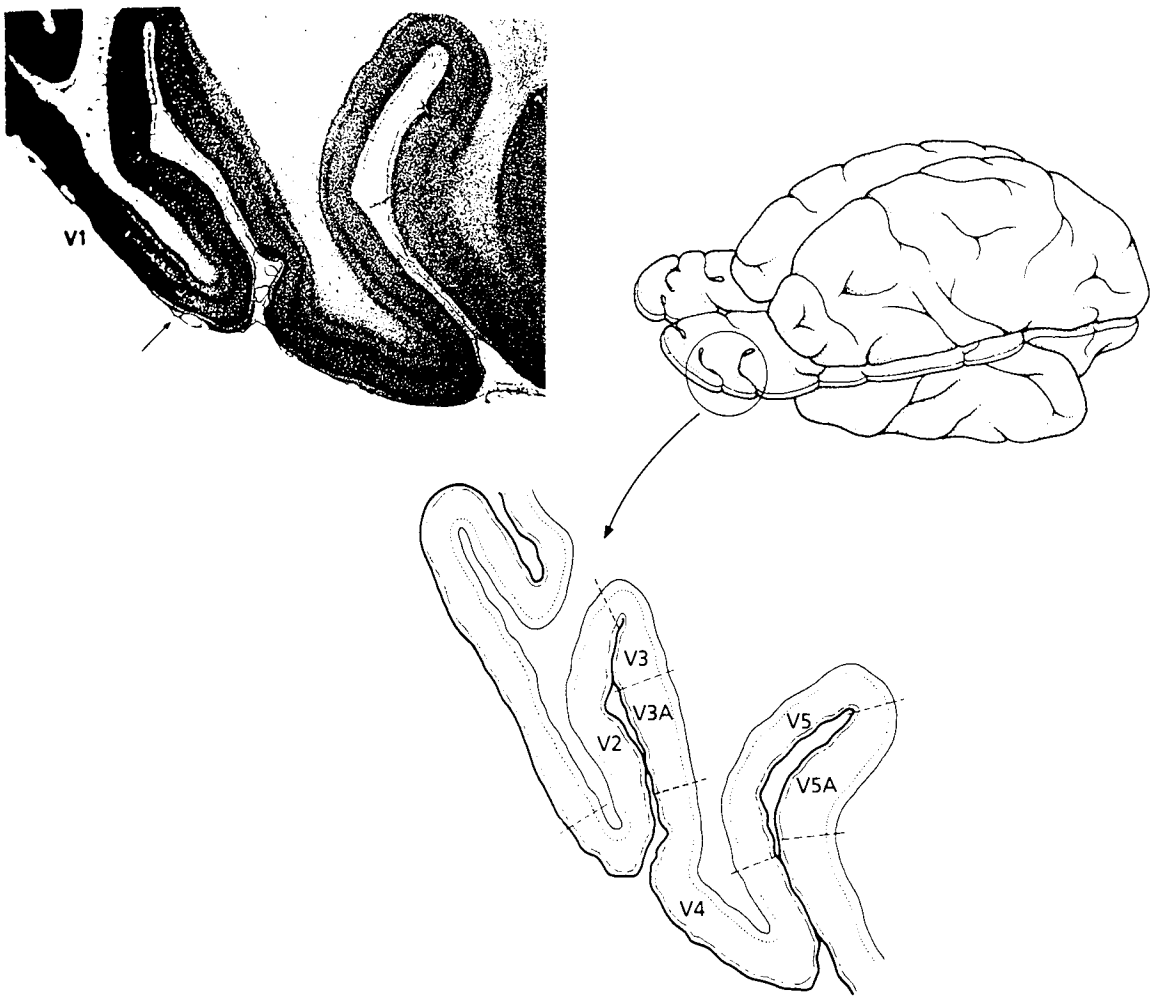

Figure 4.14. Areas V1-V5 in the macaque visual cortex. The arrow in a) shows the change in cytoarchitecture at the V1-V2 boundary. from Zeki (1993).

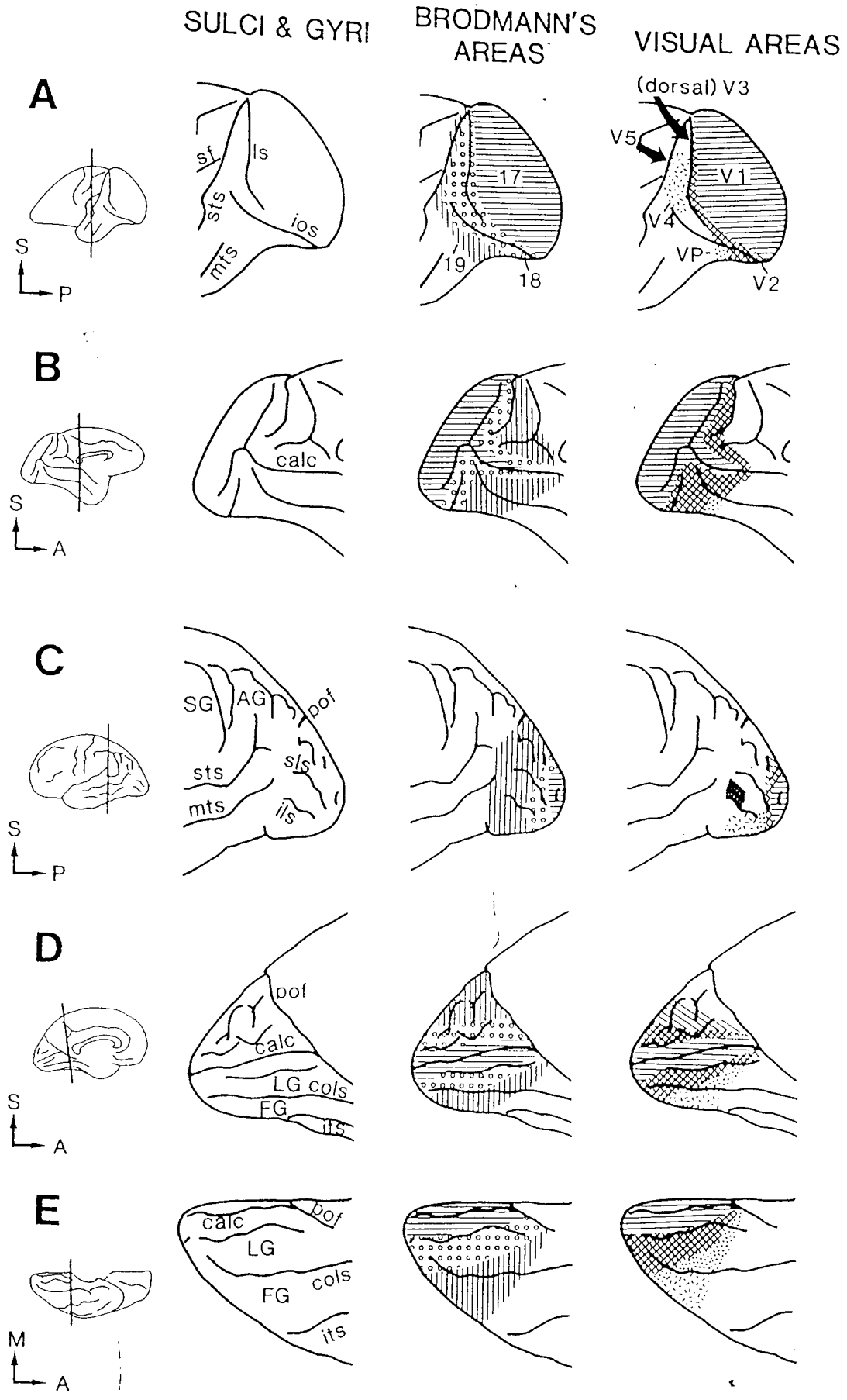

Figure 4.15. Comparison of macaque (A,B) and human (C,D,E) visual cortex and corresponding putative visual areas (from Clarke and Miklossy 1990). The authors note that although all boundaries, with the exception of V1/V2, are inferred, the presumed location of area V4 is especially approximate

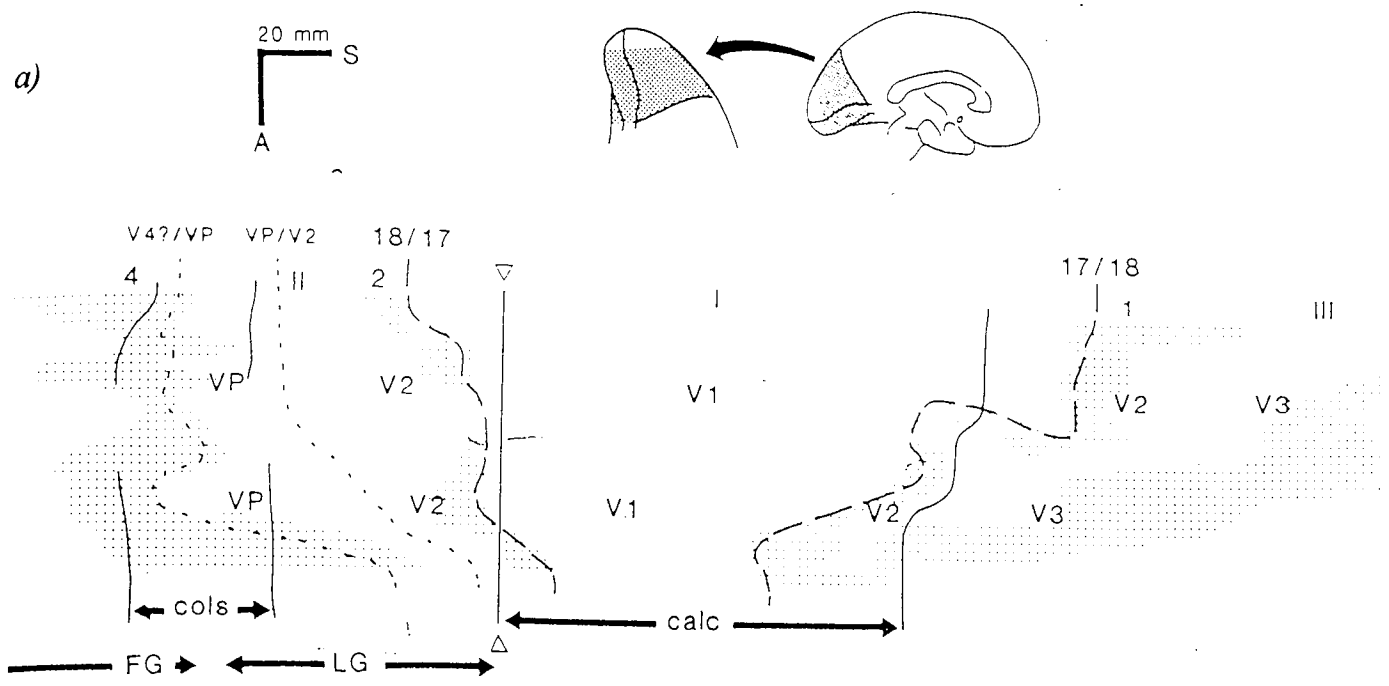

Figure 4.16. Flat reconstruction a) and 3D view b) of left occipital lobe, with callosal connections (dots) and putative visual areas (redrawn from Clarke and Miklossy 1990). Note the tapering away of visual areas as one moves more anteriorly.

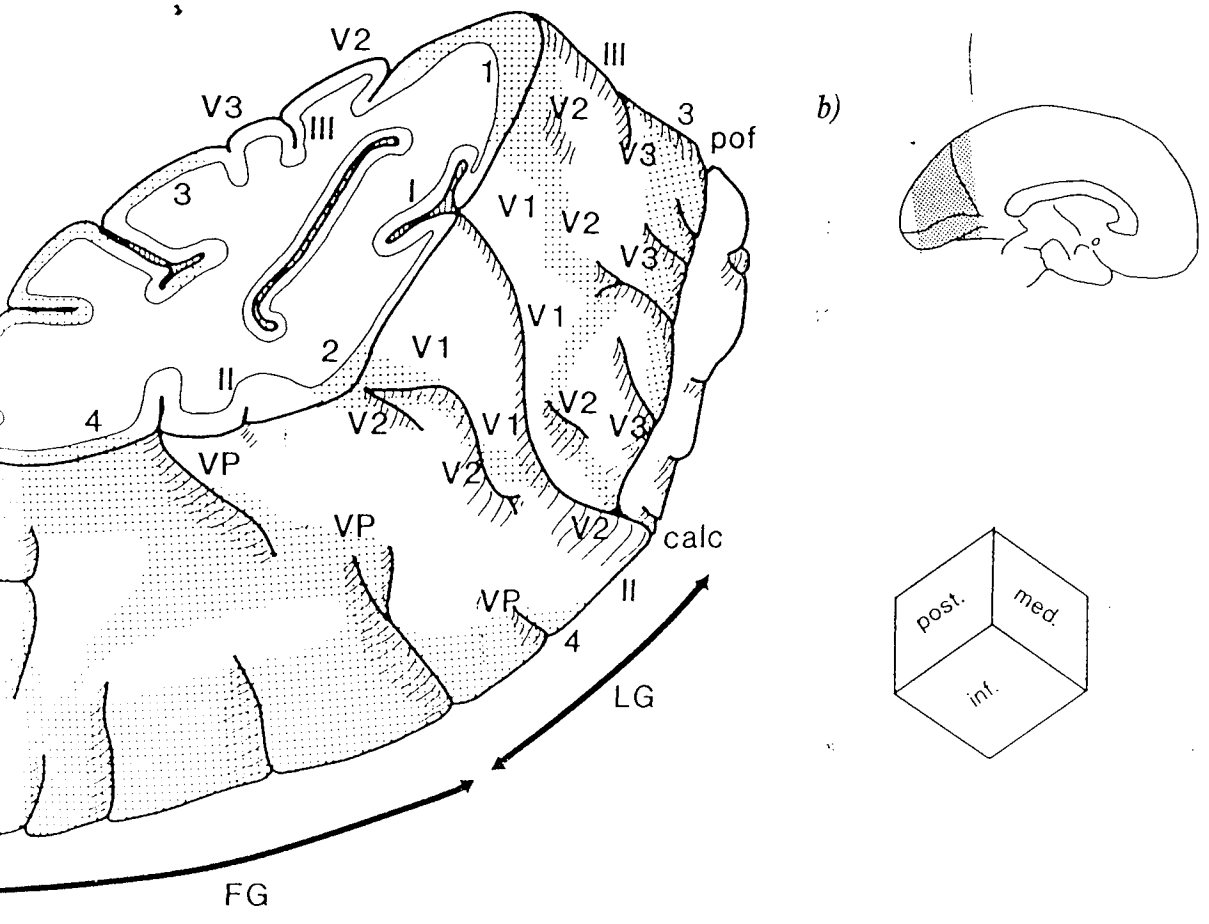

Organisation

4.3.1. Primary visual cortex (V1)

The visual cortex receives its main input from the lateral geniculate nucleus. LGN fibres project to one of the several distinct layers in V1. Area V1 is commonly thought to perform some basic analysis of the retinal image and then dispatch this information to higher visual areas (Zeki 1993). Superficial examination of V1 shows it to consist of a number of layers..

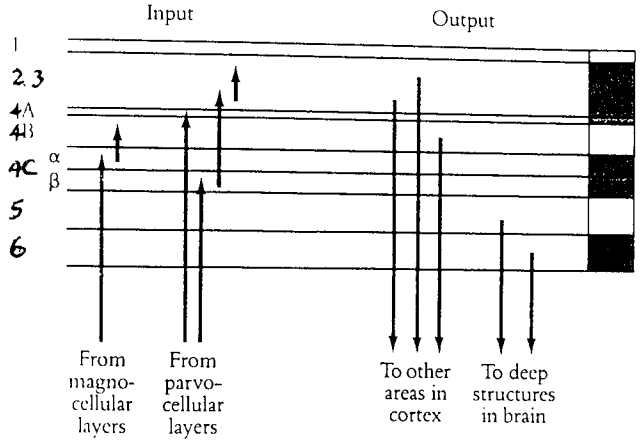

Figure 4.17. Schematic indicating the main input and output paths to the layers of V1. (from Hubel 1987).

The Layers of V1

Figure 4.17 shows classification of V1 layers according to cell structure and connectivity. Layer 4C receives input from the LGN, and is therefore the layer with most similar functional properties. Axons projecting from the magno-cellular layers of the LGN terminate in 4Cα, those from the parvo-cellular layers in 4Cβ. Tootell (1988) used chemical uptake techniques to show that low contrast visual stimuli produced activity in layer 4Cα, whereas chromatic stimulation evoked activity in layer 4Cβ. The strict eye preference shown in the layered LGN is maintained in layer 4C. Hubel and Wiesel (1977) show 'occular dominance columns' (about 0.5mm in width) running perpendicular to the cortical surface. The cells in these columns respond preferentially to input from either the left of right eye (Figure 4.18). Occular dominance is maintained in all layers of V1 although not as strongly as in 4C where strictly monocular cells can be found.

Layer 4C sends no fibres out of the cortex, but projects vertically: 4Cα to layer 4B and 4Cβ to layers 2 and 3. Movement away from layer 4C shows more sophisticated receptive field structures beginning to develop. Hubel and Wiesel (1977) divided the cells which they recorded from into two main classes : *simple*, found mostly in the region of layer 4, and *complex*, dominating the other layers. Both groups of cells showed a change in firing rate dependent on the orientation of a stimulus bar. Moving a micro-electrode perpendicular to both the cortical surface and to the occular dominance columns, Hubel and Wiesel (1977) found this cell orientation preference to be columnar in organisation. Within the movement of approximately 0.5mm, a full cycle of cell orientation preferences were recorded (Figure 4.18).

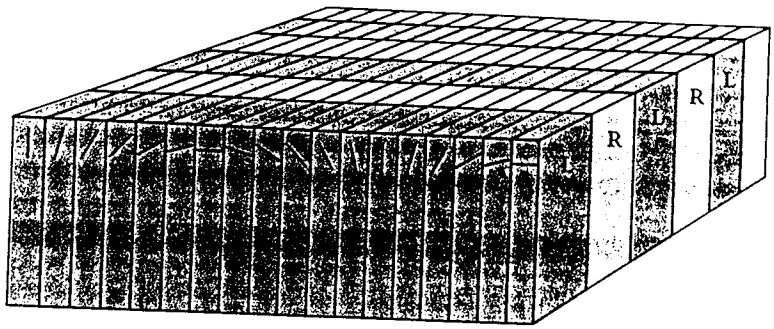

Figure 4.18. The schematic shows the division of V1 into orientation and ocular dominance columns. from Hubel (1987).

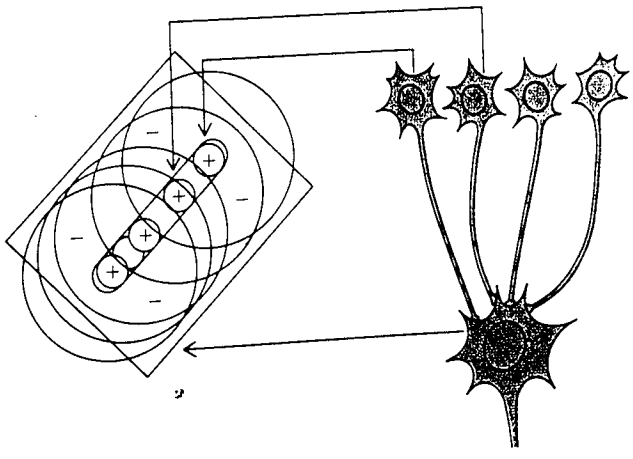

Figure 4.19. Hubel (1987) postulates how a simple cell could be created from retinal ganglion cell inputs.

Figure 4.19 shows how the behaviour of a simple cell could be accounted for in terms of a combination of concentric retinal ganglion cell responses. In turn, complex cells were thought to receive input from combinations of simple cells. A simple cell responded well to a bar at a particular fixed position and orientation, whereas a complex cell was still orientation specific yet less dependent on the position of the bar. Some complex cells - termed hypercomplex- were also found to show respond preferentially to factors such as stimulus bar length, and the direction of bar movement. Not surprisingly, complex cells have been found to exhibit non-linear spatial summation properties (De Valois et al. 1982).

Chromatic properties of V1

By staining V1 preparations with cyto-chrome oxidase, Wong-Riley (1979) revealed 'blob' like patches in layers 2 and 3. The pathway to the blobs is mediated by the P layers of the LGN which project to layers 2 and 3 via 4Cβ. Livingstone and Hubel (1984) revealed that these regions contained many cells with wavelength opponent receptive fields, low spatial resolution and poor or absent orientation tuning. Within the blobs 50% of the neurons were shown to have wavelength double opponent receptive fields (Figure 4.5, E,F). Double opponent cells provide tuning for chromatic contrast, being most sensitive to stimuli consisting of wavelength not luminance contours, e.g. a green spot on a red background. Thorell et al. (1983) recorded from a population sample of V1 cells in the macaque and found that the majority in some way responsive to purely chromatically modulated stimuli as well as luminance modulated stimuli. That the results differ from those of Hubel and Livingstone is due mainly to disparate classification systems. For example, Thorell's complex cells were found to fire in response to isoluminant bars irrespective of the spectral content of the bars and the surround. The cells were thus colour sensitive but not colour selective, differing from the double opponent cells reported by Hubel and Livingstone.

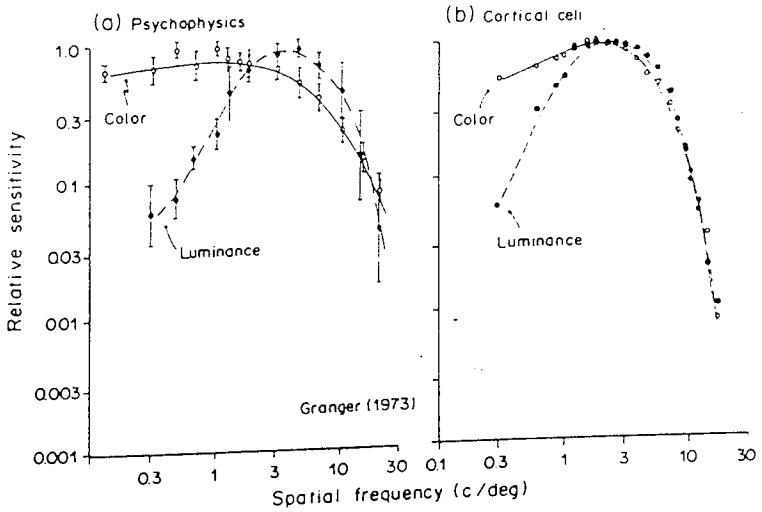

Figure 4.20. A comparison of the summated functional tuning of a population of 108 monkey V1 cortical cells (right) with data from human visual psychophysics. (from Thorell et al. 1983).

The study of Thorell et al. (1985) concluded that most V1 neurons respond in a spatially bandlimited fashion to both chromatic and luminance stimuli. A summation of such activity was (see Figure 4.20) thought to provide the basis of the psychophysical response contrast sensitivity function to luminance and chromatic grating modulation (Mullen 1985).

Outputs of V1

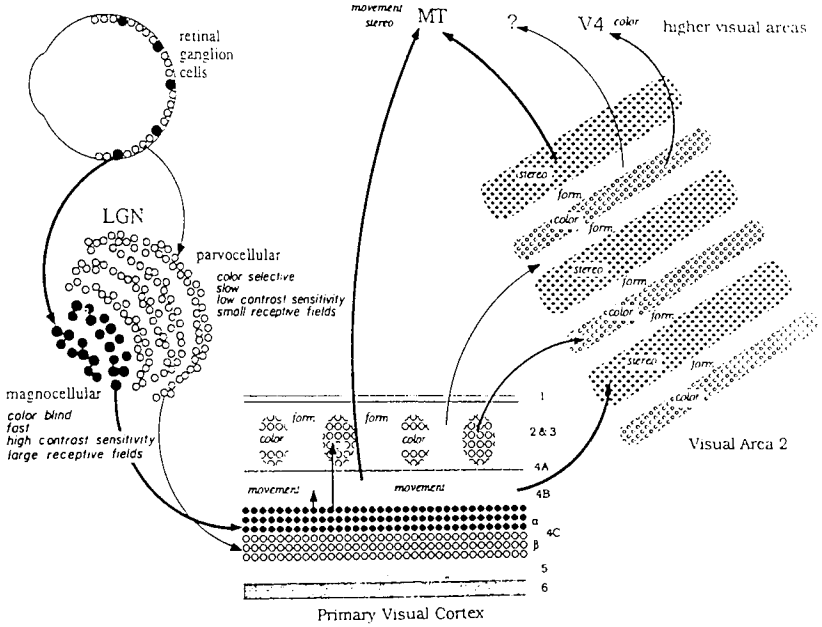

Figure 4.21. The magno and parvo streams project via V1 to higher visual areas. from Livingstone and Hubel (1987).

Figure 4.21 shows the connections from the LGN to V1 and then on to higher visual areas as postulated by Hubel and Livingstone (1989). Note the projections of layers 5 and 6 back to deeper structures such as the superior colliculus and thalamus. The efferent fibres from layers 2,3 and 4β project mainly to other cortical visual areas which are examined below.

4.3.2. V2

In the primate visual cortex, V2 surrounds V1. It is retinotopically organised (Zeki 1969), and contains functionally and anatomically distinct cell populations. Staining with cytochrome oxidase reveals anatomical division into three regions: thin-stripes, thick stripes and inter-stripes. The thin stripes receive inputs from the blobs in layers 2 and 3 of V1 and deal with the processing of chromatic information (Livingstone and Hubel 1984). The inter-stripes receive projections from the inter-blobs of V1 and are thus more form and orientation specific (Livingstone and Hubel 1984). The thick stripes of V2 receive inputs from layer 4B of V1 and project to V3 and V5 (Zeki 1993). The thin stripes and inter-stripes in turn project to area V4 (Zeki and Shipp 1989).

The cells within the thin stripes have receptive fields with similar wavelength and spot size specificity to those of the V1 blobs. However, the receptive fields of such cells

are larger than those in V1 (Zeki and Ship 1989). That is, V2 cells seem to behave in a similar way to the complex cells in V1, extending the receptive field size but maintaining stimulus specificity. V2 receives large back-projections from V4 and V5. Such projections lead Shipp and Zeki (1989) to propose that V2 is a site of 'binding'. That is the combination of the information from, the functionally tuned but spatially poorly specific, higher visual areas and, the functionally broad yet topographically well defined, V1.

4.3.3. V3

V3 receives projections from the inter-stripes of V2 and the interblobs of V1. The area contains predominantly orientation selective cells which seem to be largely wavelength unselective (Zeki 1978). Many of the cells in this area exhibit strong disparity tuning (Zeki 1978, Felleman and Van Essen 1987). V3 is thought to play a critical role in depth/form perception, and due to its relation to the M-pathway, Zeki (1993) suggests that the area is concerned with the processing of dynamic form.

4.3.4. V4

V4 maintains connections with the thin-stripes and inter-stripes of V2 and is thought to be an extension of the P- pathway responsible for colour discrimination. Zeki (1983) contends that V4 provides the *first* site of colour constancy, that is, cells are able to make discriminations on the colour of a surface independent of the illuminant (see however Dow 1993 for discussion). Desimone et al. (1985), found that cells in V4 were just as spatially selective (to bar length, width, motion, orientation etc.) as those in V1, although the receptive field sizes were significantly greater (at 1° eccentricity 16 times larger, at 3° about 36 times larger). That is, V4 cells were found to behave like 'big brothers' of the complex cells in V1. Desimone et al. (1985) also report cells with large suppressive receptive fields, extending by as much as 16° into the ipsilateral visual field. The cell's response to a particular wavelength of light could be almost totally abolished by an identical stimulus within the suppressive field. Similar form specific properties were noted, that is, the response to a grating could be diminished by increasing its size. Guld et al. (1989) found cells in V4 which they named 'filter cells'. These cells had homogenous receptive fields over a quadrant of the visual field, and at low brightness levels were able to summate spectral energy over a particular bandwidth. Such results hint at neural substrates of Land's retinex algorithm (Land 1974) which attempts to describe colour constancy. Desimone et al. (1985) suggest that such sensitivity to changes in colour and form from the background may help in figure/ground separation. Attentionally selective cells have been reported in V4 (Moran and Desimone 1985). Such cells were found to respond to a stimulus only if the stimulus was relevant to the monkey's designated task.

4.3.5. V5

V5 receives its main input from V1 and V2. V5 neurons are thought to be especially highly tuned to moving stimuli. It has been estimated that 90% of V5 cells are selective to a specific direction of motion (Zeki 1974).

4.3.6. Other cortical areas

Lesions of the inferior temporal cortex cause deficits in visual discrimination but not visuo-spatial tasks (Mishkin et al. 1983). Robinson et al. (1978) found neurons highly sensitive to stimulus shape or colour. This region would seem to receive a dominant proportion of its input from V4, and is postulated (Desimone et al. 1985) to be responsible for shape/ surface analysis.

The parietal lobe receives a large input from V3. The region is thought to contain an internal topographic map of the surroundings. Lesions in this area cause compromised reaching ability and positional judgement (Mishkin et al. 1983).

4.4. Other sub-cortical structures

There exist at least 20 subcortical structures which form reciprocal connections to the visual cortex, little however is known about what these structures contribute to visual processing. These structures are the evolutionary substrate of vision, it is therefore reasonable to assume that they contain the key to its understanding. This section shall deal with a subset of the more studied of these structures.

4.4.1. The superior colliculus

The superior colliculus is a large protuberance on the midbrain consisting of a number of distinct cellular laminae. Although at least seven laminae have been identified, they are most conveniently grouped as being either superficial (layers I-III) or deep (layers IV-VII). The connections between the superficial and deep layers are sparse. Experiments (Ograsawara et al. 1984) show that compromising the superficial layers has little effect on the function of deeper cells. Consequently, the superficial and deep layers are often treated as functionally distinct.

Inputs

The superficial layers receive more direct and abundant visual input than the deeper layers. In the cat, direct retinal input in the form of predominantly W and some Y type cells (Hoffman 1973). There is also a large indirect Y type input via cortical areas 17 and 18 (Toyama et al. 1969). In general, superficial cells are retinotopically mapped, possess relatively large receptive fields, are binocular, sensitive to slow movement and are directionally selective (Stein and Meredith 1989). Freezing of the striate cortex (Ograsawara et al. 1984) annihilates orientation preference, binocularity and directional selectivity indicating many of the superficial cell properties derive from the cortical input.

Like the cells in the superficial layers, the deeper layer cells exhibit systematic retinotopic correspondence. The receptive fields of these cells are however larger and the corresponding map therefore coarser (Meredith and Stein 1988). The deep layer cells receive direct although sparse retinal input from Y type ganglion cells (Berson and McIlwain 1982). Much of the activity in the deeper laminae seems to arise from indirect visual input , perhaps from extra-striate areas. Experiments by Ograsawara et al. (1986) revealed that in the cat, cooling of the cortical visual area located in the posterior supra-sylvian fissure (similar to monkey V5) had a profound effect on the performance of some deep layer cells.

Outputs of the superior colliculus

Most efferent fibres of the superior colliculus emerge from deeper layers and seem to be linked to the motor signals that affect the movement of eyes and head towards a stimulus (Harris 1980). It has been observed (Schiller and Stryker 1972) , that having assessed a deeper cell's receptive field, direct electrical stimulation of this area results in an eye movement to this area of the visual scene. Besides such retinotopically guided properties, cells have been found which are 'spatiotopic' (Mays and Sparks 1980). That is, even if the eye is artificially displaced prior to stimulation, the saccade reaches the correct area of the visual scene. Flash evoked response studies in man (Harding and Wright 1986) have suggested that, besides the geniculo-cortical route, a tectal pathway also mediates the flow of visual (M type) information from retina to visual cortex.

Function

The superior colliculus is thought to play a large part in guiding eye movements and visual attention. Unilateral ablation of the superior colliculus causes severe contralateral hemifield neglect (Sprague and Meikle 1965). The colliculi, connected via the intertectal commissure, seem to have mutually inhibitory effect on one another. Studies by Sprague (1966) on the cat found that unilateral ablation of visual cortex, which results in contralateral cortical blindness, could be largely compensated for by removal of the ipsilateral superior colliculus.

Chapter 5.

Whole system function and architecture

The heading of this chapter derives from figure 1.1, it outlines what can be inferred about human visual processing by the use of external objective (e.g. PET, EEG) and subjective (e.g. psychophysical) measures of performance.

Firstly, the properties of chromatic and luminance mechanisms inferred from behavioural studies are discussed and visual stimuli designed to isolate these mechanisms outlined.

Secondly, Visually Evoked Potential (VEP) measures are discussed which seem to reflect the activity of neural elements of similar function to those identified in the primate. The section goes on to examine VEPs evoked by stimuli specific to the psychophysical chromatic and luminance mechanisms and suggests the cortical areas involved.

Finally, the evidence for the existence of a cortical area specialised for colour vision is examined. The existence of such an area is confirmed by the exclusive loss of colour vision experienced by brain damaged patients and PET functional imaging studies of healthy subjects.

5.1. Psychophysics of colour vision

It is helpful to adopt the psychophysical concept that the visual system is devised of of two independent pathways : a luminance and a chromatic pathway (Kelly 1974; Mullen 1985; Banks and Allen 1993).

Typically, stimuli that vary only in intensity and not wavelength are chosen to excite preferentially the luminance pathway, whereas stimuli which vary in wavelength but not intensity (termed 'isoluminant') are used to excite the chromatic pathway. One such stimulus, which is also highly spatial frequency specific, is derived from the superposition of two sinusoidal gratings. Red and green (or blue and yellow) bars sinusoidally modulated in intensity at a specific spatial frequency are superimposed by some optical apparatus. Ideally the peak amplitude red and green stimulus wavelengths are chosen so as to overlie the LWS and MWS cone action spectra (Mullen 1985).

Adding the gratings in same spatial phase produces a yellow-black grating such that both LWS and MWS cones produce the same output for a particular part of the stimulus. Adding in anti-phase should ideally produce a red-green grating where each stimulus point preferentially stimulates either LWS or MWS cones. In the first case, the resultant grating is modulated purely in luminance, in the second purely in wavelength. In both cases the screen has the same average luminance.

Mullen (1985) used two gratings superimposed in spatial anti-phase. R and G were defined as the DC luminance levels of the two sinusoids both at the same fixed contrast.

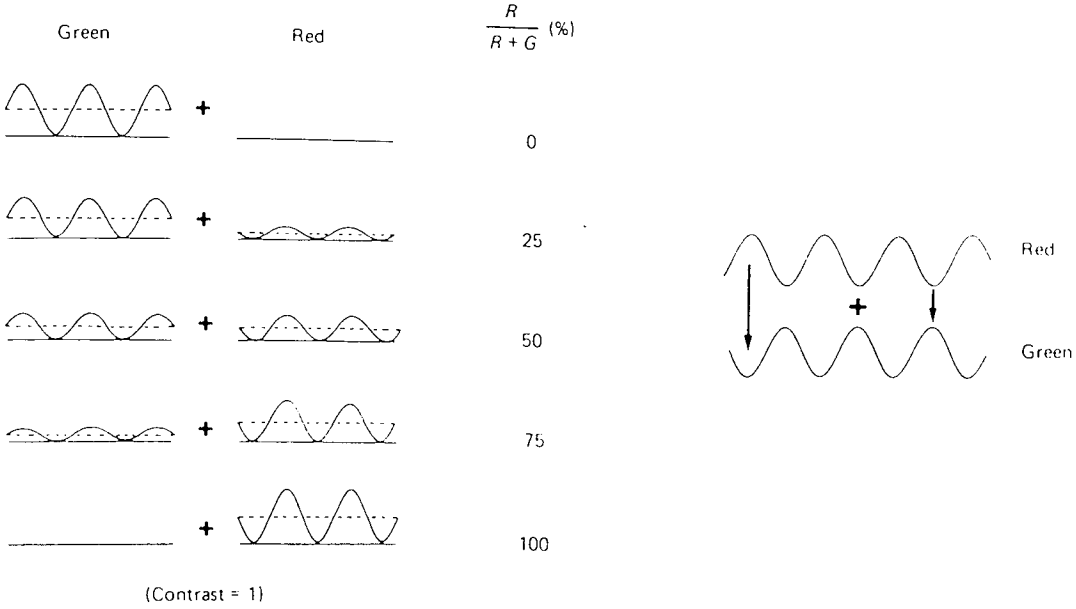

Figure 5.1. Colour contrast is used to alter the balance of the red and green sinusoids within the stimulus whilst keeping the mean screen luminance constant. from Mullen (1985).

Whilst keeping the mean luminance (R+G) constant, the relative intensity of the two sinusoids (R /(R+G)) was varied, Mullen termed this quantity *colour contrast*. By altering colour contrast (see Figure 5.1), the balance of luminance to chromatic modulation in the stimulus is changed. At 100% and 0% the stimulus appears either red-black or green-black and is dominated by luminance modulation. At 50% the stimulus is red-green, without luminance but with strong chromatic contour.

Using these well defined stimuli, Mullen (1985) set out to isolate the spatial characteristics of the chromatic and luminance pathways. Contrast sensitivity curves for gratings of various spatial frequencies were produced as the colour contrast was varied (Figure 5.2a). The sensitivity at isoluminance was taken to be due to a chromatic mechanism; at 0 and 100% due to a luminance mechanism. The chromatic mechanism was found to be predominantly spatially low-pass, beginning to fall off at around 1cpd. The luminance mechanism was found to have a bandpass characteristic, peaking at around 0.8-4cpd (Figure 5. 2b).

The temporal characteristics of the two pathways were reported in experiments by Wisowaty (1981) and verified by an alternative approach (using impulse response functions) of Burr and Morrone (1993). The results (Figure 5. 3) show a low pass chromatic mechanism thresholding at around 16-20Hz and a bandpass luminance mechanism, peaking at around 8Hz, and thresholding at around 30-40Hz.

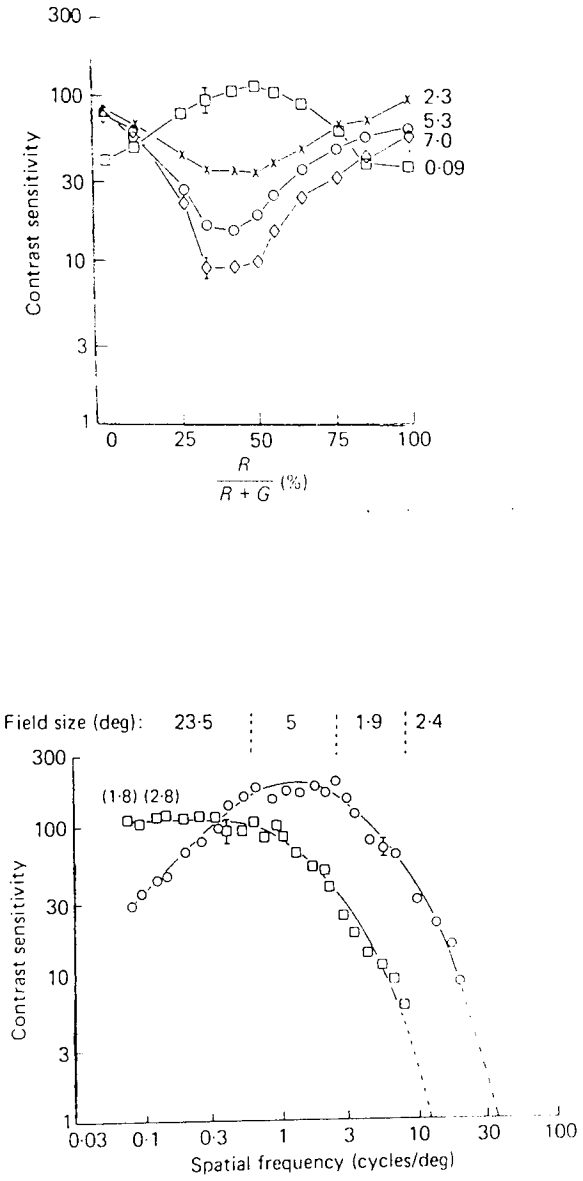

Figure 5.2. a) At each spatial frequency (represented by different symbols) , Mullen (1985) varied colour contrast, and measured contrast sensitivity. Contrast sensitivities at 0 and 100% colour contrast were attributed to a luminance mechanism. The largest deviation in contrast sensitivity occurred at around isoluminance, and was attributed to the operation of a chromatic mechanism.

In b) Plotting the results obtained at various spatial frequencies reveals the chromatic mechanism to be spatially low-pass and the luminance mechanism to be spatially band-pass.

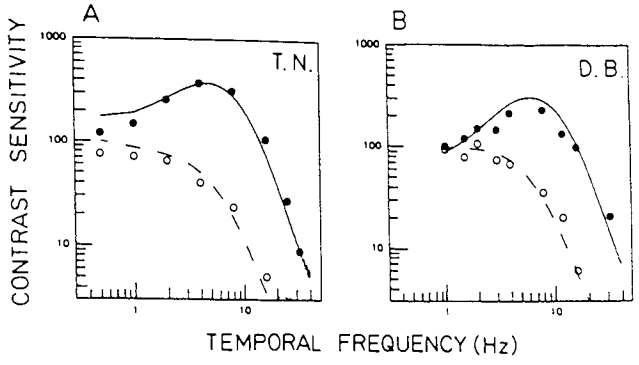

Figure 5.3. Contrast sensitivity for detection of chromatic (open circles) and luminance (filled circles) gratings as counterphasing frequency is varied. from Burr and Morrone (1993).

5.2. Aside : Chromatic aberration

All experiments involving colour vision are complicated by the fact that different wavelengths of light are refracted by the eye by different amounts. The effect is known as chromatic aberration. Typically, red and green light exhibit a chromatic difference in focus, or longitudinal chromatic aberration, of 0.5D (Figure 5.4). Chromatic difference in magnification of the sinusoids, or transverse chromatic aberration can also have significant experimental consequence (Faubert et al. 1994). At low spatial frequencies (<1cpd) , the effects of chromatic aberration are relatively benign (Green et al. 1980; Flitcroft 1989). However, at all spatial frequencies, chromatic aberration will result in the introduction of *some* luminance contour into a physically isoluminant grating.

The effects of chromatic aberration can generally be eliminated by good experimental design. For example, Regan (1973) used separate monitors to create each of the red and green gratings. Simply viewing the monitors at different distances was sufficient to largely null the effects of chromatic aberration.

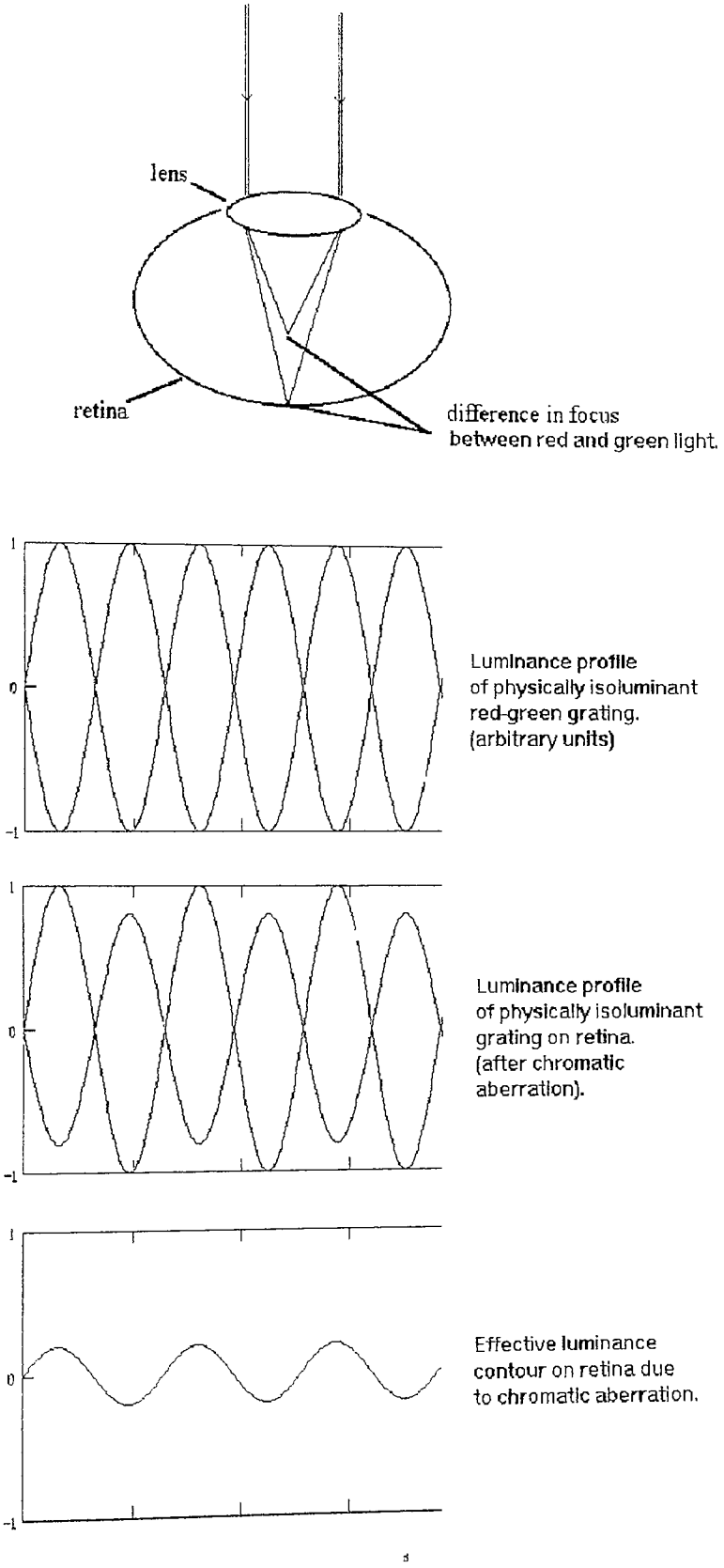

Figure 5.4. Longitudinal chromatic aberration introduces a difference in focus between red and green stimuli of approximately 0.5 Dioptres. The blurring of one of the sinusoids introduces luminance contour into the retinal image of a physically isoluminant grating (the x axis indicates distance along the retina).

5.3. VEP data

The scalp VEP is a measure of coherent activity of large cell populations. This section begins by showing how low level ganglion cell projections to the visual cortex can be picked up in the VEP. Refining the stimulus, using gratings rather than blank field stimulation, psychophysical correlates begin to appear. The progression is made from achromatic to chromatic grating stimuli where the results of VEP experiments with similar paradigms to those of Mullen's are examined. The section concludes with a brief summary which outlines the consensus opinion concerning the origin of the VEP correlates to the chromatic and achromatic mechanisms.

5.3.1. Uniform field stimulation

Regan (1970) showed that the amplitude of the second harmonic of the human VEP to monochromatic flicker corresponded well to the psychophysical human spectral sensitivity or V_λ curve (Figure 5. 5a). Based on results of Lee and Martin (1989) one would expect the origin of such response to be a projection of the magno-cellular pathway.

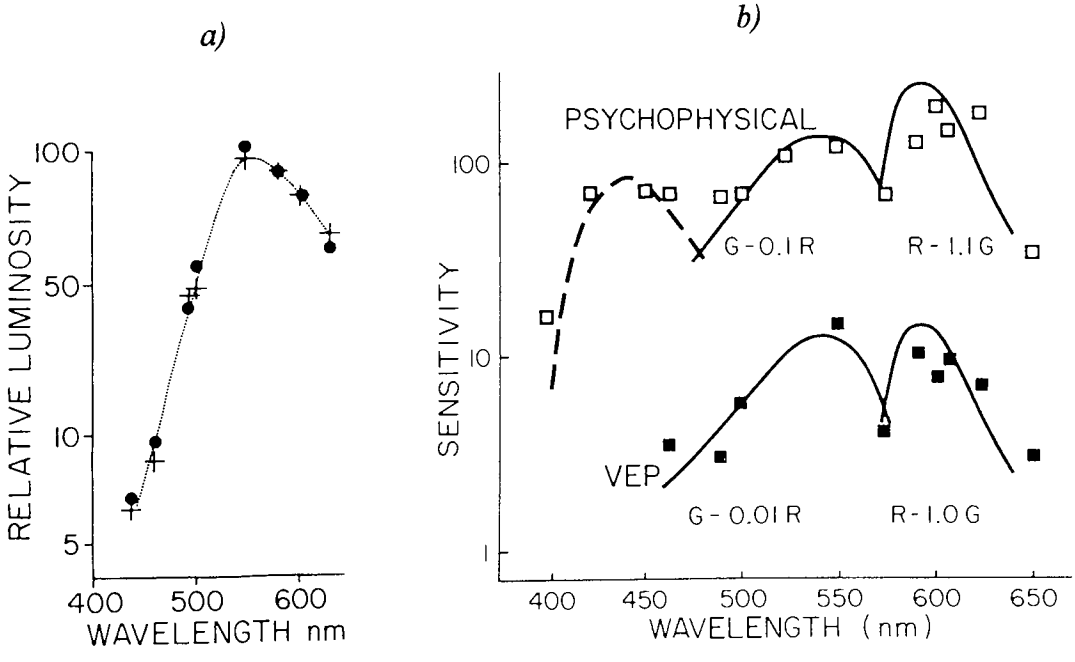

Figure 5.5. a) The correlation between the relative luminous efficiency curves assessed with psychophysical (dots) and VEP (crosses) measures is clear. from Regan (1970). b) VEP sensitivity (in this case, reciprocal test flash luminance to produce 4.5uV N1-P1 component) correlates well with psychophysical data thought to relate to colour opponent mechanisms. from Zrenner (1983).

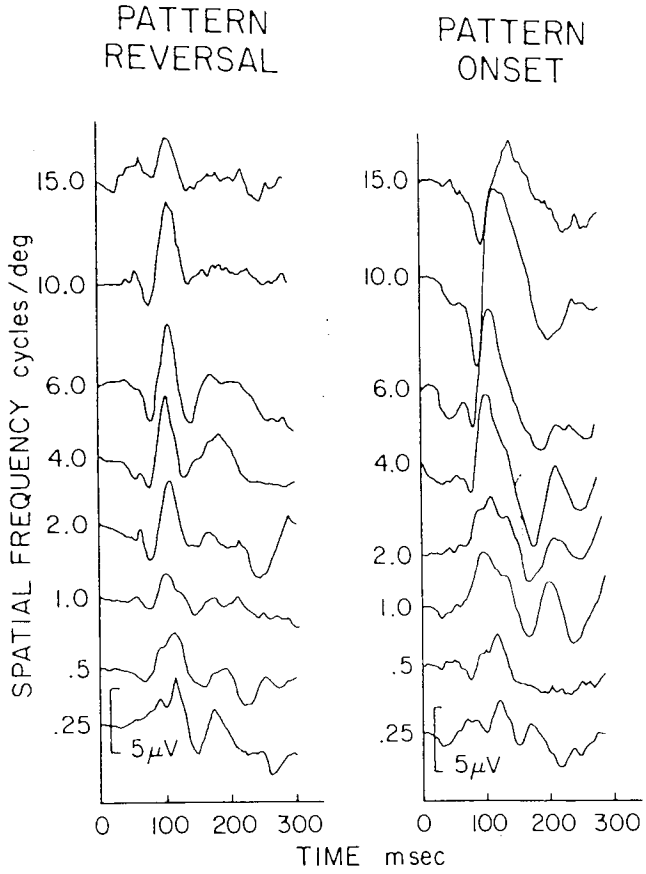

Figure 5.6. VEPs to sinusoidal grating onset and reversal (positive up). Note N1(70-100ms) -P1(90-120ms), and a later P2 (around 200ms).From Plant et al. (1983).

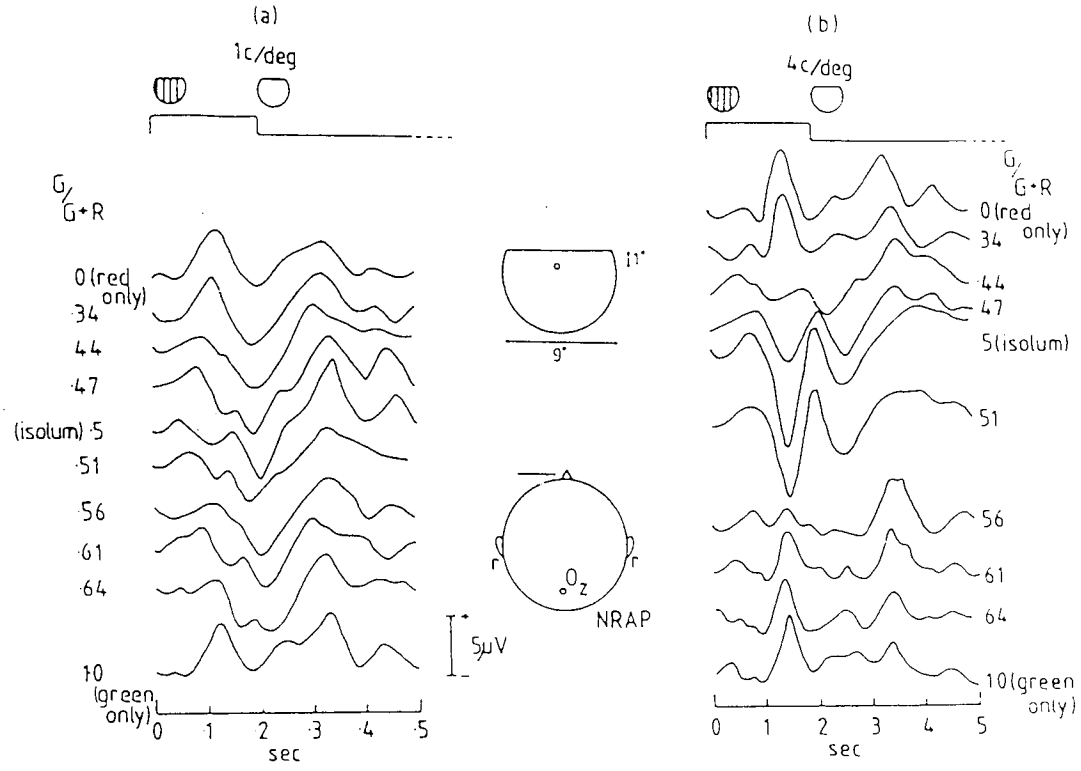

Figure 5.7. VEPs generated in response to sinusoidal grating onset for various colour contrasts at 1 and 4cpd. At 4cpd note the distinct change in waveform morphology: the 120-140ms component changes from predominantly positive to negative as isoluminance is approached. At 1cpd, however, rather than an abrupt polarity reversal, a consistent phase shift effect at isoluminance is apparent. (from Murray et al. (1987)).

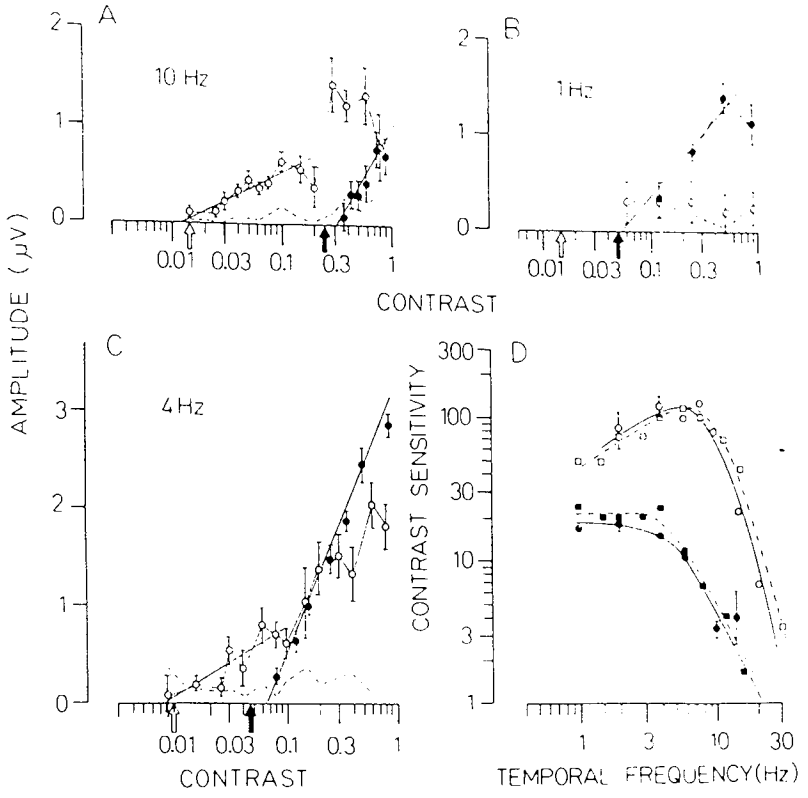

Figure 5.8. A, B and C show chromatic (solid) and luminance VEP amplitude in response to grating onset stimulation at various temporal frequencies. Note that the chromatic data is more readily fit with a single regression line, whereas the luminance data seems best described by the overlap of two functional mechanisms. D shows the high correlation between temporal frequency vs. contrast sensitivity curves of extrapolated VEP thresholds and psychophysical data. From Fiorentini et al. (1991).

Zrenner (1983) found VEP responses (in terms of spectral sensitivity) correlated well with psychophysical data and invasive recording at the level of parvo-cellular ganglion cells (Figure 5.5b).

In order to isolate higher functional elements however, more complex stimuli are required.

5.3.2. Pattern stimulation

Much early work on the pattern VEP involved the use of high contrast checkerboard patterns. Such patterns elicit large responses with little intra-individual variation. They are therefore clinically useful in the identification of diseases which affect the visual pathway (Halliday et al. 1973, Regan 1989). Although evocative, the checkerboard stimulus is poorly spatial frequency and orientation specific. Conversely, although clinically little used, sinusoidal gratings provide stimuli with narrow band spatial frequency tuning. VEP results using sinusoidal grating stimuli are often directly comparable to psychophysically obtained data.

There are two standard modes of patterned stimulus presentation: onset and reversal. 'Onset' meaning that the pattern evolves from a background of the same average luminance. 'Reversal' implying that the checkerboard or grating pattern shifts in spatial phase by 180°. Pattern onset and reversal paradigms of presentation have been found to preferentially stimulate the tonic and phasic systems respectively (Kulikowski 1979).

Grating onset stimulation

VEPs to the onset of sinusoidal gratings (Plant et al. 1983; Kulikowski and Leisman 1982; Fiorentini et al. 1991) consist of two major peaks N1 (70-100ms) and P1(90-120ms). In some subjects a later N2-P2 component is visible at around 200ms. Component latency has been found to be highly dependent on stimulus contrast and spatial frequency (Parker and Salzen 1977; Plant et al. 1983). The underlying mechanisms which give rise to the pattern onset VEP are unclear. At low spatial frequencies, Kulikowski (1989) found the overall response waveform changed little whether the stimulus was onset or reversing. Kulikowski (1989) attributed the response to the projection of magno-cellular pathway, since any tonic components would be presumably degraded by the reversal paradigm. However, at *all* spatial frequencies tested, chromatically modulated stimuli produced differing responses to onset and reversal paradigms. The results of Kulikowski (1989) seem to indicate that low spatial frequency gratings (<=1cpd) elicit little response from the parvo-cellular system *unless* they are chromatically modulated.

Plant et al. (1983) report the increasing prominence of the N1 component as spatial frequency was increased. This prominent negativity at high spatial frequency (see also Drasdo 1969; Russel 1991) could be due to some fine pattern mechanism, perhaps with a parvo-cellular substrate. Kulikowski and Leisman (1983) found the appearance of the P2 component to correlate with psychophysical threshold for grating detection. Likewise, at higher spatial frequencies, this later component was shown to diminish in

the reversal paradigm (Plant et al. 1983). The P2 component therefore might also emanate from a predominantly tonic or parvo-cellular driven source.

Conversely, Parker and Salzen (1977) used reaction time measures in conjunction with VEPs, and found no evidence for exclusive activation of either phasic or a tonic mechanism. Similarly, Russel (1991) attributes the N1-P1 complex to activity of two overlapping contrast sensitive mechanisms.

Chromatic pattern onset stimulation

Murray et al. (1987) used sinusoidal grating onset of a similar stimulus to that of Mullen (1985). As the colour contrast of a grating of around 2-6cpd was altered, they reported that the 120-140ms response component underwent a "*distinct change from being predominantly negative around the isoluminant point to positive going either side of this*". Murray notes that the differences in chromatic/achromatic response morphology to be much less significant at low spatial frequencies, not correlating with Mullen's psychophysical chromatic and luminance contrast sensitivity functions. Fiorentini et al. (1991) reproduced the experiment of Murray using 1cpd plaid patterns. A VEP with positivity at 92ms and negativity at 120ms was obtained. The polarity of the responses contrasts to the N1-P1 complex found in other studies. The early component was attributed to activity of a luminance mechanism, the later component to a chromatic mechanism.

Chromatic pattern reversal stimulation

Fiorentini et al. (1991) used steady state stimulation with counterphasing plaid patterns, the amplitude of the 2nd harmonic VEP component was measured. Extrapolation of the response back to threshold corresponded well to the psychophysically observed temporal frequency characteristics of the chromatic and luminance mechanisms (Figure 5.8). It was also noted that the curve for VEP amplitude against grating contrast was smooth for chromatic stimuli yet seemed to consist of two branches for luminance stimuli. The results lead the group to conclude that a single, possibly parvo-cellular, mechanism mediates the chromatic response whereas the luminance response might consist of both parvo- and magno-cellular mechanisms. Such a conclusion is well supported by single cell studies (see retinal ganglion section).

Summary

The interpretation of results is challenging due to the wide range of stimuli used in such experiments. The consensus (Murray et al. 1985; Kulikowski 1989) is that the neural origin of the chromatic responses is the activity of opponent cells stemming from the tonic pathway along the V1/V2 border. The luminance type responses are thought to arise from activity in both tonic and phasic pathways (Fiorentini et al. 1991) also projecting to V1 and V2. Single cell studies by Thorell et al. (1985) indicate that cells in V1 alone could be responsible for the human psychophysical curves. If the neural origin of both achromatic and chromatic mechanisms is so similar, the very different morphology of the chromatic and achromatic responses is hard to explain, yet possibly

reflects the relative time courses of two streams of information. The involvement of higher visual areas in the response was ruled out in the monkey by Kulikowski and Carden (1989). They showed that the bilateral ablation of V4 resulted in no significant change in the scalp recorded evoked response to chromatic or achromatic grating onset. However, as the authors point out the VEP in the monkey has a different morphology to that in the human. Also, a large number of V1 neurons are bound to be involved in any central visual field stimulus. This portion of V1, which is predominantly radial, is likely to produce activity which dominates electrical potential measurements made on the scalp. It is not surprising therefore that the activity of the more functionally specific, hence smaller, visual areas is not evident on the VEP.

5.4. Evidence for a specific cortical colour area

Louis Verrey in 1888 was the first to report a patient suffering from cerebral hemi-achromatopsia. Achromatopsia has since been defined as *"an acquired disorder of colour perception involving all or part of the visual field, caused by focal damage to the visual association cortex or subadjacent white matter"* (Damasio 1985). Furthermore, *"Patients with achromatopsia can have intact visual acuity, spatial contrast sensitivity and stereo acuity in the colourless field"* Rizzo and Damasio (1989). The condition is often accompanied by scotoma located in the upper quadrant of the same hemifield. Lenz (1921) noted that the condition of achromatopsia correlated with lesions around the area of the fusiform gyrus. Specifically, the upper visual field scotomas ,which suggest proximity to V1, led Zeki (1991) with the aid of PET scans, to assert that human V4 is to be found on the lower limb of the fusiform gyrus.

Similarly, the condition of akinetopsia has been reported (Hess et al. 1989). Patients suffering from this condition lose motion perception and see the world as a series of still-frames. This would appear to indicate damage to an area concerned primarily with motion such as human V5.

The existence of such specific functional deficits coexisting with otherwise normal vision puts a strong case for functional localization in human visual processing. Interestingly, patients with lesions in V1, although devoid of perception within the scotoma, are often unconsciously aware of colours and motion. The phenomenon is known as 'blindsight'.

Functional imaging studies on healthy subjects using PET scans have revealed similar specialised cortical areas. Lueck et al. (1989) showed that a subject viewing a Mondrian showed an increase in activity around the lingual and fusiform gyrus, a possible site of human V4. The same subject, viewing a pattern consisting of moving random dots, showed cortical activation in a distinct area nominated as 'human V5'. In both cases, the areas V1 and possibly V2 were shown to be active. Unfortunately, present day PET scans have poor temporal and spatial resolution (figure 1.5), and it is therefore impossible to identify the sequence of activation of , or exact location of, these areas.

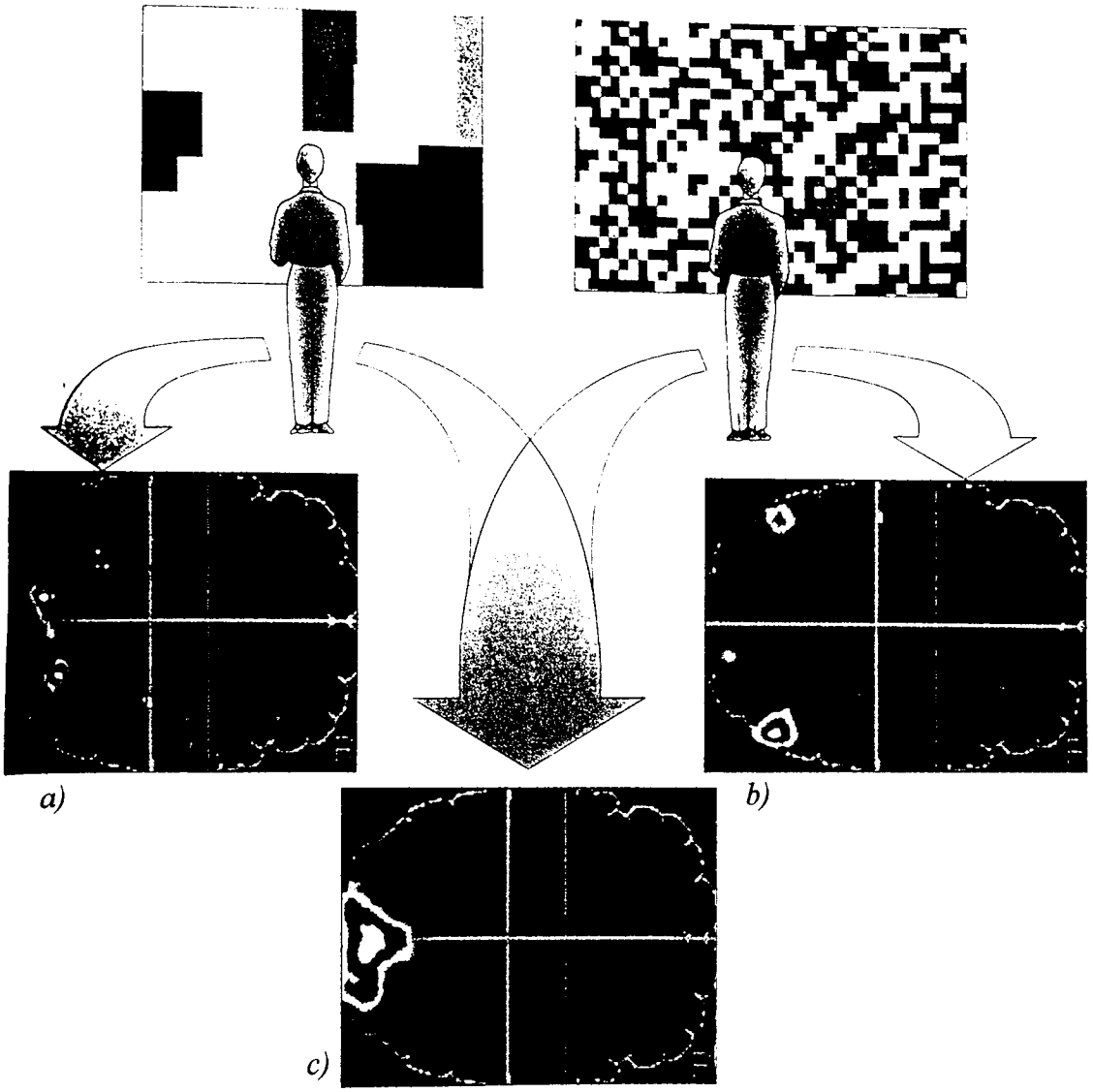

Figure 5.9. PET scans reveal distinct regions of increased cerebral blood flow when stimulated with a) a coloured Mondrian pattern and b) a pattern of moving dots. These regions of activity seem to correspond well with postulated sites of human V4 in (a) and V5 in (b). c) Demonstrates that in both cases areas V1 and V2 were active, implying that both motion and colour information are processed at these sites. from Zeki (1990).

Chapter 6.

The human visual evoked magnetic response to chromatic and achromatic gratings

6.1. Introduction

The experiments described in this section were designed to investigate the neurophysiological basis of the chromatic and luminance processing mechanisms that have been inferred from psychophysical studies (Kelly 1974; Mullen 1985).

There is a general consensus that luminance information is carried by both magno- and parvo-cellular streams, whereas chromatic information is carried exclusively by the parvo-cellular stream (Derrington and Lennie 1984; Merigan 1987). Both magno-cellular and parvo-cellular streams project to layer 4 of V1 and then on to extra-striate visual areas (Zeki 1973; Livingstone and Hubel 1984). From a study of a sample of macaque V1 complex cells, Thorell et al. (1984) propose that the human psychophysical chromatic and luminance contrast sensitivity functions reflect properties of V1 neurons. In man, scalp recorded evoked potentials to gratings modulated in chromaticity and luminance are markedly different. Such differences may be accounted for by activity of chromatically opponent cells situated along the V1/V2 boundary (Carden et al. 1985; Murray et al. 1987).

Experiments using PET (Lueck et al. 1989; Zeki et al. 1991) provide evidence for a cortical area, centred around lingual and fusiform gyri, that is responsive to chromatically modulated stimuli, and may be the human equivalent of monkey area V4. Furthermore, patients suffering from the condition of achromatopsia tend to have lesions around this area (Lenz 1921; Rizzo and Damasio 1989).

It is clear from PET and lesion studies that there is a cortical area in humans responsive to colour; why do electrophysiological studies, using chromatically modulated gratings, not indicate activity beyond the striate cortex ?

In an attempt to address these problems evoked magnetic responses to the onset of a range of grating stimuli, whose parameters were varied to preferentially activate either the chromatic or luminance pathways, were recorded. The results show a change in the balance of activity between two distinct cortical areas.

6.2. Methods

6.2.1. Rationale for stimulus

Mullen (1985) defines the colour contrast of two mono-chromatic gratings added in spatial anti-phase as R/(R+G), where R and G are the mean luminance levels of a red/black and a green/black grating of some fixed contrast. As the colour contrast is

varied, the balance of luminance to chromatic information within the stimulus changes. At 50% colour contrast, the stimulus is modulated purely in chromaticity whereas at 0% colour contrast it consists of primarily luminance modulation. Retinal isoluminance does not necessarily occur at a colour contrast of 50% (Mullen 1985, Flitroft 1989) therefore rather than define a single stimulus to be subjectively isoluminant, it is prudent to examine a range of stimuli of varying colour contrast. Over this range there will not necessarily be any stimulus which is isoluminant, however any change in the balance of activity between chromatic and luminance mechanisms, should be evident. Human behavioural data suggests that luminance contrast sensitivity is independent of the wavelength of monochromatic grating stimuli used (Van Nes and Bowman 1967; Mullen 1985) and therefore it should be sufficient to examine colour contrasts ranging up to isoluminance, in this experiment however colour contrast was varied from 0% (red-black) to 70% (more green than red) in 10% steps.

The psychophysical sensitivity of the chromatic mechanism (Mullen 1985) is spatially low-pass beginning to fall off at around 1cpd, whereas that for the luminance mechanism is bandpass peaking at around 0.8-4 cpd. Since it is required to compare the amplitude of the evoked response contribution from each mechanism, it makes sense to choose a spatial frequency where the two mechanisms have comparable sensitivity. In this experiment gratings of 1cpd were used.

In order to minimise luminance artefact due to retinal cone pigment variation (Wright 1946) and inhomogeneity of CRT display, the stimulus was presented within a two degree radius hemi-field window (Figure 6.1).

Pattern onset presentation is thought to favour the tonic P cell population, whereas pattern reversal is thought to excite preferentially M cells (Kulikowski et al. 1979). Since P cells account for 80% of retinal ganglion cells and underlie both the luminance and chromatic processing pathways, in this experiment the pattern onset paradigm was used.

6.2.2. Stimulus

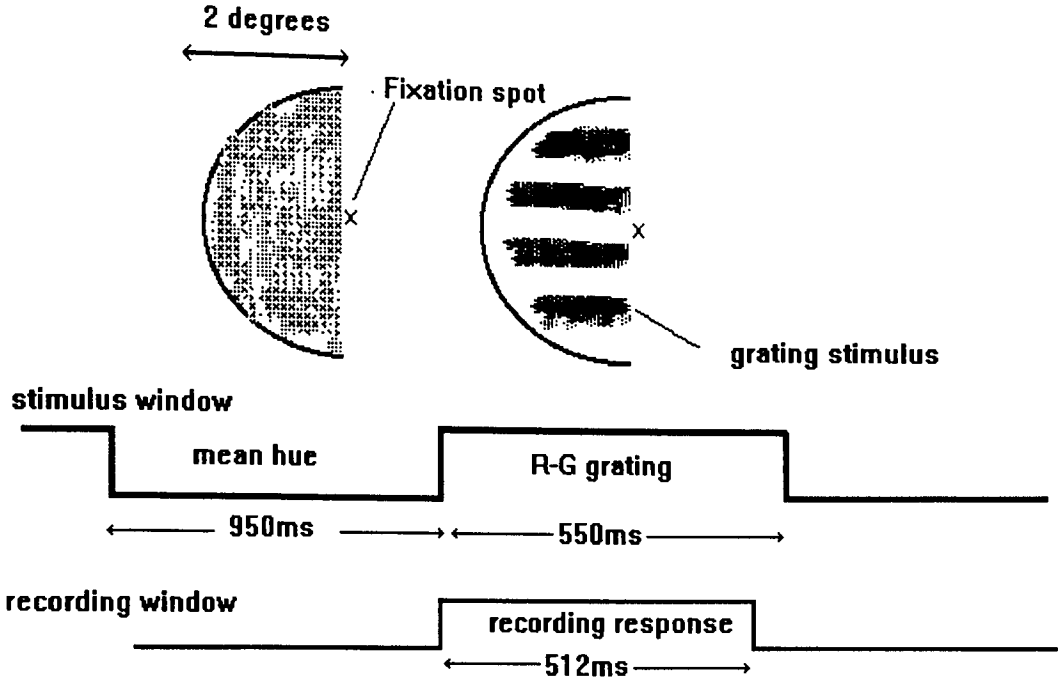

Figure 6.1. The stimulus was a 1cpd grating windowed by a 2° radius hemi-circle and was in the subject's left visual field along the horizontal meridian. The grating appears from a background of the same mean luminance and hue within a square temporal envelope. The mean screen luminance (R+G) was kept constant at 11cd/m^2. The grating was presented for 550ms, and the inter-stimulus interval was 1.5 seconds. The first 512ms of evoked response to grating onset was recorded. The stimulus was generated using a Cambridge Research System VSG 2/2 graphics board connected to a monitor running at 100Hz with phosphors of CIE chromaticity coordinates: x: 0.64, y:0.33.

6.2.3. Magnetic measurements

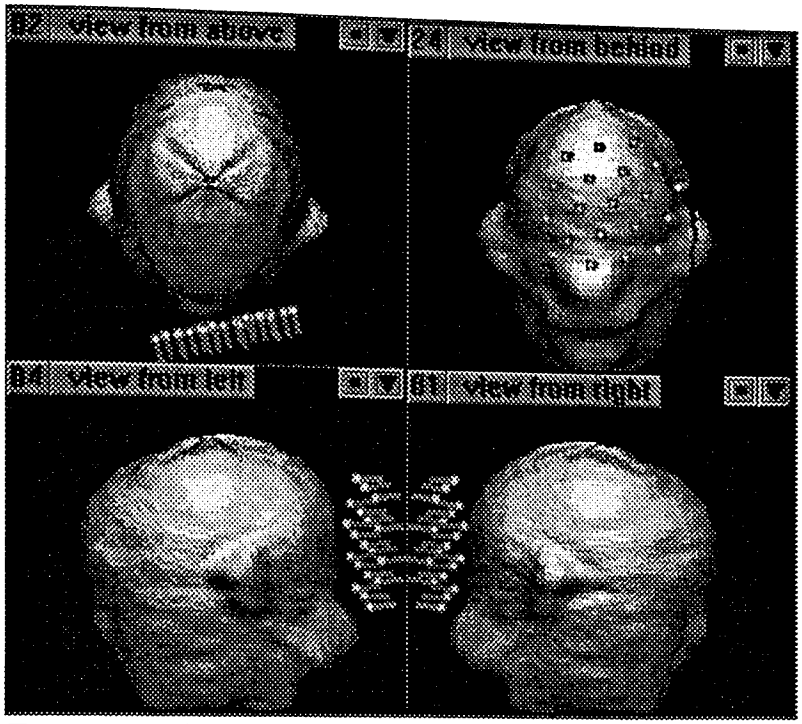

Figure 6.2. The position of the 19 channel detector array with respect to the subjects head. The array is approximately symmetric about the nasion-inion plane, and so as to lie approximately above the right occiput, displaced laterally by 10°.

For each colour contrast, the subject was instructed to fixate a spot on the centre of the hemi-field edge (figure 6.1) for the duration of fifty stimulus presentations. Evoked magnetic responses to stimulus onset were recorded using a 19 channel array of 2nd-order axial gradiometers of 5cm baseline (Matlashov et al. 1992). Each subject was seated, their forehead resting on a horizontal platform, and each viewed the stimulus CRT binocularly through a series of surface-silvered mirrors. The gradiometer array was positioned as in figure 6.2. The position of the subject's nasion and two pre-auricular points recorded using the Polhemus pen (see chapter 2) along with an outline of the occipital scalp region; all of this information was used for subsequent co-registration with MRI images. For each stimulus condition, the evoked response to 50 grating onsets were recorded in 512ms epoch segments. Responses were analogue filtered (106Hz 4th order Butterworth filters) and sampled at 1kHz by a 16bit ADC. Having recorded evoked responses to a complete range of colour contrasts, the experiment was repeated in order to control for subject head movement. Data sets for four right handed subjects (1 male, 3 female; age range 25-32) were collected.

6.2.4. Analysis

After acquisition, data were averaged and anti-averaged. Phase shifts introduced by the anti-aliasing filters were digitally corrected for (chapter 2) and reference noise cancellation was used to attenuate environmental noise sources (chapter 3). The data was then frequency discrimination filtered from 2-30Hz. Monte Carlo analysis was used to generate 32 sets of channel data with added Gaussian white noise. The noise added

was calculated by assessment of the RMS noise on the filtered anti-average for each channel. The head was modelled as a spherical conductor of concentric conductivity boundaries, best fit spheres were fit to digitised points around the occiputs of each subject. Neural sources were modelled as single current dipoles and this model was fit to each of the noise added data sets by minimisation of the chi-square statistic (Press et al. 1989; Supek and Aine 1990). The average gamma Q probability obtained was used to assess the validity of the proposed model. Given that the dipolar model was acceptable, the 95% confidence volume ellipsoids for the equivalent current dipole location were calculated.

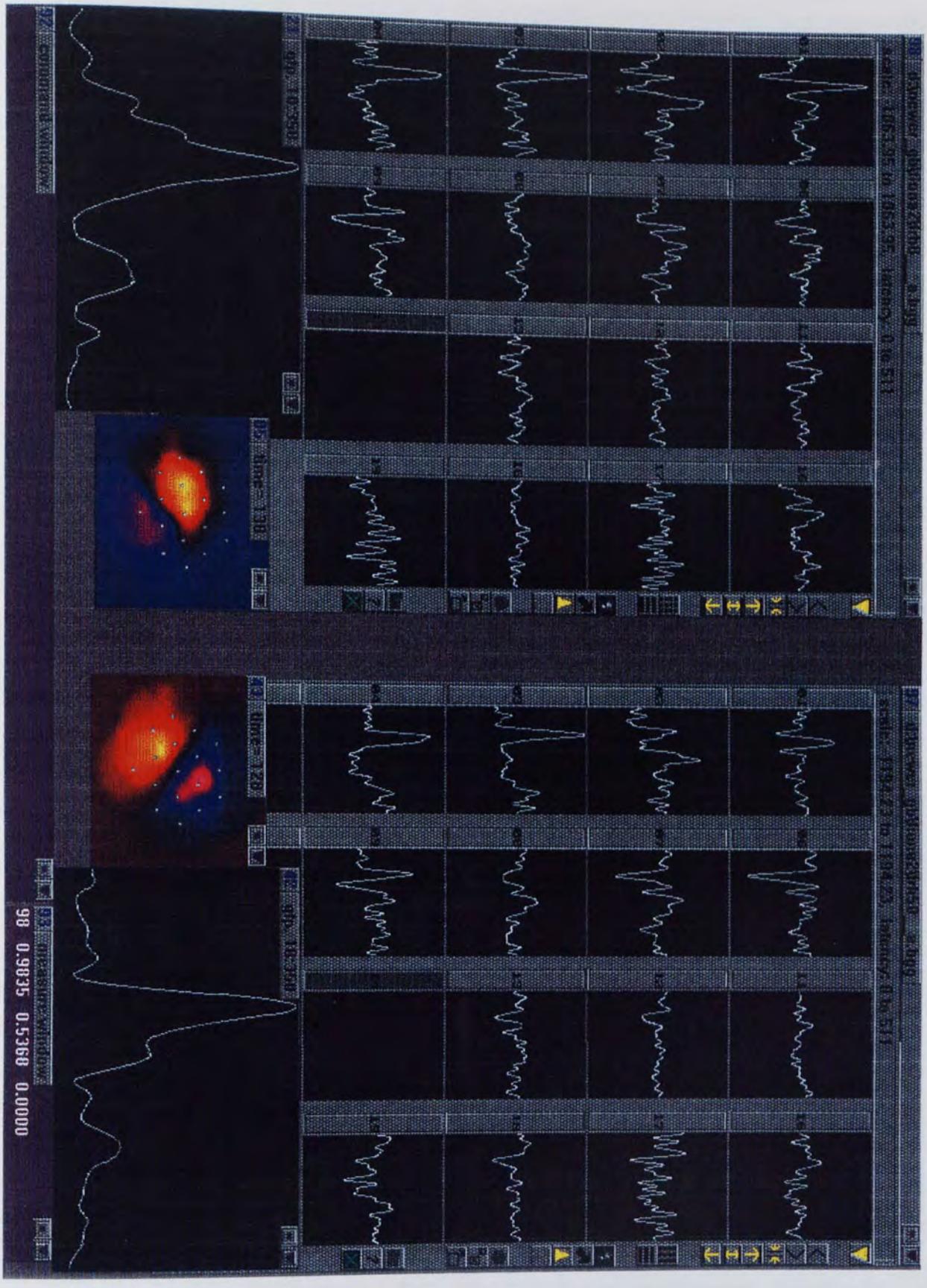

Figure 6.3. Magnetic evoked responses to 0% (left) and 50% colour contrast for subject FF. In lower portion of diagram, global field power is shown as a function of latency in milli-seconds. The pseudo-colour contour maps (red represents field out of head, blue represents field into head) show the field distributions at the latencies which correspond to the peaks in the power function.

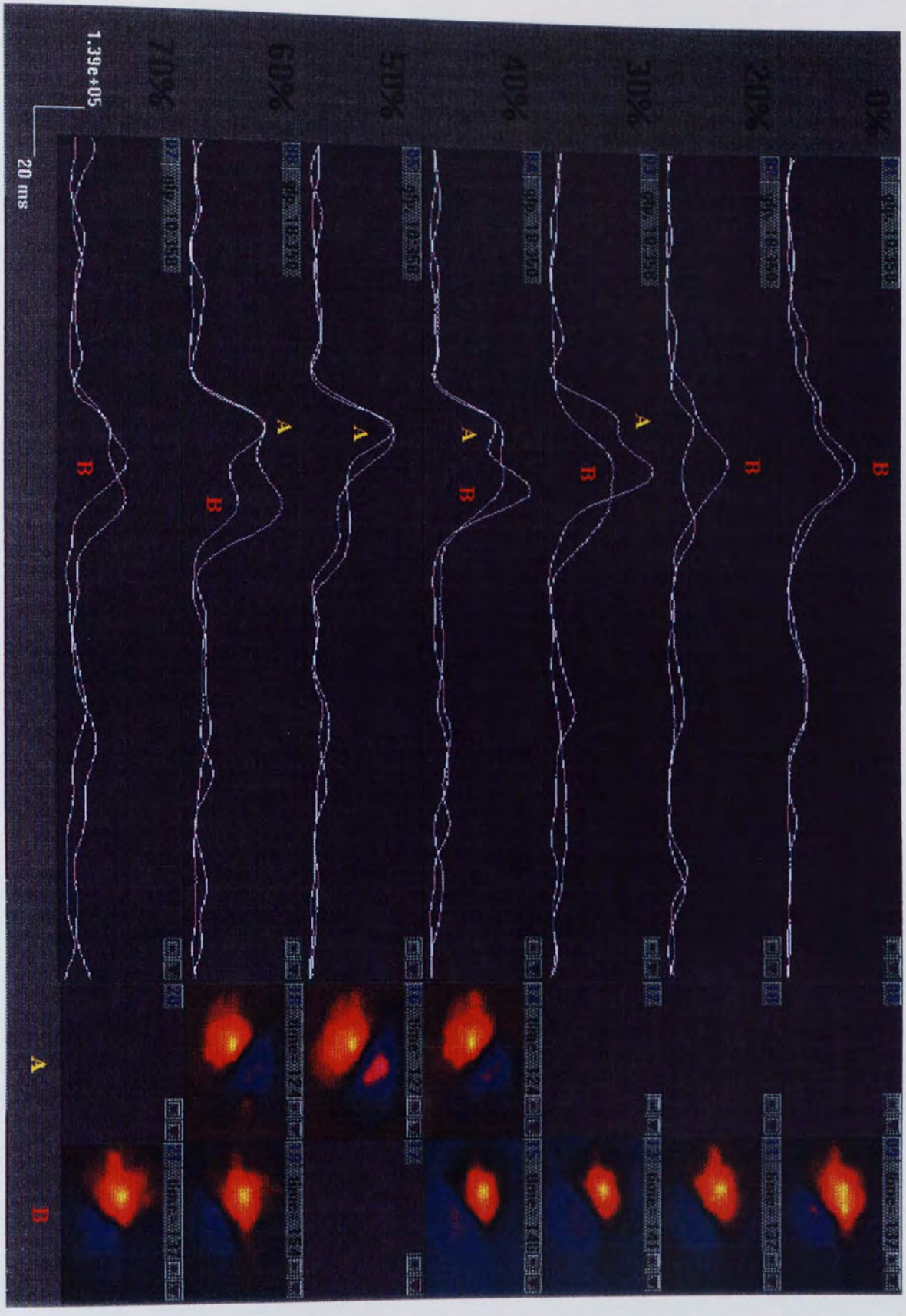

Figure 6.4. Global field power plots (in fT^2) derived from evoked responses to sinusoidal gratings of colour contrast 0-70% for subject FF. Data for a repeat run is shown at each colour contrast. Peaks in the power plots are labelled A (occuring at latencies of 124-127ms) and B (occuring at latencies 137-154ms). Note that the earlier peak (A) only occurs for colour contrast 30-60% and that the later peak (B) is absent at a colour contrast of 50%. The pseudo-coloured maps show the magnetic field strength at latencies corresponding to the early (A) and late (B) peaks in the power plots. The field pattern generated for peak A differs markedly to that generated for peak B. Note, however, that the field patterns do not vary with colour contrast.

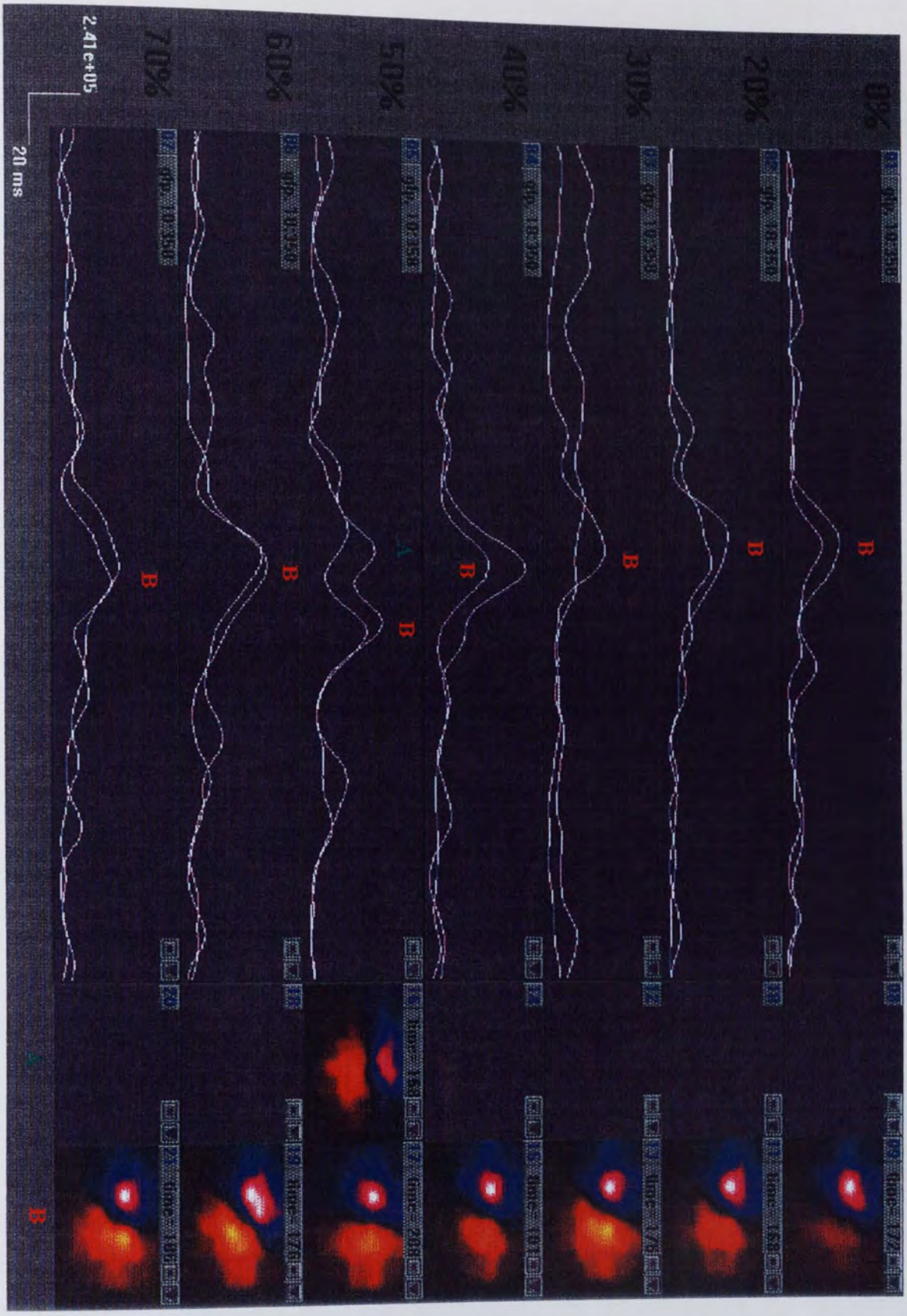

Figure 6.5. Global field power plots derived from evoked responses to sinusoidal gratings of colour contrast 0-70% for subject KDS. Data for a repeat run is shown at each colour contrast. Peaks in the power plots are labelled A (occurring at 168ms) and B (occurring at latencies 168-208ms). Note that the earlier peak (A) only occurs for colour contrast 50% when the latency of peak B increases by 30ms. The pseudo-coloured maps show the magnetic field strength at latencies corresponding to the early (A) and late (B) peaks in the power plots. The field pattern generated for peak A differs markedly to that generated for peak B.

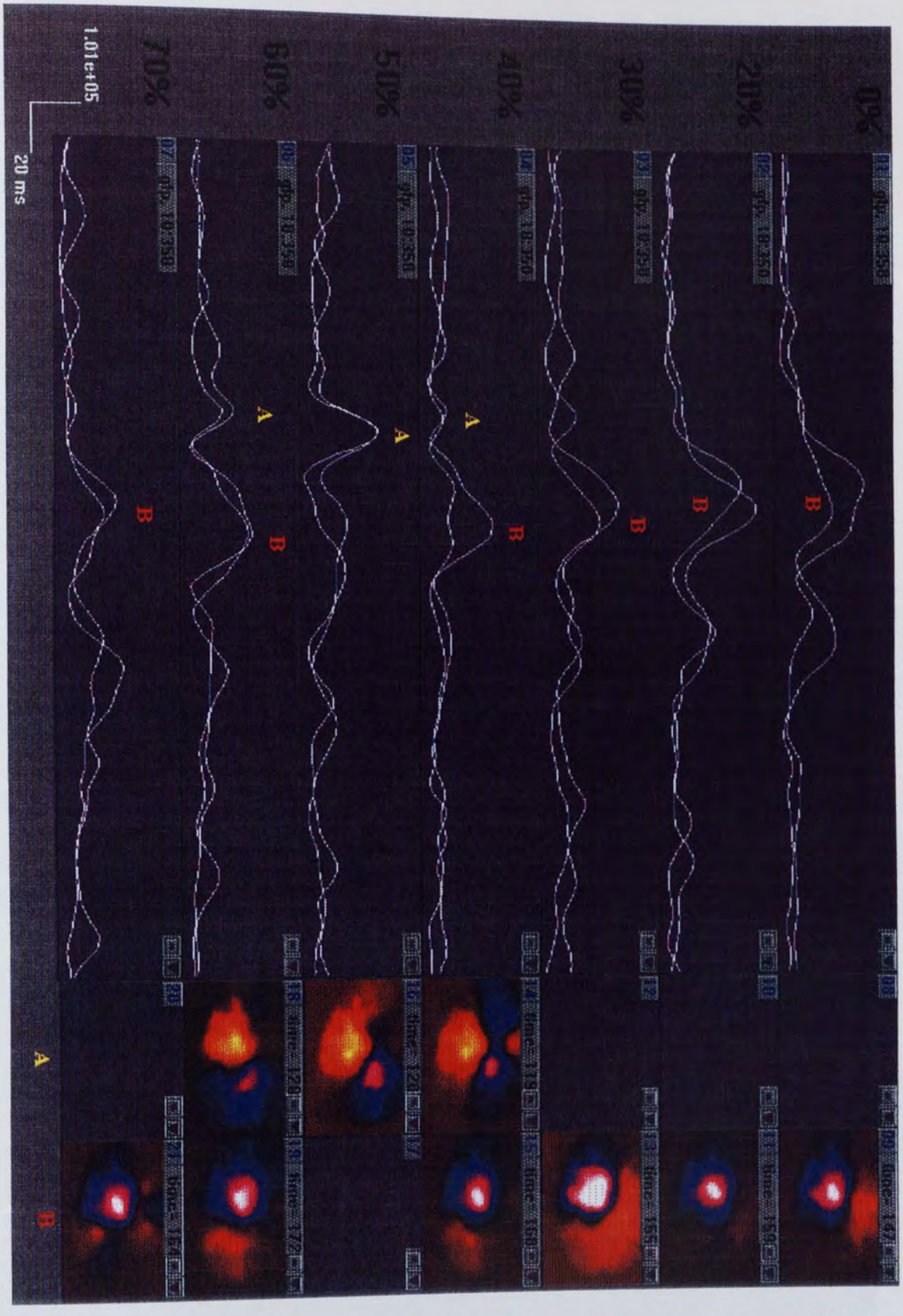

Figure 6.6. Global field power plots derived from evoked responses to sinusoidal gratings of colour contrast 0-70% for subject JA. Data for a repeat run is shown at each colour contrast. Peaks in the power plots are labelled A (119-128ms) and B (occurring at latencies 147-164ms). Note that the earlier peak (A) only occurs for colour contrast 40-60% and that peak B is absent at colour contrast 50%. The pseudo-coloured maps show the magnetic field strength at latencies corresponding to the early (A) and late (B) peaks in the power plots. Despite the low signal to noise ratio of the data, it is clear that the field pattern generated for peak A differs markedly to that generated for peak B.

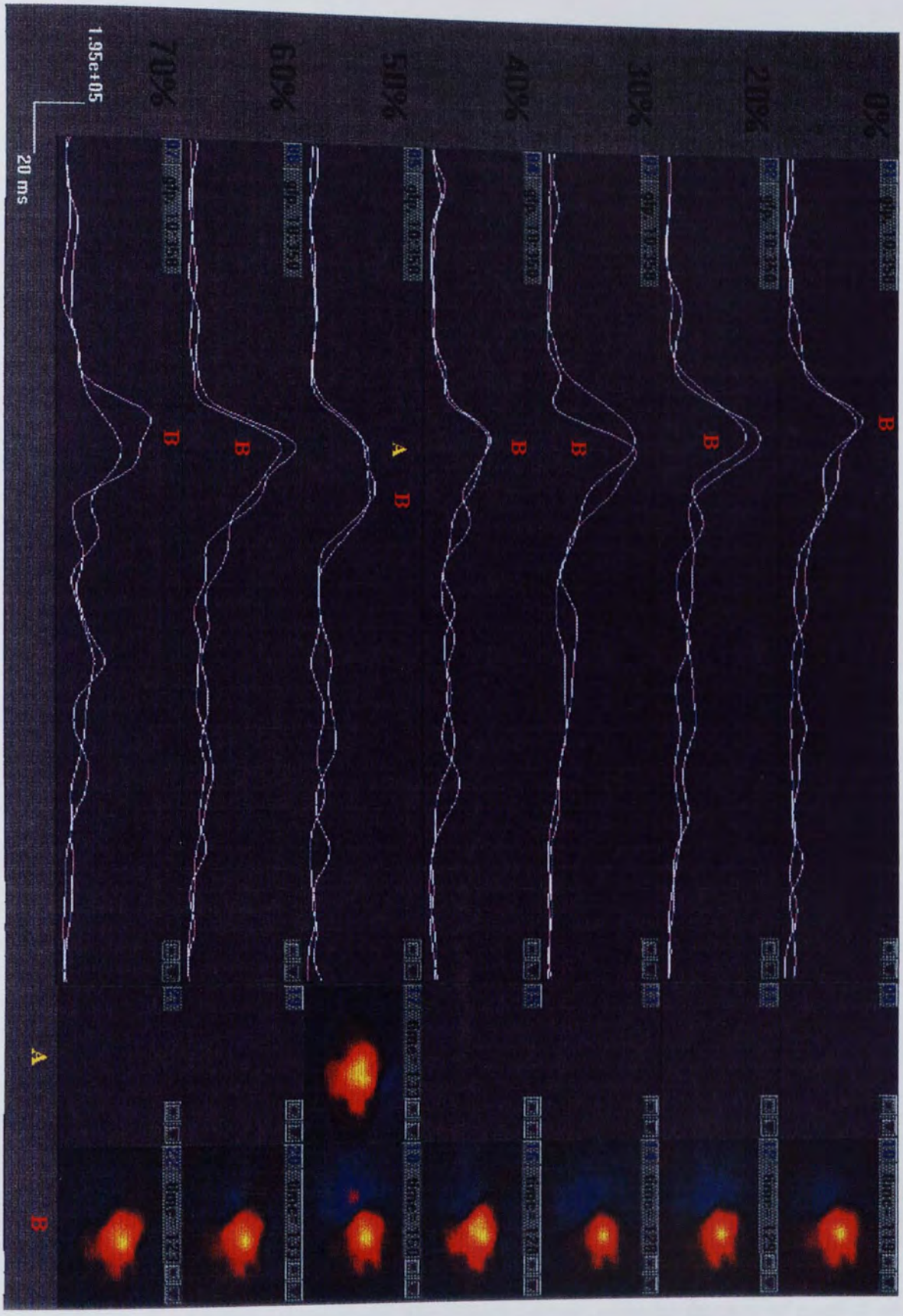

Figure 6.7. Global field power plots derived from evoked responses to sinusoidal gratings of colour contrast 0-70% for subject VT. Data for a repeat run is shown at each colour contrast. Peaks in the power plots are labelled A (133ms) and B (119-150ms). Note that peak (A) only occurs for colour contrast 50% where the latency of peak B increases by 20ms. The pseudo-coloured maps show the magnetic field strength at latencies corresponding to the early (A) and late (B) peaks in the power plots.

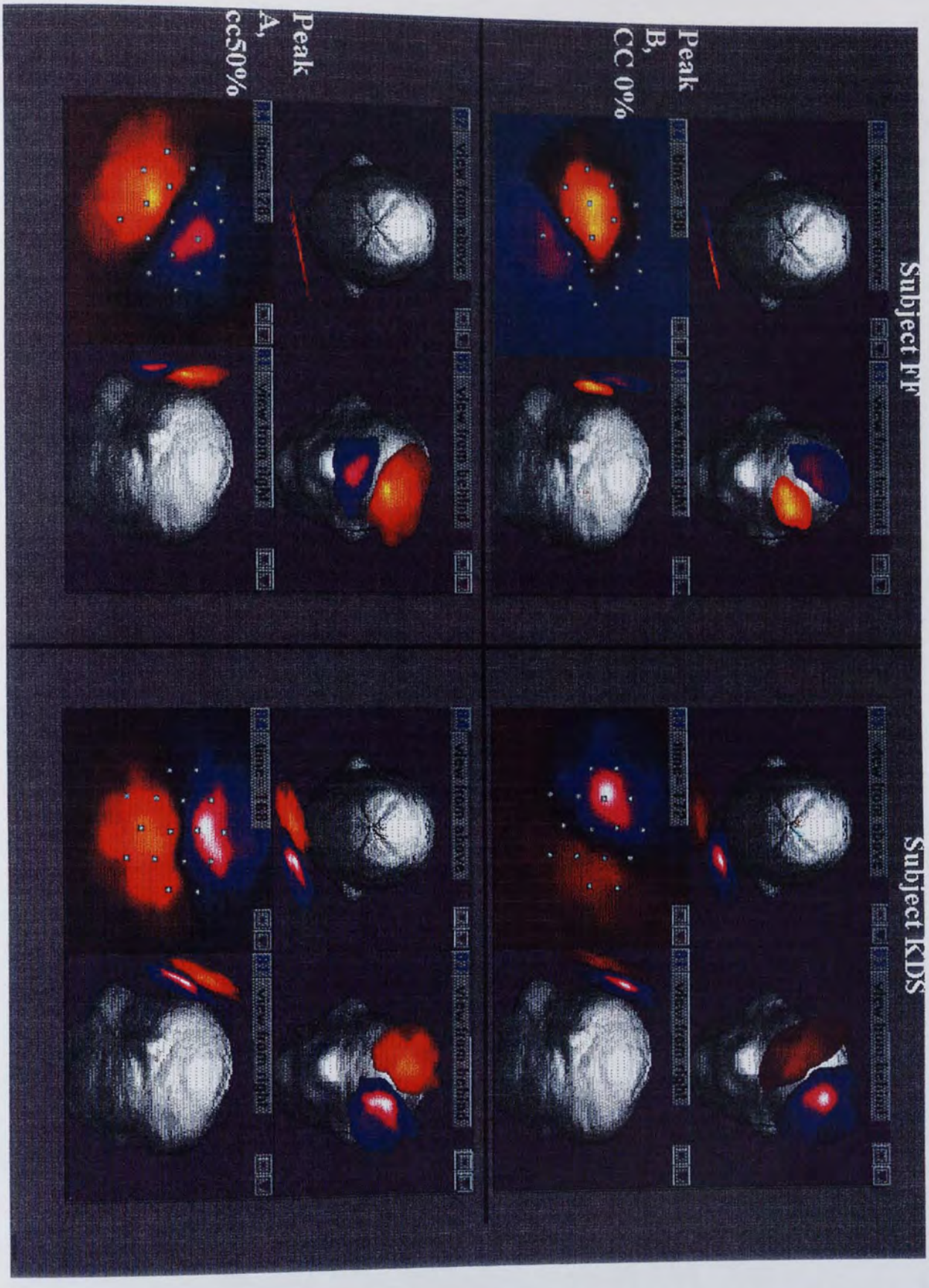

Figure 6.8.(continued overleaf). The pseudo-colour maps at latency of peak A at colour contrast 50% and at latency of peak B for colour contrast 0% of figures 6.4-6.7 plotted over a schematic head. The fourth quadrant of each block shows the map as displayed in the figures 6.4-6.7 along with the working detector positions. The field maps for peak B are similar in subject pairs KDS and VT and FF and JA. The field maps for peak A are similar in FF, JA and VT.

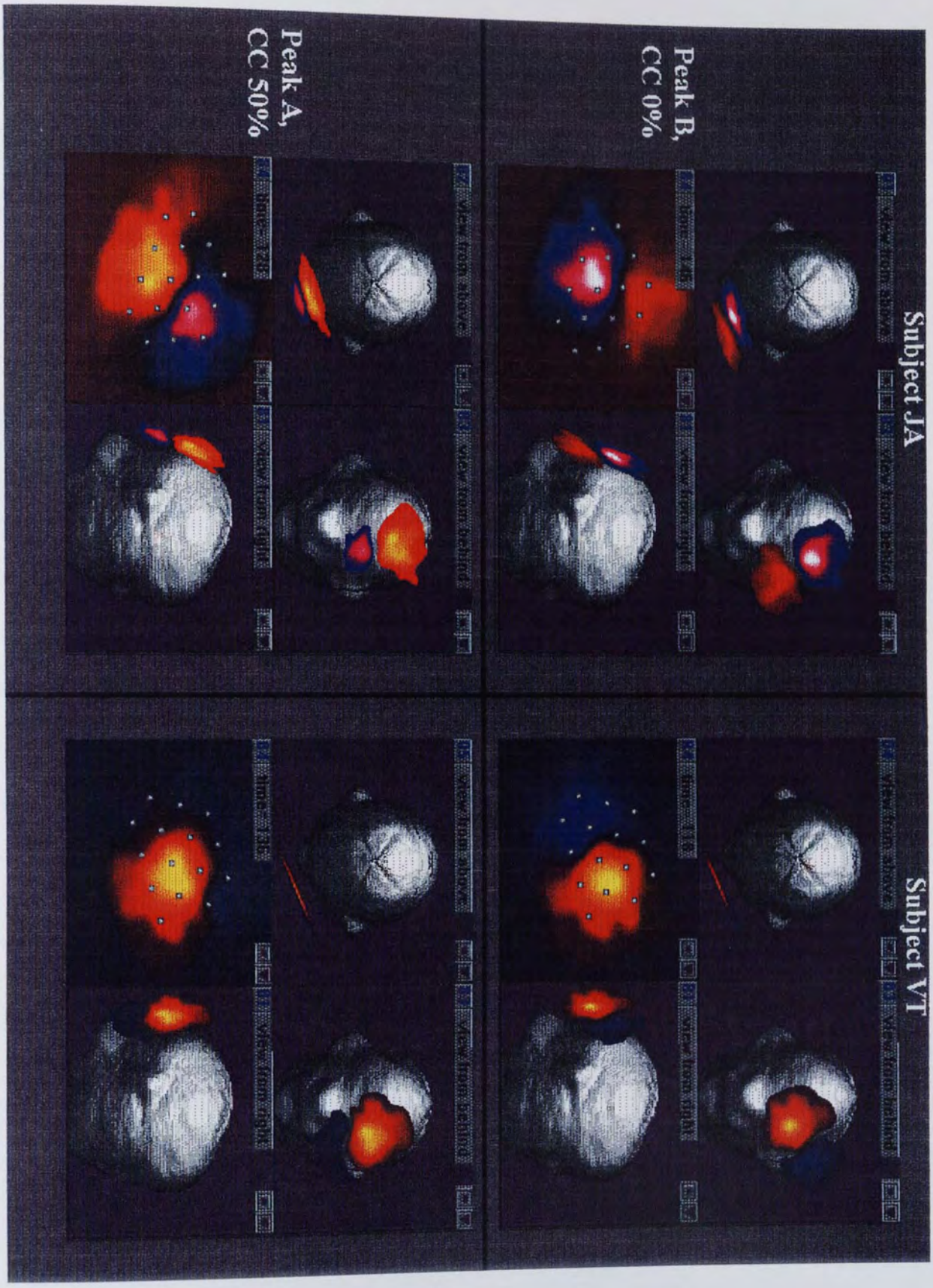

Figure 6.8. (continued).

4.1.3. Results.

In all subjects, responses (~1pT) to both luminance and chromatically modulated grating stimuli were recorded in several gradiometer channels (figure 6.3). The inset in figure 6.3 shows a plot of the global field power for the data, alongside a pseudo-colour map showing the field distribution at the latency of peak power.

At each colour contrast, a plot of global field power and a map of magnetic field distribution at the latency corresponding to the two major power peaks, labelled A and B, are plotted (figures 6.4-6.7). In all of the four subjects, a distinct pattern of activity emerges. At low colour contrasts (high luminance contrasts), a power peak B (at around 140ms) with distinctive field distribution is identifiable. At colour contrasts of around 50%, the response is dominated by an earlier peak A (at latency 120ms). The field distribution at the latency of peak A is markedly different to that at the latency of peak B. At around 50% colour contrast, peak B is either abolished (figures 6.4,6.6) or increases in latency by 20-30ms (figures 6.5,6.7). The magnetic field maps corresponding to the latency of each peak are similar across colour contrasts. There is large inter-subject variability in response latency.

Figure 6.8 shows the field maps at the latencies of peaks A and B plotted over a schematic subject head. Map B has similar morphology in two subject pairs (FF and JA, KDS and VT). The morphology of map A is similar in three subjects (FF ,JA, VT) and looks like a dipolar source pointing to the right side of the head.

6.2.5. Control for chromatic aberration

A control experiment was conducted to ensure that luminance artefacts introduced by ocular accommodation could not be responsible for the pattern of results observed. The difference in accommodation between the red (602nm) and green (526nm) light is approximately 0.5 dioptres (Mullen 1985). Given a 6mm pupil and a 1cpd grating, the normal range of accommodation alone could produce a change in the retinal colour contrast of around 3% (Allen et al. 1993; Green et al. 1980).

For each colour contrast the implicit amount of luminance contrast of a red-black grating stimulus was calculated and this alone presented (Figure 6.9). In this experiment, a 5% luminance contrast grating was presented in order to simulate the possible effects of chromatic aberration on a physically isoluminant stimulus. Figure 6.9 shows that as isoluminance is approached, the magnetic evoked responses to equivalent luminance contrast gratings are of negligible amplitude.

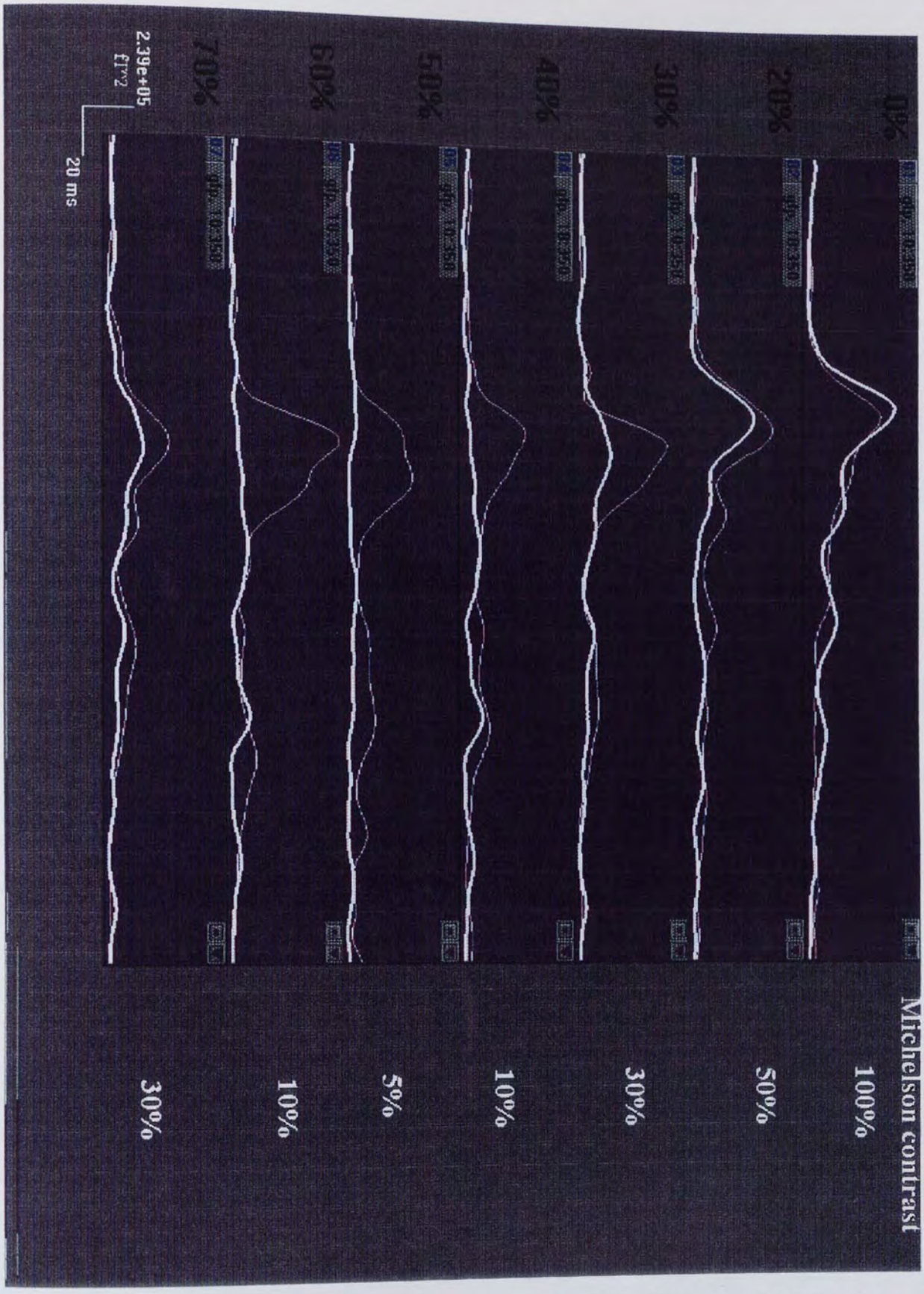

Figure 6.9. Subject VT. Global field power as a function of Michelson contrast of a red-black sinusoidal grating (thick trace). For comparison, the power plots of the red-green stimuli (from figure 6.7) are plotted (thin trace) alongside their comparable colour contrast. The responses to the isoluminant grating are compared to those of 5% luminance contrast. For luminance contrasts of less than 10% there is little or no response. That is, the responses observed to isoluminant gratings are not accounted for by detection of luminance artefact.

6.2.6. Dipolar models

It is unclear how many neural mechanisms underlie each principal peak observed in the global field power plots of the magnetic evoked responses. The simplest assumption is that each of the peaks is due to a distinct dipolar source. The data in tables 1-4 show average chi-square, gamma Q probability and percentage of variance measures for the postulated single dipole model at the identified peak latencies. At each power peak latency, the data are well modelled as single dipole sources in 3 of the 4 subjects (Gamma Q>0.001, Press et al. 1989).

Figure 6.10 shows dipole plots and confidence regions for chromatic and achromatic generators. In all subjects, the dipoles fit to latency of peak A and those fit to latency of peak B localize to distinct neural sites. Co-registration of the data with MRI scans for subjects FF and KDS reveals the anatomical position of these areas (figures 6.11 and 6.12). Figure 6.11 shows subject FF with the 95% confidence limit ellipsoid for dipole location fit to the latencies of peaks A and B for the full range of colour contrasts. At latencies of individual peaks A and B, the confidence ellipsoids overlap over the full range of colour contrasts indicating that the activity is explained by the same two underlying neural generators. However, for FF the confidence ellipsoids of sources A and B never overlap indicating that the generators of the two peaks are spatially, as well as temporally, distinct. The data is more variable for KDS, and there is some overlap of confidence regions, however dipole orientations (figure 3.5) clearly indicate that the neural sources responsible for peaks A and B are distinct.

CC (%)	Peak	latency (ms)	$\chi 2_r$	gamma Q	% Var	95% conf vol (mm^3)
0	B	138	2.75	0.001	81	116
20	B	139	1.75	0.027	85	1582
30	B	140	1.85	0.038	83	175
40	B	148	1.66	0.070	86	92
60	B	155	2.0	0.022	81	417
70	B	146	0.81	0.700	75	554
40	A	124	2.75	0.001	83	43
50	A	125	1.83	0.038	87	64
60	A	126	2.41	0.022	85	107

Table 1. Subject FF. Statistics for Monte Carlo analysis of the single dipole model. Gamma Q and $\chi 2_r$ values based on 12 degrees of freedom (5 dipole parameters, 17 operative channels). Both peaks A and B have gamma Q values >=0.001 indicating that the current dipole model is not unreasonable.

CC (%)	Peak	latency (ms)	$\chi 2_r$	gamma Q	% Var	95% con vol (mm^3)
0	B	172	0.57	0.009	88	2261
20	B	174	1.0	0.486	89	237
30	B	174	2.45	0.004	79	759
40	B	182	0.38	0.843	90	643
50	B	207	1.36	0.260	87	300
60	B	181	1.09	0.342	88	237
70	B	186	2.09	0.019	77	395
50	A	177	1.09	0.454	85	560

Table 2. Subject KDS. 11 degrees of freedom. Both peaks are reasonably modelled as dipolar.

CC (%)	Peak	latency (ms)	$\chi 2_r$	gamma Q	% Var	95% vol (mm^3)	con
0	B	152	1.909	0.030	83	344	
50	A	126	1.818	0.049	84	157	

Table 3. Subject JA. 11 degrees of freedom. Both peaks are reasonably modelled as dipolar.

CC (%)	Peak	latency (ms)	$\chi 2_r$	gamma Q	% Var	95% vol (mm^3)	con
0	B	120	16	10^{-29}	66	1244	
50	A	135	4.5	10^{-6}	85	1	
50	B	152	13	10^{-23}	74	176	

Table 4. Subject VT. 10 degrees of freedom. Note the decrease in gamma Q by several orders of magnitude, it is unlikely that the data is accounted for by activity of a single dipolar source.

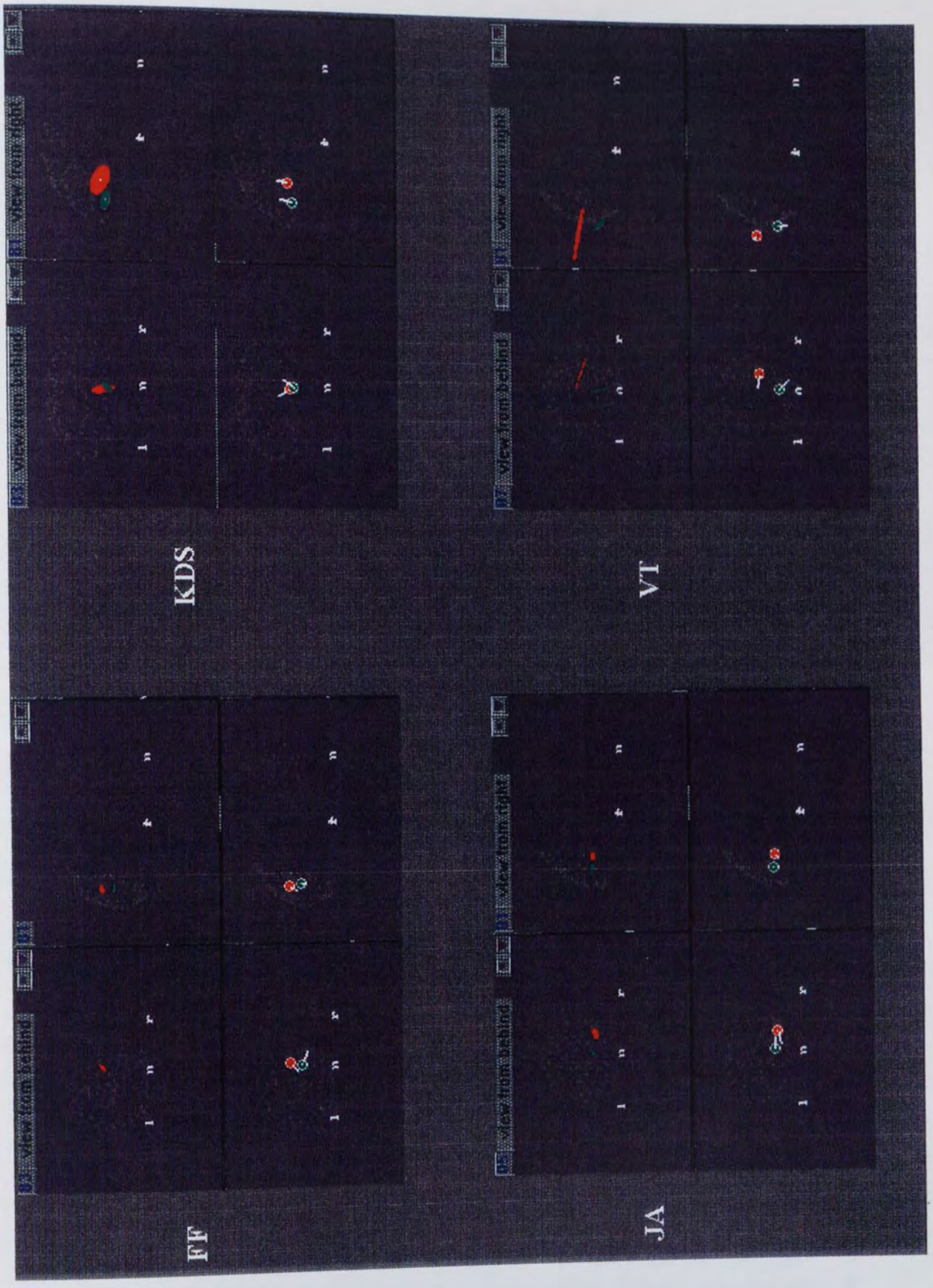

Figure 6.10. The coronal and sagittal views of 95% confidence regions (upper sections) and average dipole position and orientation (lower sections) for all four subjects. Plotted are dipole fits at latency of peak B at 0% colour contrast (red), and dipole fits at latency of peak A at 50% colour contrast (green). The grey dots denote digitised points on the subject's head.

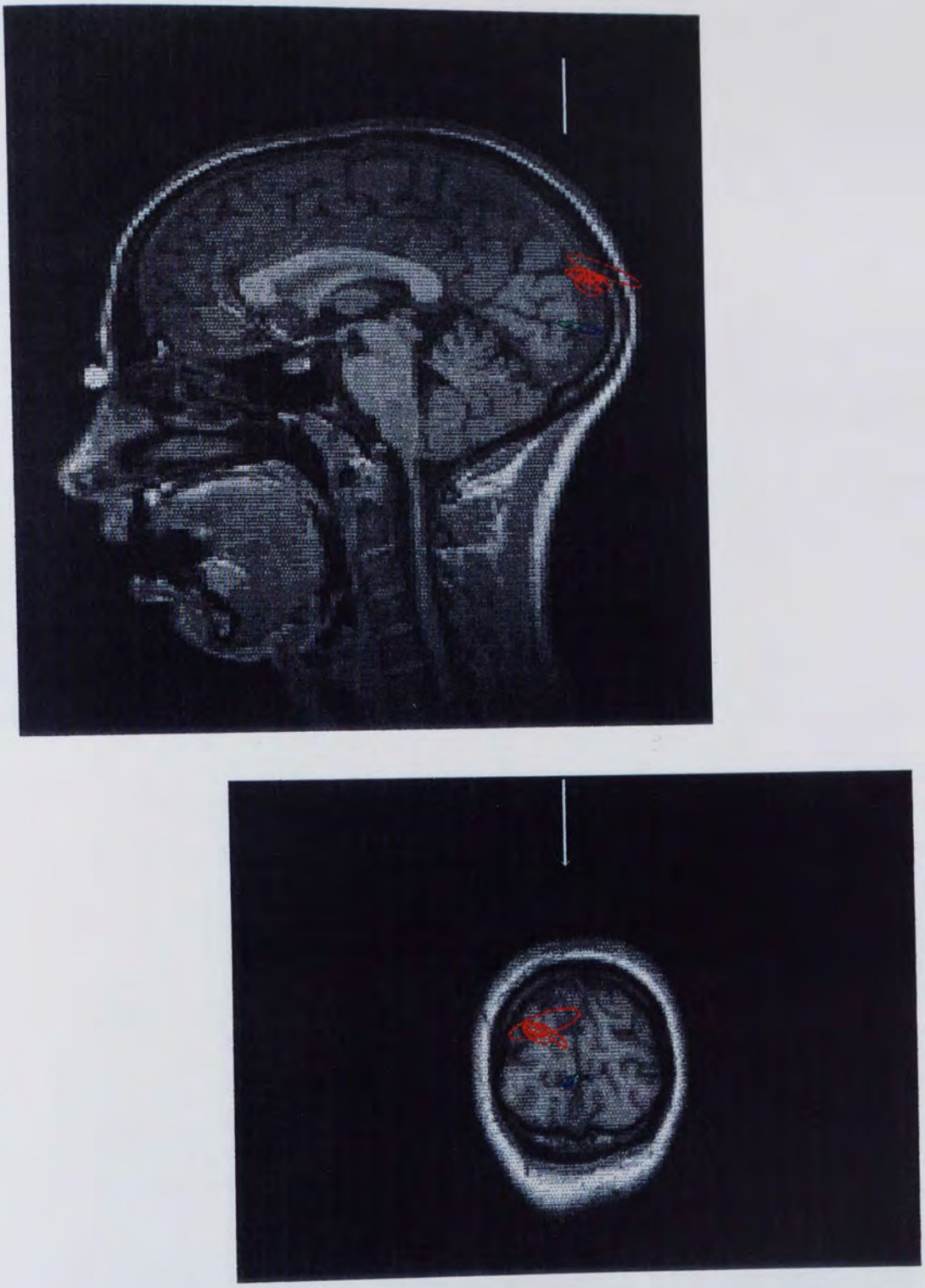

Figure 6.11. Coronal (as viewed from the front) and sagittal MRI section for subject FF. 95% confidence ellipsoids for the location of an equivalent current dipole at latency of peak A at {50%} (green) , {40,60%} (blue) colour contrast and at latency B for {0%,20%,30%,40%,60%,70%} (red) colour contrast. Note that the dipole positions are stable across stimulus conditions, indicating that peaks A and B are accountable for by the activity of two single, stationary dipolar sources. Note that the generator of peak A lies midline on the lip of the calcarine fissure, whereas the generator of peak B is more posterior and superior.

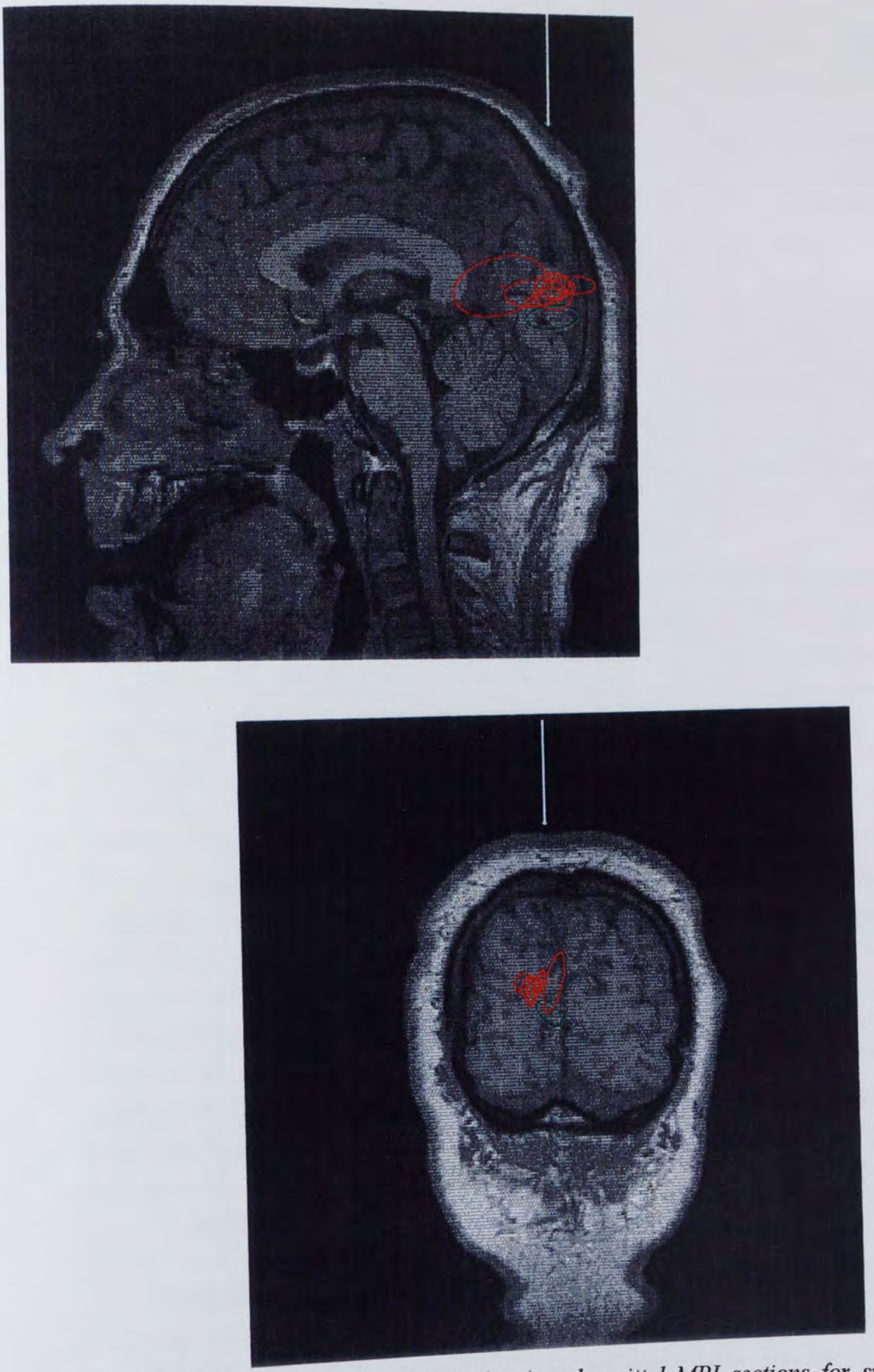

Figure 6.12. Coronal (viewed from front) and sagittal MRI sections for subject KDS. Above left is a coronal view, as viewed from the front, right is a sagittal section at the level of the white arrow. 95% confidence ellipsoids for the location of an equivalent current dipole at latency of peak A {50%} (green) and peak B {0-70%} (red) are shown.

6.3. Discussion

Global power peak A only appears at around physical isoluminance, it is reasonable to assume that it relates to the activity of a centre maximally sensitive to chromatic contrast. The behaviour of peak B is consistent with the activity of a mechanism responsive to luminance contrast since it is absent, or considerably delayed at physical isoluminance.

In three of the four subjects studied the activity underlying each of global power peaks A and B is well modelled as a current dipole. These sources are temporally, and anatomically distinct in their activation Co-registration with MRI shows that the chromatic dipole lies along the midline within the calcarine fissure and possibly extends onto the lingual or cuneal gyrus, whereas the luminance dipole tends to be superior and more variable in location. Both sources have relatively long latencies (130-180 ms), and there is large latency variability between subjects.

Considerable anatomical data shows that the human striate cortical area V1 lies within the calcarine sulcus (Brindley 1972; Clarke and Miklossy 1992). The location of the chromatic source is therefore consistent with a V1 origin. However, the source location is not consistent with the fact that the stimulus was positioned in the central visual field. In man, the central two degrees of vision maps almost exclusively to the dorsal area of primary visual cortex at the occipital poles (figure 6.13) (Horton and Hoyt 1991; Fox et al. 1987). Furthermore, the cortical magnification formuli proposed by Daniel and Whitteridge (1961) and extrapolated to the human (Horton and Hoyt 1991, figure 6.14), indicate that the cortical area activated by any stimulus decreases rapidly as the stimulus becomes more eccentric. If the 2° hemi-field stimulus does map beyond the poles in either of the two subjects, one would therefore expect any equivalent current dipole source to be biased posteriorly. The chromatic source in both subjects is around 2-3cm along the calcarine fissure from the occiput. If this were V1 activity, it would correspond to a visual stimulus centred at least 5° of eccentrically (figure 6.14). It is possible that V1 is active yet the location of the active area, at the occipital pole and dorsal surface and therefore radial, means that it will produce no external magnetic field (see chapter 1).

If the chromatic source is not in area V1, in which human visual area is it situated ?

Monkey physiology shows that both V2 and V4 also contain large proportions of chromatically tuned cells (Livingstone and Hubel 1984; Zeki 1973). The start of area V2 is defined by the border of the callosal connections which link the receptive fields of V1 neurons along the vertical meridian (Zeki 1969). In the human, these connections extend around V1, becoming lateral to it at the occipital pole (Clarke and Miklossy 1992). In the monkey, the receptive fields of V1 and V2 neurons run adjacent along the vertical meridian, yet diverge along the horizontal meridian. Any central visual

field stimulus should therefore activate an area of V2 close to the occiput and more lateralised to that of V1. Since the chromatic dipole is neither posterior, nor lateralised, a V2 response can be dismissed.

It is proposed that the chromatic dipole reflects V4 activity. This would place human V4 on the lingual gyrus, possibly extending superiorly around the calcarine sulcus onto the cuneal gyrus and inferiorly onto the fusiform gyrus. This view does not accord with that of Zeki (1993) who proposes that human V4 lies exclusively on the fusiform gyrus. Zeki puts forward two arguments to support his proposition. First is that lesions in the lingual gyrus do not always lead to achromatopsia, and there is some clinical evidence to support this (Bogousslavsky et al. 1987). Second, that V4 does not lie in the lingual gyrus since the space is occupied by V2, is not supported by recent anatomical studies (Brindley 1972; Clarke and Miklossy 1992) which reveal a tapering of area V1 as one moves anteriorly (figure 6.15, 4.15). This tapering means that V2 actually moves from the lingual gyrus and into the calcarine fissure as one move anteriorly. This tapering is also clearly shown in the PET data of Zeki et al. (1991), figure 6.9.

The lingual site of V4 would help explain why the condition of achromatopsia is often accompanied by peripheral upper visual field scotomas (Damasio 1985). The proposed site of human V4 (figure 6.17) would mean that it lies adjacent to peripherally mapped V1 neurons. Were V4 situated on the fusiform gyrus, lesions in this area would have to be very large to consistently affect V1. Furthermore, in the monkey, V4 is indeed situated anterior to V1 and shows no superior or inferior bias (figure 6.16).

The luminance related dipole seems to lie on the superior bank of the occiput yet its location is highly variable between subjects. The long latencies and their high inter subject latency variability could indicate that both luminance and chromatic sources are of extra-striate origin. The luminance source would seem to be consistent with V2 or V3 activity. V3 is more likely since, the activity is relatively late, after V4, and the generator is not especially lateralised nor posterior, as one would expect for a central visual field stimulus to V2.

More experimental work is required to confirm the hypotheses presented, the following experiments are proposed which might initiate such studies:

i) Although in this data two experimental runs provide repeatable dipole locations, there was no subject head movement restraint employed. That is, it is possible that the subjects moved between digitisation of the three fiduciary points and actual data acquisition. Any movement artefact, as well as errors due to location of fiduciary points, could be minimised by using a 'bite-bar' arrangement (Singh et al. 1995). At present co-registration errors could limit the localisation of activity to as much as $1cm^3$.

ii) Although chi-square measures indicate that the dipolar model used is not unreasonable, there may be models (e.g. distributed source) which better describe the

underlying neural generators. A comparison between two such source modelling approaches might be informative.

iii) Anatomically, it would be informative to establish the extent of the striate area in each subject, which can vary widely between individuals (Brindley 1972). For example, the extent of V1 could be established by high resolution MRI imaging (Clark et al. 1992).

iv) Functionally, VEP studies may reveal activity of radially oriented generators which correspond to striate cortical activity related to the central visual field stimuli. Indeed, VEP studies (Carden et al. 1985; Murray et al. 1987) have concluded that the human response to isoluminant chromatic stimuli reflects V1 activity.

v) The extent of peripheral V1 could also be assessed using magnetometry by estimating source locations as stimulus eccentricity is increased. If the chromatically responsive source lies within V1 then its location should be highly dependent on stimulus eccentricity; if however it reflects V4 activity then, due to the larger receptive field sizes of V4 neurons (Desimone et al. 1985), its location should remain relatively constant.

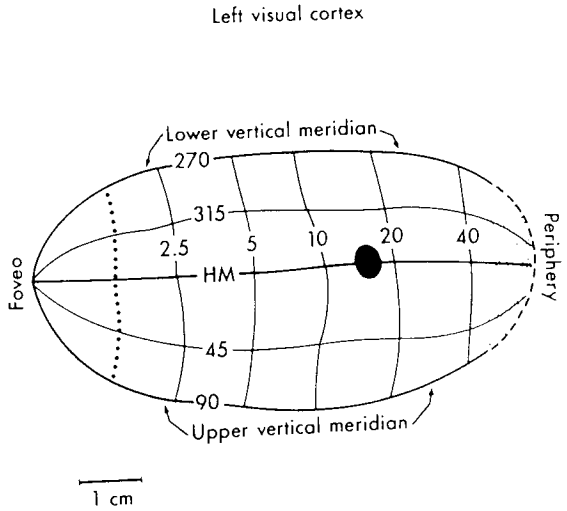

Figure 6.13. Schematic map showing the projection of the right visual hemi-field onto the left visual cortex. The row of dots indicates where the striate cortex folds around the occipital pole. redrawn from Horton and Hoyt (1991).

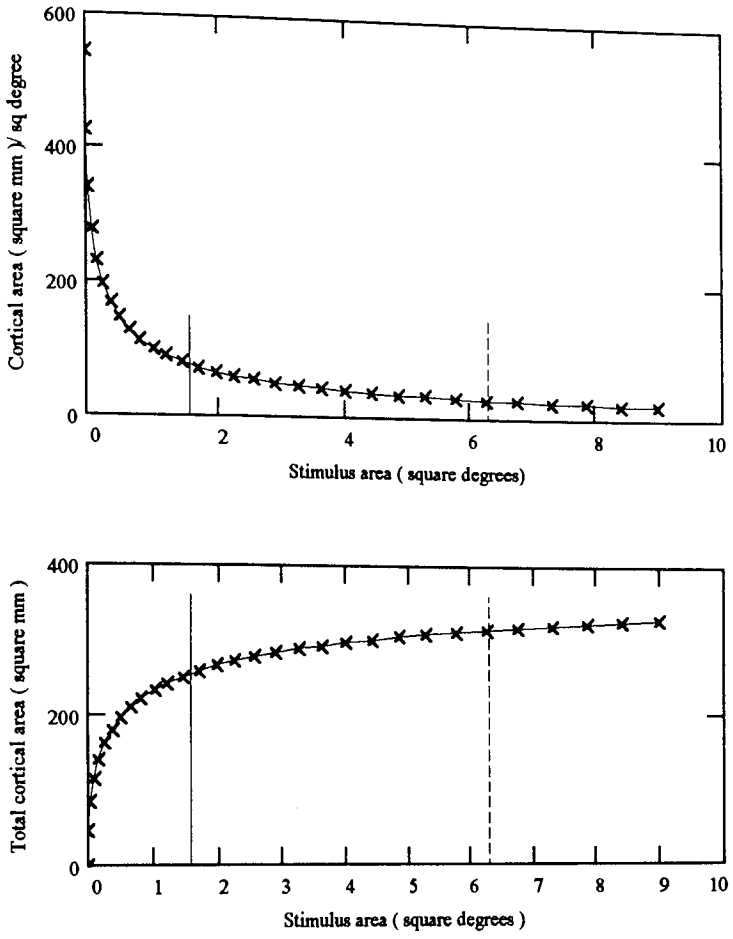

Figure 6.14. Estimate of striate cortical area mapped to per square degree of visual field (above). The lower curve shows the total cortical area mapped to by a stimulus of a certain size. Curves are based on the estimate of Horton and Hoyte (1991) adjusted from the monkey data of Daniel and Whitteridge (1961) to fit measured human parameters. The solid line and dashed vertical lines corresponds to stimulus areas subtended by 1° and 2° hemifields. From the lower curve, for a 2° hemifield stimulus, the central 1° accounts for ~75% of the cortex activated.

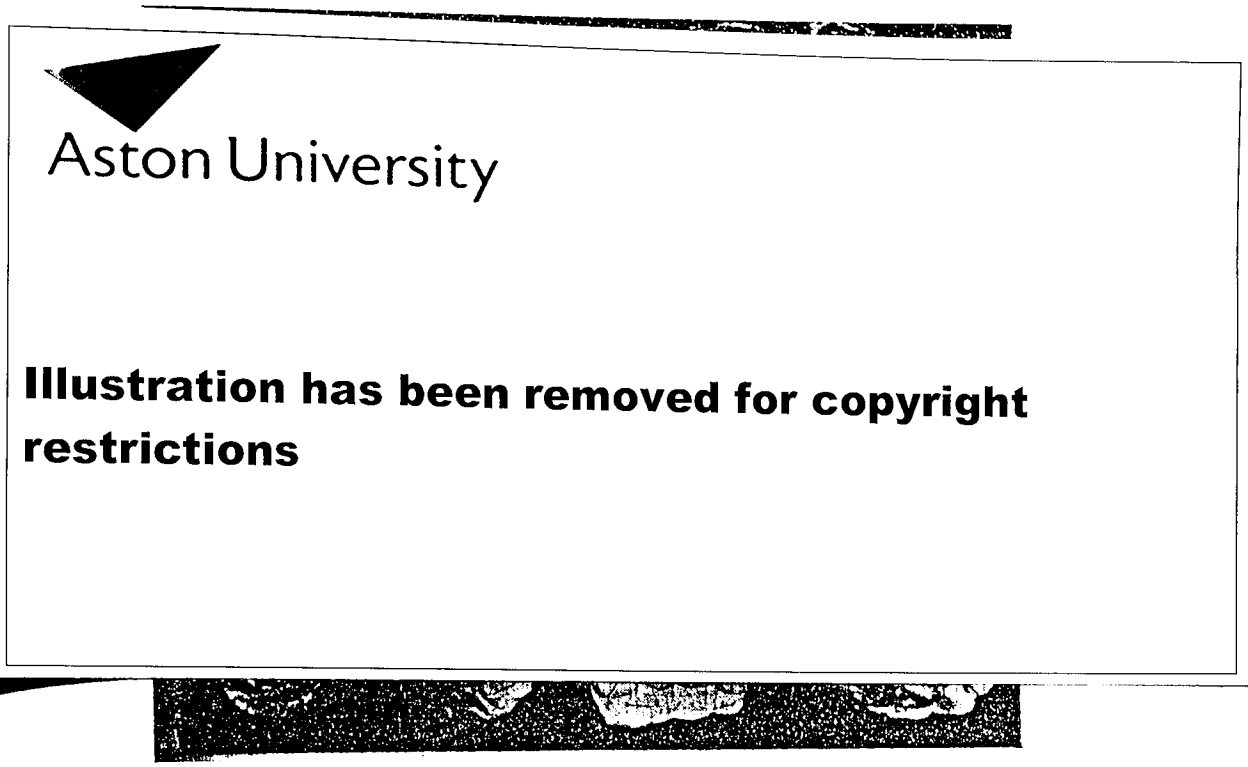

Figure 6.15. Posterior and medial aspects of six pairs of plaster casts of normal brains where the extent of striate cortex is marked in black (from Brindley 1972)

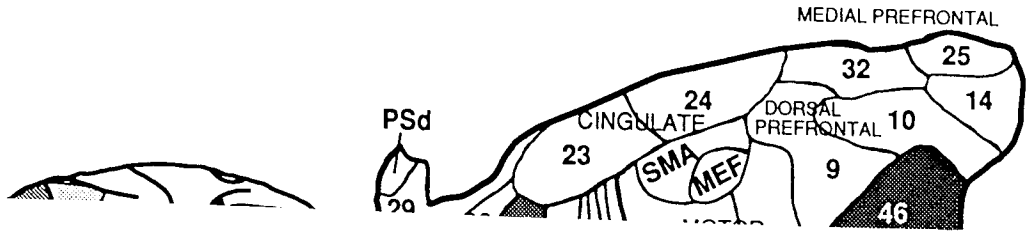

Aston University

Illustration has been removed for copyright restrictions

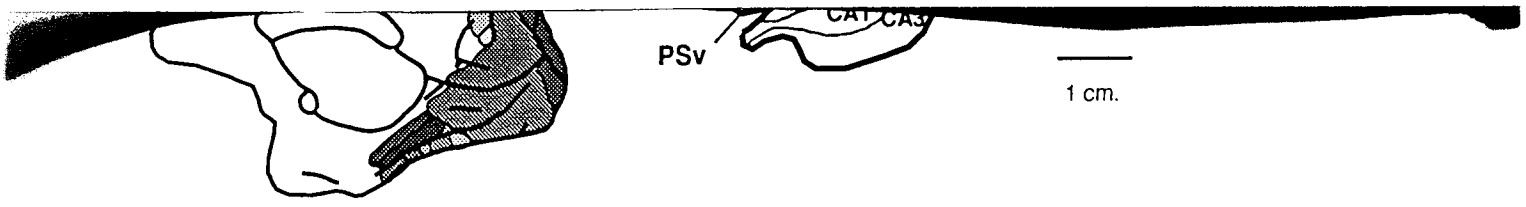

Figure 6.16. Two dimensional map of the cerebral cortex of the right hemisphere in the macaque monkey brain. To simplify the 2D presentation, a relieving cut has been made along the V1/V2 boundary. Here 32 separate cortical areas are labelled. Note only that V4 is anterior to V1 and not especially skewed superiorly or inferiorly. from Felleman et al. (1991).

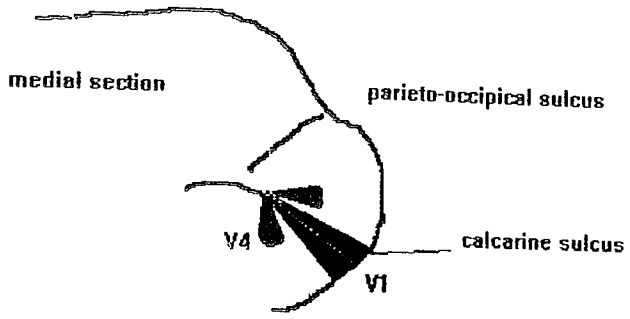

Figure 6.17. A possible site of human V4. Note the tapering of V1 meaning that peripheral V1 is straddled by V4. The diagram is purely schematic designed to illustrate the possible organisation of the areas V1 and V4, no attempt has been made to identify areas V2 and V3.

Chapter 7.

Conclusions

The calibration of gradiometer arrays using a grid of straight wires is limited by the accuracy of construction of both the gradiometers and the wire grid. The principal limitation of the technique is that the gradiometers must have relatively high intrinsic balances (figure 2.16). For the Aston system, optimal grid parameters were determined (section 2.6.3). Simulations using this grid configuration, with gradiometer balance of 10^{-4} and wire spacing error of 0.25mm RMS suggest an achievable accuracy of calibration in gain of 0.3% in position of 0.3mm and in orientation of 0.6°. In practice, the standard deviation of the *absolute* errors in channel positions and orientations were found to be 1.1mm and 1.03° (figure 2.18) which arose principally from the digitisation system used (section 2.7). However, the *relative* standard deviations of the gradiometer parameters between repeated calibrations were 0.049%, 0.27mm and 0.055° (figure 2.18). The statistical estimates derived from the practical results demonstrate that the model assumptions of the simulation studies are justified (figure 2.21). The study is unique in that it is the first in which the validity of the models used is investigated. Likewise the results improve upon all previously achieved.

It was shown that superior performance of a reference noise cancellation filter is achieved when the filter is applied to the DC corrected running average (section 3.3.1). LMS filter performance was shown to be well predicted by the analytical form based on epoch-length statistical estimates (section 3.5). In the steady state, the filter can be assumed to be driven by a non-stationary step input arising at epoch boundaries (section 3.6.2). Using this driving step approach, filter misadjustment due to non-stationarities in typical neuromagnetic measurements was found to decrease as epochs were added to the running average (figure 3.40). An optimal progression for the filter time constant is proposed (47) which improves upon fixed time constant filter performance (figure 3.40). Since the neuromagnetic signal is a-priori unknown, the results of this study provide, for the first time, a solid analytical base on which to estimate the noise both added and removed by any adaptive filter implementation.

The incorporation of the time-derivatives of the reference channels was found to improve the performance of the adaptive filtering algorithm by 15-20% for unaveraged data, falling to 5% with averaging (figure 3.46). Due to the computational cost and risk of signal corruption, this method is not recommended for the processing of averaged data.

Using the calibration and adaptive filtering techniques developed in this thesis, the neuromagnetometer was applied to the task of identifying the functional elements involved in the cortical processing of colour and luminance patterns in humans. The global magnetic field power of evoked responses to the onset of sinusoidal gratings was

shown to have distinct chromatic and luminance sensitive components (figures 6.4-6.7). Analysis of the results, using a single equivalent current dipole model, shows that these components arise from activity within two distinct cortical locations (section 6.2.6). Co-registration with MRI shows that the chromatically responsive area lies along the midline within the calcarine fissure, possibly extending onto the lingual and cuneal gyrus (figures 6.11,6.12). It is argued that this area may be the human homologue of the primate cortical area V4.

References

Alexander S.T. (1986). "Adaptive signal processing". ed D. Gries. Springer - Verlag. New York.

Allen D., Banks M.S., Norcia A.M., (1993)."Does chromatic sensitivity develop more slowly than luminance sensitivity?". Vision Res. Vol 33, pp 2553-2562.

Balish M., Muratore R. (1990). "The Inverse problem in electroencephalpography and magnetoencephalography". In :Advances in Neurology, Vol 54: Magnetoencephalography. Ed: Satsumi Sato. Raven Press, New York.

Bamidis P.D., Ioannides A.A. (1993). "Relating function (MEG) to structure (MRI) ". 9th International Conference on Biomagnetism, Book of Abstracts. Vienna, eds Deeke L., Baumgartner C., Stroink G. , Williamson S.J. pp241-242.

Barlow H.B., Levick W.R. (1965). "The mechanisms of directionally selective units in the rabbit's retina". J. Physiol. Vol 178, pp 477-504.

Barnes S., Werblin F.S. (1986). "Gated currents generate single spike activity in amacrine cells of the tiger salamander retina". Proc.Natl. Acad. Sci. USA. Vol 83, pp 1509-1512.

Baule G., McFee R. (1963). "Detection of the magnetic field of the heart". Am. Heart J. Vol 66. pp 95-96.

Baylor D.A., Lamb T.D., Yau K.W. (1979). J. Physiol. Vol 288, pp 589-611.

Berson D.M., McIlwain J.T. (1982). "Retinal Y cell activation of deep layer cells in superior colliculus of cat". J.Neurophysiol., Vol 47,pp 700-714.

Boback P., Bodis-Wollner I., Harnois C., Thornton J. (1984). "VEPs in humans reveal high and low spatial contrast mechanisms". Invest.Opthal.Vis. Sci. Vol 25 pp 104-107.

Blakemore C, Vital Durand, F. (1986). "Organization and post natal development of the monkey's lateral geniculate nucleus". J. Physiol. Vol 380, pp 453-491.

Blakemore C.B, Vital Durand, F. (1981). "Distribution of X- and Y-cells in the monkeys lateral geniculate nucleus". J. Physiol. Vol 320, pp 17P-18P.

Bogousslavsky J.J, Miklossy J., Deruaz J.P., Assal G., Regli F. (1987). "Lingual and fusiform gyri in visual processing : a clinico pathological study of altidudinal hemianopia. J. Neurol. Neurosurg. Psychiatry Vol 50, pp 607-614.

Brodmann K. (1909). "Vegleichende Localisationslehre der Grosshirinde in ihern Prinzipien dargestellt auf Grund des Zellenbaues". Leipzig. Johann Ambrosius Bath.

Bruno A.C., Dolce C.S., Soares S.D., Costa Ribeiro P., 1989, "Spatial Fourier Technique for Calibrating Gradiometers", Advances in Biomagnetism. eds Williamson S.J. Plenum Press.New York. pp 709-712.

Buchanan D,S. (1989). "Impact of different noise sources in the spherical model : a simulation". in : Advances in Biomagnetism : Eds Williamson S.J, Hoke M., Stroink G., Kotani M. Plenum Press. New-York and London. pp 539- 543.

Buchanan D.S. and Paulson D.N., 1989, "Neuromagnetometer Calibration using an array of small coils", Advances in Biomagnetism. eds Williamson S.J et al. Plenum Press.New York. pp 705-708.

Burkhalter A., Van Essen D.C. (1986). "Processing of colour, form, and disparity information in areas VP and V2 of ventral extra-striate cortex of the macaque monkey". Journal of Neuroscience Vol 6, pp 2327-2351.

Burr D.C and Morrone M. C. (1993) "Impulse response functions for chromatic and achromatic stimuli ". J.Opt. Soc. Am. A. Vol 10, No.8, pp 1706-1713.

Cadzow J. A. 1987, "Foundations of Digital Signal Processing and Data Analysis", Macmillan Publishing Company. NY.

Cantor R., Ryhanen T., Drung D., Koch H., Seppa H.(1991). "Design and optimization of dc SQUIDs fabricated using a simplified four level process". IEEE Trans. Magn. Vol 27, pp 2927-2931.

Carden D., Kulikowski J.J, Murray I.J., Parry N.R.A (1985). "Human occipital potential evoked by the onset of equiluminant gratings". J. Physiol. 242. 70-71p.

Casagrande V.A., Norton T.T. (1991). In : The Neural Basis of Visual function. ed Leventhal A.G.; from series :Vision and Visual Dysfunction. 4. Macmillan Press.

Chalupa L.M. (1989). "Visual Function of the Pulinvar". In : The Neural Basis of Visual function. ed Leventhal A.G.; from series :Vision and Visual Dysfunction. 4. Macmillan Press.

Clarke J. (1977). "Superconducting quantum interference devices for low frequency measurements". in Superconductor Applications : SQUIDs and Machines, B.B. Schwartz and S.Foner Eds. New York, NY, Plenum,pp 67-124.

Clarke J. (1989). "Principles and Applications of SQUIDs". Proc. IEEE, Vol 77, No. 8, pp 1208-1223.

Classen J.H. (1975). "Coupling considerations for SQUID devices". J. Appl. Phys.Vol 46. pp 2268-2275.

Cleland, B.G., Levick W.R. (1974). "Properties of rarely encountered types of ganglion cells in the cat's retina and an overall classification". J. Physiol. Vol 240, pp 457-492.

Crick F.H.C. (1994)."The astonishing hypothesis". publ. Simon and Schuster Ltd.

Cuffin B.N., 1986, "The effects of measurement errors and noise on MEG moving dipole inverse solutions", IEEE Trans. Biomed.Eng. vol BME-33,pp 854-861.

Cuffin B.N., Cohen D. (1977). "Magnetic fields of a dipole in special volume conductor shapes". IEEE Trans. Biomed. Eng. vol 24, pp 372:381.

Dacey M.D., Petersen M.R. (1992). "Dendritic field size and morphology of midget and parasol ganglion cells of the human retina". Proc. Natl. Acad. Sci. USA. Vol 89, pp 9666-9670.

Dacey M.D. (1993). "The Mosaic of Midget Ganglion Cells in the Human Retina". J. Neuroscience. Vol 13, pp 5334-5355.

Damasio A.R. (1985)."Disorders of complex visual processing: agnosias, achromatopsia, Balint's syndrome and related difficulties of orientation and instruction". Principles of Neural Biology. ed Mesulam M.M. Contemporary Neurology Series. Philadelphia : F.A. Davis.

de Lange, H. (1958). "Research into the dynamic nature of the human fovea-cortex systems with intermittent and modulated light; II Phase shift in brightness and delay in colour perception". J. Opt. Soc. Am. Vol 48, 784-789.

De Monasterio, F.M., Gouras, P.(1975). "Functional properties of ganglion cells of the rhesus monkey retina". J. Physiol. Vol 251, pp 167-195.

Derrington, A. M, Lennie P. (1984). "Spatial and temporal contrast sensitivity of neurons in the lateral geniculate nucleus of the macaque", J.Physiol. Lond. Vol 357, pp 219-240.

Desimone R, Schein S.J., "Visual properties of neurons in area V4 of the macaque: Sensitivity to stimulus form". J. Neurophysiol 1987, vol 57 pp 835-868.

Drasdo N. (1969). "Cortical potentials evoked by pattren presentation in the foveal region". In : Evoked Potentials : Barber C. MTP Press.

Ducla-Soares E.(1989). "Volume current effects on MEG and modelling". Advances in Biomagnetism : Eds Williamson S.J, Hoke M., Stroink G., Kotani M. Plenum Press. New-York and London. pp 533-538.

Eckhorn R., Bauer R., Jordan W., Brosch M., Kruse W., Munk M., Reitboeck H.J. (1988). "Coherent oscillations: a mechanism of feature linking in the visual cortex ?". Biol. Cybern, Vol 60, pp 121-130.

Fagaly R.L. (1990). "Neuromagnetic Instrumentation". In :Advances in Neurology, Vol 54: Magnetoencephalography. Ed: Satsumi Sato. Raven Press, New York.

Faubert J, Bilodeau L, Simonet P. (1994)."Colour motion sensitivity and transverse chromatic aberration". In: Vision Science and Its Applications. Technical Digest Series, Vol.2 (Optical Soceity of America, Washington, DC, 1994).

Falconer D.D, Ljung L.(1978). "Application of Fast Kalman Estimation to Adaptive Estimation". IEEE Trans. on Communications. vol COM -26, pp 1439-1445.

Felleman D.J., Van Essen D.C. (1991). Cerebral Cortex. Vol 1, p 1.

Flitcroft D.I. (1989). "The interactions between chromatic aberration, defocus and stimulus chromaticity: implications for visual physiology and colorimetry". Vision Res. Vol 29, pp 349-360.

Fiorentini A., Burr D.C., Morrone C.M. (1991). "Temporal characteristics of colour vision: VEP and psychophysical measurements". From Pigments to Perception. eds Valberg A. and Lee B.B. Plenum Press NY. pp 139-149.

Findlay, J.M. (1969). "Spatial integration effect on visual acuity". Vision Resarch vol 9, pp 157-166.

Enroth-Cugell C, Robson J.G. (1966). "The contrast sensitivity of retinal ganglion cells of the cat". J. Physiol. Vol 187, pp 517-522.

Felleman D.J. and Van Essen D.C. (1987). "Receptive field properties of neurons in area V3 of macaque monkey extra-striate cortex". J.Neurophysiol. Vol 57, pp 889-920.

Fieseler T., Nowak H., Ioannides A.A. (1993). "Model Studies of the accuracy of the conducting sphere model in magnetoencephalography using the spheroid". In : Recent Advances in Biomagnetism, 9th International conference on Biomagnetism, Book of Abstracts : eds Deeke L., Baumgartner C., Stroink G., Williamson S.J.pp 251-252.

Fox P.T., Mintum M.A., Raichle M.E. et al. (1986). "Mapping human visual cortex with positron emission tomography". Nature Vol 323, pp 806-809.

Fox P.T. Miezin F.M., Allman J.M., Van Essen D.C., Raichle M.E. (1987). "Retinotopic organisation of the human visual cortex with positron emission tomography". J. Neurosci, Vol 7, pp 913-922.

Fujimaki N., Tamura H., Suzuki H., Imamura T., Hasuo S., Shibatomi A. "A single chip SQUID". Advances in Biomagnetism. eds Williamson S.J et al. Plenum Press.New York. pp 705-708.

Fylan F. (1995). personal communication.

Geisler W.S. (1989). "Sequential ideal-observer analysis of visual discriminations". Psychological Review, Vol 96, pp 26-314.

Gibson J.J. (1954). "The visual perception of objective motion and subjective movement". Psychol. Rev. ,Vol 64, pp 304-314.

Gouras P. (1968). Identification of cone mechanisms in monkey ganglion cells. J. Physiol. Vol 199, pp 533-547.

Gouras P, Zrenner, E. (1979). Enhancement of luminance flicker by colour opponent mechanisms. Science, Vol 205, pp 587-589.

Gouras P, Zrenner E , (1981) "Colour coding in the primate retina". Vision Res. Vol 21, pp 1591-1598.

Grasse K.L., Cynader M.S. (1982). "Electrophysiology of the medial terminal nucleus of the accessory optic system in the cat". J. Neurophysiol., Vol 48, pp 490-504.

Grasse K.L., Cynader M.S. (1984). "Electrophysiology of the lateral and dorsal terminal nuclei of the cat accessory optic system". J. Neurophysiol., Vol 51, pp 276-293.

Grasse K.L., Cynader M. (1989). "The Accessory Optic System in Frontal Eyed Animals". In : The Neural Basis of Visual function. ed Leventhal A.G.; from series :Vision and Visual Dysfunction. 4. Macmillan Press.

Green D.G., Powers M.K., Banks M.S. (1980). "Depth of focus, eye size and visual acuity". Vision Res. Vol. 20, pp 827-835.

Guld D., Anderson V.O., Nielsen E. (1989). "Does pre-striate area V4 in monkeys process colour in agreement with the theory of Edwin Land". Seeing Contour and Colour. eds Kulikowski J.J. et al. Pergamon Press. pp 788-794.

Guy C.N., Cayles A., Walker S., Leedham-Green K. (1989). "A multi-channel biomagnetometer". Advances in Biomagnetism. eds Williamson S.J et al. Plenum Press.New York. pp 661-664.

Hamalainen M, Hari R, Ilmoniemi R. J., Knuutila J., Lounasmaa O V. (1993). Rev. Mod. Phys., Vol 65, No. 2. pp 414-496.

Harding G.F.A. (1993). "How surgeons could navigate the brain". New Scientist 140 (1903). pp 28-31.

Harding G.F.A., Wright C.E. (1986). "Visual evoked potentials in acute optic neuritis". In: Optic Neuritis, Eds: Hess R.F., Plant G.T., Cambridge University Press. pp 230-254.

Hari R., Ilmoniemi R.J. (1986). "Cerebral magnetic fields". CRC Critical Reviews in Biomed. Engineer., Vol 14:93-126.

Harris L.R. (1980). "The superior colliculus and movements of the head and eyes in cats". J. Physiol., Vol 300, pp 367-391.

Hasson R. (1991). "Mixed MEG / EEG imaging : a way forward". In : Biomagnetci Loaclisation and 3D modeling", eds J. Neonen, H.M. Rajala, T. Katila. May 1991, pp 125-135. Helsinki University of Technology, Dept. of Technical Physics.

Heiss, W.D., Pawlik G., Herholz, K., Wagner, R., Wienhard K. (1985). "Regional cerebral glucose metabolism in man during wakefulness, sleep and dreaming". Brain Res. Vol 327, pp 362-366.

Hendricks, I.M., Holliday I.E., Ruddock, K.H. (1981). "A new class of visual defect: spreading inhibition elicited by chromatic light stimuli". Brain Vol 104, pp 813-840.

Hess R.H., Barker C.L., Zihl J. (1989). "The 'motion blind' patient : low level spatial and temporal filters". J. Neurosci, Vol 9, pp 1628-1640.

Hoffman , K.-P. (1973). "Conduction velocity in pathways from retina to superior colliculus in the cat: A correlation with receptive field properties". J. Neurophysiol. Vol 36, pp 409-424.

Horton J.C., Hoyt WF (1991). "The representation of the visual field in the human striate cortex : a revision of the classic Holmes map", Arch Opthalmol vol 109 ,p 816.

Howell, E.R. and Hess R.F. (1978). "The functional area for summation to threshold for sinusoidal gratings". Vision Reseach Vol 18, pp 369-374.

Hubel D.H. (1988), "Eye, brain and Vision", publishers: Scientific American Library.

Hubel D.H., Livingstone M.S. (1989). "Segregation of Form, Colour, Movement and Depth Processing : Anatomy and Physiology". Seeing Contour and Colour. eds Kulikowski J.J. et al. Pergamon Press. pp 116-119.

Hubel D.H., Wiesel T.N. (1977). "Functional architecture of macaque monkey visual cortex (Ferrier Lecture). Proc. R. Soc. Lond. B Vol 198, pp 1-59.

Huotilanen M., Ilmoniemi R.J., Tiitinen H., Lavikainen J., Alho K., Kajola M., Simola J., Naatanen R. (1993). "Eye-blink removal for multichannel MEG measurements". In : Recent Advances in Biomagnetism, 9th International conference on Biomagnetism, Book of Abstracts : eds Deeke L., Baumgartner C., Stroink G., Williamson S.J.

Jaycox J.M. and Ketchen M.B., 1981, "Planar coupling scheme for ultra low noise dc SQUIDs", IEEE Trans Magn, vol MAG-17,pp 400-403.

Jones R, Keck M.J. (1978). "Visual evoked response as a function of grating spatial frequency". Invest Opth Vis Sci; 1978, Vol 17, pp 652-659.

Kaplan E. (1991). "Recptive fields in the cat and monkey". In : The Neural Basis of Visual function. ed Leventhal A.G.; from series :Vision and Visual Dysfunction. 4. Macmillan Press.

Kaplan E, Shapely R.M. (1982). "X and Y cells in the lateral geniculate nucleus of macaque monkeys". J. Physiol. 1982. Vol 330, pp 125-143.

Ketchen M.B., Kopley T., Ling H. (1984). "Minature SQUID susceptometer". Appl. Phys. Lett, col 44, oo 1008-1010.

Knuutila J. "Development of Multichannel SQUID Magnetometers for Neuromagnetic Measurements", 1987, Ph.D Thesis. Helsinki University of Technology.

Knuutila J., Ahlfors S, Ahonen A, Hailstrom J, Kajola M, Lounasmaa O. V, and Visa Vikman, 1987, "Large-area low-noise seven-channel dc SQUID magnetometer for brain research", Rev. Sci. Instrum. 58 (11), pp 2145, 2156.

Knuutila J, Hamalainen M.S., 1989, "On Spatial Locating Accuracy of Multichannel Magnetometers", Advances in Biomagnetism. eds Williamson S.J et al. Plenum Press.New York. pp 713- 715.

Kuffler S.W. (1953). "Discharge patterns and functional organization of mammalian retina". J. Neurophysiol. Vol 16, pp 37-68.

Kuffler S.W., Nicholls J.G. (1973). "A cellular approach to the function of the nervous system", Sunderland Mass, Sinauer Assoc.

Kulikowski J.J. (1977). "Visual evoked potentials as a measure of visibility". in: Visual Evoked potentials in man ,ed Desmedt J.E.. Oxford, Clarendon, pp168-183.

Kulikowski J.J., Bishop P.O., Kato H. (1979). "Sustained and transient responses by cat striate cells to stationary flashing light and dark bars". Brain Res. Vol 170, pp 362-367.

Kulikowski J.J., Carden D. (1989) "Scalp visual evoked potentials to chromatic and achromatic gratings in macaques with ablated visual area 4". Seeing Contour and Colour. eds Kulikowski J.J. et al. Pergamon Press. pp 586-590.

Kulikowski J.J., Leisman G. (1973). "The effect of nitrous oxide on the realtion between the evoked potential and contrast threshold ". Vision Res, Vol 13, pp 2079-2086.

Kulikowski J.J., Parry N.RA.(1987). "Human occipital potentials evoked by achromatic or chromatic checkerboards and gratings". J. Physiol 388. 45P

Kulikowski J.J, Russell M.A.H. (1989)."Electroretinograms and visual evoked potentials elicited by chromatic and achromatic gratings".Seeing Contour and Colour. eds Kulikowski J.J. et al. Pergamon Press. pp 21-35.

Land, E,H. (1974). "The retinex theory of colour vision". Proc. R. Instn. G.B. Vol 47, pp 23-58.

Lee B.B., Martin P.R. (1989). "Chromatic and Luminance channels in the primate visual pathway" ,Seeing Contour and Colour. eds Kulikowski J.J. et al. Pergamon Press. pp 21-35.

Lehnertz K. , Lutkenhoner B., Hoke M., Pantev C. (1989). "Considerations on a spatio- temporal two-dipole model". Advances in Biomagnetism : Eds Williamson S.J, Hoke M., Stroink G., Kotani M. Plenum Press. New-York and London. pp 563-567.

Lenz, G. (1921). Zwei Sektionsfalle dopelseitiger zentraler Farbenhemianopsie. Z. Ges. Neurol. Psychiatr. Vol 71, pp135-186.

Leventhal A.G., Rodieck R.W., Dreher B. (1981). "Retinal ganglion cell classes in the Old World monkey: Morphology and central projections". Science 1981. Vol 213, pp 1139-1142.

Ling F., Proakis J.G. (1984). "Numerical accuracy and stability: Two problems of adaptive estimation algorithms caused by round-off error ". Proc. ICASSP-84. pp 30.3.1-30.3.4, San Diego, Calif. March.

Livingstone M.S., Hubel D.H. (1984). "Anatomy and physiology of a colour system in the primate visual cortex". Journal of Neurosience Vol. 4, pp 309-359.

Mangel S.C., Miller R.F. (1987). "Horizontal cells contribute to the receptive field surround of ganglion cells in the rabbit retina". Brain Res. Vol. 414, pp 182-186.

Marrocco R.T., McClurkin J.W. (1985). "Evidence for spatial structure in the cortical input to the monkey lateral geniculate nucleus". Exp. Brain Res. Vol 59 pp 50-56.

Mathews V.J., Xie Zhenhua. (1993). "A stochastic gradient adaptive filter with gradient adaptive step size". IEEE Trans. Sig. Proc.Vol 41, pp 2075-2087.

Matlashov A., Slobodchikov V., Bakharev A., Zhuravlev Y., Bondarenko N.. (1993). "Biomagnetic Multi-Channel System built with 19 Cryogenic probes". in Booko f Abstracts, 9th International conference on Biomagnetism. Vienna. Eds L. Deecke, C. Baumgartner , G, Stroink, S.J. Williamson. pp 284-285.

Mays L.E., Sparks D.L. (1980). "Dissociation of visual and saccade-related responses in superior colliculus neurons". J.Neurophysiol. Vol 43, pp 207-232.

Meredith M.A., Stein B.E. (1988). "Multiple visual maps in deep superior colliculus of cats". Soc. Neurosci. Abst., Vol 14, pp 831.

Merigan W.H. (1987). "Assessing the role of parallel pathways in primates", Seeing Contour and Colour. eds Kulikowski J.J. et al. Pergamon Press. pp 198-206.

Mishkin M, Ungerleider L.G., Macko K.A. (1983). "Object vision and spatial vision : Two cortical pathways". Trends Neurosci, Vol 6 pp 414-417.

Milner P.M. (1974). "A model for visual shape recognition". Psychol. Rev, Vol 6, pp 521-535.

Moran J., Desimone R. (1985). "Selective attention gates visual processing in the extra-striate cortex". Science. Vol 299, pp 782-784.

Morrone M.C., Burr D.C., Fiorentini A. (1993). "Development of Infant Contrast Sensitivity to Chromatic Stimuli". Vision Res. Vol. 33. No 17, pp 2535-2552.

Murray I.J., Parry N.R.A, Kulikowski J.J. (1987). Clin. Vision Sci. 1, pp 231-244

Mullen K.T. (1985). "The contrast sensitivity of human colour vision to red-green and blue-yellow chromatic gratings". J. Physiol. Vol 359, pp 381-400.

Musselwaite M.J., Jeffreys D.A. (1982). "Pattern evoked potentials and Bloch's law". Vision Res. 1982. Vol 22, pp 897-903.

Nunez P.L. (1989). "Towards a physics of the neocortex". In: Advanced methods of physiological systems modeling, vol 2. Ed Marmarelis V.Z. New York: Plenum Press. pp 241-259.

Nunez P.L. (1990). "Localization of Brain Activity with EEG". In :Advances in Neurology, Vol 54: Magnetoencephalography. Ed: Satsumi Sato. Raven Press, New York.

Ogasawara K.,McHaffie J.G., Stein B.E. (1984). "Two visual corticotectal systems in the cat". J. Neurophysiol. Vol 52, pp 1226-1245.

Parker D.M., Salzen E.A., Lishman J.R. (1982). "Visual evoked potentials elicited by the onset and offset of sinusoidal gratings: Latency, waveform and topographic characteristics". Invest Opthalmol Vis Sci. Vol 22, pp 675-680.

Perry V.H., Oehler R.,Cowey A. (1984). "Retinal ganglion cells that project to the dorsal lateral geniculate nucleus in the macaque monkey". Neuroscience, Vol 12, pp 1101-1123.

Peterhans, E., Heydt ,R. von der. (1989). Mechanisms of contour perception in the monkey visual cortex. II. Contours bridging gaps. J. Neurosci. Vol 9 , pp 1749-1763.

Peters A., Jones E.G. (1984). "Classification of cortical neurons". In : Cerebral Cortex. Vol 1 : Cellular components of the cerebral cortex. Plenum Press.

Plant G.T., Zimmern R.L. , Durden K. (1983). "Transient visually evoked potentials to the pattern reversal and onset of sinusoidal gratings". Electroenceph. Clin. Neurophysiol. Vol 56, pp 147-158.

Proakis J.G., Manolakis D.G. (1988). "Introduction to Digital Signal Processing"

Purpura , K., Kaplan, E., Shapely R.M. (1988). "Background light and contrast gain of primate P and M retinal ganglion cells". Proc. Natl. Acad. Sci. USA, Vol 85, pp 4534-4537.

Ramon y Cajal S. (1954). "Neuron theory or reticular theory". Madrid. Instituto Ramon y Cajal.

Regan D. (1970). "An objective method of measuring the relative spectral luminosity curve in man". J. Opt. Soc. Am. 1970. Vol 60, pp 856-859.

Regan D. (1973). "Evoked potentials specific to spatial patterns of luminance and colour". Vision Res. Vol 13, pp 2381-2402.

Regan D. (1989). Human Brain Electrophysiology: Evoked potentials and Evoked Magnetic Fields in Science and Medicine. Elsevier.

Regan D., Speckreijse H.. (1974). "Evoked potential indications of colour blindness", Vision Res. Vol 14, pp 89-95.

Rizzo M, Damasio A.R. (1989). "Acquired central achromatopsia",Seeing Contour and Colour. eds Kulikowski J.J. et al. Pergamon Press. pp 758-767.

Robinson D.L., Goldberg M.E., Stanton G.B., (1978). "Parietal association cortex in the primate: Sensory mechansims and behavioural modulations". J. Neurophysiology, Vol 41, pp 910-932.

Rodieck, R.W., Stone, J. (1965). "Analysis of receptive fields of cat retinal ganglion cells". Vision Res. Vol 5, pp 583-601.

Rodieck, R.W., Bimmoeller, K.F., Dineen, J. (1985). "Parasol and midget ganglion cells of the human retina". J. Comp. Neurol. Vol 233, pp 115-132.

Rodieck R.W. (1988). "The primate retina". In : Comparative Primate Biology, 4, Neurosciences. pp 202-278. New York : Alan R. Liss.

Romani G. L.(1989). "Fundamentals of neuromagnetism". Advances in Biomagnetism : Eds Williamson S.J, Hoke M., Stroink G., Kotani M. Plenum Press. New-York and London. pp 33-47.

Sarvas J. (1987). "Basic mathematical and electromagnetic concepts of the biomagnetic inverse problem". Phys. Med. Biol, Vol 32, pp 11-22.

Saude T. (1993). "Occular Anatomy and Physiology". Blackwell Scientific Publications.

Scherg M. (1989). "Fundamentals of dipole source potential analysis". In : Auditory evoked magnetic fields and potentials. eds : Hoke M., Grandiori F., Romani G.L. Advances in audiology. vol 6. Basel : Karger.

Schiller P.H., (1982) "Central connections of the retinal ON and OFF pathways". Nature, vol 297, pp 580-583.

Schiller P.H. (1985). "A model for the generation of visually guided saccadic eye movements". in Models of the Visual Cortex, eds Rose D, Dobson V.G. New York, Wiley 1985, pp 62-70.

Schiller P.H. (1986). "The central visual system". Vision Res. Vol 26, pp 1351-1388.

Schiller P.H., Colby C.L., (1983). "The responses of single cells in the lateral geniculate nucleus of the rhesus monkey to colour and luminance contrast". Vision Res, Vol 23, 1631-1641.

Schiller P.H., Koerner F. (1971). "Discharge characteristics of single units in superior colliculus of the alert rhesus monkey". J. Neurophysiol., Vol 34, pp 920-936.

Schiller P., Logotheis N. (1990). "The colour-opponent and broad band channels of the primate visual system". Trends Neurosci. Vol 13, pp 392-398.

Schiller P.H., Malpeli J.G. (1977) "Properties and tectal projections of monkey retinal ganglion cells". J. Neurophysiol. Vol 40 pp 428-445.

Schiller P.H., Sandell J.H., Maunsell J.H.R.,(1986) "Functions of the ON and OFF channels of the visual system". Nature, vol 322, pp 824-825.

Schiller P.H., Stryker M. (1972). "Single unit recording and stimulation in superior colliculus of the alert rhesus monkey". J. Neurophysiol. Vol 35, pp 915-924.

Shapely, R.M. and Enroth Cugell, C. (1984). "Visual adaptation and retinal gain controls". Progress in Retinal Research, Pergammon Press, Vol 3, pp 262-346.

Shapiro S.L, Stark R.F., Teukolsky S.J. (1985). "The search for gravitational waves". Am. Sci, vol 73, pp 248-257.

Sherk H., LeVay S. (1983)."Contribution of the cortico-claustral loop to receptive field properties of the cat". J. Neurosci. Vol 3, pp 2121-2127.

Shimogawara M, Kado H. (1993). "Noise reduction methods of exotic magnetic noise source". In : Recent Advances in Biomagnetism, 9th International conference on Biomagnetism, Book of Abstracts : eds Deeke L., Baumgartner C., Stroink G., Williamson S.J. pp 307-308.

Singh K.D.S, Furlong P.L., Holliday I.E. , Harding G.F.A. "A comparision of bite-bar and head-based co-registration using Monte Carlo simulation". In preparation.

Smith V.C., Pokorny J. (1975). "Spectral sensitivity of the foveal cone photopigments between 400 and 500nm". Vision Res, Vol. 15, pp 161-171.

Sprague J.M. "Visual, acoustic and somestheic deficits in the cat after cortical and midbrain lesions". In: The Thalamus, Eds: Purpura D.D. and Yahr M. New York: Columbia Univ. Press 1966. pp 391-417.

Sprague J.M., Meikle T.H. Jr. (1965). "The role of the superior colliculus in visually guided behaviour". Exp. Neurol. ,Vol 11, pp 115-146.

Stein B.E., Meredith A.M. (1989)."Functional Organization of the Superior Colliculus ". In : The Neural Basis of Visual function. ed Leventhal A.G.; from series :Vision and Visual Dysfunction. 4. Macmillan Press.

Stok C.J. (1987). "The influence of model parameters on EEG/MEG single dipole source estimation", IEEE Trans. Biomed. Eng. BME-34, pp 289-296.

Stromeyer, C.F., Cole, G. R., Kronauer, R. E., (1987). "Chromatic suppression of cone inputs to the luminance flicker mechanisms". Vision Res. Vol 27. pp 1113-1137.

Supek S. and Aine C.J., 1993, "Simulation Studies of Multiple Dipole Neuromagnetic Source Localization : Model Order and Limits of Source Resolution", IEEE Trans. Biomed. Eng., vol 40, No. 6, pp 529-540.

Thorell L.G., De Valois R.L., Albrecht D.G. (1984). "Spatial mapping of monkey V1 cells with pure colour and luminance stimuli". Vision Res. Vol 24, 751-769.

Torre, V., Poggio T. (1981). "An application: A synaptic mechanism possibly underlying motion detection". In : Theoretical approaches in neurobiology, pp 39-46. Cambridge ,MA: MIT Press.

Tortora G.J., Anagnostakos N.P. (1984). "Principles of Anatomy and Physiology". Harper International Edition.

Tootell, R.B. H., Hamiltion, S.I., Switkes, E. (1988). "Functional anatomy of macaque striate cortex. IV contrast and magno-parvo systems", J. Neurosci, Vol 8, 1594-1609.

Toyama K., Matsunami K., Ohno T. (1969). "Antidromic identifictaion of association, commissural and corticofugal efferent cells in cat visual cortex". Brain Res. Vol 14, pp 513-517.

Ts'o D.Y., Gilbert C.D. (1988). The organization of chromatic and spatial interactions in the primate striate cortex. J. Neurosci. Vol 8, pp 1712-1727.

Van Essen D.C. (1985). Functional organization of primate visual cortex. in Peters A., Jones E.G. (eds): Cerebral Cortex. New York, Plenum, 1985, vol 3, pp 259-330.

Van Nes F.L. , Bouman M.A. (1967). Spatial modulation transfer in the human eye. Journal of the Optical Society of America. Vol 57, pp 401-406.

Van der Horst G.J.C, De Weert C.M, Bouman M.A. (1967). "Transfer of spatial chromaticity contrast at threshold in the human eye". Journal of the Optical Society of America , Vol 57, pp 260-266.

Verrey L. (1888). Hemiachromatopsie droite absolue. Archs. Opthalmol. (Paris) Vol 8. pp 281-301.

Wellstood F.C., Urbina C., Clarke J. (1987). "Low frequency noise in dc superconducting quantum interference devices below 1K". Appl. Phys. Lett., Vol 50, pp 772-774.

Werblin, F.S., Dowling J.E. (1969). "Organization of the retina of the mudpuppy, Necturus maculosu. II. Intracellular recording". J. Neurophysiol., Vol 32, pp339-355.

Werblin, F.S. (1972). "Lateral interactions at inner plexiform layer of vertebrate retina: Antagonistic response to change". Science, Vol 175, pp 1008-1010.

Werblin, F.S., Maguire, G., Lukasiewicz P., Eliasof S. and Wu S.M. (1988). "neural interactions mediating the detection of of change in the retina of the tiger salamander". Vis. Neurosci, Col 1, pp 317-329.

Widrow B., Mabtey P., Griffiths L., Goode B. (1967). "Adaptive antenna systems". Proc. IEEE, Vol 55, pp 2143-2159.

Widrow B., Glover J.R., McCool J.M., Kaunitz J., Williams C.S., Hearn R.H., Zeidler J.R, Dong E., Goodlin R.C. (1975)."Adaptive Noise Cancelling : Principles and Applications". Proc. IEEE, Vol 6, No. 12, pp 1692-1716.

Widrow B., McCool J., Larimore M.G., Johnson C.R. (1976). "Stationary and non-stationary learning characteristics of the LMS Adaptive filter". Proc. IEEE, Vol 64, No. 8., pp 1151-1162.

Widrow B., Stearns S.D. (1985). "Adaptive signal processing". Englewood Cliffs, NJ: Prentice-Hall.

Widrow B, Walach E. (1984). "On the statistical efficiency of the LMS algorithm with non stationary inputs". IEEE Trans. Inf. Theory. Vol IT-30.

Wiesel, T.N., Hubel D.H. (1966)."Spatial and chromatic interractions in the lateral geniculated body of the rhesus monkey". J. Neurophysiol. Vol 29, pp 1115-1156.

Williamson S.J., Kaufman L. (1981). "Biomagnetism". Journal of Magnetism and Magnetic Materials. Vol 22 p 129.

Williamson S.J, Kaufman L. (1989). "Theory of neuroelectric and neuromagnetic fields". In : Auditory electric and magnetic fields. eds :Grandori F., Hoke M., Romani G.L. Karger.

Willis A.(1994). personal communication.

Wisowaty J.J. (1981). "Estimates of teh temporal response characteristics of chromatic pathways". J. Opt. Soc. Am. Vol 71, pp 970-977.

Wong-Riley M. (1979). "Changes in the visual system of monocularly sutured or nucleated cats demonstrable with cytochrome oxidase histochemistry". Brain Res. vol 171, pp 11-28.

Wright W.D.(1946). "Researches on normal and defective colour vision". London, Kimpton, 1946.

Zanow F. Verhoef R., Knosche T., Peters M.J. (1993). "Are standard head models superior to the sphere model in MEG source localizations ?". In : Recent Advances in Biomagnetism, 9th International conference on Biomagnetism, Book of Abstracts : eds Deeke L., Baumgartner C., Stroink G., Williamson S.J. pp 253-254.

Zeki S.M. (1969). "Representaion of central visual fields in the pre-striate cortex of monkey". Brain Res Vol 14, p 271.

Zeki, S.M. (1974). "Functional organization of a visual area in the posterior bank of the superior temporal sulcus of the rhesus monkey". J. Physiol.(Lond). Vol 236, pp 549-573.

Zeki, S.M. (1978). "The third visual complex of rhesus monkey pre-striate cortex". J. Physiol.(Lond). Vol 277,pp 245-72.

Zeki S.M. (1983). "Colour coding in the cerebral cortex: The reaction of cells in monkey visual cortex to wavelengths and colours". Neuroscience Vol 9, 741-756.

Zeki, S.M. (1993). "A vision of the brain ".publ. Blackwell Scientific.

Zeki, S.M. and Shipp S. (1989). "Modular connections between V2 and V4 of macaque monkey visual cortex ". Eur. J. Neurosci. Vol 1, 494-506.

Zeki, S.M. and Shipp S. (1990). "Functional segregation within area V2 of macaque monkey visual cortex". In :Seeing Contour and Colour, edited by J.J. Kulikowski , C.M. Dickinson and I.J. Murray. Pergamon Press, Oxford. pp 120-124.

Zeki, S., Watson J.D.G, Lueck C.J. et al.(1991). "A direct demonstration of functional specialization in the human visual cortex". J. Neurosci. Vol 11, pp 641-649.

Zihl J., Cramon, D. von , Mai N., (1983). "Selective disturbance of movement vision after bilateral brain damage". Brain Vol 106, pp 313-340.

Zrenner E. (1983). Neurophysiological Aspects of Colour Vision in Primates. New York, Springer-Verlag.

Appendix : Estimate of LMS jitter noise

Continuing from chapter 3, section 3.2.8. Jitter noise in the LMS algorithm can be thought of as due to the error between the ideal gradient step and its stochastic approximation.

That is, the gradient estimate can be expressed as

$$\tilde{\nabla}(n) = \nabla(n) + \mathbf{G}(n)$$

Where **G** is the vector representing the noise involved in the approximation.

In the steady state, that is, around the optimal solution

$$\mathbf{G}(n) = -2.y(n).\mathbf{x}(n)$$

$$\text{cov}[\mathbf{G}(n)] = E[\mathbf{G}(n)\mathbf{G}^T(n)] = 4.E[y^2(n).\mathbf{x}(n).\mathbf{x}^T(n)]$$

At the optimal solution, the filter output and references are independent, hence

$$\text{cov}[\mathbf{G}(n)] = 4.E[y^2(n)]E[\mathbf{x}(n).\mathbf{x}^T(n)] = 4E_{\min}.\mathbf{R}$$

Pre-multiplying by the modal matrix **M** (12) gives the transformed gradient noise vector **G'** where

$$\mathbf{G}(n)' = \mathbf{M}^{-1}\mathbf{G}(n)$$

and

$$\text{cov}[\mathbf{G}'] = 4E_{\min}.\Lambda$$

which gives a noisy decoupled weight update equation of

$$\mathbf{v}'(n+1) = \mathbf{v}'(n) + \mu(-\Lambda.\mathbf{v}'(n) + \mathbf{G}'(n))$$

If **x** is uncorrelated over time then the gradient noise will be uncorrelated with the weight vector, and it can be shown (Widrow, 1975) that

$$\text{cov}[\mathbf{v}_j'] = \mu.E\min.(\mathbf{I} - \mu.\Lambda)^{-1}$$

or for small μ

$$\text{cov}[\mathbf{v}_j'] = \mu.E\min$$

The above expresses the decoupled weight covariance due to the noise implicit in the stochastic approximation of gradient. A useful measure is the amount of excess MSE due to this weight variance. From (16) :

$$\text{Average excess mse} = \text{E}[\mathbf{v}'^T\Lambda\mathbf{v}'] = \sum_{i=0}^{i=N-1} \lambda_i.E[(v_i')^2]$$

Leading to an expression for the average excess noise due to jitter

$$\text{Jitter noise} = \mu.E_{\min}\sum_{p=0}^{n-1}\lambda_p.(\frac{1}{1-\mu\lambda_p}), \quad (48).$$

For nominally orthogonal reference channels, and small μ, the above is often (Widrow 1976) approximated by

$$\text{Jitter noise} = \mu . E_{min} . \text{tr}\,(\mathbf{R}) \qquad 48.$$

It is more instructive to express noise as a proportion of the useful signal power. At this point therefore the dimensionless quantity M or misadjustment is introduced, defined as

$$M = \frac{\text{Average excess mse}}{E_{min}}$$

Misadjustment due to jitter is therefore

$$M_{jitter} = \mu . tr(\mathbf{R})$$

It is clear from the above that jitter noise is directly proportional to μ; and in the case of nominally equal eigenvalues, misadjustment increases as reference channels are added to the system.